Finite Element Implementation and Adaptive Methods in Coupled Problems

Vom Promotionsausschuss der
Technischen Universität Hamburg

zur Erlangung des Akademischen Grades

Doktor-Ingenieur (Dr.-Ing.)

genehmigte Dissertation

von
Christos Vokas

aus
Kavala, Griechenland

2021

1. Gutachter:	Prof. Dr.-Ing. Manfred Kasper
2. Gutachter:	Prof. Dr.-Ing. Otto von Estorff
Prüfungsvorsitzender:	Prof. Dr. rer. nat. Daniel Ruprecht

Tag der mündlichen Prüfung: 29. Juni 2021

DOI: https://doi.org/10.15480/882.3857

Abstract

This thesis revolves around three key elements. The first one is the Finite Element Method. The second is field coupling and consequently Coupled Problems. The third is Adaptivity. The Finite Element Package PolyDE serves as the basis of conducting the necessary work, in order to implement coupled physics modes and test adaptive algorithms on them.

Coupling effects are a central characteristic in the simulation of Microsystems. A general Partial Differential Equation framework which has been applied to the PolyDE code, allows for the simultaneous field-solution of multiple-field problems, once the respective physics mode has been implemented. The effort towards the implementation shall be minimal. As an example, the same framework is able to host piezoelectricity and incompressible fluid flow. The derivation of various physics modes and the realization through the mapping of the material parameters to the PDE coefficients of the general PDE, are presented as a major component of this report. In this thesis-approach, only one global equation system of the type "$\mathbf{Ax} = \mathbf{b}$" is numerically solved for, in order to simultaneously obtain field solutions for all the involved problem fields. There is no sequential approach such as solve for one field first and then use the solution as the input to the second field problem.

Based on the existing implementation of adaptive codes for single-field problems, this work goes in the direction of extending their usability, by programming them to treat multi-field problems based around the PolyDE general PDE structure. The complexities that immediately arise, such as the common mesh and the non-common element orders for the different fields in multi-field problems, indicate that this is an area that can offer a wide range of possibilities for further research. The functionality of the developed *h*-adaptive multi-field algorithm, has been proven on all problem test cases. The developed *p*-adaptive multi-field algorithm has behaved as expected. For the *hp*-adaptive algorithms, the experimentation has provided initial results which are presented, and can be utilized as a basis for future research in the quest for more sophisticated *hp*- generally applied algorithms, that could ideally treat a wide range of problems, from wave to fluidic and others.

Acknowledgements

First, I thank Prof. Dr.-Ing. Manfred Kasper, the advisor during my experimentation with the Finite Element Method. I thank him for the provided guidance and assistance which have contributed towards the completion of my dissertation. I additionally thank Prof. Dr.-Ing. Otto von Estorff and Prof. Dr. rer. nat. Daniel Ruprecht for acting as the 2nd examiner and the examination-chair respectively.

I mention Prof. Dr.-Ing. Hoc Khiem Trieu and Prof. Dr.-Ing. Jörg Müller, and acknowledge them for heading the Institute of Microsystems Technology, during my presence as an employee at the location.

I thank preceding employees at the Institute of Microsystems Technology, namely Marc Schober, Bodin Kasemset and Razi Abdul Rahman, for their preceding work, mainly their contributions to the involved software package. I also thank Guilherme Brondani Torri, former Master student, for his contribution.

I mention my former colleagues Timo Lipka and Jury Anatzki. Timo has been the one office-sharing colleague during my stay at the Institute and it was a pleasure joining him for his cigarette breaks or for short walks around the campus. I additionally thank both Timo and Jury for my graduation-hat assembly and presentation respectively.

Last but certainly not least I thank my immediate family for their provided assistance and their frequent visits to Hamburg, either for supporting me during my stay there or for tourism purposes.

Contents

List of Symbols

$\mathbf{A}$	Matrix system left hand side
A	Thermal expansion tensor
$\mathbf{b}$	Matrix system right hand side
C	Elasticity tensor
c	Mass concentration
c_p	Specific heat
$\boldsymbol{D}$	Electric displacement
D	Molecular diffusivity
$\boldsymbol{E}$	Electric field
E	Energy
e	Piezoelectric tensor
e^t	Converse piezoelectric tensor
$\bar{e}$	Electron charge
$e^2_{\bar{T}:i}$	Element-wise refinement indicator
$\boldsymbol{F}$	Body force
f	PDE scalar source term
g	PDE vector source term
h	Element diameter
i	Index number
$\acute{\imath}$	Structural mechanics index
$\grave{\imath}$	Structural mechanics index
$\boldsymbol{J}$	Current density
j	Index number
$\acute{\jmath}$	Structural mechanics index
$\grave{\jmath}$	Structural mechanics index
k	Index number
$\acute{k}$	Structural mechanics index
k_B	Boltzmann's constant
l	Index number
$\acute{l}$	Structural mechanics index
M	Stress-temperature tensor
N_A	Avogadro's constant
n	Number of fields
P	Pyroelectric tensor
p	Fluidic pressure
p_E	Element polynomial order
Q_{ted}	Thermoelastic dissipation
q	Value in Neumann boundary condition
q	Produced heat
R_i	Error indicator for field i
$r_{(\bar{T}):i}$	Element residual for field i
S	Seebeck coefficient
T	Temperature field
T_0	Reference temperature

$\bar{T}$	Triangle
$\acute{T}$	Neighboring triangle
u	PDE field variable
u_{st}	Mechanical displacement
u_x	*x*-displacement field
u_y	*y*-displacement field
v	Test function
$\boldsymbol{v}$	Vector velocity
v	Scalar velocity
v_x	*x*-velocity component field
v_y	*y*-velocity component field
W	Error estimator weighing factor
$\mathbf{x}$	Matrix system vector of unknowns
z	Ionic valence
α	PDE material parameter
β	PDE material parameter
β_{PML}	Perfectly matched layer damping parameter
Γ_{D}	Dirichlet boundary condition
Γ_{N}	Neumann boundary condition
γ	PDE material parameter
ε_0	Permittivity of free space
ε_{r}	Relative permittivity
$\varepsilon_{\mathrm{st}}$	Elasticity strain
$\varepsilon_{\mathrm{st}\theta}$	Thermal strain
$\eta^2_{\bar{T}:i}$	Element-wise error estimator
λ	Thermal conductivity
μ	Dynamic viscosity of the fluid
ν	PDE material parameter
ξ	Shape function
Π	Peltier coefficient
ρ	Material density
ρ_f	Space charge density of free ions
σ	Electric conductivity
σ_{st}	Elasticity stress
Φ	Electric potential field
Ω	Computational domain
ω	Angular frequency

1. Introduction

1.1. The Finite Element Method

The Finite Element Method (or FEM for short) is technically employed in order to numerically analyze physical structures and phenomena and simulate their behavior. It can find approximate solutions of Partial Differential Equations (or PDEs) and consequently field plots can be obtained. In numerical effort terms, a field-level simulation (Figure 1-2) roughly stands between a component simulation (Figure 1-1), and an atomic-level simulation [65].

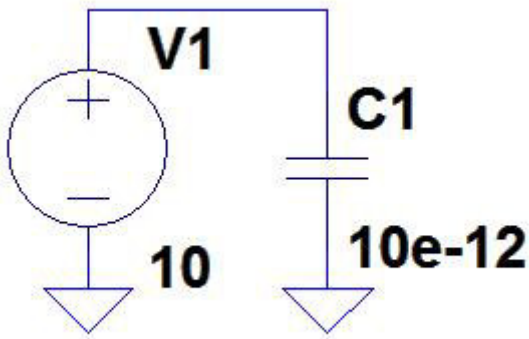

Figure 1-1 SPICE representation of a 10pF capacitor with a plate potential difference of 10V

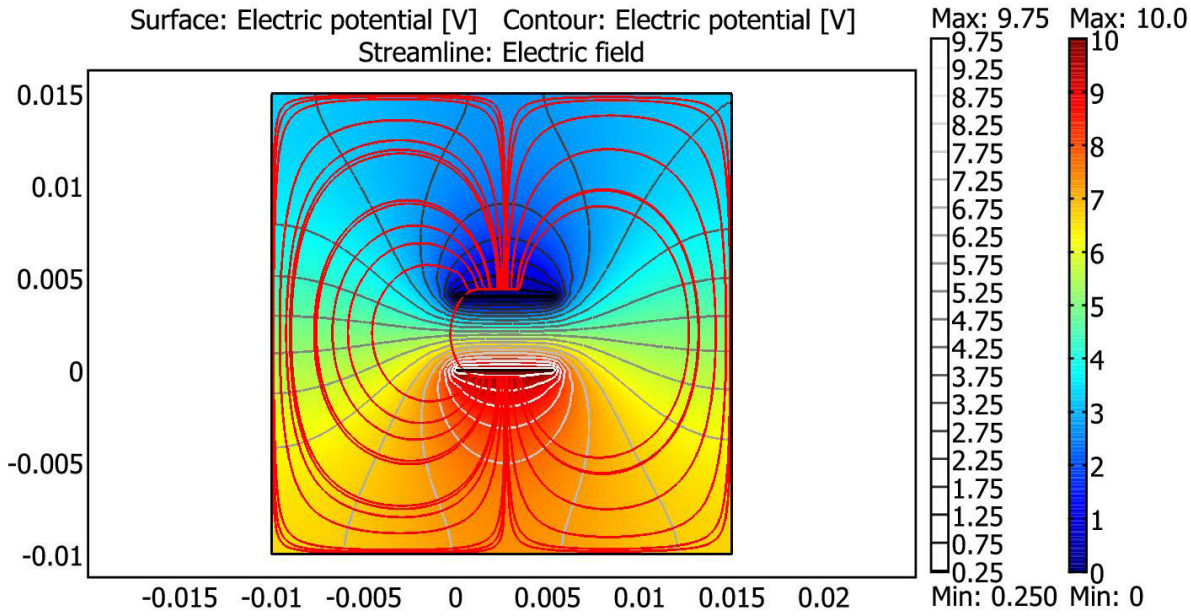

Figure 1-2 Field solution obtained for a parallel plate capacitor of approximately 10pF under an applied voltage of 10V. The two scales to the right of the plot denote the electric potential in Volts

Figure 1-1 and Figure 1-2 are meant to represent the same capacitor in the condition of a plate potential difference of 10 Volts, but whereas in the component representation [71] there is 1 Degree of Freedom (DOF), in the field representation [25] there are 1257 DOFs and this means the system should be solved for 1257 unknown potential values.

The origin of the FEM can be traced back in the 1940s and some of the pioneers are Alexander Hrennikoff [56], Richard Courant [27], Olgierd Zienkiewicz [133] and Boris Galerkin [48]. The first technical application of the FEM was for structural analysis in the 1950s. Since that decade, the application range has been widened to a larger number of phenomena. Some of these phenomena are: heat transfer, electromagnetism, gravity and fluid flow.

In the present days, a wide range of FEM simulation programs is available for use. Some of these programs are mainly commercial and some of them primarily serve research purposes and their internal functionality can be freely investigated [84, 4, 29, 25].

1.2. Coupled Problems and their importance

In the finite element method, the term "coupled" can be employed among other usages, in order to describe a type of multiple-field problems. A multiple-field problem is one where a numerical solution to more than one field has to be obtained. At a first stage the solution to these fields can be obtained independently for everyone, by neglecting any possible physical interaction between them. At a second stage there may be a numerical setup where one field influences a second one but the opposite influence is missing. This is then described as a unidirectional coupled problem. The third stage is the situation where a field influences and is also influenced by the other field in a bidirectional manner. In the last case the problem is fully coupled. Table 1-1 makes use of two fields, the temperature (T) and the electric potential field (Φ), in order to demonstrate the three points that were just mentioned.

Table 1-1 Multiple-field problems categorized in three types, based on the existence of coupling effects

Uncoupled	T	-
	-	Φ
Unidirectional Coupling	T	$T \leftarrow \Phi$
	-	Φ
Bidirectional Coupling	T	$T \leftarrow \Phi$
	$\Phi \leftarrow T$	Φ

For multiple-field problems where the number of fields is larger than 2, defining the type of coupling is trickier. If there is at least one field that influences and is simultaneously influenced by another one, then this type can be classified as a bidirectional but not fully

coupled problem. If all fields influence and are also influenced by every other field, then this is a fully coupled problem. Table 1-2 demonstrates these points by taking into account the *x*-displacement field (u_x), the *y*-displacement field (u_y) and the temperature field (T).

Table 1-2 Three-field problem with bidirectional and full coupling

Bidirectional Coupling	u_x	$u_x \leftarrow u_y$	$u_x \leftarrow T$
	$u_y \leftarrow u_x$	u_y	$u_y \leftarrow T$
	-	-	T
Full Coupling	u_x	$u_x \leftarrow u_y$	$u_x \leftarrow T$
	$u_y \leftarrow u_x$	u_y	$u_y \leftarrow T$
	$T \leftarrow u_x$	$T \leftarrow u_y$	T

The importance of coupled field problems, lies in the fact that today many miniaturized devices, such as fuses, diodes and transistors, need to be comprehensively studied and modeled before they reach the market. For example the reliability of a transistor can be predicted more accurately if the thermal strain and stress fields are simultaneously modeled with the temperature field. The manufacturer can more accurately indicate that if transistor "X" ran at a constant 70°C, then it would have a lifetime of three years. If it ran at a constant 40°C, then it would have a longer lifetime. Although the reliability of such a transistor can also be tested physically in the laboratory, modeling considerably reduces the development and physical testing costs.

Additionally, the simulation of coupled problems plays a very important role in the microsystem industry. Microsystem devices heavily take into account the interaction between fields. For example the mixing ability of a microfluidic mixer can be controlled by electrodes that produce an electric field in the region of fluid flow. Another example is a thermal actuator, where the mechanical displacement is influenced by the temperature field.

1.3. Adaptive methods for finite elements

As mentioned in Section 1.1, the finite element method can obtain approximate solutions to partial differential equations. Approximate means, that the solution cannot numerically reproduce the physical field with 100% accuracy. The question that arises then is how accurate the solution is and furthermore, what can be done to improve it and hence improve the reliability of the numerical simulation.

For the accuracy judgment, mathematical constructs have already been produced which are called "error indicators". Additionally, for the improvement of the solution at the critical areas of the field, techniques have already been implemented which are described as "adaptation techniques". The purpose that an adaptation technique serves is to balance between solution accuracy improvement and computational resources.

1.4. Motivation

Having the possibility to simultaneously solve for many fields is advantageous in the modeling of devices, however it greatly increases the number of DOFs and hence the computational complexity and effort. The scope of this thesis is to not only implement and experiment with multi-field physics modes on a general framework, but also to produce adaptive algorithms, apply them on this general multi-field framework and test their functionality.

1.5. Chapters overview

The following chapter (Chapter 2), first presents a partially philosophical discussion on field definition and then on multi-field problems and microsystems. It then proceeds by presenting a literature review on comparable simulation techniques. The reason behind this first review part, is to single out the finite element method from the rest of the techniques, in terms of its direct multiple-field solvability. Once this is done, it presents a review on milestones of the finite element method development, and intends to portray these milestones as motivation for the work in the actual thesis. After that, the fundamental formulae behind the finite element method are demonstrated in detail, and also how these formulae can be used in a coupled field framework. The chapter closes by presenting the derivation of several multi-field physics modes, and also their respective mapping to the general partial differential equation.

Chapter 3 first presents a review on error estimation and FEM adaptation methods and their application on coupled problems by means of algorithm presentation. It then presents aspects of the software package which is being developed internally at the institute [66]. It displays some of its organizational features and it also discusses the necessity of the integration of a more recent linear-equations-system solver package [35].

Chapters 4 and 5 present the results obtained after testing all of the newly implemented multi-field adaptive algorithms on three coupled problems. The choice of the physics modes for testing, was made in terms of their relation to microsystems and in terms of their complexity. Each of the problems has at least three fields to be solved for and two of the problems are nonlinear. The testing of complicated physics modes produced a large number of result-figures. In order not to exhaust the chapters with these figures, many of them have been placed in Appendix A1 and Appendix A2, should the reader wish to investigate them.

Chapter 6 is a review of the achievements of the thesis work and makes suggestions for further improvements and possible future additions to the internally developed software package [66].

2. The Finite Element Method in Coupled Problems

2.1. Fields, coupled problems and usage of comparable simulation techniques in coupled problems

2.1.1. Field in physics

As already stated in Section 1.2, in the finite element method, the term "coupled problem" can be used to describe a multiple-field problem. Before analyzing the importance of coupled problems further, the definition of a field is first given. From the Encyclopaedia Britannica [44]:

"*field, in physics, a region in which each point is affected by a force*"

Some types of fields are: the electric field, the magnetic field and the gravitational field. When a charged particle is placed in the region of an electric field, it experiences an electric force. When a particle with mass is placed in the region of a gravitational field, it experiences a gravitational force.

Before proceeding to the presentation of various fundamental finite element formulations later on in the chapter, a discussion that is to some extent philosophical, concentrates on the distinction between two fields. These two fields are both related to motion but yet they are considered separate. The first is the thermal field [70]. The scalar field quantity that is used to describe it is the temperature. For a particle or a group of particles, the temperature is an indication of the mean kinetic energy of the particle or particles, moving relative to the centre of mass of the particle or the body which the particles are part of. A particle can be an atom, whereas a group of particles can be a group of similar atoms or a molecule. The thermal field indicates the thermal energy that is stored in the volume in which these particles exist.

The question that arises is what happens to a particle if it is introduced in the region of the thermal field. If the temperature of the particle is the same as the temperature at the field point of introduction, then nothing happens in the thermal sense. For a particle of different temperature, the answer is that it will be forced to a change of its thermal energy. However, unlike the electric force that will tend to accelerate or decelerate a charged particle in the direction of the electric field, the tendency towards a new thermal equilibrium will alter the temperature of the individual particle. If the temperature of the particle is higher than the temperature at the field point of introduction, then energy will flow outwards from the particle to the surrounding field. In the opposite case, the energy flow will be inwards.

The second field to look at is the velocity field. Unlike the thermal field which is scalar, the velocity field is a vector field. In two spatial dimensions it has two scalar components, whereas in three spatial dimensions it has three scalar components. This is because the

velocity field has magnitude like the thermal field, but it additionally has direction. The laminar flow of water particles in a water channel can be described by the velocity field [106]. The velocity field is an indication of the kinetic energy of the flowing particles. If a zero-velocity particle is placed in the region of the velocity field, it will experience a force that will increase the speed of the particle and it will give a direction to its speed, hence velocity.

As stated earlier, the temperature is an indication of kinetic energy, and the velocity is as well an indication of kinetic energy. Both quantities are concerned with kinetic energy but they are different. The difference is the following: the temperature is concerned with disordered motion or oscillation, whereas the velocity is concerned with ordered motion. From this it is deduced that when a particle is placed in the region of a simultaneously thermal and velocity field, it will experience both a thermal (disordered vibration) force and a velocity (ordered kinetic) force.

From a simulation point of view, the simultaneous treatment of thermal and velocity field, allows for the attainment of a higher degree of problem information and accuracy compared to the treatment of only one field. Figure 2-1 demonstrates this point with a channel that has two inlets and one outlet.

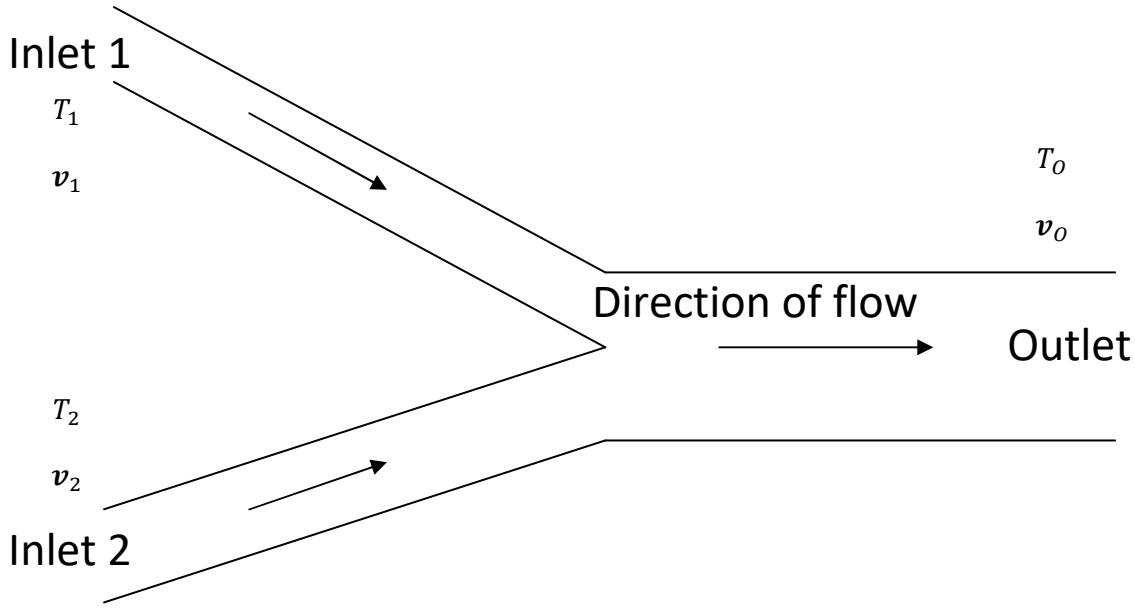

Figure 2-1 Double inflow, single outflow channel

Suppose that the total energy that is entering the channel from inlets 1 and 2 is already known. From the simulation, the total energy that leaves the channel through the outlet is expected to be obtained. Assuming that there are no friction losses between the fluid and the channel walls, the energy entering the channel should equal the energy that is leaving the channel. Therefore:

$$E_{KIN,1} + E_{TH,1} + E_{KIN,2} + E_{TH,2} = E_{KIN,O} + E_{TH,O} \quad (2.1)$$

If the thermal field is neglected, then the only calculation that can be made is:

$$E_{KIN,1} + E_{KIN,2} = E_{KIN,O} \quad (2.2)$$

This automatically assumes that:

$$E_{TH,1} + E_{TH,2} = E_{TH,O} \quad (2.3)$$

This assumption means that the problem is decoupled. It means that temperature does not affect velocity. However, it is known from physics that temperature affects pressure and that in a flow problem, a pressure gradient can affect the velocity of the fluid. Hence temperature and velocity should be coupled. Therefore the assumption in (2.4), is more accurate than the ones in (2.2) and (2.3).

$$E_{Total,1} + E_{Total,2} = E_{Total,O} \quad (2.4)$$

(2.4) allows for the conversion of thermal energy to ordered kinetic energy and vice versa.

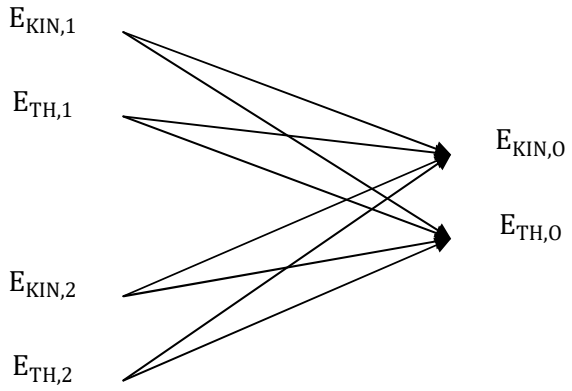

Alternatively the problem of Figure 2-1 could be simulated on the atomic level. A model for every atom in the flow channel, where each model would include information for the overall motion of the atom, without distinguishing into vibration or flow motion could be created. The difficulty with that approach is that it requires a huge amount of computational resources, and that with modern day computers is an impossible task. The field simulation aims to categorize the different types of atomic behavior and simulate these behaviors on a large number of atoms collectively.

2.1.2. Multi-field problems

One term that is widely employed in the area of FEM simulation is "multi-physics". In [26] it is stated that "it is a multi-physics world". Although there may be some argument that there is only one physics governing our world, in the simulation sense, this term partially intends to point to solution obtaining numerical procedures of higher complexity. The position of this thesis is that the world is governed by a single physics but with multiple fields. For example gravity and electromagnetism both belong to the wider physics context but they are separate fields. They can both exist in the same space but each point in the simultaneous presence of the two fields is affected by two forces, namely the electromagnetic and the gravitational. Any usage of the term multi-physics in this thesis is considered purely in an engineering and numerical analysis sense, since quite a number of simulation software companies and engineers employ this term today. Table 2-1 mentions a few of these uses by picking out "multi-physics" phrases from a few software packages.

Table 2-1 The usage of the term "multi-physics" in a few software packages

Software Package	Statement of interest	Reference
ADINA	**Multiphysics** problems are encountered when the response of a system is affected by the interaction between several distinct physical fields.	[1]
ANSYS	**Multiphysics** Solutions Simulation for the Real World.	[5]
COMSOL	With a **multiphysics** capable simulation tool, you can correctly capture the important aspects of your design.	[26]
Elmer	Elmer is an open source **multiphysical** simulation software.	[29]
SIMULIA	Through the years additional **multiphysics** capabilities have been added, such as fluid, thermal, and electrical couplings, to name a few.	[33]

According to a survey in [81], modeling and simulation of multi-physics problems can be categorized into multi-field, multi-domain and multi-scale procedures. Multi-field denotes the excitation of a system by more than one physical fields. The thermal expansion of a heated metal block is an example of a multi-field problem that involves the temperature and the mechanical displacement fields. Multi-domain denotes the interaction among continuum representations of systems with significantly different properties through sharable boundaries. One example of a multi-domain problem is the propagation of gas bubbles inside a liquid. Multi-scale is used in order to denote different modeling length scales such as the meter and the micrometer scale and the bridging (information passing) between these scales. One point to note about [81] is that there is little emphasis on FEM.

To put the work of this thesis into the wider multi-physics context, one of the intentions is to present a general mathematical formulation that allows for the solution of multi-field problems with an arbitrary number of fields. There is reasonable suspicion that this is the direction that a software package like [25] and others follow. However the internal workings of many packages are not openly accessible. The formulation can be applied to different length scales, however there is no focus on coupling and passing information between the different length scales. The programming aspects and the algorithmic development that accompany the mathematical formulation, focus solely on the finite element method. The literature review in Section 2.1.4, aims to provide conclusive evidence deduced from the research of various authors, as to why the alternatives to the finite element method are considered to be weaker choices.

A chronological investigation into multi-field effects, reveals the discovery of the thermoelectric effect in 1821, by Thomas Johann Seebeck [104]. Historically, this effect can be described as one of the first, if not the first coupled-field phenomenon to be observed. Seebeck discovered that a temperature difference induces an electric potential difference and hence a flow of electric current in a closed circuit configuration. In 1834, Jean Charles Athanase Peltier [96] discovered the reverse effect, namely the Peltier effect. An electric potential difference generating a current flow, can cause a temperature gradient.

Although Seebeck and Peltier discovered coupled field phenomena, they did not provide any field formulations. The first scientist to do so was Claude-Louis Navier by presenting the Navier-Stokes equations [22] for incompressible fluids in 1822. Further works on multi-field formulations include electrodynamics by James Clerk Maxwell [76] and coupled thermoelasticity by Maurice Anthony Biot [17]. Piezoelectricity was discovered in 1880 by Jacques Curie and Pierre Curie [30]. It is a coupled field phenomenon involving the electric field (electrostatics) and the mechanical displacement field. Magnetothermoelasticity [108] invloves the magnetic, the thermal and the mechanical displacement fields.

The number of fields in present day multi-field problems can range from two up to approximately five but it can vary according to the definition. Assuming the magnetic potential to be a scalar quantity in a given problem, magnetothermoelasticity can be considered to be a three-field problem in two dimensions and in three dimensions as well. This consideration is done on the basis that the mechanical displacement (elasticity) field is a single vector field. Alternatively it can be considered to be a four-field problem in two dimensions and a five-field problem in three dimensions. This alternative consideration is done on the basis that the 2D mechanical displacement in essence comprises of two fields whereas the 3D mechanical displacement of three fields. The difference is that in the former case, scalar and vector fields are mixed in the problem formulation, whereas in the latter case, all fields are scalar, because vector fields are split into scalar field components in the problem setup. In this thesis the second approach is used. The reason for doing so is adherence to an approach that is as general as possible and consequently simplicity in the programming implementation of new physics modes.

The paper [54] presents a classification scheme for coupled-field problems. It distinguishes between geometrical, physical property, numerical method and time constant coupling. The physical property coupling is done in terms of the material parameters and the source terms according to this scheme. To put this thesis into perspective once more, out of the four coupling types, of interest is the physical property coupling. This type of coupling can be further grouped into three categories. The first category involves coupling in terms of the material parameters, where for every field equation a material parameter adds a contribution of another field quantity to this equation. To demonstrate this (2.5) and (2.6) are considered. The former is a simplified form of the heat equation [70] whereas the latter is a current density-electric field continuity equation [51] with a zero time derivative.

$$-\nabla \cdot \lambda \nabla T = 0 \tag{2.5}$$

where: λ is the thermal conductivity
T is the temperature field

$$-\nabla \cdot \sigma \nabla \Phi = 0 \tag{2.6}$$

where: σ is the electric conductivity
Φ is the electric potential field

The field quantities of (2.5) and (2.6) are uncoupled. To couple them the Peltier and Seebeck coefficients are introduced [50]. (2.5) becomes (2.7) and (2.6) becomes (2.8).

$$-\nabla \cdot \lambda \nabla T - \nabla \cdot \sigma \Pi \nabla \Phi = 0 \tag{2.7}$$

where: Π is the Peltier coefficient

$$-\nabla \cdot \sigma S \nabla T - \nabla \cdot \sigma \nabla \Phi = 0 \tag{2.8}$$

where: S is the Seebeck coefficient

The second category involves coupling in terms of the source terms. An example of this type of coupling is Joule heating [11]. In resistive heating as this phenomenon is also called, the flow of electric current through a conductor releases heat. The heat produced is given by (2.9).

$$q = \boldsymbol{J}\boldsymbol{E} \tag{2.9}$$

where: q is the produced heat
$\boldsymbol{J}$ is the current density vector
$\boldsymbol{E}$ is the electric field vector

The electric field is equal to the negative gradient of the electric potential as in $\boldsymbol{E} = -\nabla\Phi$. The current density is given by $\boldsymbol{J} = \sigma(-\nabla\Phi - S\nabla T)$. By introducing the power term q of (2.9) in (2.5), (2.10) is obtained.

$$-\nabla \cdot \lambda\nabla T = \sigma(-\nabla\Phi)^2 + \sigma S\nabla\Phi\nabla T \tag{2.10}$$

In (2.10), the electric field appears at the right-hand side of the equation and at least in FEM terms, right-hand side indicates source terms. The difference between the material parameter coupling and the source term type of coupling is that the first one is linear whereas the second one is considered non-linear. In field numerical analysis terms, linear translates to setting up a system of equations once (a matrix system $\mathbf{Ax} = \mathbf{b}$), whereas non-linear translates to setting up the matrix system multiple times (and updating the source terms after every iteration in this case).

The third category involves coupling in terms of dependent material parameters. In (2.5) and (2.6), the thermal and the electric conductivity respectively both depend on the temperature T. (2.11) and (2.12) include the dependency on T.

$$-\nabla \cdot \lambda(T)\nabla T = 0 \tag{2.11}$$

$$-\nabla \cdot \sigma(T)\nabla\Phi = 0 \tag{2.12}$$

This type of coupling is - similarly to the second one - non-linear and requires a non-linear iterative type of solving, since with every temperature change, the material parameters and the system of equations should be assembled again.

2.1.3. Coupled problems and microsystems

The description "microsystem devices" refers to miniaturized devices whose feature size generally lies in the micrometer range i.e. one to one thousand micrometers. The total device size however as a functioning system can be larger than one millimeter. These devices fall into two major categories which are the sensors and the actuators. The sensors are employed in order to sense (i.e. measure a physical quantity) whereas the role of the actuators is to act as an energy converter and generate motion.

In Table 2-2 [64], various examples of coupled phenomena in microsystem applications are presented. By looking at the mentioned field types in Table 2-2, one thing to note is that there are separate table-cells for the definitions of the acoustic and the mechanical field types. However, an acoustic wave in a solid medium can be regarded as a time-harmonic mechanical displacement field type. In [120], a surface acoustic wave device has been simulated, by considering two scalar mechanical displacement fields and a scalar electric potential field.

The finite element method plays an important role in the simulation of coupled problems in microsystems. In [74], a model of an acceleration sensor is analyzed by using finite element simulation. The paper mentions acceleration (which is related to a force in structural mechanics) and capacitance (electrostatics). One of the strengths of the finite element method, especially when triangular elements are employed, is its flexibility in adapting to different geometrical figures by discretizing them with high accuracy. This can be very important when for example a comb-like sensor structure, with a high number of fingers, needs to be simulated.

Table 2-2 Coupled fields and application examples in microsystems

Type of field	Mechanical	Electric	Magnetic	Acoustic	Fluid	Thermal
Mechanical	-	RF MEMS Micromirror Micromotor Capacitive microsensor	Micro switch Micropump Magnetic microactuator	Resonance and SAW sensors	Micropump Microvalve Pressure microsensor	Micro switch Shape memory microactuator Bimetal microactuator
Electric	Piezoelectrics Piezoresistivity	-	Electromagnetic microvalve	Microphone	Micromixer Micro flow injector	Temperature microsensor
Magnetic	Magnetostriction Magnetic stress	Eddy current	-	Microsensor	Flow control device Gas microsensor	Thermomagnetic actuator
Acoustic	Surface acoustic wave	Piezoelectrics in SAW	Magnetically induced acoustic wave	-	Acoustic-fluid microsensor	Thermoacoustic microcooler
Fluid	Fluid/solid interaction	Electrokinetic flow	Paramagnetic flow MHD	Acoustic-fluid pressure	-	Micro heat exchanger Flow microsensor Ink jet head
Thermal	Thermal stress	Dielectric losses	Joule heating	Thermoacoustic energy	Heat convection	-

Section 2.3 later in this chapter, demonstrates the adaptation of several coupled physics modes to a general mathematical formulation. The scope of this arrangement is the implementation of a global matrix that accommodates, not only the separate fields but also the coupling effects. It is not clear why the author of [64] has positioned certain entries in the upper parts of the table and other entries in the lower parts. The scheme for the actual thesis however, is that just like in Table 2-2, where there is a split in upper and lower parts separated by diagonal spaces, equivalently, there should be a split in the global matrix, in upper, lower and diagonal parts. The upper and the lower parts of the global matrix should correspond to the coupling effects.

2.1.4. Comparable simulation techniques for coupled problems

This section presents and discusses some alternative methods that have thus far also been employed in the numerical treatment of coupled problems. The formulation of the coupled problems is meant to be given in terms of partial differential equations. Therefore, in most cases, the methods under discussion are PDE targeting methods. To mention them in advance, this section discusses the Finite Difference Method (FDM), the Boundary Element Method (BEM), and the Finite Volume Method (FVM). The discussion is made by means of examples that were considered in a literature search.

The exact purpose of the investigation in Section 2.1.4, is to single out the finite element method, as the more appropriate method when regarding the direct solvability of coupled problems in a single global matrix framework. Sequential field computations in coupled problems in the following review are to be considered as a sign of weakness.

The finite difference method in coupled problems

In the paper [78], the finite difference method is employed in order to solve coupled blood flow, plasma flow and chemical transport in a blood flow problem. The geometry of the problem is divided into two computational domains, which are coupled through a boundary Γ. The blood flow in the first subdomain is described by the Navier-Stokes equation system for incompressible fluid flow. The plasma flow in the second subdomain is described by Darcy's law. The chemical transport in the blood flow is modeled by a chemical concentration equation which is called advection-diffusion equation.

The first part towards the solution of this problem is to make the flow equations (Navier-Stokes) discrete, via a so-called explicit finite difference method. The point of interest for discussion is the following. After a few steps of mathematical derivations and term substitutions the authors come to an equation where the unknown quantity is the pressure. A finite difference grid is set up from which pressure is computed. After obtaining the pressure, they then use two of their earlier derived equations which link the two scalar fluid velocities and the pressure, in order to calculate these velocities. This is already an indication for the actual thesis work, that the suitability of the finite difference method for coupling multiple fields is hindered, since from solving the Navier-Stokes equations alone, the solution process has already become sequential. The second part towards obtaining the solution is solving a simpler pressure equation which is derived from Darcy's law, for the second subdomain. Once again, after obtaining the pressure, the two scalar flow velocities are calculated for the second subdomain. This process is, similarly to the first subdomain process, sequential. For the coupling between the two subdomains, the velocities and pressure of their common boundary Γ have to match. To do so, they use the pressure which is calculated from the first subdomain as the boundary condition for the second subdomain. They then calculate the velocities for the

second subdomain and use them back as a boundary condition to the first subdomain. There are no overlapping fields, only sequential coupling through boundary conditions.

The impression from [78] is that the finite difference method has been employed in order to solve a specific problem with a specific sequence of calculations. The methodology used in order to solve this particular problem could have a modest reuse.

Concerning finite differences in coupled problems, the paper [86] is considered. The title of this paper sounds general since it refers to coupled, nonlinear elliptic partial differential equations, without mentioning some particular type of field. In the content of the paper they - on an example basis - refer to coupling between two fields, the electric potential φ and the mass concentration c. The coupling lies in the fact that the right-hand side of both equations depends on the field quantities φ and c. For demonstration purposes they show a rectangular grid on an xy plane. The unknowns are given ascending indices i in the x direction and ascending indices j in the y direction. Nodes are equidistant in x and y. The interesting point in their approach is that they create a vector of unknowns where the φ unknowns are placed first, followed by the c unknowns. One disappointing fact is that there is no investigation about extending this method to three or even higher number of field problems. Furthermore the computation starts for $j = 1$, by creating an equation system of $2\mathrm{NI}$ equations with $2\mathrm{NI}$ unknowns where NI is the number of nodes along x. It then repeats for values of $j > 1$. Already, this is a sequential procedure just to cover a two dimensional rectangular grid which additionally gives no meshing flexibility like the finite element method would do. In addition and since this is a nonlinear problem, nonlinear iterations are also required. The story becomes already too complicated for a simple grid on a two-field problem and it would not be worth trying to adapt this method to a higher number of fields.

Continuing with the review on finite differences in coupled phenomena, the paper [83] was investigated. One thing to note in this paper, is that the authors state in the introduction: "Many authors, when focusing on coupled phenomena problems, have adopted finite element solution procedures". Although they do not analyze deeper into this statement, it is a good indication that the finite element method had already started to gain ground in the treatment of coupled problems compared to the finite difference method. Concerning the geometry of the problem, although the authors do not provide a drawing, one can understand from the indication of *length* and *diameter* in the model system parameters that a cylinder is being analyzed. In their system of partial differential equations, in total they use four PDEs. One can distinguish between four field quantities which are the pressure, the electric potential, the molar concentration and the temperature. The solution plots obtained show the variation of these four quantities along the length of the cylinder. These are not field plots but line plots. After writing the derivative terms of the PDEs by using expansions in Taylor series they state that "the equations of the numerical model result uncoupled and can be solved for each time step". They point that in the solution procedure first the pressure is calculated, followed by the electric potential, the concentration of species and the temperature. Overall this is once again a sequential solving procedure and together with the inflexible finite difference grid, proves

further the weakness of the FDM in developing into a general coupled problem solving technique.

One more paper concerning finite differences and coupled problems to discuss, is the paper [130]. The problem domain is rectangular and it is split into two subdomains. The upper one is solid, whereas the lower one is fluidic. They use two equations, one of them being the elastic dynamic equation for the solid and the other the Navier-Stokes for the fluid. The interesting point is that they write both equations in a - as they call it - common form. This indicates a kind of mapping the physical equations to some common mathematical equation and this is as well of high interest for the work in the current thesis. The disappointing fact is that they present different cells (equivalent to elements in FEM) for the solid and the fluid. That means that they solve one equation in every subdomain without any field overlap and the coupling is done through the internal common boundary condition.

From the sample of finite difference coupled problem papers that has been investigated, it is evident that they have not indicated a general approach for multi-field problems. Although one of them attempts to map the equations to a common mathematical framework, the flexibility that the field overlap offers is missing in all of them. The suitability of FDM for the general treatment of coupled problems was not proven.

The finite element method has some advantages compared to the finite difference method. First it offers a better description of the problem geometry. The treatment of thin sections and complex shapes is superior to the finite difference method. Additionally, the finite difference method is not suited for adaptive grid refinement, with the same ease that the finite element method is suited for adaptive mesh refinement. Also, the finite difference method necessitates the generation of a large mesh (rectangular cells) and a large number of nodes, therefore, in order to keep the computation cost as low as possible, lower approximation should be used within each cell.

The boundary element method in coupled problems

In the boundary element related book [111], published in 1994, there is a statement that the finite element method has enjoyed a huge popularity over the last twenty years because of its applicability to a variety of different engineering problems. The author however, also makes a case in what is seen to be supportive of the boundary element method. He argues that despite the general applicability of the finite element method, this method has some drawbacks. He mentions that models can be difficult and time consuming to build, check and change. Also that it can be difficult to reach the required accuracy, particularly for problems involving stress and other concentrations. There is a real danger - he mentions - of accepting results of numerical analysis all too ready as the absolute truth.

It is worth noting that in the early nineties, personal computers typically had RAM space of four to sixteen Megabytes. Nowadays, personal computers have a typical RAM space of

approximately four to sixteen Gigabytes which is a three orders of magnitude increase. Surely the boundary element method is more memory efficient when it comes to storing the problem description, since the governing equations are reduced to contain only surface integrals and all the volume integrals are removed by mathematical manipulation. On the other hand however, the boundary element method gives rise to fully populated matrices, when the finite element method gives rise to sparsely populated matrices.

In the paper [93], the boundary element method is applied in the analysis of fracture mechanics in 2D anisotropic piezoelectric solids. One interesting comment to extract from the paper's introduction is that the BEM is particularly suited to cases where the domain of interest extends to infinity. Concerning the coupled problem approach, the piezoelectric constitutive relations clearly form a coupled problem where the mechanical displacement and the electric potential are the two coupled fields. In the treatment of the piezoelectric problem, the constitutive relations are grouped into a single equation. However no general mathematical equation is presented and no mapping of physics to mathematics is indicated as it shall be done later in this thesis. Instead a very problem specific approach is followed where Green's functions for anisotropic piezoelectric solids in an infinite plane, half-plane and two-jointed dissimilar half-planes are used. Overall this is a specific type of problem for a specific type of geometry.

The paper [3] presents the application of the boundary element method to 2D thermoelastic contact problems. In the abstract of the paper, there is a statement that reads: "The stationary heat conduction equations and the elastic ones, which are coupled through thermal resistance, are solved independently by means of an iterative process". Clearly there is no generality in this approach. The work is only intended for a specific type of problem.

In the paper [101] a boundary element method is developed in order to be applied to the vibration of beams. The paper mentions arbitrarily shaped beam cross-sections in order to mention generality. However there is no mention of generality in terms of a partial differential equations.

In the further literature search concerning coupled problems with the boundary element method, it was not possible to somewhere come across the application of a general multi-field non-iterative technique. An additional remark is that exploration of more publication lists, reveals a large number of texts on the combined use of finite and boundary elements, for example [105]. This is a considerable indication that boundary elements alone are not sufficient. Boundary elements need Green's function. Solving analytically for Green's function becomes difficult for multi-field problems, if direct coupling is intended.

The finite volume method in coupled problems

According to [52], finite volume methods are usually thought of as belonging to the class of robust, but low order methods. When it comes to unstructured grids and higher order accuracy, finite element methods are more convenient.

Searching in the literature using the "finite volume method" and "coupled problems" keywords, reveals the paper [37]. It is stated that the numerical method that is presented, can be used for both solid body stress analysis and fluid flow predictions, independently as well as in a coupled manner. This statement indicates generality in the physics mode and flexibility in the coupling. The number of problem types however is only restricted to 2. The general PDE framework in the current thesis can accommodate a much broader range of physical phenomena. Therefore the amount of generality in this paper is not sufficient. A further statement reads: "The resulting set of coupled non-linear algebraic equations is solved by employing a segregated approach, leading to a decoupled set of linear algebraic equations for each dependent variable, with a sparse diagonally dominant coefficient matrix". It is clearly indicated that the approach is segregated.

In the paper [85], a numerical method for the calculation of coupled electric and space-charge density fields in electrostatic precipitators is presented. The idea of generality concerning multiple physical phenomena is disregarded. The method employs as stated "an iterative segregated solution procedure". Once again, there is no evidence of a direct and fully coupled approach as the one in the current thesis.

In the paper [126], it is mentioned that "a general class of viscoelastic model is used to investigate numerically the pattern and strength of the secondary flows in rectangular pipes as well as the influence of material parameters on them". Although the paper mentions a coupled equation system, it also mentions that "the main feature of the method is to split the solution process into a series of steps".

From the sample of the discussed examples concerning coupled problems with the finite volume method, as well as from the rest of the paper search in the literature, no indication of a general enough technique that can deal with a wide range of physical problems was found. This together with the mentioned comment in [52], can be used as supportive evidence in the current thesis approach, in that the finite element method shall be the most appropriate numerical method in order to pursue generality in the approach. Furthermore, as it was mentioned earlier, various multi-physics FEM software are already floating on the market. Even though in many cases these FEM software packages are closed-source, their existence in the coupled problem market alone can form supportive evidence too. Overall, the finite element method can handle not only geometry flexibility but multi-field problem flexibility at the same time.

2.1.5. FEM coupled problems and motivation behind the thesis approach

Having considered alternative numerical methods in the treatment of coupled problems in Section 2.1.4, the actual section discusses the finite element method in coupled problems. It does so in terms of historical development, as it aims to identify the milestone papers in coupled problem treatment using FEM. In doing so, the actual thesis convention where coupled problems implies multiple scalar fields, is adhered to. By this, a discussion on the motivation behind the thesis approach is elaborated upon.

In the paper [131], the author presents his personal view on the origins, milestones and directions of the finite element method. He mentions that the origins of the method lie in aircraft structural engineering. With the scalar-field convention used in the actual thesis in mind, this is a structural mechanics coupled problem. [131] discusses the derivation of a more general finite element procedure wherein a set of discrete algebraic equations via a stiffness matrix is assembled. In his particular discussion the strain and stress fields are presented as vector fields, hence scalar field-coupling is present.

The paper [113] is considered as the start of the engineering finite element method. At one point in the paper, the author extends Hooke's Law to two dimensions and mentions a matrix of stiffness influence coefficients. Once again, two dimensions in a structural mechanics problem is considered as a coupled problem. Consequently, the actual thesis introduces a perspective where the engineering finite element method is already a coupled problem method in its inception.

In the publication [6], which consists of a series of articles published in the mid 1950s, the author considers elastic structures while taking thermal strains into his consideration. It is noticeable that the author does not make an explicit reference to the finite element method in his publication. As he mentions however, the most important contributions arising from his articles are the matrix methods of analysis. Referring to that time (1950s), it is stated that matrix formulation is ideally suited for modern automatic computation. This statement points to the consideration of the author's work as an essentially finite element method development but without the explicit reference to the method. The publication contains lengthy derivations concerning matrix formulations. It is evident from his work and it is also a fact that in those times, the processing power of computers was non-existent compared to modern standards. It is a pity that there is a lack of the typical modern contour plots, as this would help visualize the thermal field and clearly reveal the author's intention concerning the coupling effect. Nevertheless, from his matrix equations alone, the coupling between elasticity and thermal effects can clearly be noted at some points in his work.

In the journal article [110], a theorem for linear orthotropic thermoelastic solids is presented. According to the authors, the displacement vector and a scalar stress variable are considered as the mechanical state variables. They relate the scalar stress variable to temperature change. In addition, they associate their formulation to the development of finite element computer algorithms. The authors explicitly mention the constitutive equation which

links the stress and strain tensors though a compliance tensor, and also the strain tensor and temperature change through the thermal expansion tensor. The paper includes a sequence of formulation derivations, however it does not contain any example plots, since it is clearly titled as a theorem paper. Nevertheless, it is of importance for the actual thesis, since the derivation of the thermoelastic physics mode in the internally-developed institute code, focuses on a similar constitutive equation which links stress and strain through a stiffness - instead of compliance - tensor.

An additional journal paper, which focuses on thermoelasticity is [67]. The paper makes mention of a specific type of coupled problem, namely that of anisotropic incompressible and nearly-incompressible thermoelasticity. The author employs the finite element method in order to find solutions to two axisymmetric problem arrangements. The author presents the equation linking the stresses with the strains through the anisotropic elastic constants, and the stresses with temperature change though the anisotropic thermal expansion coefficients. In order to change from a compliance to a stiffness type of equation in matrix notation, the author mentions an inversion. What is of significance is that this paper produces plots of stress values versus radial distance. No plots of temperature are produced, since the temperature variable is only used in order to better approximate stress. Up to 12 elements are employed towards obtaining the solution which is quite reasonable given the year of the paper which is 1969.

According to [131], the wide application of the finite element method beyond structural mechanics, occurs after 1965. In particular, the method was applied to the engineering area of fluid mechanics. With regards to the actual thesis, fluid mechanics is also considered a type of coupled problem.

In the article [87] which is dated from 1969, the author mentions the generation of finite element models in the time domain, and certain problems in wave propagation, kinetic theory of gases, non-linear partial differential equations, non-linear continuum mechanics and fluid dynamics. This is a clear effort from the side of the author towards expanding the finite element method and making it applicable to a greater set of problem types. Furthermore, of interest is the mentioning of the mapping from global nodal points into appropriate local points. Concerning finite elements in the time-domain, a scalar-valued function to be defined on a four-dimensional space-time domain is mentioned. In a structural mechanics problem that would mean three scalar displacement fields and a scalar time parameter. The scalar-field approach of the author is compatible with the approach of the actual thesis. In the part of his paper which is concerned with the kinetic theory of gases, a six-dimensional velocity-space is mentioned. In that, there are three scalar field variables to denote the position of a molecule, and another three to denote the velocity components of the molecule. Concerning the application of the finite element method to fluid dynamics, the fluid velocity scalar-components are considered to be the problem variables. [87] can be regarded as a milestone paper in the treatment of coupled problems with the finite element method, even though no problem test-cases are presented.

A further study on the application of the finite element method to fluid flow was presented in [90] in the year 1972. The authors at that time, noticed that there was great potential for the usage of the finite element method in flow problems. On a side note and to make reference to earlier comments in the actual thesis, [90] identifies Courant as the man who initiated the discussion on the underlying ideas of the finite element method, and Turner et al. as the formal presenters of the method. The paper produces results for a number of test problems. Of interest is that the velocity plots are scalar and are separated into *x*-velocity and *y*-velocity components. The actual thesis is in conformity with this scalar field representation.

In the finite element textbook [132], two classes of coupled problems are illustrated. The fluid-structure interaction is characterized as a Class I problem by the authors. In this type of problem, coupling occurs on domain interfaces via the boundary conditions imposed there. A literature search reveals that research on the fluid-structure problem type, gains momentum in the mid-1970s Even though this problem type creates a bridge between structural mechanics and fluid-flow problems, there is a lack of overlapping fields. It forms a significant contribution to the historical development of the finite element treatment of coupled problems, however the actual thesis focuses on overlapping fields. The authors also define a Class II problem, the one where the various domains overlap. In the Class II problem, coupling occurs through the governing differential equations, describing different physical phenomena. To demonstrate this problem type, the authors present a soil-pressure water interaction example.

In the finite element related paper [88], discrete models of the linear and non-linear electrothermomechanical behavior of continuous bodies are developed. The paper is dated from 1971, which means that within 15 years since the engineering introduction of the finite element method in 1956, the method had already expanded beyond the mainstream mechanical and fluidic type problems to more ambitious problem areas. In the paper, long theoretical derivations of formulae are presented. The coupling between the mechanical, electrical and thermal fields in most natural phenomena is explicitly mentioned. Once again a few sample problems are investigated which are limited mainly by the processing computer power of that time.

In the publication [109], a numerical solution of the Navier-Stokes equations using the finite element technique is presented. The authors portray the use of the method in fluid mechanics as a relatively new innovation for that time. Additionally, they speak of FEM as being advantageous compared to the finite difference method. They present two formulations, one including the variables of velocity and pressure, and one using stream function and vorticity. They come to the conclusion that the velocity-pressure formulation has been proven to be more viable. The current thesis presents an implementation of the velocity-pressure formulation too.

The paper [23] from 1974, is titled in a general manner as it presents various areas of application of the finite element method. The author speaks of a great advantage concerning FEM, in relation to the development of computer programs. He also refers to it as a general numerical procedure for the approximate analysis of arbitrary structures and structural

systems. The author demonstrates generality in terms of various engineering examples, however most of these examples are of the structural mechanics type.

In the text [53], the finite element method is employed, in order to analyze the vibrations of coupled fluid-structure systems. This paper serves to demonstrate expansion of FEM towards further types of coupling. Even though, coupling effects are present in their publication, there is deviation from the actual thesis work, in that the current concern lies in coupling overlapping fields and not in coupling geometrical domains through boundary conditions. Further work on fluid-structure interactions is presented in [39].

For the purpose of a few more brief references to coupled problems, further usage of the finite element method is demonstrated in the paper [123] from 1991, for the treatment of fluid-thermal problems in a sequential field computation manner. Additionally in [15] from 2000, a finite element survey for piezoelectric problems is presented which graphically indicates the great expansion of FEM usage in this type of problems in the 1990s. In [114] from 2004, FEM is utilized the treatment of microstructured optical waveguide problems.

Having identified a sample of papers in the previous paragraphs, which are concerned with the finite element method in coupled problems, and having provided a discussion on them, in the following text of the current section, the point of view of the actual thesis is summarized. Already from the early stages of the introduction of the finite element method in structural mechanics, the two-dimensional problem setups imply overlapping scalar fields and therefore coupled problems. Soon suggestions for the expansion of the method to further problem types follow. The problem area of fluid-flow is the one that perhaps catches the biggest part of the research interest in the expansion of the engineering usage of finite elements. Almost simultaneously, further types of coupling emerge such as electrothermoelasticity. The fluid-thermal and fluid-structure coupling types also emerge soon. The finite element method also expands to treat electromagnetic problems.

At around the early-1980s or even slightly earlier, the concepts of polynomial adaptation and mesh refinement emerge as is mentioned in [9], and also in the citations from that paper towards further literature. This emergence automatically implies a new finite element research field on error estimation and polynomial or mesh adaptation. The majority of the research papers that focus on finite element adaptation, apply their technique on a specific problem type. Further information on error estimation and adaptation techniques is presented in Section 3.1 later on in the text. The actual thesis aims to make a contribution on providing a framework that is general enough in order to treat multiple types of coupled problems, while at the same time be able to accommodate multiple adaptation techniques within the same framework. The framework should consequently be able to apply the adaptation techniques on a variety of physical problems. Attention is given to microsystem related physics modes, namely the electrical, the mechanics and the fluidic application modes.

Before bringing the current literature review section to an end, findings from an investigation into FEM applications with emphasis on coupled problems are also discussed.

The functionality of FEM computer programs which possess comparable features to PolyDE [66], are to be inferred as a source of additional motivation behind the actual thesis approach.

The paper [115] from 2007, introduces the *hp*-FEM System called HERMES. In the words of the authors it is a high-performance modular finite element system, employing multi-physics and *hp*-FEM techniques, wherein the finite element technology is fully separated from the physics of the solved problems. In the actual thesis, this separation is also present and it is implied by the mapping of several physics modes to a general partial differential equation which is mathematically solved for by the program. Furthermore, the webpage of the HERMES software [55] displays a list with some of the package's characteristics. It can reach a polynomial degree of 10, whereas PolyDE, thanks to previously conducted research [98], can reach a polynomial degree of 20. HERMES can follow a multiple mesh approach for coupled problems, whereas PolyDE shall entirely follow a single mesh and also single global matrix approach for coupled problems. The motivation behind this decision is to avoid the transfer of field-solutions between multiple meshes. Consequently this means that a coupled problem that is linear shall be computed in a single step.

The dissertation [43] provides a brief discussion on open source adaptive hp-FEM software applications. One of the mentioned applications is hp90 [94], which however seems to have a focus on Maxwell problems and not a more general multiphysics aspect. One more mentioned application is Concepts [45], then again it seems not to have a strong multiphysics aspect as well. The document [43], apart from listing the aforementioned FEM applications, it also acknowledges that it is itself a contributor to the HERMES software package. In the coupling strategies section of the document, it is mentioned that all physical fields are computationally treated as isolated problems and can be separately solved both in space and time. The overall impression regarding HERMES, is that even though it seems to follow a development direction that is closest to that of PolyDE, there is a lack of interest towards experimenting deeper with the single global matrix approach.

The closed-source software COMSOL Multiphysics [25], does not provide exploration access to the inner workings of their code. It is nevertheless possible to draw a few conclusions from their reference manual [24]. In Chapter 16 of the manual, they describe equation-based modeling. At one point, a general form PDE system is mentioned. It is understood that in the case of several field variables (hence a coupled problem), a single vector of unknowns is created where all the field variables are packed together. The system of equations thus takes a form similar to that of a single-field problem. From this, it can be further assumed that this is the approach that COMSOL follows with respect to the predefined multiphysics program modules, and not just the general PDE module. The question as to how COMSOL proceeds with manipulating and solving the coupled problems global equation systems remains private to them.

2.2. The coupled problems approach used in this thesis

2.2.1. Linear problems

The mathematical formulation of coupled problems is based on the following partial differential equation [65].

$$-\nabla \cdot (\nu \nabla u + \gamma u) + \beta \nabla u + \alpha u = f + \nabla \cdot g \tag{2.13}$$

The field quantity u is a scalar field quantity. (2.13) corresponds to a single field problem. The remaining terms of (2.13) are:

ν	:	material parameter	rank-2 tensor
γ	:	material parameter	rank-1 tensor
β	:	material parameter	rank-1 tensor
α	:	material parameter	scalar
f	:	source term	scalar
g	:	source term	rank-1 tensor

To proceed in the creation of a coupled problem, at least two field quantities are needed. This translates to at least two PDEs of type (2.13). For a two-field problem the mathematical formulation looks as in (2.14).

$$\begin{aligned} -\nabla \cdot (\nu_1 \nabla u_1 + \gamma_1 u_1) + \beta_1 \nabla u_1 + \alpha_1 u_1 &= f_1 + \nabla \cdot g_1 \\ -\nabla \cdot (\nu_2 \nabla u_2 + \gamma_2 u_2) + \beta_2 \nabla u_2 + \alpha_2 u_2 &= f_2 + \nabla \cdot g_2 \end{aligned} \tag{2.14}$$

In (2.14) however, the coupling effects are not yet included. To allow for the coupling effects, coupling material parameters are needed. If (2.14) is rewritten with the coupling effects included, then (2.15) is obtained.

$$\begin{aligned} &-\nabla \cdot (\nu_{11} \nabla u_1 + \gamma_{11} u_1) + \beta_{11} \nabla u_1 + \alpha_{11} u_1 \\ &-\nabla \cdot (\nu_{12} \nabla u_2 + \gamma_{12} u_2) + \beta_{12} \nabla u_2 + \alpha_{12} u_2 \\ &\qquad = f_1 + \nabla \cdot g_1 \\ &-\nabla \cdot (\nu_{21} \nabla u_1 + \gamma_{21} u_1) + \beta_{21} \nabla u_1 + \alpha_{21} u_1 \\ &-\nabla \cdot (\nu_{22} \nabla u_2 + \gamma_{22} u_2) + \beta_{22} \nabla u_2 + \alpha_{22} u_2 \\ &\qquad = f_2 + \nabla \cdot g_2 \end{aligned} \tag{2.15}$$

To generalize (2.15) for an arbitrary number of fields, it is rewritten as in (2.16).

$$\sum_{j=1}^{n} \left(-\nabla \cdot \left(\nu_{ij} \nabla u_j + \gamma_{ij} u_j\right) + \beta_{ij} \nabla u_j + \alpha_{ij} u_j\right) = f_i + \nabla \cdot g_i \qquad i \in [1,2,\dots,n] \tag{2.16}$$

The number of fields in (2.16) is indicated with n. The coupling of the fields in (2.16) is done in terms of the material parameters. This type of coupling is linear. The reason is that when a system of equations is set up, no more than one iteration is needed in order to solve the resulting matrix system.

Suppose that the computational domain Ω that is shown in Figure 2-2 is given. This domain has boundary conditions Γ_D and Γ_N. At Γ_D a Dirichlet boundary condition is imposed, whereas at Γ_N a Neumann boundary condition is imposed.

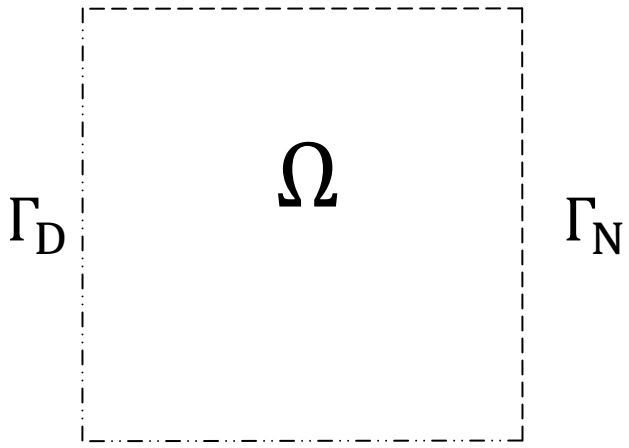

Figure 2-2 Computational domain Ω with boundary conditions Γ_D and Γ_N

$$\begin{array}{ll} \text{At } \Gamma_D & u = u_D \\ \text{At } \Gamma_N & \nu\nabla u + \gamma u + g = u_N + qu \end{array} \tag{2.17}$$

At a Dirichlet boundary condition the field u is given a predefined value u_D, whereas at a Neumann boundary condition, the normal of the divergence components of the PDE is given a value equal to $u_N + qu$.

The coupled form of the general PDE in (2.16) is written in the so called "strong form". In the following, the derivation of the "weak form" is demonstrated. First the PDE is multiplied by a test function v_i (2.18). Then it is integrated over the domain Ω (2.19). In (2.19), the source term g is brought to the left-hand side of the equation.

$$\sum_{j=1}^{n}\left(-\nabla\cdot\left(\nu_{ij}\nabla u_j + \gamma_{ij}u_j\right) + \beta_{ij}\nabla u_j + \alpha_{ij}u_j\right)v_i = (f_i + \nabla\cdot g_i)v_i \tag{2.18}$$
$$i \in [1,2,\dots,n]$$

$$\iint_{\Omega} \sum_{j=1}^{n} \left(-\nabla \cdot \left(\nu_{ij}\nabla u_j + \gamma_{ij}u_j + g_i\right) + \beta_{ij}\nabla u_j + \alpha_{ij}u_j\right)v_i \, d\Omega = \iint_{\Omega} f_i v_i d\Omega \qquad (2.19)$$
$$i \in [1,2,\dots,n]$$

By applying Green's theorem (2.20) is obtained [65].

$$\begin{aligned} &\iint_{\Omega} \sum_{j=1}^{n} \left(\nu_{ij}\nabla u_j + \gamma_{ij}u_j + g_i\right)\nabla v_i \, d\Omega - \oint_{\Gamma} \sum_{j=1}^{n} \left(\nu_{ij}\nabla u_j + \gamma_{ij}u_j + g_i\right)v_i d\Gamma \\ &+ \iint_{\Omega} \sum_{j=1}^{n} \left(\beta_{ij}\nabla u_j + \alpha_{ij}u_j\right)v_i \, d\Omega \\ &= \iint_{\Omega} f_i v_i d\Omega \end{aligned} \qquad (2.20)$$
$$i \in [1,2,\dots,n]$$

In the following the setup process of one element matrix is demonstrated. To every element, local and global geometrical nodes are assigned. The local nodes are assigned for the purpose of building the element matrix, whereas the global nodes are used for the accumulation of the element matrix entries into the global matrix. Figure 2-3 demonstrates an example of a global-local correspondence of the node indices for one element.

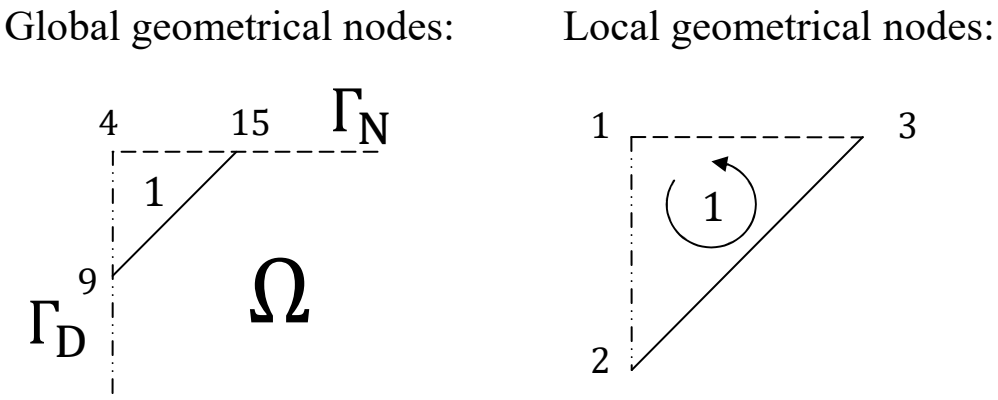

Figure 2-3 Global and local geometrical nodes indication of element 1

For a single-field problem, three DOFs should be assigned to a first order element. For a multiple-field problem the total number of assigned DOFs is equal to the number of fields times the number of DOFs for one field. That is assuming the element is of the same order in all fields. Figure 2-4 demonstrates this assignment.

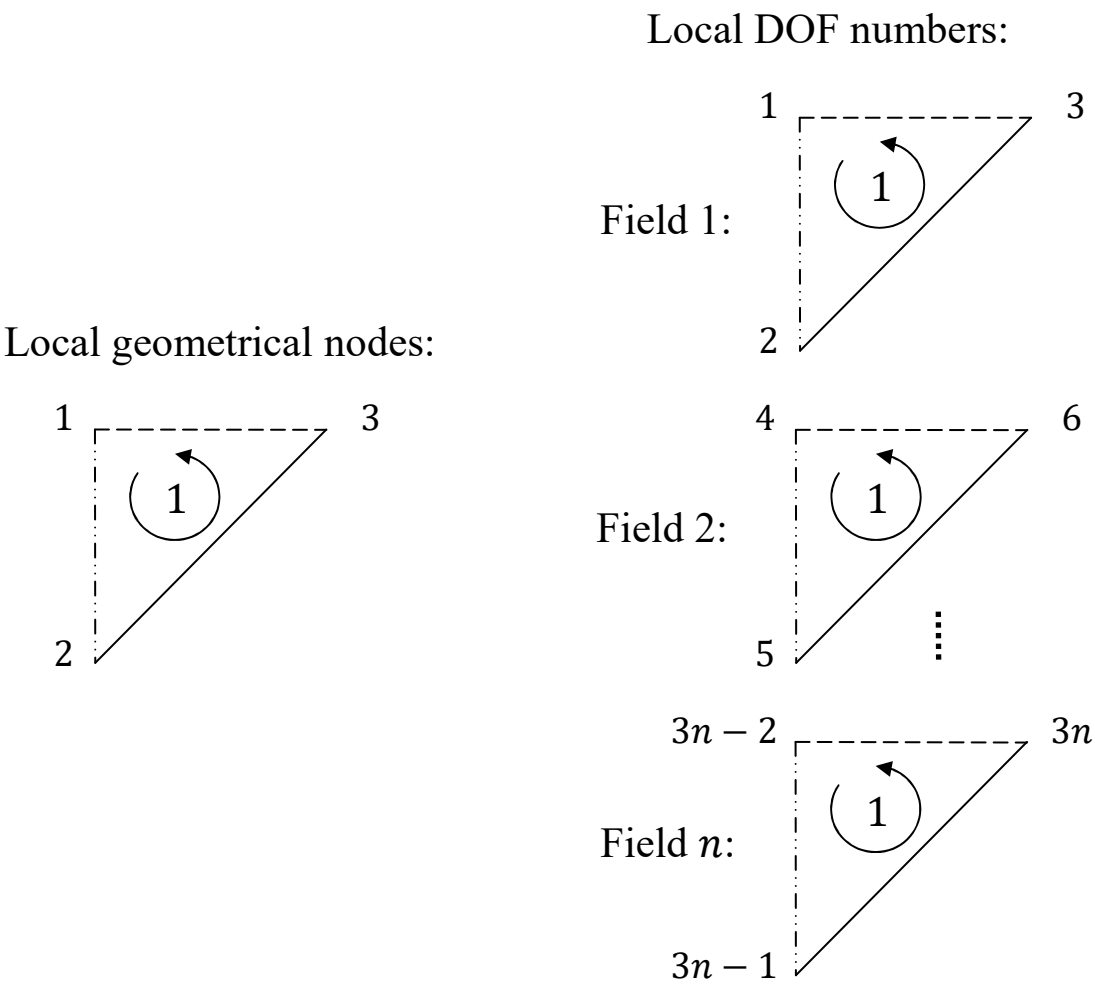

Figure 2-4 Local geometrical nodes and local DOF numbers for a multiple-field problem element

The weak form of the general PDE in (2.20) can be rewritten by introducing the general Neumann boundary conditions. The treatment of the Dirichlet boundary conditions is done directly in the element matrix equation system. In the n-field case with $i \in [1,2,\dots,n]$, the Neumann boundary condition is given by:

$$\sum_{j=1}^{n}\left(\nu_{ij}\nabla u_j + \gamma_{ij}u_j + g_i\right)\cdot\mathbf{n} = u_{N,i} + \sum_{j=1}^{n} q_{ij}u_j \tag{2.21}$$

By assuming that $q_{ij} = 0$ when $i \neq j$, i.e. uncoupled boundary conditions, then:

$$\sum_{j=1}^{n}\left(\nu_{ij}\nabla u_j + \gamma_{ij}u_j + g_i\right)\cdot\mathbf{n} = u_{N,i} + q_i u_i \tag{2.22}$$

In (2.21) and (2.22), $\cdot\,\mathbf{n}$ refers to the normal of the divergence components.

By bringing (2.22) in (2.20), (2.23) is obtained.

$$\begin{aligned}\iint_{\Omega}\sum_{j=1}^{n}\left(\nu_{ij}\nabla u_j+\gamma_{ij}u_j+g_i\right)\nabla v_i\,d\Omega-\oint_{\Gamma_N}\left(u_{N,i}+q_i u_i\right)v_i d\Gamma_N\\+\iint_{\Omega}\sum_{j=1}^{n}\left(\beta_{ij}\nabla u_j+\alpha_{ij}u_j\right)v_i\,d\Omega\\=\iint_{\Omega}f_i v_i d\Omega\\i\in[1,2,\dots,n]\end{aligned}\tag{2.23}$$

The source terms can now be brought to the right-hand side (2.24):

$$\begin{aligned}\iint_{\Omega}\sum_{j=1}^{n}\left(\nu_{ij}\nabla u_j+\gamma_{ij}u_j\right)\nabla v_i\,d\Omega-\oint_{\Gamma_N}\left(q_i u_i\right)v_i d\Gamma_N\\+\iint_{\Omega}\sum_{j=1}^{n}\left(\beta_{ij}\nabla u_j+\alpha_{ij}u_j\right)v_i\,d\Omega\\=\iint_{\Omega}f_i v_i d\Omega-\iint_{\Omega}g_i\nabla v_i d\Omega+\oint_{\Gamma_N}u_{N,i}v_i d\Gamma_N\\i\in[1,2,\dots,n]\end{aligned}\tag{2.24}$$

Example-wise (2.24) can be written explicitly in the case of $n=2$:

$$\begin{aligned}\iint_{\Omega}\left(\nu_{i1}\nabla u_1+\gamma_{i1}u_1\right)\nabla v_i\,d\Omega+\iint_{\Omega}\left(\nu_{i2}\nabla u_2+\gamma_{i2}u_2\right)\nabla v_i\,d\Omega\\-\oint_{\Gamma_N}\left(q_i u_i\right)v_i d\Gamma_N\\+\iint_{\Omega}\left(\beta_{i1}\nabla u_1+\alpha_{i1}u_1\right)v_i\,d\Omega+\iint_{\Omega}\left(\beta_{i2}\nabla u_2+\alpha_{i2}u_2\right)v_i\,d\Omega\\=\iint_{\Omega}f_i v_i d\Omega-\iint_{\Omega}g_i\nabla v_i d\Omega+\oint_{\Gamma_N}u_{N,i}v_i d\Gamma_N\\i\in[1,2]\end{aligned}\tag{2.25}$$

To transform (2.25) into a linear equation system, u is replaced with $\sum_{l=1}^{3}\xi_l\,u_l$ and v with ξ_k. If ξ is a first order shape function, then it holds $k,l\in[1,2,3]$. (2.26) is obtained.

$$
\begin{aligned}
&\sum_{l=1}^{3}\Bigg\{\iint_{\Omega}\left(\nu_{i1}\nabla\xi_{l,1}+\gamma_{i1}\xi_{l,1}\right)\nabla\xi_{k,i}\,\mathrm{d}\Omega\mathrm{u}_{l,1}\\
&+\iint_{\Omega}\left(\nu_{i2}\nabla\xi_{l,2}+\gamma_{i2}\xi_{l,2}\right)\nabla\xi_{k,i}\,\mathrm{d}\Omega\mathrm{u}_{l,2}\\
&-\oint_{\Gamma_\mathrm{N}}\mathrm{q}_i\xi_{l,i}\xi_{k,i}\mathrm{d}\Gamma_\mathrm{N}\mathrm{u}_{l,i}\\
&+\iint_{\Omega}\left(\beta_{i1}\nabla\xi_{l,1}+\alpha_{i1}\xi_{l,1}\right)\xi_{k,i}\,\mathrm{d}\Omega\mathrm{u}_{l,1}\\
&+\iint_{\Omega}\left(\beta_{i2}\nabla\xi_{l,2}+\alpha_{i2}\xi_{l,2}\right)\xi_{k,i}\,\mathrm{d}\Omega\mathrm{u}_{l,2}\Bigg\}
\end{aligned}
\qquad (2.26)
$$

$$
=\iint_{\Omega}f_i\xi_{k,i}\mathrm{d}\Omega-\iint_{\Omega}g_i\nabla\xi_{k,i}\mathrm{d}\Omega+\oint_{\Gamma_\mathrm{N}}\mathrm{u}_{\mathrm{N},i}\xi_{k,i}\mathrm{d}\Gamma_\mathrm{N}
$$

$$
i\in[1,2]
$$

$$
k,l\in[1,2,3]
$$

In (2.26), there are four indices in the equation, i and j are field indices, whereas k and l are shape function indices. For every material parameter, shape function and field variable, the indices are assigned in the following manner:

ν_{ij}	2 field indices
γ_{ij}	2 field indices
β_{ij}	2 field indices
α_{ij}	2 field indices
$\xi_{l,i}$	shape function index, field index
$\xi_{l,j}$	shape function index, field index
$\xi_{k,i}$	shape function index, field index
$\mathrm{u}_{l,i}$	shape function index, field index
$\mathrm{u}_{l,j}$	shape function index, field index

A first order element in a two-dimensional two-field problem has six DOFs. Therefore the element matrix for this element has thirty six entries. The load vector has six entries.

$$
\begin{bmatrix}
\mathrm{A}_{1111} & \mathrm{A}_{1112} & \cdots & \mathrm{A}_{1213}\\
\mathrm{A}_{1121} & \mathrm{A}_{1122} & & \\
\vdots & \vdots & \ddots & \vdots\\
\mathrm{A}_{2131} & \mathrm{A}_{2132} & \cdots & \mathrm{A}_{2233}
\end{bmatrix}
\begin{bmatrix}\mathrm{u}_{1,1}\\ \mathrm{u}_{2,1}\\ \mathrm{u}_{3,1}\\ \mathrm{u}_{1,2}\\ \mathrm{u}_{2,2}\\ \mathrm{u}_{3,2}\end{bmatrix}
=
\begin{bmatrix}\mathrm{r}_{1,1}\\ \mathrm{r}_{2,1}\\ \mathrm{r}_{3,1}\\ \mathrm{r}_{1,2}\\ \mathrm{r}_{2,2}\\ \mathrm{r}_{3,2}\end{bmatrix}
\qquad (2.27)
$$

The short form of the element matrix is:

$$A_{ijkl}u_{l,j} = r_{k,i} \tag{2.28}$$

(2.28) represents the system of six equations with six unknowns. Setting $i = 1$ and $k = 1$ in (2.28), yields the short form of the first equation of (2.27). It reads:

$$A_{1j1l}u_{l,j} = r_{1,1} \tag{2.29}$$

Once all the element work is done, a global linear equation system of the form $\mathbf{Ax} = \mathbf{b}$ is obtained, where $\mathbf{b}$ stands for right-hand side. The global matrix $\mathbf{A}$ may be divided into sub-matrices that separate the coupling from the non-coupling effects. (2.30) shows a global matrix equation system. The global unknown vector $\mathbf{x}$ is subdivided into vectors $\mathbf{x}_1 \cdots \mathbf{x}_n$ where n is the number of fields.

$$\begin{bmatrix} \mathbf{A}_{11} & \cdots & \mathbf{A}_{1n} \\ \vdots & \ddots & \vdots \\ \mathbf{A}_{n1} & \cdots & \mathbf{A}_{nn} \end{bmatrix} \begin{bmatrix} \mathbf{x}_1 \\ \vdots \\ \mathbf{x}_n \end{bmatrix} = \begin{bmatrix} \mathbf{b}_1 \\ \vdots \\ \mathbf{b}_n \end{bmatrix} \tag{2.30}$$

The non-diagonal parts of $\mathbf{A}$ stand for the coupling effects.

2.2.2. Nonlinear problems

In the case of nonlinear problems, the construction of the global linear equation system $\mathbf{Ax} = \mathbf{b}$, has to be repeated until the steady-state solution is reached. That is to solve the system with the help of a linear solver package once, obtain the solution $\mathbf{x}$, feed the solution back to the global equation system and solve again. When the steady-state solution is reached the difference in $\mathbf{x}$ between two successive steps is minimal and therefore the iteration stops. Fixed point iteration [32] may, in general, not converge. It is however considered sufficient for the problem test cases, which are presented in this thesis. (2.31) shows the case where matrix $\mathbf{A}$ is dependent on the solution $\mathbf{x}$.

$$\mathbf{A}(\mathbf{x}) \cdot \mathbf{x} = \mathbf{b} \tag{2.31}$$

For $\mathbf{x_0} = \mathbf{0}$, $\mathbf{x_1}$ is calculated as in (2.32).

$$\mathbf{A}(\mathbf{x_0}) \cdot \mathbf{x_1} = \mathbf{b} \tag{2.32}$$

For every iteration the difference in $\mathbf{x}$ in the energy norm is calculated as in (2.33).

$$\|\Delta\mathbf{x}\|_{\mathrm{E}} = \Delta\mathbf{x}^{\mathrm{T}} \cdot \mathbf{A} \cdot \Delta\mathbf{x} \tag{2.33}$$

In (2.34) the calculation of the difference energy norm is shown specifically for the first iteration:

$$\|\Delta\mathbf{x}\|_{\mathrm{E}} = (\mathbf{x_1} - \mathbf{x}_0)^{\mathrm{T}} \cdot \mathbf{A}(\mathbf{x_0}) \cdot (\mathbf{x_1} - \mathbf{x}_0) \tag{2.34}$$

Simultaneously the energy norm of $\mathbf{x}$ is calculated as in (2.35).

$$\|\mathbf{x}\|_{\mathrm{E}} = \mathbf{x}^{\mathrm{T}} \cdot \mathbf{A} \cdot \mathbf{x} \tag{2.35}$$

In order to check if the steady-state has been reached the condition in (2.36) is questioned.

$$\|\Delta\mathbf{x}\|_{\mathrm{E}} < \delta \, \|\mathbf{x}\|_{\mathrm{E}}? \tag{2.36}$$

In (2.36) δ is a multiplying factor depending on the accuracy that has to be achieved. In the program this value is set to e.g. $\delta = 1 \cdot 10^{-3}$. If the condition is met the nonlinear iteration stops and steady-state is assumed.

2.3. Derivation of coupled physics modes

In this section, the derivation and the mapping of several coupled physics modes to the general mathematical formulation is presented. For all the physics modes the two dimensional formulation is presented. At this point and before proceeding with the mapping, it is helpful in terms of clarity, to first expand (2.15) and demonstrate the simultaneous usage of field indices and tensor indices in (2.37), with the display of a two-field (u_1 and u_2) fully coupled problem. This simultaneous usage eventually requires four indices for ν, three for γ and β, two for α and g and one for f.

$$\begin{aligned}
&-\nabla\cdot\left(\begin{bmatrix}\nu_{1111} & \nu_{1112}\\ \nu_{1121} & \nu_{1122}\end{bmatrix}\nabla u_1+\begin{bmatrix}\gamma_{111}\\ \gamma_{112}\end{bmatrix}u_1\right)+\begin{bmatrix}\beta_{111}\\ \beta_{112}\end{bmatrix}\nabla u_1+\alpha_{11}u_1\\
&-\nabla\cdot\left(\begin{bmatrix}\nu_{1211} & \nu_{1212}\\ \nu_{1221} & \nu_{1222}\end{bmatrix}\nabla u_2+\begin{bmatrix}\gamma_{121}\\ \gamma_{122}\end{bmatrix}u_2\right)+\begin{bmatrix}\beta_{121}\\ \beta_{122}\end{bmatrix}\nabla u_2+\alpha_{12}u_2\\
&\qquad\qquad=f_1+\nabla\cdot\begin{bmatrix}g_{11}\\ g_{12}\end{bmatrix}\\
&-\nabla\cdot\left(\begin{bmatrix}\nu_{2111} & \nu_{2112}\\ \nu_{2121} & \nu_{2122}\end{bmatrix}\nabla u_1+\begin{bmatrix}\gamma_{211}\\ \gamma_{212}\end{bmatrix}u_1\right)+\begin{bmatrix}\beta_{211}\\ \beta_{212}\end{bmatrix}\nabla u_1+\alpha_{21}u_1\\
&-\nabla\cdot\left(\begin{bmatrix}\nu_{2211} & \nu_{2212}\\ \nu_{2221} & \nu_{2222}\end{bmatrix}\nabla u_2+\begin{bmatrix}\gamma_{221}\\ \gamma_{222}\end{bmatrix}u_2\right)+\begin{bmatrix}\beta_{221}\\ \beta_{222}\end{bmatrix}\nabla u_2+\alpha_{22}u_2\\
&\qquad\qquad=f_2+\nabla\cdot\begin{bmatrix}g_{21}\\ g_{22}\end{bmatrix}
\end{aligned}\tag{2.37}$$

The two-field fully coupled equation system in (2.37), can be expressed in a general form that accommodates an arbitrary number of fields. This is demonstrated in (2.38).

$$-\nabla\cdot\left(\nu_{ijkl}\nabla u_j+\gamma_{ijl}u_j\right)+\beta_{ijl}\nabla u_j+\alpha_{ij}u_j=f_i+\nabla\cdot g_{il}\tag{2.38}$$

In (2.38), the indices i,j are assigned as field-indices in order to indicate the coupling and non-coupling effects. The tensor indices in (2.38) are indicated by the letters k,l.

In the following sections, every physics mode shall correspond to a field-wise divided matrix, which shall demonstrate the mapping on the material parameters ν,γ,β,α as well as on the source terms f,g. A significant amount of effort was invested in the following derivations and the work is considered a step forward from the initiation of the coupled problems framework [119]. Coming from an internal discussion [60], the work [64], even though it previously handled coupled FEM problems as well, it did not have a major contribution to reusability. The biggest contribution was in implementing paramagnetic oxygen flow, and that is a specific type of problem. In the actual section, the aim is to demonstrate reusability. The implemented physics modes are not in general dedicated only to microsystems applications, consequently the reusability can reach beyond the micro-area, should that be wished.

2.3.1. Thermoelectricity (coupled problem with two fields)

Linear thermoelectricity is a two-field physics mode where the first field is the temperature and the second the electric potential. Coupling between the fields is done via the Peltier and Seebeck coefficients [50]. The equation system for thermoelectricity has already been given in (2.7) and (2.8). Below in (2.39) and (2.40), the material parameters of the equation system are written explicitly. In doing so, there is adherence to the index notation style of (2.38).

$$\begin{bmatrix} \nu_{1111} & \nu_{1112} \\ \nu_{1121} & \nu_{1122} \end{bmatrix} = \begin{bmatrix} \lambda_{11} & \lambda_{12} \\ \lambda_{21} & \lambda_{22} \end{bmatrix} \quad \begin{bmatrix} \nu_{1211} & \nu_{1212} \\ \nu_{1221} & \nu_{1222} \end{bmatrix} = \begin{bmatrix} \sigma_{11} & \sigma_{12} \\ \sigma_{21} & \sigma_{22} \end{bmatrix} \Pi \tag{2.39}$$

$$\begin{bmatrix} \nu_{2111} & \nu_{2112} \\ \nu_{2121} & \nu_{2122} \end{bmatrix} = \begin{bmatrix} \sigma_{11} & \sigma_{12} \\ \sigma_{21} & \sigma_{22} \end{bmatrix} S \quad \begin{bmatrix} \nu_{2211} & \nu_{2212} \\ \nu_{2221} & \nu_{2222} \end{bmatrix} = \begin{bmatrix} \sigma_{11} & \sigma_{12} \\ \sigma_{21} & \sigma_{22} \end{bmatrix} \tag{2.40}$$

The parameters λ and σ are tensors. The Peltier and Seebeck coefficients can also be tensors in general. The current equation system corresponds to the physics mode in the form that was implemented in the PolyDE program code.

The implementation of the physics mode was driven by the intention of simulating a Peltier cooling element. A potential difference was introduced to a Peltier cooling structure through the appropriate boundary conditions and the resulting thermal difference was observed [119]. No source terms were taken into account in the simulation. The two equations correspond to overlapping fields over the same material regions. In terms of the tensor indices i and j, a coupling effect is indicated, when the corresponding material parameters have $i \neq j$.

Before proceeding to the mapping of the material parameters to the field-wise divided matrix, the material parameters given in (2.39) and (2.40) are written explicitly with regards to (2.7) and (2.8). The following equation system is obtained.

Field indices in the material parameter tensors are avoided:

$$-\nabla \cdot \begin{bmatrix} \lambda_{11} & \lambda_{12} \\ \lambda_{21} & \lambda_{22} \end{bmatrix} \nabla T - \nabla \cdot \begin{bmatrix} \sigma_{11} & \sigma_{12} \\ \sigma_{21} & \sigma_{22} \end{bmatrix} \Pi \nabla \Phi = 0 \tag{2.41}$$

$$-\nabla \cdot \begin{bmatrix} \sigma_{11} & \sigma_{12} \\ \sigma_{21} & \sigma_{22} \end{bmatrix} S \nabla T - \nabla \cdot \begin{bmatrix} \sigma_{11} & \sigma_{12} \\ \sigma_{21} & \sigma_{22} \end{bmatrix} \nabla \Phi = 0 \tag{2.42}$$

(2.43) demonstrates the mapping of the parameters of (2.41) and (2.42) to the two-field mathematical framework. The corresponding portion of the global linear equation system $\mathbf{Ax} = \mathbf{b}$ is presented directly above the parameters.

A		**x**	**b**
$\nu_{11} = \begin{bmatrix} \lambda_{11} & \lambda_{12} \\ \lambda_{21} & \lambda_{22} \end{bmatrix}$ $\gamma_{11} = 0$ $\beta_{11} = 0$ $\alpha_{11} = 0$	$\nu_{12} = \begin{bmatrix} \sigma_{11} & \sigma_{12} \\ \sigma_{21} & \sigma_{22} \end{bmatrix} \Pi$ $\gamma_{12} = 0$ $\beta_{12} = 0$ $\alpha_{12} = 0$	$u_1 = T$	0
$\nu_{21} = \begin{bmatrix} \sigma_{11} & \sigma_{12} \\ \sigma_{21} & \sigma_{22} \end{bmatrix} S$ $\gamma_{21} = 0$ $\beta_{21} = 0$ $\alpha_{21} = 0$	$\nu_{22} = \begin{bmatrix} \sigma_{11} & \sigma_{12} \\ \sigma_{21} & \sigma_{22} \end{bmatrix}$ $\gamma_{22} = 0$ $\beta_{22} = 0$ $\alpha_{22} = 0$	$u_2 = \Phi$	0

(2.43)

2.3.2. Structural mechanics (coupled problem with two fields)

Since in the used mathematical framework, all the fields are scalar, structural mechanics in two-dimensions is considered a coupled problem with two fields, namely the x- and the y-displacement. An application example of this physics mode in microsystems is the simulation of a comb-like capacitive accelerometer.

A three-dimensional structural mechanics physics mode is typically called solid stress-strain [25]. To construct the two-dimensional structural mechanics physics mode, either plane stress or plane strain has to be assumed. Most literature on material parameters, provide the elasticity matrices C in the three-dimensional form by taking symmetry properties into account, and thereby reducing the number of indices. For this reason, an analytic derivation is presented below which starts from the 3D formulation and gradually reduces to the 2D case. The stress-strain relationship is given by (2.44) [132].

$$\sigma = C\varepsilon \tag{2.44}$$

where: σ is the rank-2 stress tensor
C is the rank-4 elasticity tensor
ε is the rank-2 strain tensor

In order to make the material parameter mapping to the PDE process smoother, the subscript $\langle\ \rangle_{st}$ is introduced. It stands for stress or strain, and is used firstly to introduce stress and strain alternative but also equivalent tensors, and secondly in order to avoid any confusion with the quantities of the electric conductivity σ and the electric permittivity ε. Field or tensor

indices are appended to the subscript by using a colon separation $\langle \quad \rangle_{\mathrm{st}:ijkl}$. Applying the divergence $(\nabla \cdot)$ operator to both sides of (2.44) after introducing the subscript $\langle \quad \rangle_{\mathrm{st}}$ yields (2.45).

$$\nabla \cdot \sigma_{\mathrm{st}} = \nabla \cdot (C \varepsilon_{\mathrm{st}}) \tag{2.45}$$

By definition, the mechanical strain is related to the gradient of the mechanical displacement. In three geometrical dimensions, there is a total of three normal stresses and six shear stresses to be considered. From the literature and for clarification, in (2.46), the full strain tensor ε, without the $\langle \quad \rangle_{\mathrm{st}}$ subscript is presented. Simultaneously the strain tensor alternative $\varepsilon_{\mathrm{st}}$ is presented as a mathematical construct, in the form that is useful the current thesis.

$$\text{Literature:} \quad \begin{bmatrix} \varepsilon_{xx} & \varepsilon_{xy} & \varepsilon_{xz} \\ \varepsilon_{yx} & \varepsilon_{yy} & \varepsilon_{yz} \\ \varepsilon_{zx} & \varepsilon_{zy} & \varepsilon_{zz} \end{bmatrix} = \begin{bmatrix} \frac{\partial u_x}{\partial x} & \frac{1}{2}\left(\frac{\partial u_x}{\partial y} + \frac{\partial u_y}{\partial x}\right) & \frac{1}{2}\left(\frac{\partial u_x}{\partial z} + \frac{\partial u_z}{\partial x}\right) \\ \frac{1}{2}\left(\frac{\partial u_y}{\partial x} + \frac{\partial u_x}{\partial y}\right) & \frac{\partial u_y}{\partial y} & \frac{1}{2}\left(\frac{\partial u_y}{\partial z} + \frac{\partial u_z}{\partial y}\right) \\ \frac{1}{2}\left(\frac{\partial u_z}{\partial x} + \frac{\partial u_x}{\partial z}\right) & \frac{1}{2}\left(\frac{\partial u_z}{\partial y} + \frac{\partial u_y}{\partial z}\right) & \frac{\partial u_z}{\partial z} \end{bmatrix}$$

$$\text{Alternative for current thesis:} \quad \begin{bmatrix} \varepsilon_{\mathrm{st}:xx} & \varepsilon_{\mathrm{st}:xy} & \varepsilon_{\mathrm{st}:xz} \\ \varepsilon_{\mathrm{st}:yx} & \varepsilon_{\mathrm{st}:yy} & \varepsilon_{\mathrm{st}:yz} \\ \varepsilon_{\mathrm{st}:zx} & \varepsilon_{\mathrm{st}:zy} & \varepsilon_{\mathrm{st}:zz} \end{bmatrix} = \begin{bmatrix} \frac{\partial u_x}{\partial x} & \frac{\partial u_x}{\partial y} & \frac{\partial u_x}{\partial z} \\ \frac{\partial u_y}{\partial x} & \frac{\partial u_y}{\partial y} & \frac{\partial u_y}{\partial z} \\ \frac{\partial u_z}{\partial x} & \frac{\partial u_z}{\partial y} & \frac{\partial u_z}{\partial z} \end{bmatrix} \tag{2.46}$$

In the current thesis, the mechanical displacement is generally denoted with u_{st} in order to avoid confusion with the u variable of the general PDE. By omitting indices for the moment, (2.45) is rewritten in terms of the mechanical displacement and this yields (2.47). The equation does not explicitly distinguish between normal and shear components.

$$\nabla \cdot \sigma_{\mathrm{st}} = \nabla \cdot (C \nabla u_{st}) \tag{2.47}$$

Assuming no body forces, time-harmonic or transient phenomena, (2.48) holds.

$$\nabla \cdot \sigma_{\mathrm{st}} = 0 \tag{2.48}$$

Consequently and for eventually mapping to the general PDE, (2.49) and (2.50) hold as well.

$$-\nabla \cdot \sigma_{st} = 0 \tag{2.49}$$

$$-\nabla \cdot (C \nabla u_{st}) = 0 \tag{2.50}$$

For the three-dimensional case:

$$u_{st} = \begin{bmatrix} u_x \\ u_y \\ u_z \end{bmatrix} \tag{2.51}$$

Consequently for the 2D case:

$$u_{st} = \begin{bmatrix} u_x \\ u_y \end{bmatrix} \tag{2.52}$$

(2.44) written with the $\langle \quad \rangle_{st}$ subscript and indices is shown in (2.53).

$$\sigma_{st:ij} = C_{ijkl} \varepsilon_{st:kl} \tag{2.53}$$

In (2.53), accented indices i, j, k, l are used in order to differentiate them from the field and tensor indices of (2.28). The rank-4 elasticity 3D tensor is given in (2.54).

$$C_{ijkl} = \begin{bmatrix} & j=1 & & & j=2 & & & j=3 & \\ i=1 & C_{1111} & \cdots & C_{1113} & C_{1211} & \cdots & C_{1213} & C_{1311} & \cdots & C_{1313} \\ & \vdots & \ddots & \vdots & \vdots & \ddots & \vdots & \vdots & \ddots & \vdots \\ & C_{1131} & \cdots & C_{1133} & C_{1231} & \cdots & C_{1233} & C_{1331} & \cdots & C_{1333} \\ i=2 & C_{2111} & \cdots & C_{2113} & C_{2211} & \cdots & C_{2213} & & & \\ & \vdots & \ddots & \vdots & \vdots & \ddots & \vdots & & \vdots & \\ & C_{2131} & \cdots & C_{2133} & C_{2231} & \cdots & C_{2233} & & & \\ & C_{3111} & \cdots & C_{3113} & & & & C_{3311} & \cdots & C_{3313} \\ i=3 & \vdots & \ddots & \vdots & & \cdots & & \vdots & \ddots & \vdots \\ & C_{3131} & \cdots & C_{3133} & & & & C_{3331} & \cdots & C_{3333} \end{bmatrix} \tag{2.54}$$

There is symmetry in the indices i and j as well as in k and l so that:

$$C_{ijkl} = C_{jilk} \tag{2.55}$$

For that reason they can be grouped and be represented by a single index. Grouping is done in the following manner (Voigt notation):

$$11 \rightarrow 1, 22 \rightarrow 2, 33 \rightarrow 3, 23 \rightarrow 4, 31 \rightarrow 5, 12 \rightarrow 6$$

With this grouping (2.54) is rewritten into (2.56). Due to the non-sequential increase in the index numbers, the full tensor is presented.

$$C_{\acute{\imath}\acute{\jmath}\acute{k}\acute{l}} = \begin{bmatrix} & \acute{\jmath}=1 & & & \acute{\jmath}=2 & & & \acute{\jmath}=3 & \\ \acute{\imath}=1 & C_{11} & C_{16} & C_{15} & C_{61} & C_{66} & C_{65} & C_{51} & C_{56} & C_{55} \\ & C_{16} & C_{12} & C_{14} & C_{66} & C_{62} & C_{64} & C_{56} & C_{52} & C_{54} \\ & C_{15} & C_{14} & C_{13} & C_{65} & C_{64} & C_{63} & C_{55} & C_{54} & C_{53} \\ \acute{\imath}=2 & C_{61} & C_{66} & C_{65} & C_{21} & C_{26} & C_{25} & C_{41} & C_{46} & C_{45} \\ & C_{66} & C_{62} & C_{64} & C_{26} & C_{22} & C_{24} & C_{46} & C_{42} & C_{44} \\ & C_{65} & C_{64} & C_{63} & C_{25} & C_{24} & C_{23} & C_{45} & C_{44} & C_{43} \\ \acute{\imath}=3 & C_{51} & C_{56} & C_{55} & C_{41} & C_{46} & C_{45} & C_{31} & C_{36} & C_{35} \\ & C_{56} & C_{52} & C_{54} & C_{46} & C_{42} & C_{44} & C_{36} & C_{32} & C_{34} \\ & C_{55} & C_{54} & C_{53} & C_{45} & C_{44} & C_{43} & C_{35} & C_{34} & C_{33} \end{bmatrix} \tag{2.56}$$

The tensor in (2.56) has eighty one entries which is the result of being 3D and having four indices according to $3^4 = 81$. Taking its symmetry properties into account and the fact that some of its entries appear multiple times in (2.56), it can be reduced to thirty six entries and be projected as a rank-2 tensor. This is done in (2.57).

$$C_{\grave{\imath}\grave{\jmath}} = \begin{bmatrix} C_{11} & C_{12} & \dots & \dots & \dots & C_{16} \\ C_{21} & C_{22} & \dots & \dots & \dots & C_{26} \\ \vdots & \vdots & \ddots & & & \vdots \\ \vdots & \vdots & & \ddots & & \vdots \\ \vdots & \vdots & & & \ddots & \vdots \\ C_{61} & C_{62} & \dots & \dots & \dots & C_{66} \end{bmatrix} \tag{2.57}$$

In (2.57) a modified accent is used in that $\grave{\imath} = \acute{\imath}\acute{\jmath}, \grave{\jmath} = \acute{k}\acute{l}$. $C_{\grave{\imath}\grave{\jmath}}$ in (2.57) exhibits a further symmetry property in that $C_{\grave{\imath}\grave{\jmath}} = C_{\grave{\jmath}\grave{\imath}}$. This means that the lower diagonal part (2.57) can be omitted. With the omission, (2.57) is written as in (2.58).

$$C_{\grave{\imath}\grave{\jmath}} = \begin{bmatrix} C_{11} & C_{12} & C_{13} & C_{14} & C_{15} & C_{16} \\ & C_{22} & C_{23} & C_{24} & C_{25} & C_{26} \\ & & C_{33} & C_{34} & C_{35} & C_{36} \\ & & & C_{44} & C_{45} & C_{46} \\ & & & & C_{55} & C_{56} \\ & & & & & C_{66} \end{bmatrix} \tag{2.58}$$

(2.58) is important because this is the format in which text books present the elasticity tensor of various materials. Additionally, typical FEM software packages, require the entries from the $C_{\grave{\imath}\grave{\jmath}}$ tensor, to be input as they are given in (2.58). (2.53) can now be rewritten analytically by considering only the x- and y- components, i.e. indices $1, 2$ and proceed with the mapping of the structural mechanics physics mode to the general mathematical formulation.

$$\begin{aligned}
\sigma_{st:11} &= C_{1111}\varepsilon_{st:11} + C_{1112}\varepsilon_{st:12} + C_{1121}\varepsilon_{st:21} + C_{1122}\varepsilon_{st:22} \\
\sigma_{st:12} &= C_{1211}\varepsilon_{st:11} + C_{1212}\varepsilon_{st:12} + C_{1221}\varepsilon_{st:21} + C_{1222}\varepsilon_{st:22} \\
\sigma_{st:21} &= C_{2111}\varepsilon_{st:11} + C_{2112}\varepsilon_{st:12} + C_{2121}\varepsilon_{st:21} + C_{2122}\varepsilon_{st:22} \\
\sigma_{st:22} &= C_{2211}\varepsilon_{st:11} + C_{2212}\varepsilon_{st:12} + C_{2221}\varepsilon_{st:21} + C_{2222}\varepsilon_{st:22}
\end{aligned} \tag{2.59}$$

The negative divergence operator $(-\nabla\cdot)$ can be applied to $\begin{bmatrix}\sigma_{st:11}\\ \sigma_{st:12}\end{bmatrix}$ and as well the $\begin{bmatrix}\sigma_{st:21}\\ \sigma_{st:22}\end{bmatrix}$ vectors. (2.60) is obtained.

$$\begin{aligned}
-\nabla\cdot\begin{bmatrix}\sigma_{st:11}\\ \sigma_{st:12}\end{bmatrix} &= -\nabla\cdot\begin{bmatrix}C_{1111}\varepsilon_{st:11}\\ C_{1211}\varepsilon_{st:11}\end{bmatrix} - \nabla\cdot\begin{bmatrix}C_{1112}\varepsilon_{st:12}\\ C_{1212}\varepsilon_{st:12}\end{bmatrix} \\
&\quad -\nabla\cdot\begin{bmatrix}C_{1121}\varepsilon_{st:21}\\ C_{1221}\varepsilon_{st:21}\end{bmatrix} - \nabla\cdot\begin{bmatrix}C_{1122}\varepsilon_{st:22}\\ C_{1222}\varepsilon_{st:22}\end{bmatrix} \\
-\nabla\cdot\begin{bmatrix}\sigma_{st:21}\\ \sigma_{st:22}\end{bmatrix} &= -\nabla\cdot\begin{bmatrix}C_{2111}\varepsilon_{st:11}\\ C_{2211}\varepsilon_{st:11}\end{bmatrix} - \nabla\cdot\begin{bmatrix}C_{2112}\varepsilon_{st:12}\\ C_{2212}\varepsilon_{st:12}\end{bmatrix} \\
&\quad -\nabla\cdot\begin{bmatrix}C_{2121}\varepsilon_{st:21}\\ C_{2221}\varepsilon_{st:21}\end{bmatrix} - \nabla\cdot\begin{bmatrix}C_{2122}\varepsilon_{st:22}\\ C_{2222}\varepsilon_{st:22}\end{bmatrix}
\end{aligned} \tag{2.60}$$

To distinguish between the two scalar mechanical displacement fields, once again the alternative to the strain tensor is written analytically in (2.61), by using number indices instead of x and y.

$$\varepsilon_{st} = \begin{bmatrix}\varepsilon_{st:11} & \varepsilon_{st:12}\\ \varepsilon_{st:21} & \varepsilon_{st:22}\end{bmatrix} = \begin{bmatrix}\dfrac{\partial u_x}{\partial x} & \dfrac{\partial u_x}{\partial y}\\ \dfrac{\partial u_y}{\partial x} & \dfrac{\partial u_y}{\partial y}\end{bmatrix} \tag{2.61}$$

With (2.61) in mind the u_x and the u_y components in (2.60) are grouped together. (2.62) is obtained.

$$\begin{aligned}
-\nabla\cdot\begin{bmatrix}\sigma_{st:11}\\ \sigma_{st:12}\end{bmatrix} &= -\nabla\cdot\begin{bmatrix}C_{1111}\varepsilon_{st:11} + C_{1112}\varepsilon_{st:12}\\ C_{1211}\varepsilon_{st:11} + C_{1212}\varepsilon_{st:12}\end{bmatrix} \\
&\quad -\nabla\cdot\begin{bmatrix}C_{1121}\varepsilon_{st:21} + C_{1122}\varepsilon_{st:22}\\ C_{1221}\varepsilon_{st:21} + C_{1222}\varepsilon_{st:22}\end{bmatrix} \\
-\nabla\cdot\begin{bmatrix}\sigma_{st:21}\\ \sigma_{st:22}\end{bmatrix} &= -\nabla\cdot\begin{bmatrix}C_{2111}\varepsilon_{st:11} + C_{2112}\varepsilon_{st:12}\\ C_{2211}\varepsilon_{st:11} + C_{2212}\varepsilon_{st:12}\end{bmatrix} \\
&\quad -\nabla\cdot\begin{bmatrix}C_{2121}\varepsilon_{st:21} + C_{2122}\varepsilon_{st:22}\\ C_{2221}\varepsilon_{st:21} + C_{2222}\varepsilon_{st:22}\end{bmatrix}
\end{aligned} \tag{2.62}$$

By expressing the strains in (2.62) in terms of displacement gradients, (2.63) is obtained.

$$\begin{aligned}
-\nabla\cdot\begin{bmatrix}\sigma_{st:11}\\ \sigma_{st:12}\end{bmatrix} &= -\nabla\cdot\begin{bmatrix}C_{1111} & C_{1112}\\ C_{1211} & C_{1212}\end{bmatrix}\nabla u_x - \nabla\cdot\begin{bmatrix}C_{1121} & C_{1122}\\ C_{1221} & C_{1222}\end{bmatrix}\nabla u_y \\
-\nabla\cdot\begin{bmatrix}\sigma_{st:21}\\ \sigma_{st:22}\end{bmatrix} &= -\nabla\cdot\begin{bmatrix}C_{2111} & C_{2112}\\ C_{2211} & C_{2212}\end{bmatrix}\nabla u_x - \nabla\cdot\begin{bmatrix}C_{2121} & C_{2122}\\ C_{2221} & C_{2222}\end{bmatrix}\nabla u_y
\end{aligned} \tag{2.63}$$

By using (2.50) and by replacing the $\acute{\imath}, \acute{\jmath}, \acute{k}, \acute{l}$ with the $\grave{\imath}, \grave{\jmath}$ indices according to (2.58), (2.64) is obtained.

$$\begin{aligned} -\nabla \cdot \begin{bmatrix} C_{11} & C_{16} \\ C_{16} & C_{66} \end{bmatrix} \nabla u_x - \nabla \cdot \begin{bmatrix} C_{16} & C_{12} \\ C_{66} & C_{26} \end{bmatrix} \nabla u_y = 0 \\ -\nabla \cdot \begin{bmatrix} C_{16} & C_{66} \\ C_{12} & C_{26} \end{bmatrix} \nabla u_x - \nabla \cdot \begin{bmatrix} C_{66} & C_{26} \\ C_{26} & C_{22} \end{bmatrix} \nabla u_y = 0 \end{aligned} \tag{2.64}$$

This concludes the mapping of the elasticity matrix components as they are normally retrieved from literature to our general PDE mathematical formulation. Similar to the mapping illustration for thermoelectricity in (2.43) the mapping for the 2D structural mechanics is presented in (2.65).

A		**x**	**b**
$\nu_{11} = \begin{bmatrix} C_{11} & C_{16} \\ C_{16} & C_{66} \end{bmatrix}$ $\gamma_{11} = 0$ $\beta_{11} = 0$ $\alpha_{11} = 0$	$\nu_{12} = \begin{bmatrix} C_{16} & C_{12} \\ C_{66} & C_{26} \end{bmatrix}$ $\gamma_{12} = 0$ $\beta_{12} = 0$ $\alpha_{12} = 0$	$u_1 = u_x$	0
$\nu_{21} = \begin{bmatrix} C_{16} & C_{66} \\ C_{12} & C_{26} \end{bmatrix}$ $\gamma_{21} = 0$ $\beta_{21} = 0$ $\alpha_{21} = 0$	$\nu_{22} = \begin{bmatrix} C_{66} & C_{26} \\ C_{26} & C_{22} \end{bmatrix}$ $\gamma_{22} = 0$ $\beta_{22} = 0$ $\alpha_{22} = 0$	$u_2 = u_y$	0

(2.65)

It should be reminded that the indices for ν are the field indices i, j whereas for C the $\grave{\imath}, \grave{\jmath}$ are used.

In the case of materials which are characterized by an anisotropic elasticity matrix, before proceeding with a two dimensional structural mechanics simulation, a simulation plane should be selected. This was applied in practice in the surface acoustic wave device problem, that is presented in Chapter 4. The selected simulation plane from the three-dimensional $x^{\cdot\cdot}y^{\cdot\cdot}z^{\cdot\cdot}$ geometry should be mapped to the two-dimensional $x^{\cdot}y^{\cdot}$ plane. Three superscript dots in the axis notation, are used to refer to the 3D coordinate system, whereas two dots to the 2D coordinate system.

In Figure 2-5 the $x^{\cdot\cdot}y^{\cdot\cdot}z^{\cdot\cdot}$ coordinate system as well as the mapping of the $x^{\cdot\cdot}y^{\cdot\cdot}$ and the $-y^{\cdot\cdot}x^{\cdot\cdot}$ planes is presented. In Figure 2-6 the mapping of the $z^{\cdot\cdot}x^{\cdot\cdot}$ and the $x^{\cdot\cdot} - z^{\cdot\cdot}$ planes is presented. In both figures the transformations that are done with respect to the axes of the $3D$ coordinate system are also presented. The filling of the planes with specific texture patterns aims to help in visualizing the transformations. Transformations of non-90° angles is also possible. This is illustrated in Figure 2-7.

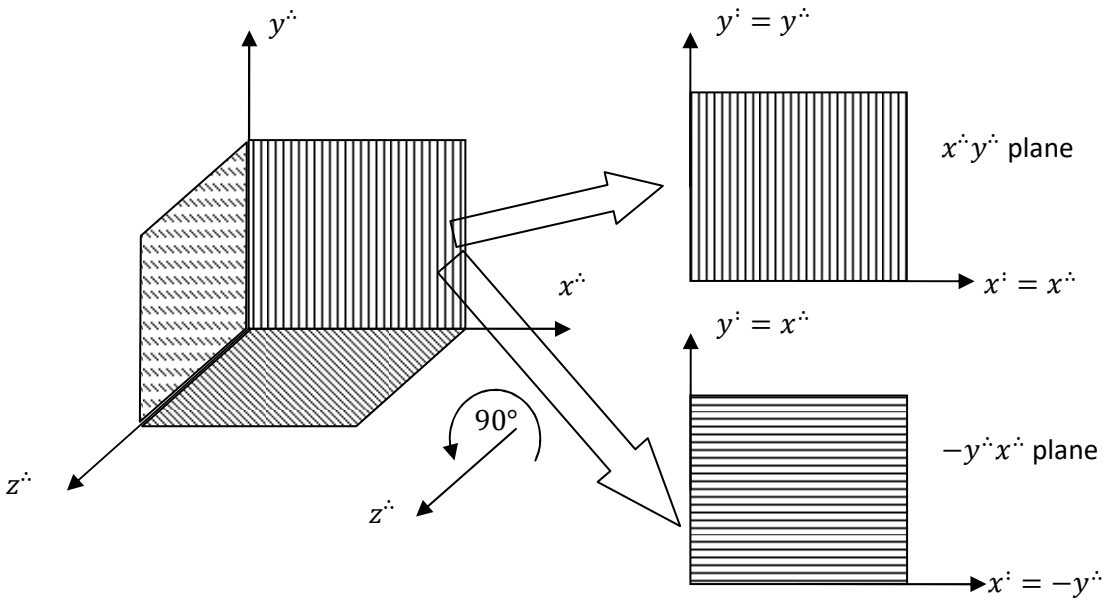

Figure 2-5 Three-dimensional $x^{\cdot\cdot}y^{\cdot\cdot}z^{\cdot\cdot}$ coordinate system and mapping of the $x^{\cdot\cdot}y^{\cdot\cdot}$ and $-y^{\cdot\cdot}x^{\cdot\cdot}$ planes on the $x^{\cdot}y^{\cdot}$ system

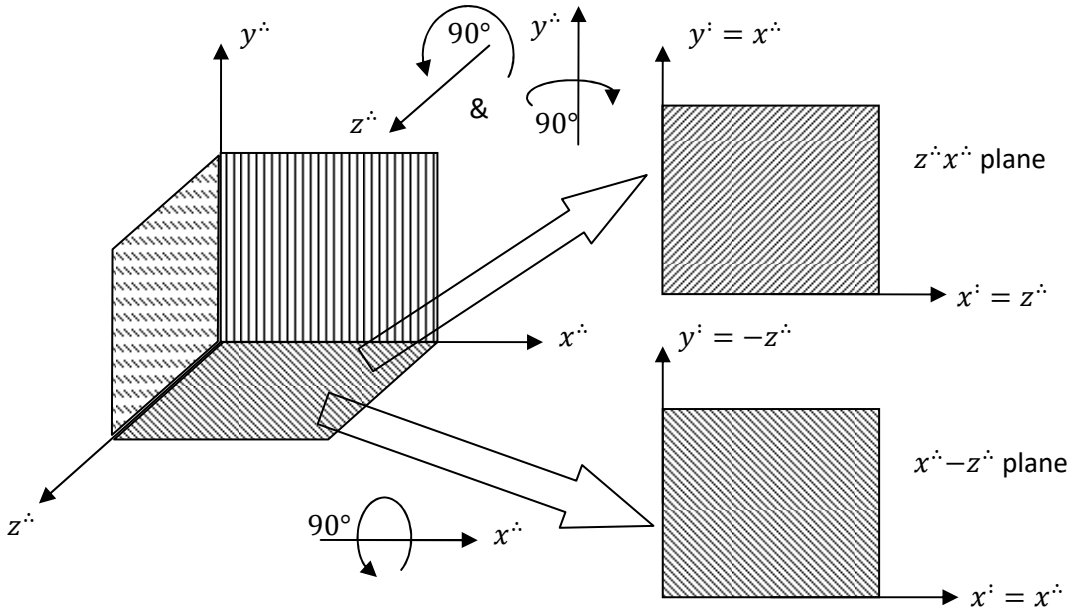

Figure 2-6 Three-dimensional $x^{\cdot\cdot}y^{\cdot\cdot}z^{\cdot\cdot}$ coordinate system and mapping of the $z^{\cdot\cdot}x^{\cdot\cdot}$ and $x^{\cdot\cdot} - z^{\cdot\cdot}$ planes on the $x^{\cdot}y^{\cdot}$ system

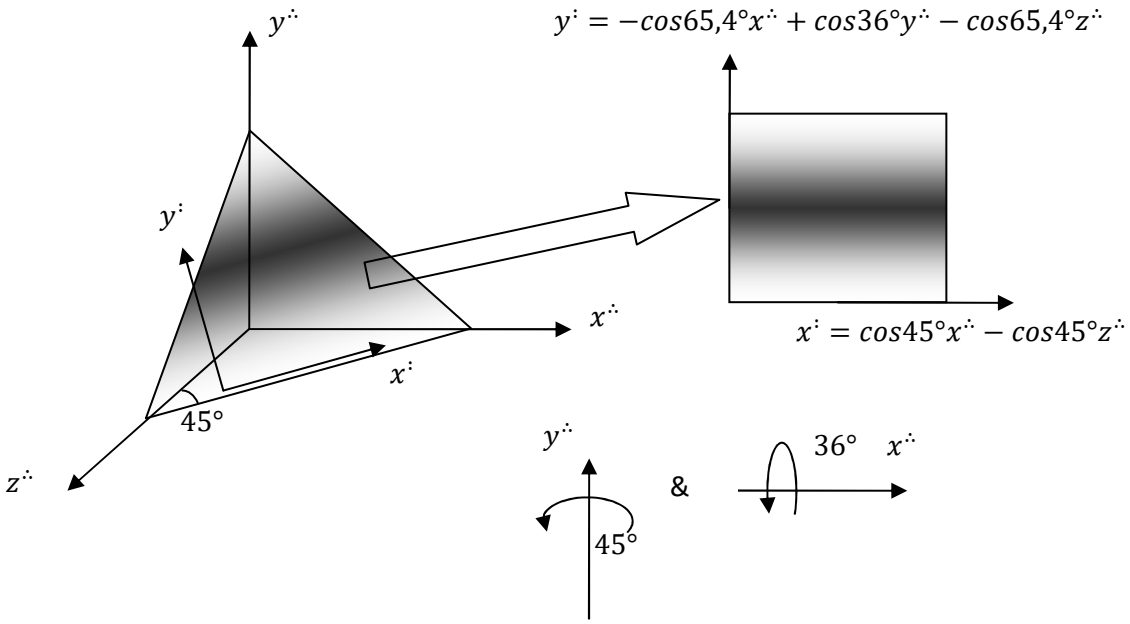

Figure 2-7 Three-dimensional $x''y''z''$ coordinate system and mapping of a non-90° plane to the $x'y'$ system

Every transformation is done on a basis of a transformation matrix. The transformation matrices for all transformations presented in Figure 2-5, Figure 2-6 and Figure 2-7 are given in Table 2-3. It is worth noting that during the transformation the z-axis should not be neglected. It can only be neglected after the transformation is finished and then the z' component can be disregarded.

Table 2-3 Transformation matrices for the transformations of Figure 2-5, Figure 2-6 and Figure 2-7

$\begin{bmatrix} x' \\ y' \\ z' \end{bmatrix} =$	$x''y''$ plane from Figure 2-5	$\begin{bmatrix} 1 & 0 & 0 \\ 0 & 1 & 0 \\ 0 & 0 & 1 \end{bmatrix}$	$\begin{bmatrix} x'' \\ y'' \\ z'' \end{bmatrix}$
	$-y''x''$ plane from Figure 2-5	$\begin{bmatrix} 0 & -1 & 0 \\ 1 & 0 & 0 \\ 0 & 0 & 1 \end{bmatrix}$	
	$z''x''$ plane from Figure 2-6	$\begin{bmatrix} 0 & 0 & 1 \\ 1 & 0 & 0 \\ 0 & 1 & 0 \end{bmatrix}$	
	$x'' - z''$ plane from Figure 2-6	$\begin{bmatrix} 1 & 0 & 0 \\ 0 & 0 & -1 \\ 0 & 1 & 0 \end{bmatrix}$	
	Transformation from Figure 2-7	$\begin{bmatrix} cos45° & 0 & -cos45° \\ -cos65{,}4° & cos36° & -cos65{,}4° \\ cos55{,}1° & cos54° & cos55{,}1° \end{bmatrix}$	

Transformation is performed by tensor-multiplying the elasticity matrix C_{ijkl} with the transformation matrix. For simplicity the multiplication that results in the mapping of the $x''y''$ plane on the $x'y'$ plane is shown since it leaves the elasticity matrix unchanged. This is shown in (2.66).

$$\overbrace{C_{ijkl}}^{after\ transformation} = \begin{bmatrix} 1 & 0 & 0 \\ 0 & 1 & 0 \\ 0 & 0 & 1 \end{bmatrix} \overbrace{C_{ijkl}}^{before\ transformation} \tag{2.66}$$

In the resulting elasticity matrix, all the z-related entries can be disregarded as shown in (2.67).

$$\overbrace{C_{ijkl}}^{after\ transf.} = \begin{bmatrix} & j=1 & & & j=2 & & & j=3 & \\ i=1 & C_{1111} & C_{1112} & - & C_{1211} & C_{1212} & - & - & - & - \\ & C_{1121} & C_{1122} & - & C_{1221} & C_{1222} & - & - & - & - \\ & - & - & - & - & - & - & - & - & - \\ i=2 & C_{2111} & C_{2112} & - & C_{2211} & C_{2212} & - & - & - & - \\ & C_{2121} & C_{2122} & - & C_{2221} & C_{2222} & - & - & - & - \\ & - & - & - & - & - & - & - & - & - \\ & - & - & - & - & - & - & - & - & - \\ i=3 & - & - & - & - & - & - & - & - & - \\ & - & - & - & - & - & - & - & - & - \end{bmatrix} \tag{2.67}$$

2.3.3. Thermoelasticity (coupled problem with three fields)

In thermoelasticity, a third scalar field is present, additionally to the two mechanical displacement fields. This is the temperature T. The temperature produces an additional thermal strain which is shown in (2.68) [42]. An application example of this physics mode, can be the investigation of the effect of acceleration forces on a sensor, under different temperature conditions.

$$\sigma_{st} = C\varepsilon_{st} - C\varepsilon_{st\theta} \tag{2.68}$$

where: $\varepsilon_{st\theta}$ is the rank-2 thermal strain tensor

The thermal strain is related to the temperature via the thermal expansion rank-2 tensor. This is shown in (2.69).

$$\varepsilon_{st\theta} = AT \tag{2.69}$$

where: A is the rank-2 thermal expansion tensor

With (2.69), the relationship in (2.68) is written as in (2.70).

$$\sigma_{st} = C\varepsilon_{st} - CAT \tag{2.70}$$

The tensor multiplication of C with A results in the so called stress-temperature tensor which is indicated with M (2.71).

$$M_{ij} = C_{ijkl}A_{kl} \tag{2.71}$$

In two spatial dimensions, this tensor has four entries which are:

$$M_{ij} = \begin{bmatrix} M_{11} & M_{12} \\ M_{21} & M_{22} \end{bmatrix} \tag{2.72}$$

In order to map the individual entries of the M tensor to the general mathematical formulation, (2.60) needs to be revisited. In (2.60), it is seen that the first equation is related to the $\sigma_{st:11}$ and the $\sigma_{st:12}$ stresses, whereas the second equation is related to the $\sigma_{st:21}$ and $\sigma_{st:22}$ stresses. Since $\sigma_{st:ij}$ shares the same indices with M_{ij}, M_{11} and M_{12} are mapped to the first, whereas M_{21} and M_{22} are mapped to the second equation. The mapping is done via the general PDE coefficient γ. The two following equations are obtained.

$$
\begin{aligned}
-\nabla\cdot\begin{bmatrix}\sigma_{st:11}\\ \sigma_{st:12}\end{bmatrix} &= -\nabla\cdot\begin{bmatrix}C_{1111}\varepsilon_{st:11}\\ C_{1211}\varepsilon_{st:11}\end{bmatrix} - \nabla\cdot\begin{bmatrix}C_{1112}\varepsilon_{st:12}\\ C_{1212}\varepsilon_{st:12}\end{bmatrix}\\
-\nabla\cdot\begin{bmatrix}C_{1121}\varepsilon_{st:21}\\ C_{1221}\varepsilon_{st:21}\end{bmatrix} &- \nabla\cdot\begin{bmatrix}C_{1122}\varepsilon_{st:22}\\ C_{1222}\varepsilon_{st:22}\end{bmatrix} - \nabla\cdot\begin{bmatrix}-M_{11}\\ -M_{12}\end{bmatrix}T\\
-\nabla\cdot\begin{bmatrix}\sigma_{st:21}\\ \sigma_{st:22}\end{bmatrix} &= -\nabla\cdot\begin{bmatrix}C_{2111}\varepsilon_{st:11}\\ C_{2211}\varepsilon_{st:11}\end{bmatrix} - \nabla\cdot\begin{bmatrix}C_{2112}\varepsilon_{st:12}\\ C_{2212}\varepsilon_{st:12}\end{bmatrix}\\
-\nabla\cdot\begin{bmatrix}C_{2121}\varepsilon_{st:21}\\ C_{2221}\varepsilon_{st:21}\end{bmatrix} &- \nabla\cdot\begin{bmatrix}C_{2122}\varepsilon_{st:22}\\ C_{2222}\varepsilon_{st:22}\end{bmatrix} - \nabla\cdot\begin{bmatrix}-M_{21}\\ -M_{22}\end{bmatrix}T
\end{aligned}
\tag{2.73}
$$

The inverse thermoelastic effect describes the variations in temperature caused by the mechanical deformations. A time-harmonic term is introduced in (2.73) and by doing this and rewriting (2.73) by means of the mechanical displacements u_x and u_y, (2.74) is obtained. The time-harmonic term, eventually serves in simulating a surface acoustic wave sensor as a test case in the current thesis. Thermoelasticity and the time-harmonic term are combined with the piezoelectric effect in this case.

$$
\begin{aligned}
-\nabla\cdot\begin{bmatrix}C_{11} & C_{16}\\ C_{16} & C_{66}\end{bmatrix}\nabla u_x - \nabla\cdot\begin{bmatrix}C_{16} & C_{12}\\ C_{66} & C_{26}\end{bmatrix}\nabla u_y - \nabla\cdot\begin{bmatrix}-M_{11}\\ -M_{12}\end{bmatrix}T - \rho\omega^2 u_x = 0\\
-\nabla\cdot\begin{bmatrix}C_{16} & C_{66}\\ C_{12} & C_{26}\end{bmatrix}\nabla u_x - \nabla\cdot\begin{bmatrix}C_{66} & C_{26}\\ C_{26} & C_{22}\end{bmatrix}\nabla u_y - \nabla\cdot\begin{bmatrix}-M_{21}\\ -M_{22}\end{bmatrix}T - \rho\omega^2 u_y = 0
\end{aligned}
\tag{2.74}
$$

where: ρ is the density of the material
ω is the angular frequency

In (2.74), $-\omega^2$ is obtained by replacing the second time derivative $\frac{\partial^2}{\partial t^2}$ with $(j\omega)^2$. The units of the two equations are $\frac{\mathrm{N}}{\mathrm{m}^3}$.

To make it a three-field physics mode the temperature equation is needed. Starting with (2.5), the time-related heat capacity term is added to it. (2.75) is obtained.

$$
-\nabla\cdot\lambda\nabla T + j\omega\rho c_p T = 0 \tag{2.75}
$$

where: c_p is the specific heat capacity

In (2.75) the first time derivative $\frac{\partial}{\partial t}$ is replaced with $j\omega$. The units of the equation are $\frac{\mathrm{W}}{\mathrm{m}^3}$. The reverse thermoelastic effect results in what is effectively a piezocaloric effect, i.e. heat of deformation. It is caused by the time-harmonic mechanical displacement. This effect is shown in (2.76).

$$
-Q_{ted} = -j\omega T_0 M\cdot\nabla u_{st} \tag{2.76}
$$

where: T_0 is a reference temperature (e.g. room temperature)
Q_{ted} is the thermoelastically dissipated power

By including in the left hand side of (2.75) the thermoelastic dissipation of (2.76), (2.77) is obtained. The temperature field T is not to be confused with the reference temperature T_0. This means that in the field plot of T, field point values are given with reference to T_0.

$$-\nabla \cdot \lambda \nabla T - j\omega T_0 M \cdot \nabla u_{st} + j\omega \rho c_p T = 0 \tag{2.77}$$

Now, for the mapping to the general PDE, the u_{st} vector is separated into u_x and u_y components. By this (2.78) is obtained. The parameters are then mapped to the β term of the general PDE and then (2.79) is obtained.

$$-\nabla \cdot \lambda \nabla T - j\omega T_0 \left(M_{11} \frac{\partial u_x}{\partial x} + M_{12} \frac{\partial u_x}{\partial y} + M_{21} \frac{\partial u_y}{\partial x} + M_{22} \frac{\partial u_y}{\partial y} \right) + j\omega \rho c_p T = 0 \tag{2.78}$$

$$-\nabla \cdot \begin{bmatrix} \lambda_{11} & \lambda_{12} \\ \lambda_{21} & \lambda_{22} \end{bmatrix} \nabla T - j\omega T_0 [M_{11} \quad M_{12}] \nabla u_x - j\omega T_0 [M_{21} \quad M_{22}] \nabla u_y + j\omega \rho c_p T = 0 \tag{2.79}$$

The presentation of the mapping of the material parameters of the complete physics mode is presented in (2.80).

A			**x**	**b**
$\nu_{11} = \begin{bmatrix} C_{11} & C_{16} \\ C_{16} & C_{66} \end{bmatrix}$ $\gamma_{11} = 0$ $\beta_{11} = 0$ $\alpha_{11} = -\rho\omega^2$	$\nu_{12} = \begin{bmatrix} C_{16} & C_{12} \\ C_{66} & C_{26} \end{bmatrix}$ $\gamma_{12} = 0$ $\beta_{12} = 0$ $\alpha_{12} = 0$	$\nu_{13} = 0$ $\gamma_{13} = \begin{bmatrix} -M_{11} \\ -M_{12} \end{bmatrix}$ $\beta_{13} = 0$ $\alpha_{13} = 0$	$u_1 = u_x$	0
$\nu_{21} = \begin{bmatrix} C_{16} & C_{66} \\ C_{12} & C_{26} \end{bmatrix}$ $\gamma_{21} = 0$ $\beta_{21} = 0$ $\alpha_{21} = 0$	$\nu_{22} = \begin{bmatrix} C_{66} & C_{26} \\ C_{26} & C_{22} \end{bmatrix}$ $\gamma_{22} = 0$ $\beta_{22} = 0$ $\alpha_{22} = -\rho\omega^2$	$\nu_{23} = 0$ $\gamma_{23} = \begin{bmatrix} -M_{21} \\ -M_{22} \end{bmatrix}$ $\beta_{23} = 0$ $\alpha_{23} = 0$	$u_2 = u_y$	0
$\nu_{31} = 0$ $\gamma_{31} = 0$ $\beta_{31} = -j\omega T_0 [M_{11} \quad M_{12}]$ $\alpha_{31} = 0$	$\nu_{32} = 0$ $\gamma_{32} = 0$ $\beta_{32} = -j\omega T_0 [M_{21} \quad M_{22}]$ $\alpha_{32} = 0$	$\nu_{33} = \begin{bmatrix} \lambda_{11} & \lambda_{12} \\ \lambda_{21} & \lambda_{22} \end{bmatrix}$ $\gamma_{33} = 0$ $\beta_{33} = 0$ $\alpha_{33} = j\omega \rho c_p$	$u_3 = T$	0

(2.80)

2.3.4. Piezoelectricity (coupled problem with three fields)

The piezoelectric physics mode is a combination of structural mechanics and electrostatics [99]. The piezoelectric formulation [15] is given in (2.81). An application example of the piezoelectric physics mode, can be in the simulation of a pressure sensor, by generating a voltage under the condition of deformation.

$$\begin{aligned} \sigma_{st} &= C\varepsilon_{st} - e\boldsymbol{E} \\ \boldsymbol{D} &= e^{t}\varepsilon_{st} + \varepsilon_0\varepsilon_r\boldsymbol{E} \end{aligned} \tag{2.81}$$

where: e is the piezoelectric rank-3 tensor
$\boldsymbol{E}$ is the electric field rank-1 tensor with $\boldsymbol{E} = -\nabla\Phi$
$\boldsymbol{D}$ is the electric displacement rank-1 tensor
e^{t} is the converse piezoelectric rank-3 tensor
ε_0 is the permittivity of free space
ε_r is the relative permittivity rank-2 tensor

The piezoelectric tensor shares two indices with the stress tensor, whereas the converse piezoelectric tensor shares two indices with the strain tensor. The indices of every quantity of (2.81) are given in (2.82). The superscript $\langle\ \ \rangle^{t}$ in the converse piezoelectric tensor stands for the transpose of the non-converse one and it refers to the compressed form of the tensor due to the symmetry in the $\acute{k}, \acute{l}$ indices. If e is reduced by one rank it becomes a matrix.

$$\begin{matrix} \sigma_{st:ij} \\ e_{ij\acute{m}} \\ \varepsilon_{st:\acute{k}\acute{l}} \\ e^{t} = e_{\acute{n}\acute{k}\acute{l}} \\ \boldsymbol{D}_{\acute{n}} \\ \boldsymbol{E}_{\acute{m}} \\ \varepsilon_{r:\acute{n}\acute{m}} \end{matrix} \tag{2.82}$$

When written down fully expanded, the three dimensional $e_{ij\acute{m}}$ tensor looks as in (2.83).

$$e_{ij\acute{m}} = \left[\begin{array}{c|ccc} & e_{111} & e_{121} & e_{131} \\ \acute{m}=1 & e_{211} & e_{221} & e_{231} \\ & e_{311} & e_{321} & e_{331} \\ & e_{112} & e_{122} & e_{132} \\ \acute{m}=2 & e_{212} & e_{222} & e_{232} \\ & e_{312} & e_{322} & e_{332} \\ & e_{113} & e_{123} & e_{133} \\ \acute{m}=3 & e_{213} & e_{223} & e_{233} \\ & e_{313} & e_{323} & e_{333} \end{array}\right] \tag{2.83}$$

Similarly to the elasticity matrix C, the symmetric indices of $e_{ijḿ}$ can be reduced to one index as in (2.84). The double entries can then be omitted as done in (2.58).

$$e_{ijḿ} = \left[\begin{array}{c|ccc} & e_{11} & e_{61} & e_{51} \\ ḿ = 1 & e_{61} & e_{21} & e_{41} \\ & e_{51} & e_{41} & e_{31} \\ & e_{12} & e_{62} & e_{52} \\ ḿ = 2 & e_{62} & e_{22} & e_{42} \\ & e_{52} & e_{42} & e_{32} \\ & e_{13} & e_{63} & e_{53} \\ ḿ = 3 & e_{63} & e_{23} & e_{43} \\ & e_{53} & e_{43} & e_{33} \end{array}\right] \tag{2.84}$$

Indices $ί, ĵ$ are replaced by $ì.$ and (2.85) is obtained. The format in (2.85) is important because this is how material property literature presents the piezoelectric tensors.

$$e_{ìḿ} = \begin{bmatrix} e_{11} & e_{12} & e_{13} \\ e_{21} & e_{22} & e_{23} \\ e_{31} & e_{32} & e_{33} \\ e_{41} & e_{42} & e_{43} \\ e_{51} & e_{52} & e_{53} \\ e_{61} & e_{62} & e_{63} \end{bmatrix} \tag{2.85}$$

For the mapping to the general mathematical formulation the $-e\boldsymbol{E}$ as well as the $e^t\varepsilon_{\mathrm{st}}$ and the $\varepsilon_0\varepsilon_{\mathrm{r}}\boldsymbol{E}$ need to be explicitly expressed. This is done by neglecting the z components.

$$\begin{aligned} -e\boldsymbol{E} &= \begin{cases} -e_{111}\boldsymbol{E}_1 - e_{112}\boldsymbol{E}_2 \\ -e_{121}\boldsymbol{E}_1 - e_{122}\boldsymbol{E}_2 \\ -e_{211}\boldsymbol{E}_1 - e_{212}\boldsymbol{E}_2 \\ -e_{221}\boldsymbol{E}_1 - e_{222}\boldsymbol{E}_2 \end{cases} \\ e^t\varepsilon_{\mathrm{st}} &= \begin{cases} e_{111}\varepsilon_{\mathrm{st:11}} + e_{112}\varepsilon_{\mathrm{st:12}} + e_{121}\varepsilon_{\mathrm{st:21}} + e_{122}\varepsilon_{\mathrm{st:22}} \\ e_{211}\varepsilon_{\mathrm{st:11}} + e_{212}\varepsilon_{\mathrm{st:12}} + e_{221}\varepsilon_{\mathrm{st:21}} + e_{222}\varepsilon_{\mathrm{st:22}} \end{cases} \\ \varepsilon_0\varepsilon_{\mathrm{r}}\boldsymbol{E} &= \begin{cases} \varepsilon_0\varepsilon_{\mathrm{r:11}}\boldsymbol{E}_1 + \varepsilon_0\varepsilon_{\mathrm{r:12}}\boldsymbol{E}_2 \\ \varepsilon_0\varepsilon_{\mathrm{r:21}}\boldsymbol{E}_1 + \varepsilon_0\varepsilon_{\mathrm{r:22}}\boldsymbol{E}_2 \end{cases} \end{aligned} \tag{2.86}$$

The $-\nabla\cdot$ operator is applied on (2.86) and consequently (2.87) is obtained.

$$\begin{aligned} -\nabla\cdot(-e\boldsymbol{E}) &= \begin{cases} -\nabla\cdot\begin{bmatrix} -e_{111}\boldsymbol{E}_1 - e_{112}\boldsymbol{E}_2 \\ -e_{121}\boldsymbol{E}_1 - e_{122}\boldsymbol{E}_2 \end{bmatrix} \\ -\nabla\cdot\begin{bmatrix} -e_{211}\boldsymbol{E}_1 - e_{212}\boldsymbol{E}_2 \\ -e_{221}\boldsymbol{E}_1 - e_{222}\boldsymbol{E}_2 \end{bmatrix} \end{cases} \\ -\nabla\cdot e^t\varepsilon_{\mathrm{st}} &= -\nabla\cdot\begin{bmatrix} e_{111}\varepsilon_{\mathrm{st:11}} + e_{112}\varepsilon_{\mathrm{st:12}} + e_{121}\varepsilon_{\mathrm{st:21}} + e_{122}\varepsilon_{\mathrm{st:22}} \\ e_{211}\varepsilon_{\mathrm{st:11}} + e_{212}\varepsilon_{\mathrm{st:12}} + e_{221}\varepsilon_{\mathrm{st:21}} + e_{222}\varepsilon_{\mathrm{st:22}} \end{bmatrix} \\ -\nabla\cdot(\varepsilon_0\varepsilon_{\mathrm{r}}\boldsymbol{E}) &= -\nabla\cdot\begin{bmatrix} \varepsilon_0\varepsilon_{\mathrm{r:11}}\boldsymbol{E}_1 + \varepsilon_0\varepsilon_{\mathrm{r:12}}\boldsymbol{E}_2 \\ \varepsilon_0\varepsilon_{\mathrm{r:21}}\boldsymbol{E}_1 + \varepsilon_0\varepsilon_{\mathrm{r:22}}\boldsymbol{E}_2 \end{bmatrix} \end{aligned} \tag{2.87}$$

Continuing from (2.87), the electric field is then expressed with the negative gradient of the electric potential and the strain terms with gradient terms of the mechanical displacements. By this (2.88) is obtained. The corresponding terms from (2.88) can now be inserted back to (2.81), after the $-\nabla\cdot$ operator is applied to (2.81) as well.

$$\begin{gathered}-\nabla\cdot(-e\boldsymbol{E})=\begin{cases}-\nabla\cdot\begin{bmatrix}e_{111} & e_{112}\\ e_{121} & e_{122}\end{bmatrix}\nabla\Phi\\ -\nabla\cdot\begin{bmatrix}e_{211} & e_{212}\\ e_{221} & e_{222}\end{bmatrix}\nabla\Phi\end{cases}\\ -\nabla\cdot e^{t}\varepsilon_{\mathrm{st}}=-\nabla\cdot\begin{bmatrix}e_{111} & e_{112}\\ e_{211} & e_{212}\end{bmatrix}\nabla u_x-\nabla\cdot\begin{bmatrix}e_{121} & e_{122}\\ e_{221} & e_{222}\end{bmatrix}\nabla u_y\\ -\nabla\cdot(\varepsilon_0\varepsilon_{\mathrm{r}}\boldsymbol{E})=-\nabla\cdot\varepsilon_0\begin{bmatrix}-\varepsilon_{\mathrm{r:11}} & -\varepsilon_{\mathrm{r:12}}\\ -\varepsilon_{\mathrm{r:21}} & -\varepsilon_{\mathrm{r:22}}\end{bmatrix}\nabla\Phi\end{gathered}\tag{2.88}$$

The mapping is now done, however there should be care with the indices before changing to the symmetric index format of the piezoelectric tensor (the one that the literature uses). The piezoelectric tensor in (2.88) uses the $\acute{\imath},\acute{\jmath},\acute{m}$ indices whereas the converse piezoelectric tensor uses the $\acute{n},\acute{k},\acute{l}$ indices. In the first and second equations of (2.88) $\acute{\imath}$ and $\acute{\jmath}$ are grouped, whereas in the third equation $\acute{k}$ and $\acute{l}$ are grouped. Assuming with the current thesis in mind, no space charge or body forces, the resulting complete piezoelectric formulation is shown in (2.89).

$$\begin{gathered}-\nabla\cdot\begin{bmatrix}C_{11} & C_{16}\\ C_{16} & C_{66}\end{bmatrix}\nabla u_x-\nabla\cdot\begin{bmatrix}C_{16} & C_{12}\\ C_{66} & C_{26}\end{bmatrix}\nabla u_y-\nabla\cdot\begin{bmatrix}e_{11} & e_{12}\\ e_{61} & e_{62}\end{bmatrix}\nabla\Phi=0\\ -\nabla\cdot\begin{bmatrix}C_{16} & C_{66}\\ C_{12} & C_{26}\end{bmatrix}\nabla u_x-\nabla\cdot\begin{bmatrix}C_{66} & C_{26}\\ C_{26} & C_{22}\end{bmatrix}\nabla u_y-\nabla\cdot\begin{bmatrix}e_{61} & e_{62}\\ e_{21} & e_{22}\end{bmatrix}\nabla\Phi=0\\ -\nabla\cdot\begin{bmatrix}e_{11} & e_{61}\\ e_{12} & e_{62}\end{bmatrix}\nabla u_x-\nabla\cdot\begin{bmatrix}e_{61} & e_{21}\\ e_{62} & e_{22}\end{bmatrix}\nabla u_y-\nabla\cdot\varepsilon_0\begin{bmatrix}-\varepsilon_{\mathrm{r:11}} & -\varepsilon_{\mathrm{r:12}}\\ -\varepsilon_{\mathrm{r:21}} & -\varepsilon_{\mathrm{r:22}}\end{bmatrix}\nabla\Phi=0\end{gathered}\tag{2.89}$$

The mapping of the material parameters to the coefficients ν,γ,β,α of the general mathematical formulation is given in (2.90).

A			**x**	**b**
$\nu_{11}=\begin{bmatrix}C_{11} & C_{16}\\ C_{16} & C_{66}\end{bmatrix}$ $\gamma_{11}=0$ $\beta_{11}=0$ $\alpha_{11}=0$	$\nu_{12}=\begin{bmatrix}C_{16} & C_{12}\\ C_{66} & C_{26}\end{bmatrix}$ $\gamma_{12}=0$ $\beta_{12}=0$ $\alpha_{12}=0$	$\nu_{13}=\begin{bmatrix}e_{11} & e_{12}\\ e_{61} & e_{62}\end{bmatrix}$ $\gamma_{13}=0$ $\beta_{13}=0$ $\alpha_{13}=0$	$\mathrm{u}_1=u_x$	0
$\nu_{21}=\begin{bmatrix}C_{16} & C_{66}\\ C_{12} & C_{26}\end{bmatrix}$ $\gamma_{21}=0$ $\beta_{21}=0$ $\alpha_{21}=0$	$\nu_{22}=\begin{bmatrix}C_{66} & C_{26}\\ C_{26} & C_{22}\end{bmatrix}$ $\gamma_{22}=0$ $\beta_{22}=0$ $\alpha_{22}=0$	$\nu_{23}=\begin{bmatrix}e_{61} & e_{62}\\ e_{21} & e_{22}\end{bmatrix}$ $\gamma_{23}=0$ $\beta_{23}=0$ $\alpha_{23}=0$	$\mathrm{u}_2=u_y$	0
$\nu_{31}=\begin{bmatrix}e_{11} & e_{61}\\ e_{12} & e_{62}\end{bmatrix}$ $\gamma_{31}=0$ $\beta_{31}=0$ $\alpha_{31}=0$	$\nu_{32}=\begin{bmatrix}e_{61} & e_{21}\\ e_{62} & e_{22}\end{bmatrix}$ $\gamma_{32}=0$ $\beta_{32}=0$ $\alpha_{32}=0$	$\nu_{33}=\varepsilon_0\begin{bmatrix}-\varepsilon_{\mathrm{r:11}} & -\varepsilon_{\mathrm{r:12}}\\ -\varepsilon_{\mathrm{r:21}} & -\varepsilon_{\mathrm{r:22}}\end{bmatrix}$ $\gamma_{33}=0$ $\beta_{33}=0$ $\alpha_{33}=0$	$\mathrm{u}_3=\Phi$	0

(2.90)

2.3.5. Incompressible fluid flow (coupled problem with three fields)

The incompressible fluid flow or Navier-Stokes equation is given in the following [106].

$$\rho\left(\frac{\partial \boldsymbol{v}}{\partial t} + \boldsymbol{v}\cdot\nabla\boldsymbol{v}\right) = -\nabla p + \mu\nabla^2\boldsymbol{v} + \boldsymbol{F} \tag{2.91}$$

where: $\boldsymbol{v}$ is the velocity of the fluid
p is the pressure of the fluid
μ is the dynamic viscosity of the fluid
$\boldsymbol{F}$ is the body force

In (2.91), $\boldsymbol{v}, \boldsymbol{F}$ are vectors, whereas p, μ are scalars. The equation units are $\frac{\mathrm{N}}{\mathrm{m}^3}$. To start with the mapping of (2.91) to the general PDE, the right-hand side and left-hand side components have to be rearranged. (2.92) demonstrates this.

$$\rho\left(\frac{\partial \boldsymbol{v}}{\partial t} + \boldsymbol{v}\cdot\nabla\boldsymbol{v}\right) + \nabla p - \mu\nabla^2\boldsymbol{v} = \boldsymbol{F} \tag{2.92}$$

The time derivative of the fluid velocity can be ignored in the stationary case. The remaining terms of (2.92) can be written more analytically (taking into account two spatial dimensions) since this will help with the mapping. (2.94) is eventually obtained.

$$\rho\left(\begin{bmatrix} v_x \\ v_y \end{bmatrix}\cdot\nabla\begin{bmatrix} v_x \\ v_y \end{bmatrix}\right) + \begin{bmatrix} \frac{\partial}{\partial x} \\ \frac{\partial}{\partial y} \end{bmatrix} p - \mu\nabla^2\begin{bmatrix} v_x \\ v_y \end{bmatrix} = \boldsymbol{F} \tag{2.93}$$

$$\rho\left(\left(v_x\frac{\partial}{\partial x} + v_y\frac{\partial}{\partial y}\right)\begin{bmatrix} v_x \\ v_y \end{bmatrix}\right) + \begin{bmatrix} \frac{\partial p}{\partial x} \\ \frac{\partial p}{\partial y} \end{bmatrix} - \mu\begin{bmatrix} \nabla^2 v_x \\ \nabla^2 v_y \end{bmatrix} = \begin{bmatrix} F_x \\ F_y \end{bmatrix} \tag{2.94}$$

In (2.94), a two-equation system is clearly seen, one equation for scalar velocity v_x and one for scalar velocity v_y. Separating the two equations and expanding the viscosity term further yields (2.95).

$$\begin{aligned} \rho v_x\frac{\partial v_x}{\partial x} + \rho v_y\frac{\partial v_x}{\partial y} + \frac{\partial p}{\partial x} - \mu\left(\frac{\partial^2 v_x}{\partial x^2} + \frac{\partial^2 v_x}{\partial y^2}\right) &= F_x \\ \rho v_x\frac{\partial v_y}{\partial x} + \rho v_y\frac{\partial v_y}{\partial y} + \frac{\partial p}{\partial y} - \mu\left(\frac{\partial^2 v_y}{\partial x^2} + \frac{\partial^2 v_y}{\partial y^2}\right) &= F_y \end{aligned} \tag{2.95}$$

The diffusion term from (2.13) when fully expanded looks as in (2.96).

$$-\nabla \cdot \nu \nabla \mathrm{u} = -\left(\nu_{11}\frac{\partial^2 \mathrm{u}}{\partial x^2} + \nu_{12}\frac{\partial^2 \mathrm{u}}{\partial x \partial y} + \nu_{21}\frac{\partial^2 \mathrm{u}}{\partial y \partial x} + \nu_{22}\frac{\partial^2 \mathrm{u}}{\partial y^2}\right) \tag{2.96}$$

Using the knowledge from (2.96) in (2.95) in order to map the viscosity term μ to ν yields (2.97).

$$\begin{aligned} \rho v_x \frac{\partial v_x}{\partial x} + \rho v_y \frac{\partial v_x}{\partial y} + \frac{\partial p}{\partial x} - \nabla \cdot \begin{bmatrix} \mu & 0 \\ 0 & \mu \end{bmatrix} \nabla v_x = F_x \\ \rho v_x \frac{\partial v_y}{\partial x} + \rho v_y \frac{\partial v_y}{\partial y} + \frac{\partial p}{\partial y} - \nabla \cdot \begin{bmatrix} \mu & 0 \\ 0 & \mu \end{bmatrix} \nabla v_y = F_y \end{aligned} \tag{2.97}$$

The remaining terms of (2.97) are all mapped to the β parameters of the general PDE. To complete the incompressible fluid flow equation system, the mass continuity equation is also needed, in its form under the assumption of incompressibility. This equation is given in (2.98), and in the current physics mode it is presented as the pressure field equation, however it does not explicitly contain any pressure variable.

$$\frac{\partial v_x}{\partial x} + \frac{\partial v_y}{\partial y} = 0 \tag{2.98}$$

The two terms of (2.98) are also mapped to the β parameters of the general PDE. The complete incompressible fluid flow equation system and the complete mapping of the material parameters are given in (2.99) and (2.100).

$$\begin{aligned} -\nabla \cdot \begin{bmatrix} \mu & 0 \\ 0 & \mu \end{bmatrix} \nabla v_x + [\rho v_x \quad \rho v_y] \nabla v_x + [1 \quad 0] \nabla p = F_x \\ -\nabla \cdot \begin{bmatrix} \mu & 0 \\ 0 & \mu \end{bmatrix} \nabla v_y + [\rho v_x \quad \rho v_y] \nabla v_y + [0 \quad 1] \nabla p = F_y \\ [1 \quad 0] \nabla v_x + [0 \quad 1] \nabla v_y = 0 \end{aligned} \tag{2.99}$$

A			**x**	**b**
$\nu_{11} = \begin{bmatrix} \mu & 0 \\ 0 & \mu \end{bmatrix}$ $\gamma_{11} = 0$ $\beta_{11} = [\rho v_x \quad \rho v_y]$ $\alpha_{11} = 0$	$\nu_{12} = 0$ $\gamma_{12} = 0$ $\beta_{12} = 0$ $\alpha_{12} = 0$	$\nu_{13} = 0$ $\gamma_{13} = 0$ $\beta_{13} = [1 \quad 0]$ $\alpha_{13} = 0$	$\mathrm{u}_1 = v_x$	F_x
$\nu_{21} = 0$ $\gamma_{21} = 0$ $\beta_{21} = 0$ $\alpha_{21} = 0$	$\nu_{22} = \begin{bmatrix} \mu & 0 \\ 0 & \mu \end{bmatrix}$ $\gamma_{22} = 0$ $\beta_{22} = [\rho v_x \quad \rho v_y]$ $\alpha_{22} = 0$	$\nu_{23} = 0$ $\gamma_{23} = 0$ $\beta_{23} = [0 \quad 1]$ $\alpha_{23} = 0$	$\mathrm{u}_2 = v_y$	F_y
$\nu_{31} = 0$ $\gamma_{31} = 0$ $\beta_{31} = [1 \quad 0]$ $\alpha_{31} = 0$	$\nu_{32} = 0$ $\gamma_{32} = 0$ $\beta_{32} = [0 \quad 1]$ $\alpha_{32} = 0$	$\nu_{33} = 0$ $\gamma_{33} = 0$ $\beta_{33} = 0$ $\alpha_{33} = 0$	$\mathrm{u}_3 = p$	0

(2.100)

The mapping of the pressure field equation to the β_{31} and β_{32} terms, could alternatively be done to the γ_{31} and γ_{32} terms of the general PDE as shown in the following:

$$\begin{gathered} -\nabla\cdot\gamma_{31}v_x-\nabla\cdot\gamma_{32}v_y= \\ -\nabla\cdot\begin{bmatrix}-1\\0\end{bmatrix}v_x-\nabla\cdot\begin{bmatrix}0\\-1\end{bmatrix}v_y= \\ -\begin{bmatrix}\frac{\partial}{\partial x} & \frac{\partial}{\partial y}\end{bmatrix}\cdot\begin{bmatrix}-1\\0\end{bmatrix}v_x-\begin{bmatrix}\frac{\partial}{\partial x} & \frac{\partial}{\partial y}\end{bmatrix}\cdot\begin{bmatrix}0\\-1\end{bmatrix}v_y= \\ \frac{\partial v_x}{\partial x}+\frac{\partial v_y}{\partial y}\end{gathered} \tag{2.101}$$

The testing of the physics mode under this mapping, did not show any computational speedup significance under the employment of the direct solver package [35], and therefore there was no further experimentation on the γ-term setup, because the β-term setup was deemed sufficient already. The parameter mapping interchange between the γ- and β- terms however, could allow for the investigation of the theory of reciprocity [91]. On the basis of finding a corresponding example test case, the provided software capability could provide the ground for further practical experimentation with the theory.

2.3.6. Piezopyroelectricity (coupled problem with four fields)

Piezopyroelectricity is a physics mode with four scalar fields, that can be regarded as an expansion to the three fields of piezoelectricity (Section 2.3.4) with one additional field, the thermal. "Pyro" stands for the pyroelectric effect. Alternatively the physics mode can be seen as an expansion to thermoelasticity [42] in Section 2.3.3, since the thermoelastic effect is also included in the formulation.. By combining the piezoelectric and thermoelastic effects for which the material parameters mapping was derived earlier, (2.102) is obtained [120]. The physics mode is presented in a time-harmonic form. The motivation is to simulate a surface acoustic wave device with thermal dissipation effects.

$$\begin{gathered} -\nabla\cdot\begin{bmatrix}C_{11} & C_{16}\\ C_{16} & C_{66}\end{bmatrix}\nabla u_x-\nabla\cdot\begin{bmatrix}C_{16} & C_{12}\\ C_{66} & C_{26}\end{bmatrix}\nabla u_y-\nabla\cdot\begin{bmatrix}e_{11} & e_{12}\\ e_{61} & e_{62}\end{bmatrix}\nabla\Phi \\ -\nabla\cdot\begin{bmatrix}-M_{11}\\ -M_{12}\end{bmatrix}T-\rho\omega^2u_x=0 \\ -\nabla\cdot\begin{bmatrix}C_{16} & C_{66}\\ C_{12} & C_{26}\end{bmatrix}\nabla u_x-\nabla\cdot\begin{bmatrix}C_{66} & C_{26}\\ C_{26} & C_{22}\end{bmatrix}\nabla u_y-\nabla\cdot\begin{bmatrix}e_{61} & e_{62}\\ e_{21} & e_{22}\end{bmatrix}\nabla\Phi \\ -\nabla\cdot\begin{bmatrix}-M_{21}\\ -M_{22}\end{bmatrix}T-\rho\omega^2u_y=0 \\ -\nabla\cdot\begin{bmatrix}e_{11} & e_{61}\\ e_{12} & e_{62}\end{bmatrix}\nabla u_x-\nabla\cdot\begin{bmatrix}e_{61} & e_{21}\\ e_{62} & e_{22}\end{bmatrix}\nabla u_y-\nabla\cdot\varepsilon_0\begin{bmatrix}-\varepsilon_{r:11} & -\varepsilon_{r:12}\\ -\varepsilon_{r:21} & -\varepsilon_{r:22}\end{bmatrix}\nabla\Phi=0 \\ -\nabla\cdot\begin{bmatrix}\lambda_{11} & \lambda_{12}\\ \lambda_{21} & \lambda_{22}\end{bmatrix}\nabla T-j\omega T_0[M_{11}\quad M_{12}]\nabla u_x-j\omega T_0[M_{21}\quad M_{22}]\nabla u_y \\ +j\omega\rho c_pT=0\end{gathered} \tag{2.102}$$

The pyroelectric effect is described by the pyroelectric tensor P which is a rank one tensor. It can be added to the third equation of (2.102) as an additional left-hand side component. (2.103) is the electric displacement equation from piezoelectricity with the added pyroelectric effect.

$$\begin{aligned} \boldsymbol{D} &= e^t \varepsilon_{\mathrm{st}} + PT + \varepsilon_0 \varepsilon_{\mathrm{r}} \boldsymbol{E} \\ \Rightarrow\ -\nabla \cdot \boldsymbol{D} &= -\nabla \cdot e^t \varepsilon_{\mathrm{st}} - \nabla \cdot PT - \nabla \cdot \varepsilon_0 \varepsilon_{\mathrm{r}} \boldsymbol{E} \end{aligned} \tag{2.103}$$

From (2.103), it is seen that the mapping coefficient of the general PDE for P is γ. The converse pyroelectric effect is expressed by means of heat which is generated due to a sinusoidal alternating electric potential. (2.104) is the temperature field equation of piezopyroelectricity written with the added converse pyroelectric effect.

$$-\nabla \cdot \lambda \nabla T - j\omega T_0 M \cdot \nabla u_{st} + j\omega T_0 P \nabla \Phi + j\omega \rho c_p T = 0 \tag{2.104}$$

The mapping coefficient of the general PDE for the converse pyroelectric effect is β. The complete mapping for the four field physics mode of piezopyroelectricity is presented in (2.105).

A				**x**	**b**
$\nu_{11} = \begin{bmatrix} C_{11} & C_{16} \\ C_{16} & C_{66} \end{bmatrix}$ $\gamma_{11} = 0$ $\beta_{11} = 0$ $\alpha_{11} = -\rho\omega^2$	$\nu_{12} = \begin{bmatrix} C_{16} & C_{12} \\ C_{66} & C_{26} \end{bmatrix}$ $\gamma_{12} = 0$ $\beta_{12} = 0$ $\alpha_{12} = 0$	$\nu_{13} = \begin{bmatrix} e_{11} & e_{12} \\ e_{61} & e_{62} \end{bmatrix}$ $\gamma_{13} = 0$ $\beta_{13} = 0$ $\alpha_{13} = 0$	$\nu_{14} = 0$ $\gamma_{14} = \begin{bmatrix} -M_{11} \\ -M_{12} \end{bmatrix}$ $\beta_{14} = 0$ $\alpha_{14} = 0$	$u_1 = u_x$	0
$\nu_{21} = \begin{bmatrix} C_{16} & C_{66} \\ C_{12} & C_{26} \end{bmatrix}$ $\gamma_{21} = 0$ $\beta_{21} = 0$ $\alpha_{21} = 0$	$\nu_{22} = \begin{bmatrix} C_{66} & C_{26} \\ C_{26} & C_{22} \end{bmatrix}$ $\gamma_{22} = 0$ $\beta_{22} = 0$ $\alpha_{22} = -\rho\omega^2$	$\nu_{23} = \begin{bmatrix} e_{61} & e_{62} \\ e_{21} & e_{22} \end{bmatrix}$ $\gamma_{23} = 0$ $\beta_{23} = 0$ $\alpha_{23} = 0$	$\nu_{24} = 0$ $\gamma_{24} = \begin{bmatrix} -M_{21} \\ -M_{22} \end{bmatrix}$ $\beta_{24} = 0$ $\alpha_{24} = 0$	$u_2 = u_y$	0
$\nu_{31} = \begin{bmatrix} e_{11} & e_{61} \\ e_{12} & e_{62} \end{bmatrix}$ $\gamma_{31} = 0$ $\beta_{31} = 0$ $\alpha_{31} = 0$	$\nu_{32} = \begin{bmatrix} e_{61} & e_{21} \\ e_{62} & e_{22} \end{bmatrix}$ $\gamma_{32} = 0$ $\beta_{32} = 0$ $\alpha_{32} = 0$	$\nu_{33} = \varepsilon_0 \begin{bmatrix} -\varepsilon_{\mathrm{r}:11} & -\varepsilon_{\mathrm{r}:12} \\ -\varepsilon_{\mathrm{r}:21} & -\varepsilon_{\mathrm{r}:22} \end{bmatrix}$ $\gamma_{33} = 0$ $\beta_{33} = 0$ $\alpha_{33} = 0$	$\nu_{34} = 0$ $\gamma_{34} = \begin{bmatrix} P_1 \\ P_2 \end{bmatrix}$ $\beta_{34} = 0$ $\alpha_{34} = 0$	$u_3 = \Phi$	0
$\nu_{41} = 0$ $\gamma_{41} = 0$ $\beta_{41} = -j\omega T_0 [M_{11} \quad M_{12}]$ $\alpha_{41} = 0$	$\nu_{42} = 0$ $\gamma_{42} = 0$ $\beta_{42} = -j\omega T_0 [M_{21} \quad M_{22}]$ $\alpha_{42} = 0$	$\nu_{43} = 0$ $\gamma_{43} = 0$ $\beta_{43} = j\omega T_0 [P_1 \quad P_2]$ $\alpha_{43} = 0$	$\nu_{44} = \begin{bmatrix} \lambda_{11} & \lambda_{12} \\ \lambda_{21} & \lambda_{22} \end{bmatrix}$ $\gamma_{44} = 0$ $\beta_{44} = 0$ $\alpha_{44} = j\omega\rho c_p$	$u_4 = T$	0

(2.105)

2.3.7. Incompressible fluid-electric (coupled problem with four fields)

The incompressible fluid-electric physics mode is a combination of incompressible fluid-flow and electrostatics [75]. Compared to (2.92), in the fluid velocity equation, a coupling component to the electric potential Φ is taken into account. (2.106) demonstrates this.

$$\rho \boldsymbol{v} \cdot \nabla \boldsymbol{v} + \nabla p + \rho_f \nabla \Phi - \mu \nabla^2 \boldsymbol{v} = \boldsymbol{F} \tag{2.106}$$

where: ρ_f is the space charge density of free ions

As seen in the incompressible fluid flow section earlier, (2.106) splits into two equations, one for v_x and one for v_y. Therefore the $\rho_f \nabla \Phi$ term is also split between these two equations. The mapping is done to the β coefficients of the general PDE. The complete mapping for the four fields (two scalar fluid velocities, pressure and electric potential) is presented in (2.107).

A				**x**	**b**
$\nu_{11} = \begin{bmatrix} \mu & 0 \\ 0 & \mu \end{bmatrix}$ $\gamma_{11} = 0$ $\beta_{11} = [\rho v_x \quad \rho v_y]$ $\alpha_{11} = 0$	$\nu_{12} = 0$ $\gamma_{12} = 0$ $\beta_{12} = 0$ $\alpha_{12} = 0$	$\nu_{13} = 0$ $\gamma_{13} = 0$ $\beta_{13} = [1 \quad 0]$ $\alpha_{13} = 0$	$\nu_{14} = 0$ $\gamma_{14} = 0$ $\beta_{14} = [\rho_f \quad 0]$ $\alpha_{14} = 0$	$u_1 = v_x$	F_x
$\nu_{21} = 0$ $\gamma_{21} = 0$ $\beta_{21} = 0$ $\alpha_{21} = 0$	$\nu_{22} = \begin{bmatrix} \mu & 0 \\ 0 & \mu \end{bmatrix}$ $\gamma_{22} = 0$ $\beta_{22} = [\rho v_x \quad \rho v_y]$ $\alpha_{22} = 0$	$\nu_{23} = 0$ $\gamma_{23} = 0$ $\beta_{23} = [0 \quad 1]$ $\alpha_{23} = 0$	$\nu_{24} = 0$ $\gamma_{24} = 0$ $\beta_{24} = [0 \quad \rho_f]$ $\alpha_{24} = 0$	$u_2 = v_y$	F_y
$\nu_{31} = 0$ $\gamma_{31} = 0$ $\beta_{31} = [1 \quad 0]$ $\alpha_{31} = 0$	$\nu_{32} = 0$ $\gamma_{32} = 0$ $\beta_{32} = [0 \quad 1]$ $\alpha_{32} = 0$	$\nu_{33} = 0$ $\gamma_{33} = 0$ $\beta_{33} = 0$ $\alpha_{33} = 0$	$\nu_{34} = 0$ $\gamma_{34} = 0$ $\beta_{34} = 0$ $\alpha_{34} = 0$	$u_3 = p$	0
$\nu_{41} = 0$ $\gamma_{41} = 0$ $\beta_{41} = 0$ $\alpha_{41} = 0$	$\nu_{42} = 0$ $\gamma_{42} = 0$ $\beta_{42} = 0$ $\alpha_{42} = 0$	$\nu_{43} = 0$ $\gamma_{43} = 0$ $\beta_{43} = 0$ $\alpha_{43} = 0$	$\nu_{44} = \varepsilon_0 \begin{bmatrix} -\varepsilon_{r:11} & -\varepsilon_{r:12} \\ -\varepsilon_{r:21} & -\varepsilon_{r:22} \end{bmatrix}$ $\gamma_{44} = 0$ $\beta_{44} = 0$ $\alpha_{44} = 0$	$u_4 = \Phi$	ρ_f

(2.107)

The fluid flow related physics modes in Sections 2.3.5 and 2.3.7, can be utilized in the simulation of micro-fluidic channels in the area of microsystems. In the actual thesis, they have been selected for the formation of two problem test cases, presented in Chapter 5.

2.3.8. Incompressible fluid-electric-mass concentration (coupled problem with five fields)

The Nernst-Planck equation can be added to the fluid-electric system of PDEs, and consequently a five-field physics mode where the fifth field corresponds to the mass concentration, can be implemented [127]. The Nernst-Planck equation is presented.

$$-\nabla \cdot D\nabla c + \nabla \cdot \boldsymbol{v}c - \nabla \cdot D\frac{z\bar{e}}{k_B T}c\nabla\Phi = 0 \tag{2.108}$$

where: D is rank-2 molecular diffusivity
c is the mass concentration
z is the ionic valence
$\bar{e}$ is the electron charge
k_B is Boltzmann's constant

When written more explicitly (2.108) looks as in (2.109).

$$-\nabla \cdot \begin{bmatrix} D_{11} & 0 \\ 0 & D_{22} \end{bmatrix}\nabla c + \nabla \cdot \begin{bmatrix} v_x \\ v_y \end{bmatrix} c - \nabla \cdot \begin{bmatrix} D_{11} & 0 \\ 0 & D_{22} \end{bmatrix}\frac{z\bar{e}}{k_B T}c\nabla\Phi = 0 \tag{2.109}$$

The ionic concentration c is a scalar field quantity in the equation system. (2.106) is rewritten as follows:

$$\rho\boldsymbol{v} \cdot \nabla\boldsymbol{v} + \nabla p + z\bar{e}cN_A\nabla\Phi - \mu\nabla^2\boldsymbol{v} = \boldsymbol{F} \tag{2.110}$$

where: N_A is Avogadro's constant

The complete mapping to the general PDE is presented in (2.111).

The fluid-electric-mass concentration physics mode was the most ambitious with regards to the software implementation due to its complexity. It was deemed that further experimentation on this physics mode would require a further research branch-off in the direction of matrix conditioning and manipulation. The direct solver package [35] could not cope well. For that purpose, special tools would be required, in order to visualize the global matrix with regards to how it is populated by entries, and then with regards to how the direct solver is affected by that. It should be reminded that for any possible future physics mode implementations, the number of fields in the general PDE framework is theoretically unlimited. However upon implementing the fluid-electric-mass concentration physics mode, it was shown that practical limits still exist. Consequently, it was assumed at that point that the practical cap software-wise was reached.

A					**x**	**b**
$\nu_{11} = \begin{bmatrix} \mu & 0 \\ 0 & \mu \end{bmatrix}$ $\gamma_{11} = 0$ $\beta_{11} = [\rho v_x \quad \rho v_y]$ $\alpha_{11} = 0$	$\nu_{12} = 0$ $\gamma_{12} = 0$ $\beta_{12} = 0$ $\alpha_{12} = 0$	$\nu_{13} = 0$ $\gamma_{13} = 0$ $\beta_{13} = [1 \quad 0]$ $\alpha_{13} = 0$	$\nu_{14} = 0$ $\gamma_{14} = 0$ $\beta_{14} = [z\bar{e}cN_A \quad 0]$ $\alpha_{14} = 0$	$\nu_{15} = 0$ $\gamma_{15} = 0$ $\beta_{15} = 0$ $\alpha_{15} = 0$	$u_1 = v_x$	F_x
$\nu_{21} = 0$ $\gamma_{21} = 0$ $\beta_{21} = 0$ $\alpha_{21} = 0$	$\nu_{22} = \begin{bmatrix} \mu & 0 \\ 0 & \mu \end{bmatrix}$ $\gamma_{22} = 0$ $\beta_{22} = [\rho v_x \quad \rho v_y]$ $\alpha_{22} = 0$	$\nu_{23} = 0$ $\gamma_{23} = 0$ $\beta_{23} = [0 \quad 1]$ $\alpha_{23} = 0$	$\nu_{24} = 0$ $\gamma_{24} = 0$ $\beta_{24} = [0 \quad z\bar{e}cN_A]$ $\alpha_{24} = 0$	$\nu_{25} = 0$ $\gamma_{25} = 0$ $\beta_{25} = 0$ $\alpha_{25} = 0$	$u_2 = v_y$	F_y
$\nu_{31} = 0$ $\gamma_{31} = 0$ $\beta_{31} = [1 \quad 0]$ $\alpha_{31} = 0$	$\nu_{32} = 0$ $\gamma_{32} = 0$ $\beta_{32} = [0 \quad 1]$ $\alpha_{32} = 0$	$\nu_{33} = 0$ $\gamma_{33} = 0$ $\beta_{33} = 0$ $\alpha_{33} = 0$	$\nu_{34} = 0$ $\gamma_{34} = 0$ $\beta_{34} = 0$ $\alpha_{34} = 0$	$\nu_{35} = 0$ $\gamma_{35} = 0$ $\beta_{35} = 0$ $\alpha_{35} = 0$	$u_3 = p$	0
$\nu_{41} = 0$ $\gamma_{41} = 0$ $\beta_{41} = 0$ $\alpha_{41} = 0$	$\nu_{42} = 0$ $\gamma_{42} = 0$ $\beta_{42} = 0$ $\alpha_{42} = 0$	$\nu_{43} = 0$ $\gamma_{43} = 0$ $\beta_{43} = 0$ $\alpha_{43} = 0$	$\nu_{44} = \varepsilon_0 \begin{bmatrix} -\varepsilon_{r:11} & -\varepsilon_{r:12} \\ -\varepsilon_{r:21} & -\varepsilon_{r:22} \end{bmatrix}$ $\gamma_{44} = 0$ $\beta_{44} = 0$ $\alpha_{44} = 0$	$\nu_{45} = 0$ $\gamma_{45} = 0$ $\beta_{45} = 0$ $\alpha_{45} = 0$	$u_4 = \Phi$	ρ_f
$\nu_{51} = 0$ $\gamma_{51} = 0$ $\beta_{51} = 0$ $\alpha_{51} = 0$	$\nu_{52} = 0$ $\gamma_{52} = 0$ $\beta_{52} = 0$ $\alpha_{52} = 0$	$\nu_{53} = 0$ $\gamma_{53} = 0$ $\beta_{53} = 0$ $\alpha_{53} = 0$	$\nu_{54} = \begin{bmatrix} D_{11} & 0 \\ 0 & D_{22} \end{bmatrix} \frac{z\bar{e}}{k_B T} c$ $\gamma_{54} = 0$ $\beta_{54} = 0$ $\alpha_{54} = 0$	$\nu_{55} = \begin{bmatrix} D_{11} & 0 \\ 0 & D_{22} \end{bmatrix}$ $\gamma_{55} = \begin{bmatrix} -v_x \\ -v_y \end{bmatrix}$ $\beta_{55} = 0$ $\alpha_{55} = 0$	$u_5 = c$	0

(2.111)

3. Adaptive Algorithms in Coupled Problems and Software Implementation

The finite element method is a computational technique, which is used to obtain approximate solutions to engineering problems. In mathematical terms, one or more dependent variables must satisfy a differential equation everywhere within a known domain of independent variables, and also satisfy specific conditions on the boundary of the domain. These problems are also called field problems [57].

If the through-the-FEM numerically obtained field is characterized by a linear distribution throughout the geometrical domain and is also singularities-free, then it can be approximated by first order elements and a coarse mesh. If the distribution is non-linear, the linear interpolation that first-order elements offer is not sufficient. Higher-order elements should be utilized. According to [47], if singularities are present in the domain, then a finer mesh (i.e. with a larger number of elements) should be utilized. Singularities are characterized as points in the domain, where the numerical values tend towards infinity. One cause for singularities could be the inconsiderate selection of boundary conditions, for example applying a predetermined value on a single node. Smaller-sized elements offer improved solution approximation in the case of a rapid-varying solution.

The first rough idea that comes to mind, is to straight away employ high order elements and a fine mesh so that the numerically obtained approximation is as accurate as possible. The problem however is that the computing power is finite. It has certainly increased in the last decades by a large margin, however it still remains finite. Furthermore, most problems happen to simultaneously posses regions of small as well as high potential gradients. This means that in some regions, the computational power invested on high order elements is well worth it, whereas in other regions it can be regarded as a waste of resources. It can be proven that fine meshes mainly help in treatment of singularity-errors. Therefore a fine mesh in a region that does not possess any singularities can be regarded as a waste of computational resources.

Most modern FEM programs posses user-friendly graphical user interfaces. Concerning the post-processing plots, they are mostly constructed by utilizing the visible color spectrum and this makes these plots attractive to the users who conduct the simulations. According to [10] the graphical display of very high quality and sophistication often obscures the quality and reliability of the computed data and gives the user unsubstantiated confidence in the results. The commercial FEM codes are in many cases used as black boxes by inexperienced users who are unable to detect gross errors in the computed results.

This is the point where adaptive algorithms come to play. Once they are integrated in the FEM programs code, they can help in the detection of the regions of the field where the numerical approximation suffers from large errors and they can decide on the element order increase or the refining of the mesh. Therefore the computational efficiency increases. A common measurement of computational efficiency in the finite element method is the "residual vs. degrees of freedom" plot.

Identifying the problematic regions of the problem's field is the task of the error-estimator. An error-estimator routine typically computes the residual on an element-by-element basis, and marks the most problematic elements, i.e. the ones that will potentially offer the best solution accuracy improvement when more degrees of freedom are invested in them. The adaptive routine can then decide on the type of the investment (element order increase or mesh refinement) in the way that it considers most efficient.

The current thesis is concerned with implementing adaptive algorithms for multi-field problems. Adaptation techniques already exist for a variety of physics modes (ranging from structural mechanics to fluidic problems and electromagnetics). In many cases, the adaptation technique concentrates on the solution improvement of a single field. The task to improve the solution of multiple fields simultaneously is considerably more challenging. This thesis attempts to make a step towards constructing adaptive algorithms which are applicable to the general multi-field PDE and therefore generally applicable to a variety of multi-field problems.

In addition to adjusting the existing single-field algorithms so that they are functional in multi-field problems, the error-estimation routine has to be adjusted so that it also works in the general multi-field problem case. When bi-directional and fully coupled problems are investigated, an error-estimator of higher sophistication is required, since the energies that individual fields posses are coupled.

3.1. A review of error estimation and adaptation techniques for the finite element method

Mainly, there are three adaptation techniques for the finite element method. These are namely the *h*-, *p*-, and *hp*-method. The *h*- version is the classical adaptive method in finite elements and it refines the mesh whereas it leaves the polynomial order of the elements unchanged [9]. The *p*- version adapts the polynomial order of the elements, whereas it leaves the mesh unchanged. In the *hp*- version both the mesh and the polynomial order of the elements are changed.

The paper [9] distinguishes between two types in the adaptive mesh construction concerning the *h*-adaptation method. In the first one, a sequence of meshes is constructed by consecutive refinement or derefinement of the particular elements. The goal in this approach is to make the elemental error indicators "η" equally distributed. Once the error estimator indicates acceptable accuracy, the mesh is accepted. In the second type of mesh construction, a crude mesh is used initially, in order to obtain the basic characteristic of the solution. Using the characteristic, a new mesh is constructed and the problem accuracy is checked. The process is repeated until the expected accuracy is achieved. The first approach is called local, whereas the second is called global. In this thesis, the global approach is followed. The reason for this is that the target is to treat multi-field problems and not just single-field. In a four-

field problem for instance, where all fields share the same mesh and same element order, there are four times more DOFs than in the single-field problem. Therefore it is reasonably more computational cost-effective to start with a crude mesh.

In the *p*-adaptation version, only the element order is adapted. The simpler way is to adapt the element order uniformly and the more sophisticated one, non-uniformly. In this thesis, the more sophisticated and at the same time more efficient, non-uniform order adaptation is followed. Furthermore, in the treatment of multi-field problems, the element order is adapted independently for every field. The weakness of the *p*-version is that it cannot treat the error arising from the presence of singularities. Therefore initial mesh choice plays an important role. The impression however in this thesis is that carefully constructing an initial mesh degrades the automation in the procedure compared to the crude initial mesh approach. Additionally, further on in the script a comparison between the three versions *h*-, *p*, and *hp*- is performed and in order to be consistent in the comparison, a crude mesh has to be used as the starting point in all three versions.

The *hp*- version simultaneously refines the mesh and increases the element order of the elements. Effectively the *hp*- version is a combination of the *h*- and *p*- versions and consequently, depending on the type of combination a variety of *hp*- algorithms can be constructed. As a basis in this thesis, the paper [103] is followed. Three of the presented *hp*-algorithms are expanded in their functionality so that they can treat multi-field problems and are tested.

An error estimator gives an estimate for the error in a solution quantity and serves as a criterion for acceptance of the solution. An error indicator is used in the adaptive refinement and it should provide sufficient local information to control the adaptation process [2]. A major requirement is that the computation of an a-posteriori estimator should have reasonable cost. This is the main reason why the concentration is on explicit residual error indicators [10, 117]. The indicator serves to identify regions of the computational domain with insufficient precision.

Error estimators and indicators have been intensively studied in the case of uncoupled problems. Explicit element-wise residual estimators are especially simple to compute. In [97], the Poisson equation in two and three dimensions with discontinuous coefficients is considered. The presented a posteriori error estimates are reliable and efficient. Definition-wise, an estimator is called reliable, if it yields an upper bound on the difference between exact and approximate solution. It is also called efficient, if it additionally provides a local lower bound for the error. A similar result is reported in [16], which also extends to the case where "ν" is a tensor. The case of the reaction-diffusion or convection-diffusion equation requires some modification, however the estimator is of similar type [116, 117]. For the Poisson equation and higher order elements in *hp*-adaptation an error indicator is derived in [79]. The estimator in this case is reliable, i.e. it provides - up to a constant which is independent of the mesh size and polynomial degree - an upper bound of the error. In contrast to first order elements, the lower bound however is *p*-dependent.

It is well known [10, 89], that the finite element method in the case of the wave equations ($\alpha < 0, \nu > 0$), suffers from pollution error. In the presence of pollution, the finite element solution oscillates around a shifted solution, because wavelength is not correctly represented. With the pollution, an additional error term appears, which is independent of the interpolation error, thus it cannot be estimated by a residual error estimator. Despite the lack of a rigorous proof, explicit and implicit residual estimators are used in [89], which is reasonable under a restriction of mesh size.

3.2. Implementing adaptive techniques in coupled problems, the linear case

In the case of coupled problems, error estimation and adaptation highly increases in complexity and publications on this topic are rare. Although residuals can be computed for each of the field quantities separately, a generalization of explicit estimators in a straightforward manner is not possible. [72] suggest to use an implicit error estimator based on a generalization of [12]. An embedded pair of FEM solutions with different orders (p+1) and mesh size (h/2) is used in [107]. This approach is quite safe, however largely increases the number of degrees of freedom.

In order to capture coupling effects in the error estimation, the approach in this thesis is to use a refinement indicator, which is based on residuals and in the style of explicit estimators by use of coupling coefficients derived on the basis of element energies. First the residual for each of the elements in each of the field solutions is computed. This is done for the internal residual (3.1) of the element and for the external residual (3.2) to (3.4). Index i stands for the respecting field, index j runs from 1 up to the number of fields n so that the coupling effects are considered in the calculation of the residuals.

$$r_{in(\bar{T}):i} = \sum_{j=1}^{n} \left(-\nabla \cdot \left(\nu_{ij} \nabla u_j + \gamma_{ij} u_j\right) + \beta_{ij} \nabla u_j + \alpha_{ij} u_j\right) - f_i - \nabla \cdot g_i \qquad i \in [1, 2, \dots, n] \tag{3.1}$$

$$r_{ex(\bar{T}):i} = \sum_{j=1}^{n} \left(\left[\!\left[\nu_{ij} \nabla u_j + \gamma_{ij} u_j\right]\!\right]\right) + \left[\!\left[g_i\right]\!\right] \qquad \partial\bar{T} \not\subset \partial\Omega \quad i \in [1, 2, \dots, n] \tag{3.2}$$

$$r_{ex(\bar{T}):i} = \sum_{j=1}^{n} \left(\nu_{ij} \nabla u_j + \gamma_{ij} u_j\right) \cdot \mathbf{n} + g_i \cdot \mathbf{n} - \left(u_{N:i} + q_i u_i\right) \qquad \partial\bar{T} \subset \partial\Omega_2 \quad i \in [1, 2, \dots, n] \tag{3.3}$$

$$r_{ex(\bar{T}):i} = 0$$
$$\partial\bar{T} \subset \partial\Omega_1 \quad i \in [1, 2, \dots, n] \tag{3.4}$$

In (3.2), the external residual evaluates the difference of normal flux density from both sides of the interface. The square brackets denote the operation: $[\![\mathrm{u}]\!] = (\mathrm{u}_{\bar{T}} - \mathrm{u}_{\acute{T}}) \cdot \mathbf{n}$, where $\bar{T}$, $\acute{T}$ refer to adjacent triangles. (3.2) is used for the edges of the element where a neighboring element exists except at boundary segments. This is indicated with: $\partial\bar{T} \not\subset \partial\Omega$. For general Neumann boundary conditions (3.3) is used and for Dirichlet boundary conditions (3.4).

The element-wise error estimator is calculated for element $\bar{T}$ and field i by taking:

$$\eta^2_{\bar{T}:i} = W_{in:i}\|r_{in:i}\|^2_{\mathrm{L}_2(\bar{T})} + W_{ex:i}\|r_{ex:i}\|^2_{\mathrm{L}_2(\partial\bar{T}\not\subset\partial\Omega)} + W_{b:i}\|r_{ex:i}\|^2_{\mathrm{L}_2(\partial\bar{T}\subset\partial\Omega_2)} \tag{3.5}$$

The weighing factors are defined as in the following [60]:

$$W_{in:i} = \frac{1}{p^2_{\bar{T}}}\min\{\nu^{-1}_{m\bar{T}} h^2_{\bar{T}}, \tilde{\alpha}^{-1}\}$$
$$W_{ex:i} = \frac{\bar{A}_{\bar{T}}}{\bar{A}_{\bar{T}} + \acute{A}_{\acute{T}}}\frac{1}{p_E}\nu^{-1/2}_{mE}\min\{\nu^{-1/2}_{mE} h_E, \tilde{\alpha}^{-1/2}\} \tag{3.6}$$
$$W_{b:i} = \frac{1}{p_E}\min\{\nu^{-1/2}_{mE}\min\{\nu^{-1/2}_{mE} h_E, \tilde{\alpha}^{-1/2}\}, -\mathrm{q}^{-1}\}$$
$$i \in [1, 2, \dots, n]$$

with the setting:

$\tilde{\alpha} \geq 0, \tilde{\alpha} \leq \alpha - \frac{1}{2}\nabla \cdot (\beta + \gamma)$
$p_E = \min\{p_{\bar{T}}, p_{\acute{T}}\}$
ν_m = minimum eigenvalue of the diffusion tensor ν
$\nu_{mE} = \max\{\nu_{m\bar{T}}, \nu_{m\acute{T}}\}$

with the eigenvalues calculation of a 2x2 tensor given by:

$$\frac{1}{2}\left(\nu_{11} + \nu_{22} \pm \sqrt{(\nu_{11} - \nu_{22})^2 + 4{\nu_{12}}^2}\right)$$

In (3.5), the L_2 norm of the internal and external residuals is taken and multiplied with the appropriate weights. The weights depend on triangle shape and area as well as the material coefficients. In (3.6), letter A refers to triangle area, letter p to polynomial order either referring to an element or a common edge of neighboring elements, letter h to element diameter and q to the Neumann boundary condition value.

Equation (3.5) works well with the *p*-adaptation algorithm that is described below; however it does not work well with the coupled *h*-adaptation algorithm. The reason is that in

p-adaptation the element order is adapted independently in each field. On the other hand in *h*-adaptation only one mesh is used for all field solutions. There are no multiple meshes. Therefore, the decision on mesh refinement has to take into account the error of all field solutions simultaneously.

In *p*-adaptation there are no problems arising from the fact that the energy-norm in different fields is measured in different units. In *h*-adaptation this turned out to be a problem. When the energy-norm in one field is arithmetically (without taking the units into account) much larger than the energy-norms in the other fields then it dominates the adaptation process, since the elements are refined mostly according to the residual error estimates in the dominating play.

To treat this problem, a refinement indicator given in (3.7) is introduced, which replaces the error estimator (3.5) during the *h*-adaptation process. It corresponds to one element and one field and is denoted by e. To the original error estimator η, the contributions of the element error estimators coming from all other fields are taken into account. Every time, η is multiplied by a factor which normalizes the energy norm and reflects the coupling between different fields (index E indicates the use of energy norm). There is a distinction between non-coupling energies (not arising from the coupling effects) and coupling energies. A coupling energy is denoted with unequal i and j indices. The new normalized element refinement indicator can now serve as a criterion in deciding on which elements to refine (split into sub-elements) during the *h*-adaptation process.

$$e^2_{\bar{T}:i} = \left\{ \eta^2_{\bar{T}:i} + \sum_{j=1, j\neq i}^{n} \left(\eta^2_{\bar{T}:j} \frac{\|\mathrm{u}\|^2_{\mathrm{E}(\bar{T}):ij}}{\|\mathrm{u}\|^2_{\mathrm{E}(\bar{T}):jj}} \right) \right\} \frac{1}{\|\mathrm{u}\|^2_{\mathrm{E}:ii}} \tag{3.7}$$

In (3.7), the energies are computed by each time adapting equation (3.8) [117], to the corresponding field effect and element, where field effect refers to either a direct effect or a coupling effect. This is in equivalence to the diagonal and off-diagonal parts of a global matrix.

$$\|\mathrm{u}\|^2_{\mathrm{E}} = \int |(\nu \nabla \mathrm{u}) \nabla \mathrm{u}| + \int |\tilde{\alpha} \mathrm{u} u| + \oint_{\partial \Omega_2} |\mathrm{q} u v| \tag{3.8}$$

The definition of energy in (3.8) is in a form, that can also be used in the treatment of wave equation problems.

3.3. Adaptive multi-field algorithms

A total of five adaptive algorithms for coupled problems have been implemented. Three of them are *hp*-algorithms adapting both element order and common mesh. The choice of these five particular algorithms, is primarily made in order to present a continuation to the previous research work [103] which was committed in the actual research institute [60].

In [103], the focus is on electromagnetic wave propagation problems, which is regarded as a particular problem type. This in effect, provided the straight-forward opportunity, to program the necessary software code modifications, and experiment with a set of adaptive algorithms on the actual multi-field PDE framework. In doing so, the implementing complexity concerning the code structures increases considerably.

Due to the existing foundation of adaptive algorithms and the existing mathematical implementation that accompanied them, most of the attention was put on the completion of the programming implementation and the acquirement of sensible results by means of test cases. In other words, the followed approach was more of a computer engineering approach, rather than a groundbreaking mathematical theory approach.

First the coupled *p*-adaptation algorithm is described:

p-adaptation

- ►Do from 1 up to the number of adaptation steps
  - ●Do from 1 up to the number of fields
    - ▬Sort residual vector (each entry corresponds to the residual of one element)
    - ▬Raise polynomial order of the worst (e.g. 5%) elements by 1
    - ▬Raise polynomial order of a further ≈25% of the elements if their residual is above some critical limit set in *maxres*
    - ▬Check if polynomial orders in neighboring elements differ by more than 1. If YES increase the order in the lower order element so that the difference is not greater than 1
    - ▬Check if polynomial orders of the same element but different fields differ by more than 2. If YES increase the order in all natures except the one with the highest order so that the difference is not greater than 2
  - ●End of fields loop
  - ●Calculate the multi-field error. This is the highest value of all field errors.
  - ●If the desired adaptation error is smaller than the multi-field error, exit the adaptation loop
- ►End of adaptation steps loop

Certain parameters in the *p*-adaptation algorithm have been left unchanged when comparing the multi-field implementation with the previously employed single-field one. The choice of raising the polynomial order of the 5% worst elements and of a further 25% of the elements residual-wise, can be adjusted. The common question is how much processing power should be invested towards the improvement of the problem solution and if it is worth it. According to [103], an empirical value of 5% has proven its usefulness on the average of various

examples. The provided statement was received as a realistic starting point. Further algorithm refinement can be achieved on the basis of the existence of a wider range of example test cases beyond the ones which are demonstrated in the current thesis.

The term critical limit set in *maxres*, is a field-related value, which is computed by taking into account the desired adaptation error set by the program user (denoted with $adapt\_error$), and a field-related computed reference value (denoted with ref_i). The term $n_{\bar{T}}$ corresponds to the total number of elements. This computation is depicted in (3.9).

$$maxres_i = \left(\frac{1}{100}\frac{adapt\_error}{n_{\bar{T}}}\right)^2 ref_i \tag{3.9}$$

The term multi-field error, simply refers to the highest value of all the individual field errors. The field error in turn, is the accumulated error over all the element errors in that particular field. The corresponding equation is given in (3.10). It is computed by taking the square root of the ratio of the accumulated element residuals over the field reference value. In (3.10), it was not deemed necessary to employ the refinement indicator given in (3.7). During the program development and the accompanying intermediate tests, it was observed that the solution differences between the employments of (3.5) and (3.7) were minimal. Additionally, due to the independent element order adaptation in every field, it proved unnecessary to introduce this cross-reference of the field energies. Ultimately, this specific decision for multi-field *p*-adaptation, was made in order to reduce computational program waste.

$$error_i = 100\sqrt{\frac{\sum_{\bar{T}=1}^{n_{\bar{T}}} \eta_{\bar{T}:i}^2}{ref_i}} \tag{3.10}$$

The computation of the field reference value, is done by accumulating over the individual element reference values in that field. This is shown in (3.11).

$$ref_i = \sum_{\bar{T}=1}^{n_{\bar{T}}} ref_{\bar{T}:i} \tag{3.11}$$

The element reference values are computed by using (3.12). To avoid confusion, the difference between (3.12) and the theoretical equation in (3.8), is that (3.12) is the direct mathematical expression of a line of code from the program. (3.12) does not explicitly display the element boundaries computation. The numerical integration is not explicitly presented as well.

$$ref_{\bar{T}:i} = \sum_{j=1}^{n} \left|(\nu \nabla u)_{ij} \nabla u_i\right| + \left|(\alpha u)_{ij} u_i\right| \tag{3.12}$$

The coupled *h*-adaptation algorithm is described in the following:

h-adaptation

►Calculate the refinement indicator $e^2_{\bar{T}:i}$ for all elements and fields.
►For each element and since $e^2_{\bar{T}:i}$ is normalized, sum $e^2_{\bar{T}:i}$ over all fields.
►Now there in only one refinement indicator vector where each entry corresponds to one element, sort this vector, place the most problematic elements first.
►Find *errmax*, the largest individual element error and *errmin*. The value in *errmin* is either equal to one tenth of *errmax* or equal to the error of the element with index given by (*number of elements*/18 + 1) in the sorted vector. The smallest of these two values is assigned to *errmin*
►Look for the elements whose error value falls between *errmax* and *errmin* and refine them.

Once again, the previous empirical investigations in the research group [60] were trusted, and the focus was set on the programming implementation aspects, and the testing of the *h*-adaptation algorithm on multi-field physics modes. Further empirical investigation of the *errmax* and *errmin* values can be achieved in the existence of further example test cases.

The FORTRAN subroutine of the coupled *hp*-adaptation algorithm is as follows. Depending on the choice of the *hp*-adaptation technique, it can branch off to three different subroutines which are also listed in the following.

hp-adaptation

►Do from 1 up to the number of adaptation steps
  ●Branch off to the selected *hp*-adaptation technique, "keypoint", "top5" or "kp_phaselag"
  ●Upon returning from the selected subroutine, refine the elements which have been tagged for refinement
  ●Do from 1 up to the number of fields
    ▬Check if polynomial orders in neighboring elements differ by more than 1. If YES increase the order in the lower order element so that the difference is not greater than 1
  ●End of fields loop
►End of adaptation steps loop

The first possible branch-off is the *hp*-adaptation technique called "keypoint".

hp-adaptation keypoint

►Set values for minimum (e.g. 5%) and maximum (e.g. 50%) number of elements raised
►Do from 1 up to the number of fields
  ●Sort residual vector
  ●Do from 1 up to the number corresponding to 5% of the elements

—If element has a keypoint or maximum polynomial degree is reached mark element for *h*-refinement
—If element is marked for *h*-refinement, decrease its polynomial order by halving it, otherwise increase polynomial order by 1
●End of 5% elements loop
●Do from the 5% number up to number corresponding to 50% of the elements (that is a further 45% of the elements)
—If the element residual is above some critical limit set in *maxres*, raise the polynomial order by 1 or otherwise if maximum polynomial order has been reached mark for *h*-refinement
●End of 5% to 50% elements loop
►End of fields loop

Corner singularities which require *h*-refinement, are assumed to be located at intersection points of two or more geometry objects, which are referred to as keypoints [103].

The second possible branch-off is the "top5" technique.

hp-adaptation top5

►Set values for minimum (e.g. 5%) and maximum (e.g. 50%) number of elements raised
►Do from 1 up to the number of fields
●Sort residual vector
●Do from 1 up to the number corresponding to 5% of the elements
—Mark element for *h*-refinement and drop its polynomial order by 1
●End of 5% elements loop
●Do from the 5% number up to number corresponding to 50% of the elements (that is a further 45% of the elements)
—If the element residual is above some critical limit set in *maxres*, raise the polynomial order by 1 or otherwise if maximum polynomial order has been reached mark for *h*-refinement
●End of 5% to 50% elements loop
►End of fields loop

The final *hp*-algorithm technique was given the name "kp_phaselag". In the PolyDE code, the elements are error-categorized dynamically as the subroutine progresses, however the algorithm below is presented in a slightly different way, in order to make it more readable and pass the idea to the reader without complications.

hp-adaptation kp_phaselag

►Do from 1 up to the number of fields
●Sort residual vector
●Categorize the elements depending on their error contribution. Category (A) for large error contribution, (B) for medium, (C) for small and (D) for marginal.
●Do for the large error contribution (A) elements
—If element has a keypoint or maximum polynomial degree is reached, mark element for *h*-refinement. In the keypoint situation, halve the polynomial order of the element as well.

—In the presence of phase-lag condition, mark element for *h*-refinement and halve its polynomial order, otherwise increase its polynomial order by 1

- ●End of (A) loop
- ●Do for the middle error contribution (B) elements
  - —If maximum polynomial degree is reached, mark element for *h*-refinement
  - —In the presence of phase-lag condition, mark element for *h*-refinement and halve its polynomial order, otherwise increase its polynomial order by 1
- ●End of (B) loop
- ●Do for the small and marginal error contribution (C and D) elements in a single loop
  - —In the presence of phase-lag condition, mark element for *h*-refinement and halve its polynomial order
  - —If element is class (D) reduce its polynomial order by 1
- ●End of (C and D) loop

►End of fields loop

The term phase-lag condition, refers to the phase difference between the numerical waves and the exact waves. This is clearly demonstrated in [59]. According to the authors of the technical report, the refinement of the mesh helps in the convergence of the discrete wavenumber towards the exact wavenumber.

According to [103], *h*-refinement should result in polynomial convergence, whereas *p*-enrichment should ideally result in exponential error convergence. The convergence plots are normally presented in the log-log manner. In that type of plot, for *h*-refinement, a convergence slop of -1 is expected from theory, as long as an element order of 2 is adopted in a 2D problem domain.

[103] focuses particularly on electromagnetic wave propagation, whereas the actual thesis focuses on a multitude of coupled problem types. Even though there are certain theoretical expectations, the convergence slopes in Chapters 4 and 5 should crucially depend on the problem setups under investigation. The laminar flow problems should presumably benefit more from *h*-adaptation and less from *p*-adaptation. The surface acoustic wave problem should obtain a more significant benefit from *p*-adaptation compared to the flow problems, however it cannot be predicted by exactly how much.

Concerning the performance of the *hp*-adaptive algorithms, it can be predicted that it shall heavily depend on algorithm design. There are algorithm branches as seen earlier, which make decisions on polynomial order reduction and the impact of these decisions is not certain. It is evident at this point, that the multitude of adaptive algorithms, in combination with the multitude of coupled physics modes constitutes complicated and uncharted territory and this makes it difficult to make more exact predictions. Nevertheless, this exploration of complexity is still considered valuable and is expected to lead to helpful conclusions, once the results are visualized. It remains to be tested and found out.

3.4. Implementing adaptive techniques in coupled problems, the non-linear case

The multi-field adaptation techniques can be applied on non-linear problems. In doing so, it could be said that the adaptation iteration loop is roughly wrapped around the non-linear iteration loop. The algorithmic sequence is demonstrated in Figure 3-1.

As a reminder form Chapter 2, the employed non-linear iteration technique is the so called fixed point iteration. The implementation of non-linearity in the code framework is necessary, in order to experiment with the adaptation algorithms on fluidic and in the future, on other non-linear problems. The non-linear iteration part of the sequence in Figure 3-1, which is marked within a square box, has been programmed in a way that can allow for its flexible swapping with other non-linear iteration techniques, should that be additionally wished.

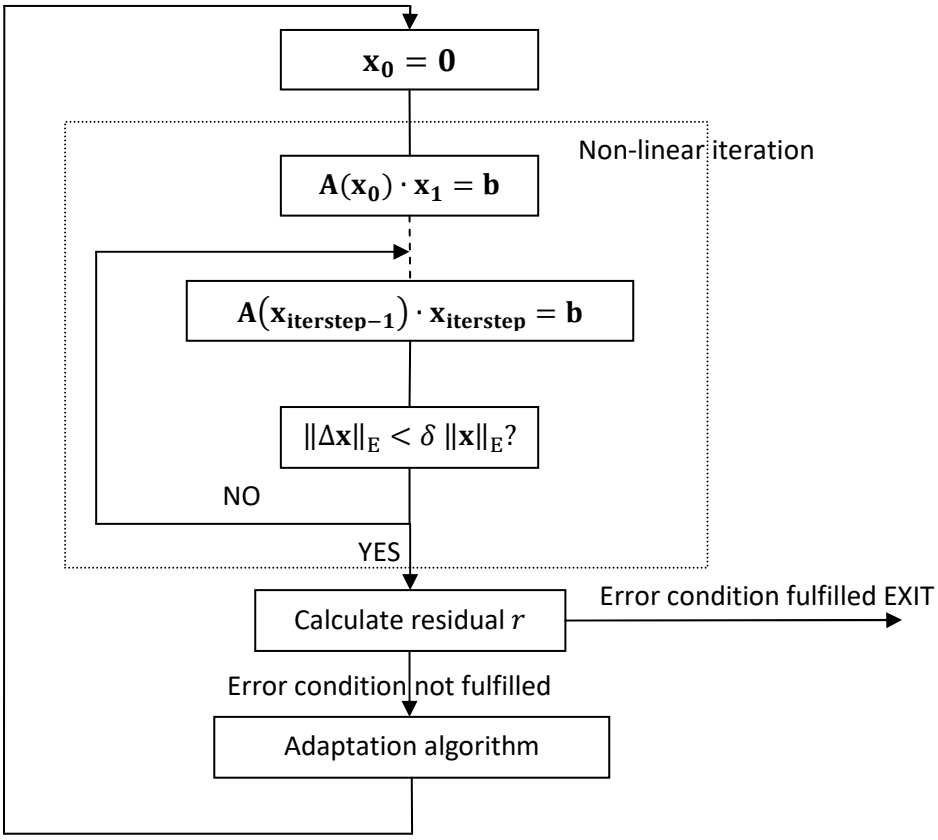

Figure 3-1 Algorithmic sequence in the application of adaptive algorithms on non-linear problems

3.5. Brief overview and current progress in PolyDE

Sections starting from 3.5 up to and including 3.8, give a brief overview of some of the programming and implementation aspects of this thesis. They act as a potentially helpful reference for future development, and also put the current work into perspective with regards to the previous coding-contributors. PolyDE [66] is the software in which the multi-field adaptive algorithms were developed and tested. In the following, the PolyDE package development structure is presented as it stood during the course of the work of this thesis.

The PolyDE development at the Institute of Microsystem Technology [60] has already lasted more than ten years. Its name is derived from "Polynomial" and "PDE". The former refers to the usage of high-order elements, whereas the latter refers to partial differential equations.

Having the possibility to develop code for an "in-house" software package is highly advantageous because it provides a high sense of freedom. It is also essential, since borrowing ideas from other closed-source FEM packages is impossible. Even for the ones that are open-source, a significant amount of time should be invested in understanding the code of these external packages.

Previous research assistant contributors to PolyDE, have worked on high order finite elements [98], implementation of coupled problems [64] and error-adaptive simulation of integrated optical components [102]. The current thesis can be regarded as a continuation of the work of [102] in the sense that the single-field adaptive algorithms are expanded for general multi-field functionality. [64] presents the implementation of coupled problems with emphasis on fluidics, however it was later concluded that the approach lacked in generality. A fluidic library was implemented in the PolyDE code (development has been halted) as a separate module with its own attributes and characteristics. Additionally, the coupling type was mostly unidirectional. With the general PDE framework that the current thesis presents, fluidic physics modes can be mapped to the general framework and the solution to fluidic problems can be obtained with the same matrix assembly and solver routines as for the rest of the physics modes. The hierarchical shape functions for two-dimensional scalar problems which were developed by [98] are an essential - and could also be described as core - component of PolyDE. In the behavioral examination of *p*-adaptive algorithms, high-order elements allow for more adaptation steps and therefore a higher number of degrees of freedom and a wider range of inspection. As a reference, work in the shape functions area [98], has now turned to three-dimensional scalar elements and following from the current thesis work, to a promising three dimensional general mathematical framework, allowing for three-dimensional fully coupled physics modes.

3.6. Software structure and projects under development

In this thesis the development of PolyDE was performed in the Visual Studio environment [82]. Development of the FEM package and compiling of the code by the other developers, was also performed with "CMake" [68].

For the compiling under Visual Studio 2008, the Intel Fortran Compiler version 11.1.065 was utilized [61]. The programming language of the internally developed routines is exclusively Fortran. This helps maintain integrity in code and avoid cross-language linkage errors. Fortran is highly suitable for numerical computations. Still today, there is a considerable amount of scientific computing code written in Fortran, for example [100]. In [20], a large list of scientific Fortran 90 code, has been brought together. One disadvantage of Fortran however is that it is less marketable than C++. Many commercial software companies nowadays develop code in C++ due to the extended graphics support. In this thesis, the objective is purely scientific and there is no assessment at all based on commercial success. Therefore Fortran is considered to possibly be the best choice.

The development of the code during the actual thesis research time, was arranged in fifteen projects. Some of them, upon compilation, were made to deliver libraries and some of them executables. All the fifteen projects are listed in Table 3-1.

Table 3-1 List of PolyDE projects

Project	Developed	Delivers
acadnet	internally	executable
blas	externally [40]	static library
femlib	internally	static library
femlib3d	internally	static library
fluidlib	internally	static library
geompack	externally [62]	static library
pgplot	externally [95]	static library
post	internally	executable
post3d	internally	executable
qmrpack	externally [46]	static library
solver	internally	executable
solver3d	internally	executable
triang	internally	executable
umfpack	externally [34]	static library
umfpackclib	external c library [35, 36] called by an internally written calling routine	static library

The four executables that are delivered with the aim of treating 2D problems are "acadnet", "triang", "solver" and "post". The purpose of "acadnet" is to convert a ".dxf" file (file format used by AutoCAD [8]) into an internal file formal. This means that it makes the drawing of two-dimensional structures in AutoCAD possible. Drawing the structure is the first step

towards conducting a two-dimensional FEM simulation. The second executable "triang" is a mesh generator which divides the geometrical domain Ω in triangles. The "solver" executable sets up a global problem equation system which is composed from the individual element equation systems and then solves the system with the utilization of an external solver package. The final executable "post" is employed in order to visualize graphically the solver-obtained solution. So overall the sequence is:

$$geometry\ draw \rightarrow mesh\ generate \rightarrow solve \rightarrow visualize\ solution$$

Compared to other packages, which possess sophisticated graphical user interfaces, PolyDE can be considered limited in terms of user friendliness. This however, does not in any way affect the worthiness of the package in terms of scientific research.

The internally developed projects, "femlib3d", "solver3d" and "post3d" are all 3D related, so they are not under consideration in this work. As far as "fluidlib" is concerned, development has stopped. The core library of PolyDE is "femlib". It includes features such as tensor transformation routines, reservation of global variables (whose names should not be assigned locally in other routines) and definition of shape functions.

The "umfpack" library is a set of routines forming the UMFPACK version 2.2 solver package. The 2.2 version was released in 1997 and is written in Fortran. It functioned as the main solver of the PolyDE package, for the solving of non-symmetric equation systems, until the integration of the newer UMPACK version 5.5 package. The version 5.5 was integrated in PolyDE in the year 2009 and is written in the C programming language. The 5.5 library and additionally a Fortran interface were compiled under Cygwin [31]. Together with a matrix format-change routine they were all merged into the "umfpackclib" library. The newer package integration was absolutely crucial in the research progress, since it can allocate computer memory dynamically and automatically, something that the older version could not achieve.

The "geompack" package is utilized by the "solver3d" project and is of no examination in the current work. The "qmrpack" is a solver package which was released approximately in 1992. This package has not been utilized in the testing of the multi-field physics modes, since after some short tests on some single-field problems it was already considered to be inadequate in performance. The "pgplot" is a package used for graphics display and is written in Fortran. It is utilized by the "post" executable.

Development has been mainly focused on the "femlib" and "solver" projects. In the "femlib" project, new physics modes were implemented by means of a Fortran source file named "pdecoeff.f90". The Fortran subroutine in "pdecoeff.f90" fetches the values for the PDE coefficients $\nu, \gamma, \beta, \alpha, f, g$ on an element basis. A further Fortran source file named "setstandardvalues.f90", provides, according to the chosen physics mode, a list of standard

values in the case when the material parameters are not provided by the user. The fact that only two source files need modifying in order to program a new physics mode, is the verification of the effort-minimizing general PDE approach.

In the "solver" project, modifications were primarily made to adaptation related source files. These are the "residual.f90", "padapt.f90", "hadapt.f90", "hpadapt.f90" and "hpffein.f90". All the mentioned files are listed in the source repository of [66]. In the modifying process, multi-field routines were derived from the existing single-field routines.

3.7. Solver packages and a short comparison between them

PolyDE for the most part, makes use of two solvers. One of them is the already mentioned UMFPACK 5.5. The second one is the SSOR conjugate gradient which is categorized as an iterative solver. More details about the SSOR-CG solver and also a comparison between iterative solvers can be found in [64].

The benefit of the iterative solver versus the direct solver UMFPACK is that it can solve for a higher number of degrees of freedom with lower memory requirements. Theoretically, the SSOR-CG solver can solve non-symmetric problems provided that they are positive definite. Even some non-positive definite problems can be resolved. The exact consideration in the current thesis, is the ability of the solver to solve non-symmetric sparse linear systems since almost all of the multi-field physics modes presented in Chapter 2 are non-symmetric. In practice however, the iterative solver experienced convergence difficulties when it came to the handling of the actual thesis non-symmetric physics modes, like for example the thermoelastic problem. For this reason, all testing results of multi-field problems were obtained with the UMFPACK direct solver. The machine on which the tests, that are presented in the next chapters, were conducted, possessed 8GB of memory and that could allow the testing of adaptation procedures up to a hundred or a few hundred thousand of degrees of freedom, depending on the adaptive algorithm used. The conditioning of the multi-field physics modes for the iterative solver or other global matrix manipulation techniques aimed at higher solver efficiency of the direct solver, could form the basis for further software development.

3.8. Parallelization of certain routines

In the work of [19], certain subroutines were parallelized in order to take advantage of modern multi-core CPUs. Parallelization was implemented by means of the OpenMP application programming interface [92].

In order to parallelize individual tasks, they have to be independent from one another. Additionally, the tasks should not require large amounts of memory, since the matrix solution process and the solver package often lead to a memory bottleneck.

The pre-solution individual assembly of each element matrix is independent from that of the others. Consequently, that provided one significant parallelization opportunity. The second parallelization opportunity arose in the post-solution element-wise residual computation. The speedup of the global matrix assembly and residual computations was very high and even close to ideal in [19]. The overall performance increase turned out to be very valuable, especially during the solving of the non-linear fluidic problems.

4. Linear Application Example (Piezopyroelectricity Surface Acoustic Wave Device)

This chapter demonstrates the practical testing of the developed multi-field adaptive algorithms. In doing so, a problem example has been set up on the basis of one of the physics modes that were derived and presented in Chapter 2. The choice of this particular physics mode was made on the basis of its complexity. As a reminder, piezopyroelectricity is a combination of two-dimensional structural mechanics, electric potential and thermal scalar fields. During the coding phase of the algorithms, tests were carried out on the simpler physics modes as well with very reasonable results according to the expectations. They were however omitted from the main body of the actual report, in order to concentrate on the more complicated physics modes since they were considered to be more valuable.

A surface acoustic wave sensor has been geometrically drawn. The presented problem is time-harmonic. The formulation of the problem is regarded as linear, since no fixed point iteration is needed towards solving the problem. Due to the high number of obtained field solutions, applied adaptive algorithms, resulting element orders and mesh sizes during the adaptation processes, a large number of resulting figures was produced. With the purpose of not saturating the chapter with these figures, many of them have been omitted from the main body of the report and are presented in Appendix A1. Error convergence plots have been deemed the most valuable for report main body presentation.

A surface acoustic wave (SAW) sensor is a device whose operation is based on the piezoelectric effect. A sinusoidal alternating voltage is applied to one or more sets of electrodes and an acoustic wave is produced in the substrate of the device. The acoustic waves that propagate on the surface of the substrate are called surface acoustic waves. The geometry of the SAW model can be investigated in Figure 4-1, together with the obtained electric field solution. For this simulation the width of the substrate is 200μm whereas the height is 30μm. The corresponding dimensions for the electrodes are 10μm and 2μm.

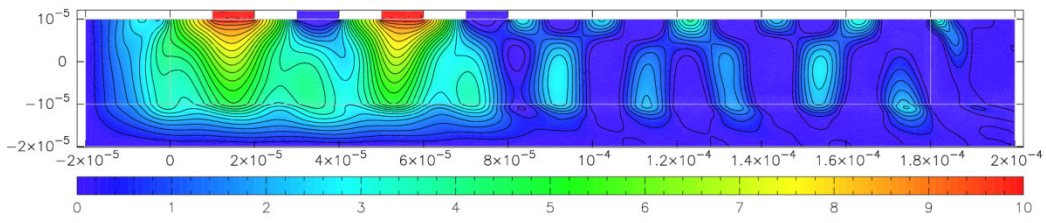

Figure 4-1 Electric Potential field plot of the SAW sensor. Solution obtained with the piezopyroelectric physics mode

Regarding Figure 4-1:

This and all subsequent geometry plots were created with "pgplot" [95]
The plot-scale appears below the geometry of the problem
The plot-units of the contour plot are Volts
The dimension-units of the given geometry are meters

Table 4-1 presents further details of the model in relation to its material parameter values. It additionally demonstrates the flagging (0 for FALSE and 1 for TRUE) of some material regions, in order to suppress the wave reflections at the internal boundaries of the geometrical model.

Table 4-1 Material data of the surface acoustic wave device model

Material	Property	Value	Units
Aluminum	Material density ρ	2700	$[\mathrm{kg/m^3}]$
	Specific heat c_p	897	$\left[\frac{\mathrm{J}}{\mathrm{kg \cdot K}}\right]$
	Thermal conductivity λ	$\begin{bmatrix} 237 & 0 & 0 \\ 0 & 237 & 0 \\ 0 & 0 & 237 \end{bmatrix}$	$\left[\frac{\mathrm{W}}{\mathrm{m \cdot K}}\right]$
	Relative permittivity ε_r	$\begin{bmatrix} 1.6 & 0 & 0 \\ 0 & 1.6 & 0 \\ 0 & 0 & 1.6 \end{bmatrix}$	
	Elasticity tensor C	$\begin{bmatrix} 11.2 & 6 & 6 & 0 & 0 & 0 \\ & 11.2 & 6 & 0 & 0 & 0 \\ & & 11.2 & 0 & 0 & 0 \\ & & & 5.2 & 0 & 0 \\ & & & & 5.2 & 0 \\ & & & & & 5.2 \end{bmatrix}$	$[\mathrm{N/m^2}] \times 10^{10}$
	Thermal expansion tensor A	$\begin{bmatrix} 23.1 & 0 & 0 \\ 0 & 23.1 & 0 \\ 0 & 0 & 23.1 \end{bmatrix}$	$[1/\mathrm{K}] \times 10^{-6}$
Lithium Niobate	Material density ρ	4600	$[\mathrm{kg/m^3}]$
	Specific heat c_p	633	$\left[\frac{\mathrm{J}}{\mathrm{kg \cdot K}}\right]$
	Thermal conductivity λ	$\begin{bmatrix} 4 & 0 & 0 \\ 0 & 4 & 0 \\ 0 & 0 & 4 \end{bmatrix}$	$\left[\frac{\mathrm{W}}{\mathrm{m \cdot K}}\right]$
	Relative permittivity ε_r	$\begin{bmatrix} 44 & 0 & 0 \\ 0 & 44 & 0 \\ 0 & 0 & 29 \end{bmatrix}$	
	Elasticity tensor C	$\begin{bmatrix} 20.3 & 5.3 & 7.5 & 0.9 & 0 & 0 \\ & 20.3 & 7.5 & -0.9 & 0 & 0 \\ & & 24.5 & 0 & 0 & 0 \\ & & & 6 & 0 & 0 \\ & & & & 6 & 0.9 \\ & & & & & 7.5 \end{bmatrix}$	$[\mathrm{N/m^2}] \times 10^{10}$

	Piezoelectric tensor e	$\begin{bmatrix} 0 & -2.5 & 0.2 \\ 0 & 2.5 & 0.2 \\ 0 & 0 & 1.3 \\ 0 & 3.7 & 0 \\ 3.7 & 0 & 0 \\ -2.5 & 0 & 0 \end{bmatrix}$	$[\mathrm{C/m^2}]$
	Thermal expansion tensor A	$\begin{bmatrix} 1.44 & 0 & 0 \\ 0 & 1.59 & 0 \\ 0 & 0 & 0.75 \end{bmatrix}$	$[1/\mathrm{K}] \times 10^{-5}$
	Pyroelectric tensor P	$\begin{bmatrix} 0 \\ 0 \\ -4 \end{bmatrix}$	$\left[\frac{\mathrm{C}}{\mathrm{m^2 \cdot K}}\right] \times 10^{-5}$
	PML flag	0	
Lithium Niobate PML damping direction: $+x$	Physical material data	As for Lithium Niobate	
	PML flag	1	
	PML attenuation directional vector	$[x \quad y \quad z] = [1 \quad 0 \quad 0]$	
	β_{PML}	1	
Lithium Niobate PML damping direction: $-x$	Physical material data	As for Lithium Niobate	
	PML flag	1	
	PML attenuation directional vector	$[x \quad y \quad z] = [-1 \quad 0 \quad 0]$	
	β_{PML}	1	
Lithium Niobate PML damping direction: $-y$	Physical material data	As for Lithium Niobate	
	PML flag	1	
	PML attenuation directional vector	$[x \quad y \quad z] = [0 \quad -1 \quad 0]$	
	β_{PML}	2	

A sinusoidal voltage of 10V in amplitude is applied at two of the electrodes whereas the other two are grounded. The frequency of the alternating input voltage is 190MHz. The substrate material is Lithium Niobate (LiNbO3) and the electrode material is Aluminum (Al). The LiNbO3 plane that is simulated is the *yx* plane. Chapter 2 already demonstrated the mapping of a desired cross section from the 3D coordinate system to the 2D coordinate system and can now be used as a reference. According to [124] the propagation velocity of the surface waves along this plane is approximately 3800m/s.

In Figure 4-2 and Figure 4-3, the *x*-displacement and *y*-displacement field solution plots are presented. Even though the wavelength of the surface acoustic waves cannot be directly extracted from the plots, it is thought to be around 20μm.

Due to the fact that in this type of problem, wave reflections result at the boundaries of the geometry, Perfectly Matched Layers have been implemented in PolyDE, in order to minimize these reflections [77, 80]. There are three rectangular PML regions in the geometry. The rightmost one damps the acoustic waves in the $+x$ direction, the leftmost in the $-x$ and the

bottom one in the $-y$ direction. The damping is implemented in terms of the material parameters by making them complex inside the PML region.

To be more precise in terms of calculations and regarding the PML regions, a damping parameter β_{PML} has been implemented in the FEM program. The additional usage of attenuation directional vectors has allowed for the flexible damping of the waves in the desired direction, should that be wished. The attenuation directional vectors are employed, only after the required transformations of the material parameter tensors have been completed. In the case of a two-dimensional problem as the current one, the z entries of the attenuation vectors are ignored.

$$\begin{gathered}[\mathrm{PML}]_x = [\mathrm{PML}]_{[1]} = 1 - \mathrm{PML}_{dir\_vector}[1] \cdot j\beta_{PML} \\ [\mathrm{PML}]_y = [\mathrm{PML}]_{[2]} = 1 - \mathrm{PML}_{dir\_vector}[2] \cdot j\beta_{PML} \\ [\mathrm{PML}]_{xy} = [\mathrm{PML}]_x \cdot [\mathrm{PML}]_y \end{gathered} \tag{4.1}$$

where: $\mathrm{PML}_{dir\_vector}[index]$ refers to the PML attenuation directional vector from Table 4-1.

$$\begin{gathered} C_{damped:\acute{\imath}\acute{\jmath}\acute{k}\acute{l}} = C_{\acute{\imath}\acute{\jmath}\acute{k}\acute{l}} \cdot \frac{[\mathrm{PML}]_{xy}}{[\mathrm{PML}]_{[\acute{\jmath}]} \cdot [\mathrm{PML}]_{[\acute{l}]}} \\ e_{damped:\acute{\imath}\acute{\jmath}\acute{m}} = e_{\acute{\imath}\acute{\jmath}\acute{m}} \cdot \frac{[\mathrm{PML}]_{xy}}{[\mathrm{PML}]_{[\acute{\jmath}]} \cdot [\mathrm{PML}]_{[\acute{m}]}} \\ \lambda_{damped:\acute{\imath}\acute{\jmath}} = \lambda_{\acute{\imath}\acute{\jmath}} \cdot \frac{[\mathrm{PML}]_{xy}}{[\mathrm{PML}]_{[\acute{\imath}]} \cdot [\mathrm{PML}]_{[\acute{\jmath}]}} \\ \varepsilon_{\mathrm{r}damped:\acute{\imath}\acute{\jmath}} = \varepsilon_{\mathrm{r}\acute{\imath}\acute{\jmath}} \cdot \frac{[\mathrm{PML}]_{xy}}{[\mathrm{PML}]_{[\acute{\imath}]} \cdot [\mathrm{PML}]_{[\acute{\jmath}]}} \\ \rho_{damped} = \rho \cdot [\mathrm{PML}]_{xy} \\ \acute{\imath}, \acute{\jmath}, \acute{l}, \acute{m} \in [1, 2] \end{gathered} \tag{4.2}$$

The reason for implementing the PML regions, is the objective of obtaining realistic solution plots and therefore associating the numerical model with a possibly equivalent real life device.

Due to the wave nature of the problem, the crucial material parameters to undergo damping-related modification, are the ones that are mapped to the general PDE material parameters ν and α. These are C, e, λ, ε_r and ρ. The damping methodology of the material parameters is displayed in (4.1) and then in (4.2). In (4.2), the structural mechanics accented indices are used, similarly to Chapter 2. The symmetry properties of tensors C and e are taken into consideration in (4.2) and this leads to a reduction of program "do" loops.

The achieved PML design with the scope of the actual thesis in mind, and consequently the presented damping methodology were deemed sufficient. Surface acoustic waves could

clearly be identified in the solution plots, and with that physics mode functionality was proven. For comparison reasons, Appendix A1 presents the same SAW geometrical structure but with the PML regions omitted [19]. The decision on parameters β_{PML} for each of the damping regions was obtained with trial and error methodology. It was also kept in mind that the PML regions should not become too large in size, as they would consume a disproportional amount of degrees of freedom compared to the problem's region of interest.

The significance of the 4-field piezopyroelectric physics mode, is that it can allow for the investigation of damping by thermoelastic dissipation (TED) simultaneously with the piezoelectric effect. The acoustic waves that are triggered by the alternating electrode voltage result in a temperature gradient according to the thermoelastic effect. This temperature gradient is illustrated in Figure 4-4. It can be seen that at the regions of greater mechanical displacement - this is the surface of the substrate where the surface waves propagate - the temperature gradient is higher. It should be noted that in Figure 4-4 the temperature contour plot is given in what is described as relative Kelvin units. Temperature deviations from a reference temperature of 0° are presented and not the absolute values.

The testing of the adaptive algorithms on the SAW device model, was performed in the following sequence. Multi-field *h*-adaptation was tested first. In order to increase the variety concerning the observation of the results, the problem domain was set to have a uniform element order of either 1, 2 or 3. This was done in order to observe the effect that the uniform element order change, can have on the error convergence slopes.

Multi-field *p*-adaptation was next to be tested. In order to increase the variety in the observations again, *p*-adaptation results were obtained by employing both the error estimator given in (3.5) and the refinement indicator in (3.7). As a reminder the refinement indicator was specifically derived due to the necessity for a mesh that is shared between the separate problem fields.

Multi-field *hp*-adaptation was last to be tested. Results were obtained from all three *hp*-adaptive algorithms. Once results for all algorithms were obtained, a sequence of additional plots was created in order to provide a direct comparison between them on a field-by-field basis.

During the sequence of accumulation of results, observations concerning the shape of the convergence curves are made. Once all results data has been accumulated, at the end of the chapter, concrete and valuable information has been extracted from the error convergence plots, in an attempt to provide a comparison between the actual results and the expectations according to theory.

For the *h*-adaptation algorithm testing, the starting and resulting mesh after 6 *h*-adaptation steps can be investigated in Figure A1-3 and Figure A1-4 respectively, in Appendix A1. Mesh refinement is observed at the following domain locations. At the electrode corners, due to the presence of singularities there. Additionally, the PML regions become highly refined at internal boundaries. There is also refinement on the surface of the LiNbO3 substrate where the surface acoustic waves propagate.

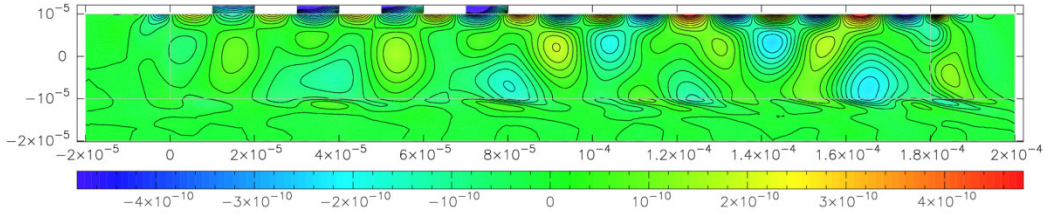

Figure 4-2 *x*-displacement field plot of the SAW sensor. Solution obtained with the piezopyroelectric physics mode

Regarding Figure 4-2:

The plot-units of the contour plot are meters

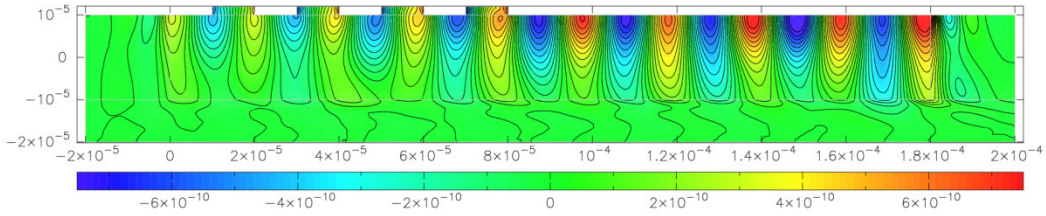

Figure 4-3 *y*-displacement field plot of the SAW sensor. Solution obtained with the piezopyroelectric physics mode

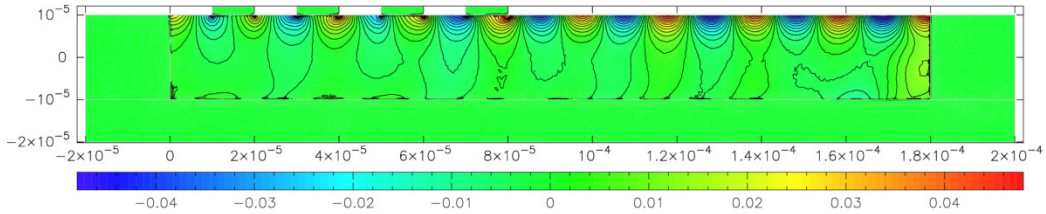

Figure 4-4 Temperature field plot of the SAW sensor. Solution obtained with the piezopyroelectric physics mode

Regarding Figure 4-4:

The plot-units of the contour plot are relative Kelvin

The results of the application of the multi-field *h*-adaptive algorithm are presented in the figures starting from Figure 4-5 and concluding with Figure 4-8. The "Error Indicator" plotted quantity is given by (4.3). The sum of the error estimators for all elements $\bar{T}$ in field i, is normalized with respect to the energy content in the same field. This is done because in a wave propagation problem, the energy content changes when the mesh is changed during the adaptation process. If the error estimator was not normalized, then it would not be clear to judge whether there is error improvement during some of the adaptation steps.

$$R_i = \sqrt{\frac{\sum_{\bar{T}} \eta^2_{\bar{T}:i}}{\sum_{j=1}^{n} \|\mathrm{u}\|^2_{\mathrm{E}:ij}}} \tag{4.3}$$

The process of refining a common mesh, in order to improve multiple field solutions at the same time raises some question marks. For example, which is the field solution where maximum convergence has to be achieved? The obvious answer to this question would be to make a common mesh refinement decision, which is, to a bigger extent, influenced by the error in the field with maximum interest. The next argument that immediately arises in this case, is that due to the fact that the fields are coupled, the error in the fields of no interest shall still contribute to the error of the field of interest. Therefore there can be no obvious answer. In this thesis, it is expected that the element wise error normalization technique, which is presented in Chapter 3, is a step in the right direction.

At this point, a few observations shall be given. In Figure 4-5, the field solution of the *x*-displacement benefits from a higher uniform element order, since for the same number of invested degrees of freedom, the slope of the error curve improves. At around 9000 degrees of freedom however, it can be seen that the order 2 curve and the order 3 curve coincide. This shows, that starting with a uniform element order of 3, can initially invest some unneeded degrees of freedom on some elements. In Figure 4-6 which is concerned with *y*-displacement, it can once again be observed that a higher uniform element order is advantageous with respect to the slope of the convergence curve.

In Figure 4-7, the error indicator curves for the electric potential field solution are presented. Using a uniform element order of 2 clearly improves the convergence curve compared to a uniform element order of 1.

In Figure 4-8, the error indicator curves for the temperature field solution are presented. The first observation is that there is overlap between all three curves for uniform element orders 1, 2 and 3. Furthermore all curves appear to have identical slopes and only after 20000 degrees of freedom, the order 1 slope starts to deviate.

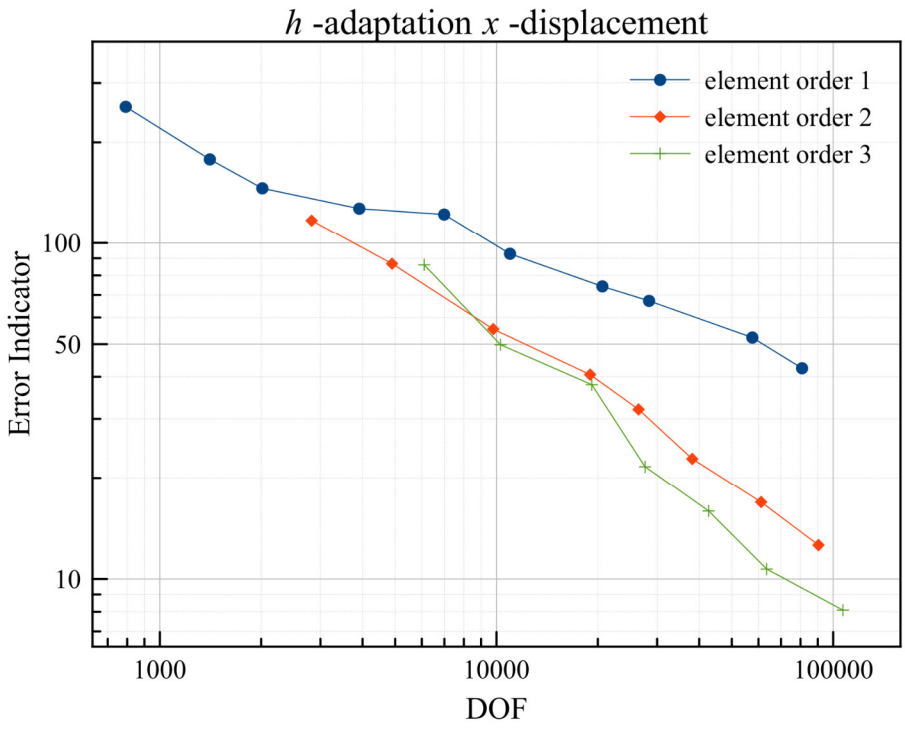

Figure 4-5 *x*-displacement error indicator given by (4.3), plotted against number of degrees of freedom, with *h*-adaptation and for uniform element orders of 1, 2 and 3

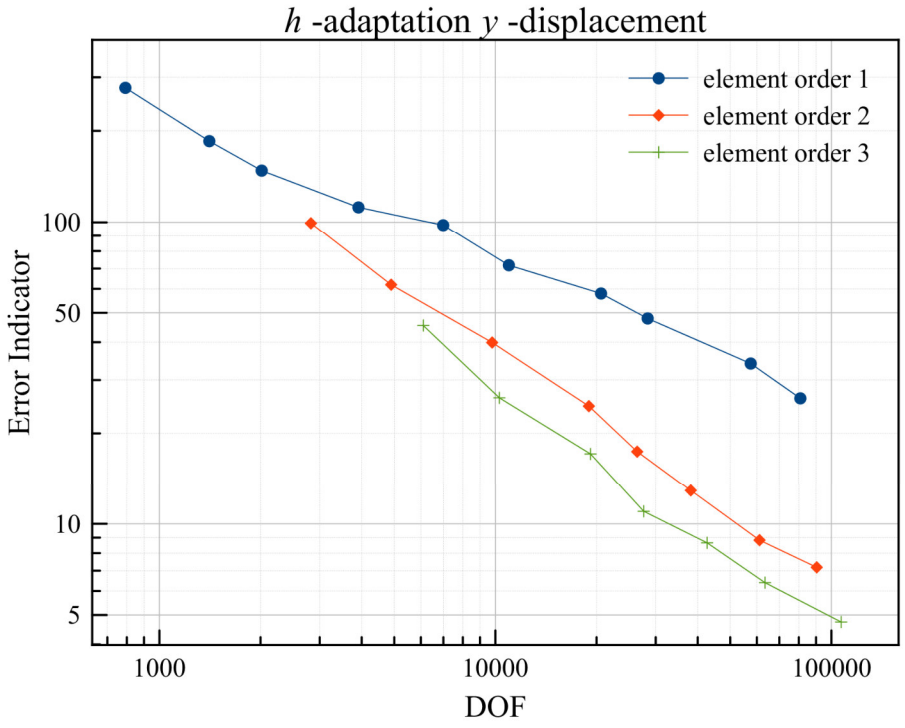

Figure 4-6 *y*-displacement error indicator given by (4.3), plotted against number of degrees of freedom, with *h*-adaptation and for uniform element orders of 1, 2 and 3

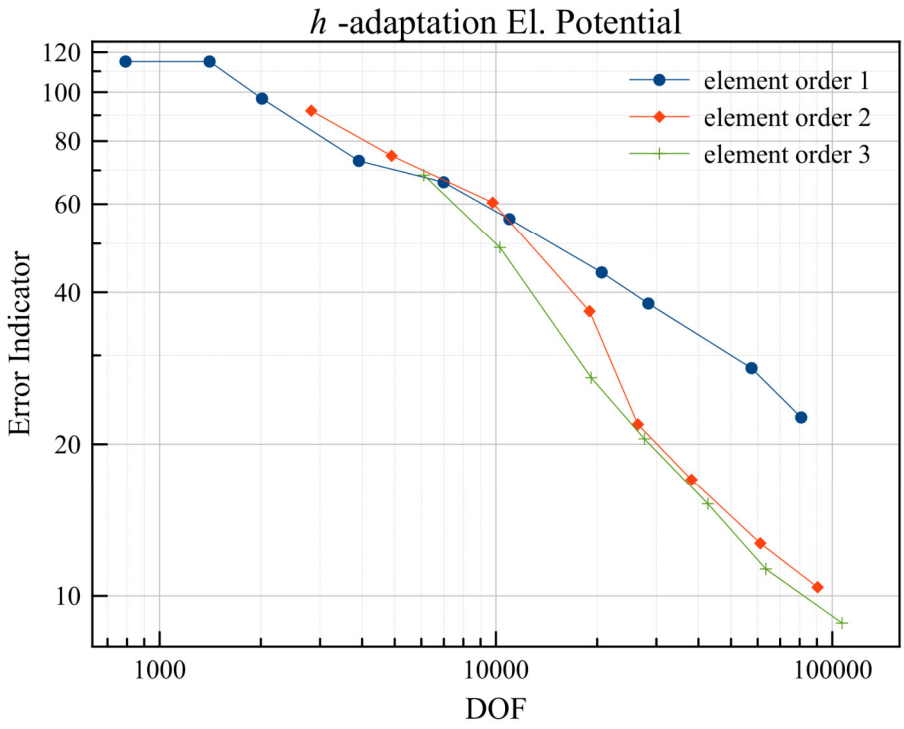

Figure 4-7 Electric Potential error indicator given by (4.3), plotted against number of degrees of freedom, with *h*-adaptation and for uniform element orders of 1, 2 and 3

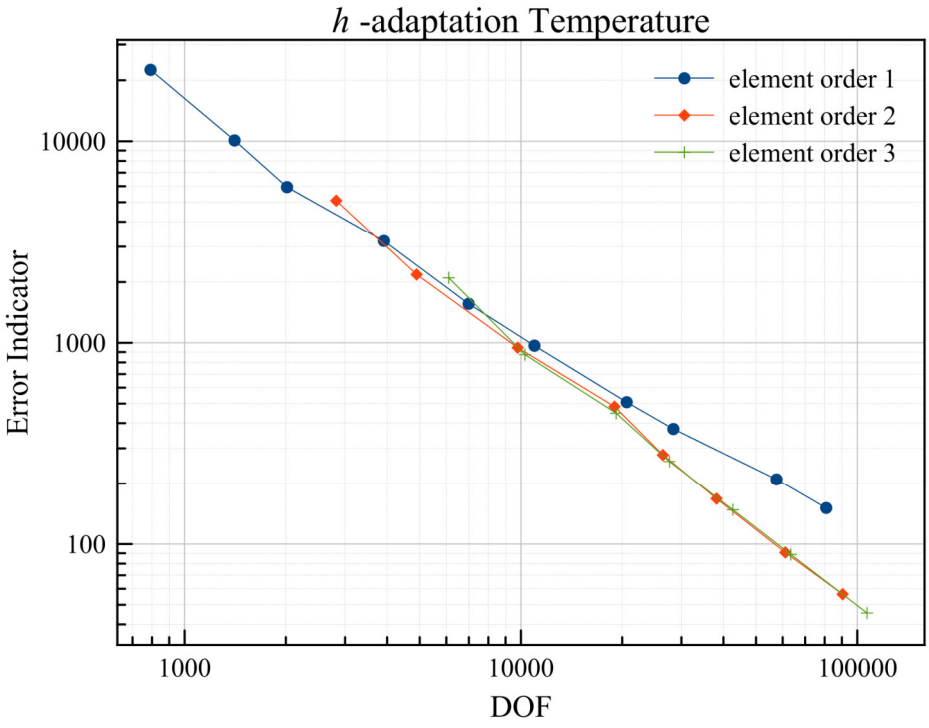

Figure 4-8 Temperature error indicator given by (4.3), plotted against number of degrees of freedom, with *h*-adaptation and for uniform element orders of 1, 2 and 3

For the *p*-adaptation algorithm testing, the starting element order for all elements and fields is set to 1. The starting coarse mesh of Figure A1-3 is used again and is not refined during the process. In order not to be repetitive in every figure, for all the remaining error indicator plots in this report, the plotted quantity is always that given by (4.3).

In Figure 4-9, error convergence curves are presented for the *x*-displacement field. Two error convergence tests were conducted. One by using the refinement indicator of (3.7), and one by using the error estimator of (3.5). Typical *p*-adaptation convergence curves are observed, since at approximately 20000 degrees of freedom, the curves enter a saturation phase. The difference in convergence characteristics between the two curves is minimal. Since it is desirable in this thesis, wherever possible, to generalize the approach, this was received as a good indication that the refinement indicator of (3.7) can be the common adaptation procedure choice, for all adaptive algorithms.

The *p*-adaptation convergence curves for the *y*-displacement field solution are presented in Figure 4-10. Once again the shape of the two curves is almost identical. Even though there is a small error difference in the range from 3000 up to 20000 degrees of freedom, eventually they converge to similar error results. The *p*-adaptation procedure enters a saturation phase at around the 20000 DOF point for this field.

In Figure 4-11, the error convergence curves for the electric potential field are presented. Similarly to the results in Figure 4-10, the two curves deviate from one another in the region from 3000 to approximately 20000 degrees of freedom.

Figure 4-12 presents the *p*-adaptation convergence curves for the temperature field. Saturation becomes vaguely noticeable at approximately 20000 degrees of freedom. Error convergence curve deviation is minimal.

The convergence curve results for the complete set of the *hp*-adaptive algorithms are presented in the sequence from Figure 4-13 to Figure 4-16. The respective field is indicated in the corresponding plot. For the *x*-displacement, the *y*-displacement and the electric potential fields, the "keypoint" algorithm offers the superior performance. For the temperature field the situation is not clear enough.

Appendix A1 presents additional plots concerning the resulting element orders and meshes after a certain number of adaptation steps with the *p*- and *hp*-algorithms. Details are given in the respective captions, should there be a wish for investigation.

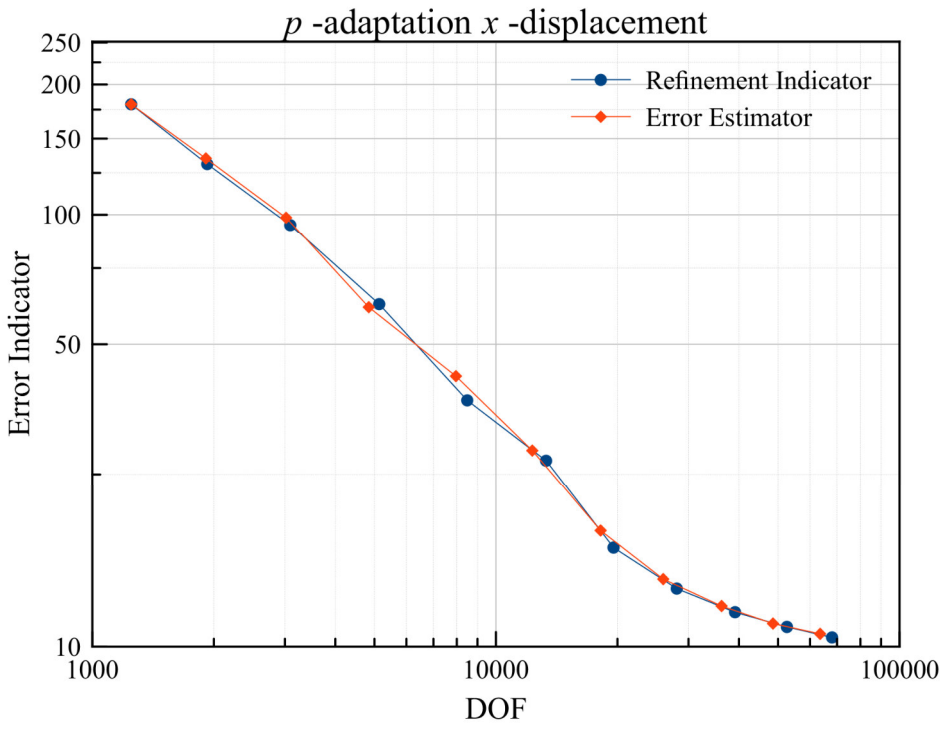

Figure 4-9 *x*-displacement error indicator plotted against number of degrees of freedom, with *p*-adaptation and by using both the refinement indicator (3.7) and the error estimator (3.5)

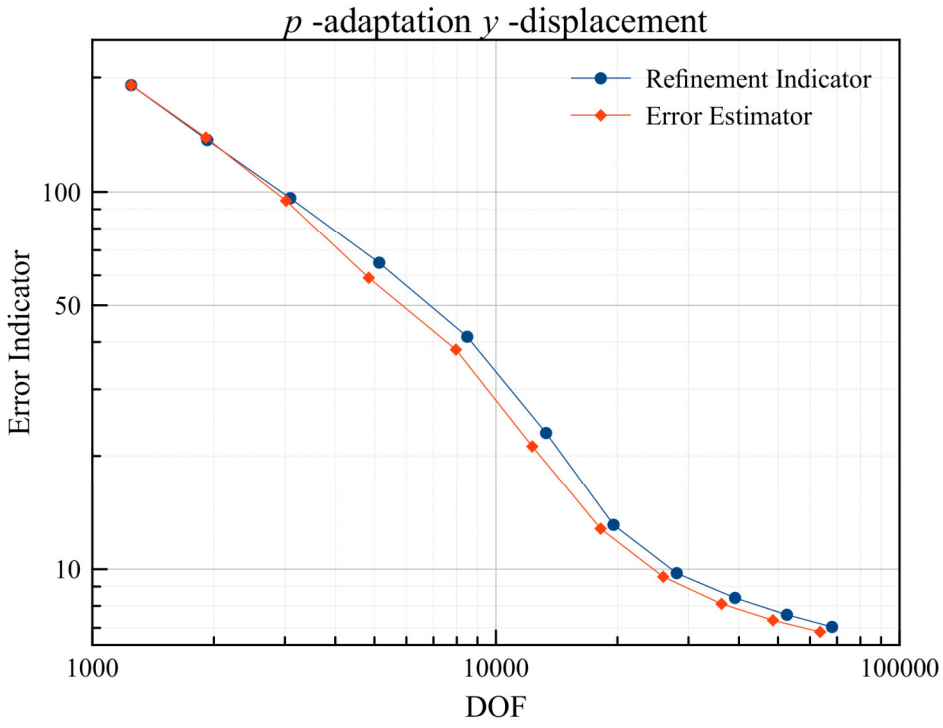

Figure 4-10 *y*-displacement error indicator plotted against number of degrees of freedom, with *p*-adaptation and by using both the refinement indicator (3.7) and the error estimator (3.5)

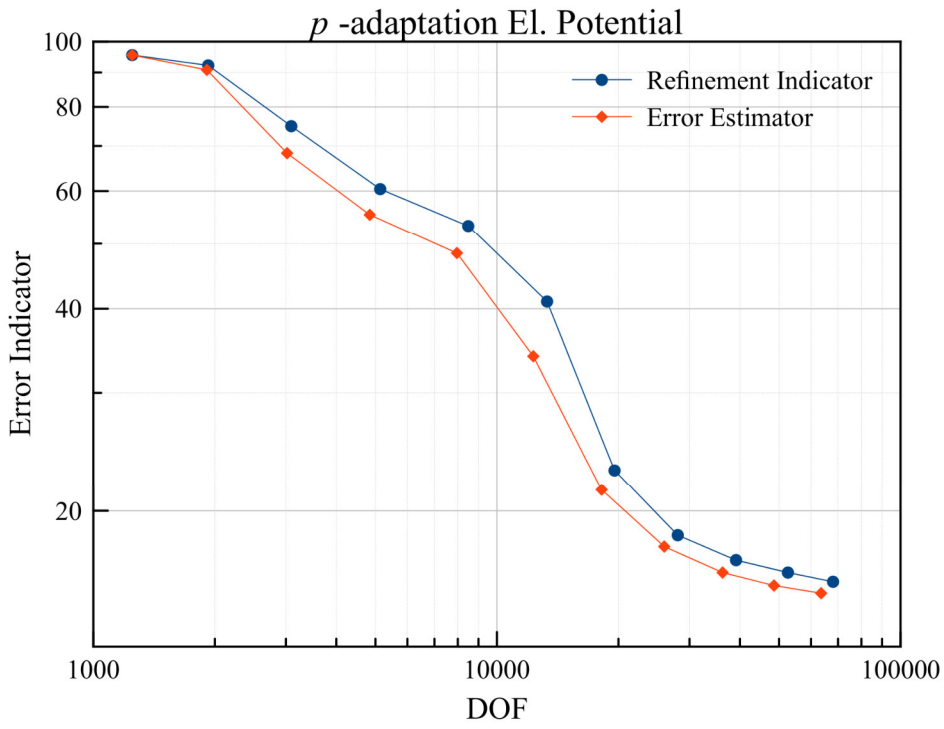

Figure 4-11 Electric Potential error indicator plotted against number of degrees of freedom, with *p*-adaptation and by using both the refinement indicator (3.7) and the error estimator (3.5)

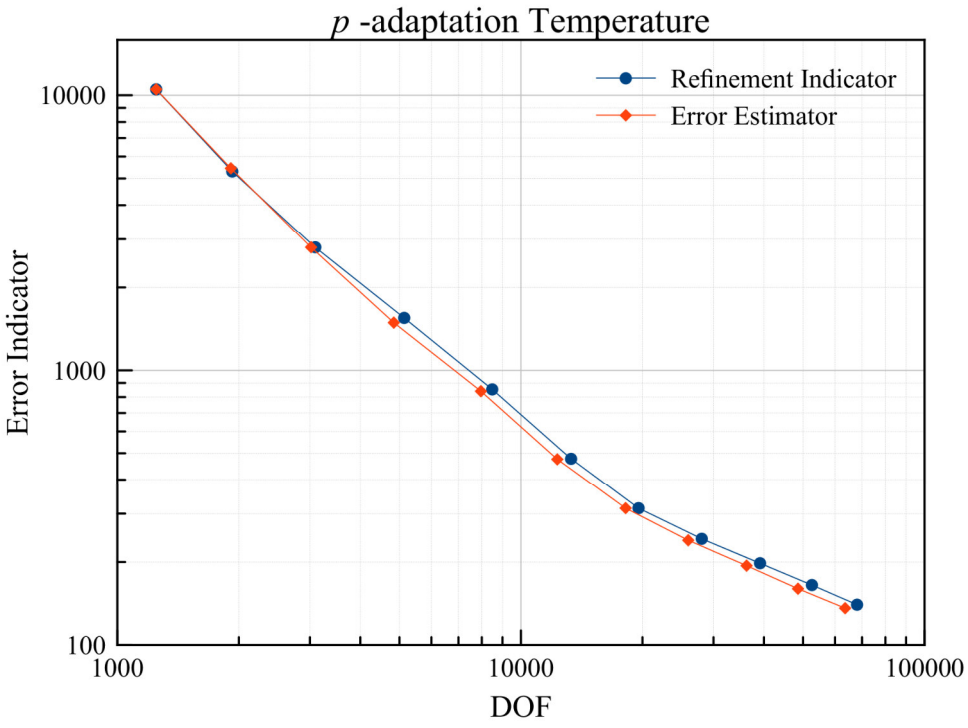

Figure 4-12 Temperature error indicator plotted against number of degrees of freedom, with *p*-adaptation and by using both the refinement indicator (3.7) and the error estimator (3.5)

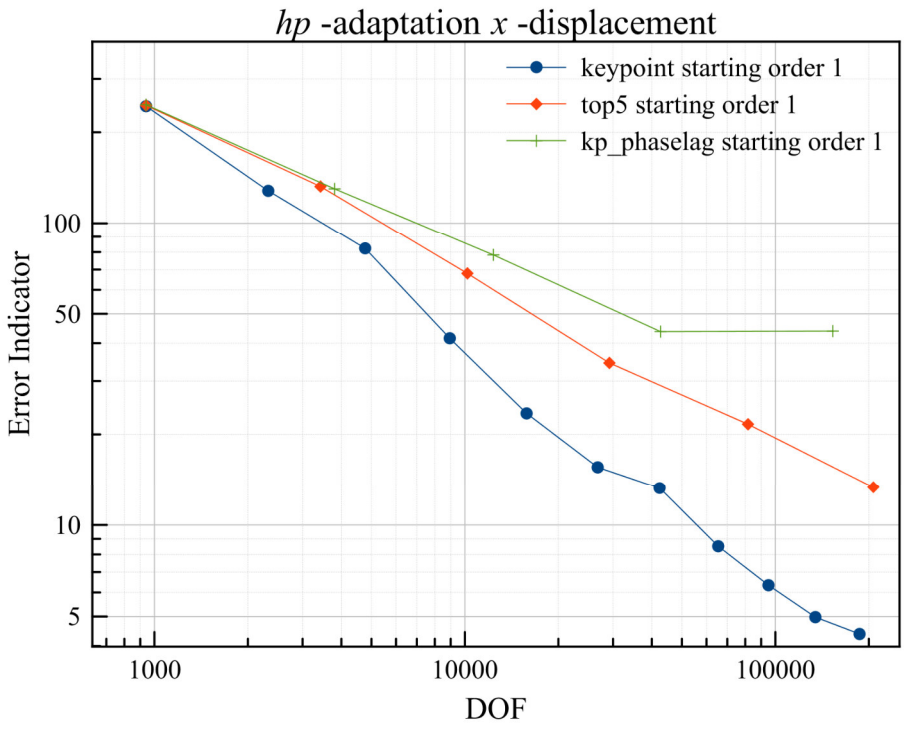

Figure 4-13 *x*-displacement error indicator plotted against number of degrees of freedom, with *hp*-adaptation and for all *hp*-adaptive algorithms

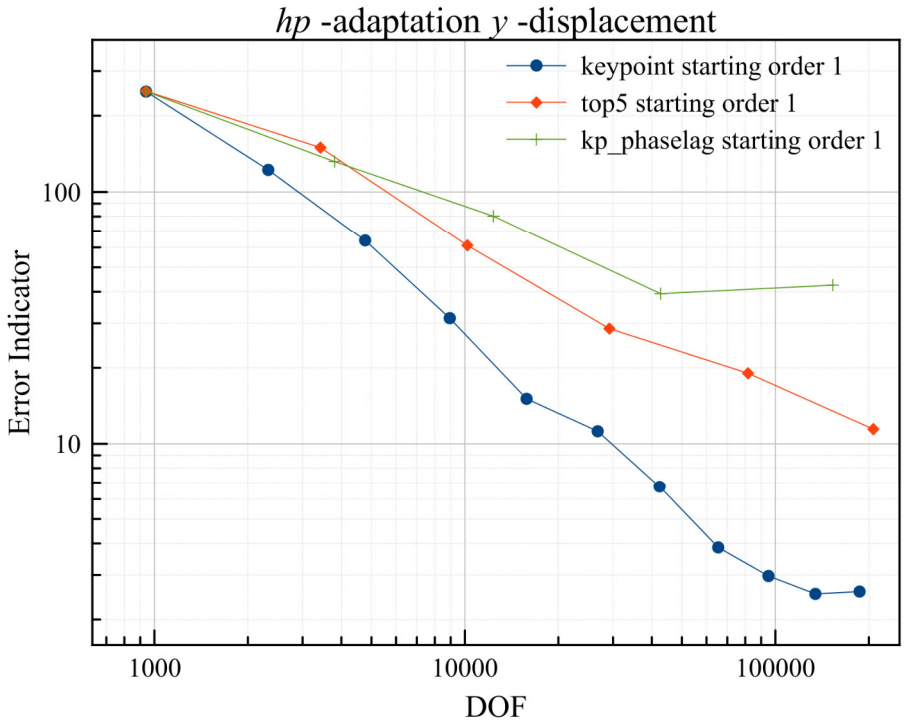

Figure 4-14 *y*-displacement error indicator plotted against number of degrees of freedom, with *hp*-adaptation and for all *hp*-adaptive algorithms

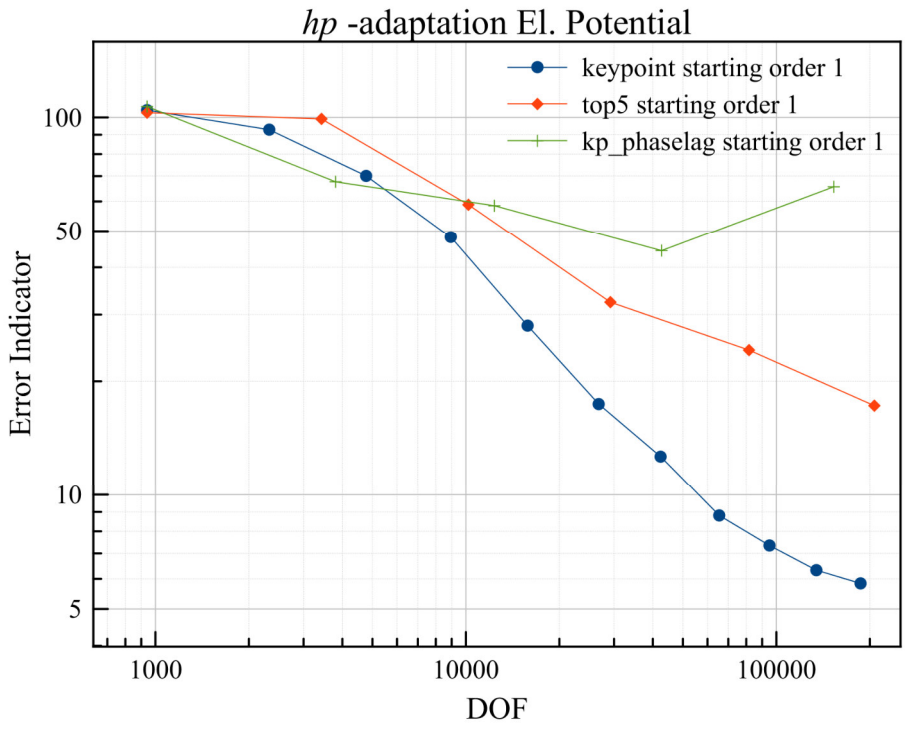

Figure 4-15 Electric Potential error indicator plotted against number of degrees of freedom, with *hp*-adaptation and for all *hp*-adaptive algorithms

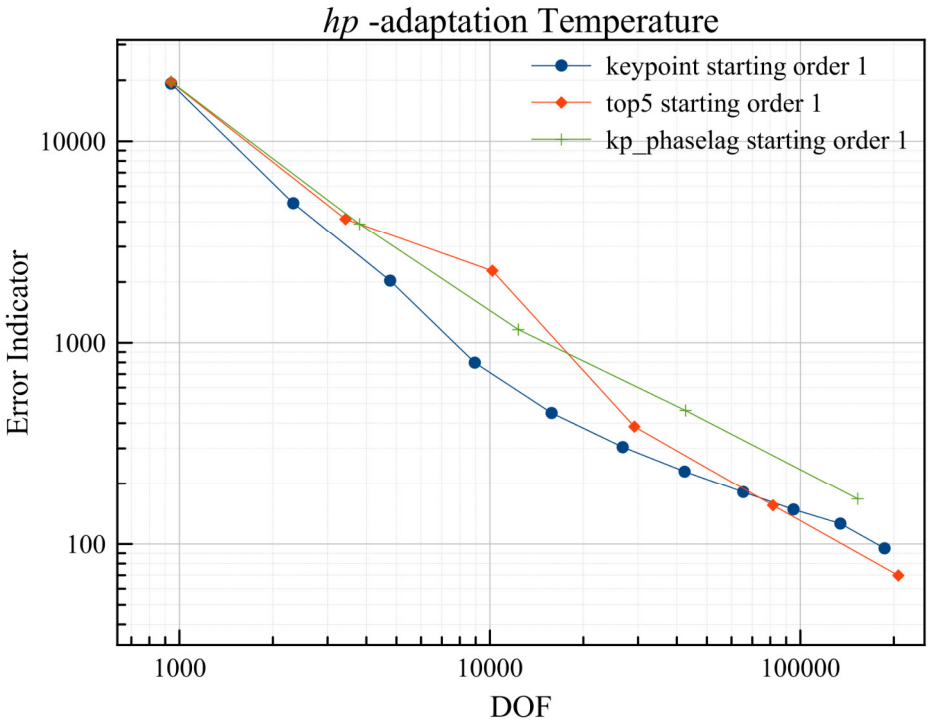

Figure 4-16 Temperature error indicator plotted against number of degrees of freedom, with *hp*-adaptation and for all *hp*-adaptive algorithms

The four plots from Figure 4-17 up to Figure 4-20, conclude this report section by comparing all five adaptive algorithms for each of the field solutions. The selected *h*-adaptation algorithm for presentation in the concluding plots, is the one with a uniform element order of 2. There is a known expectation from theory that this should correspond to a convergence slope of -1 for 2D single-field problems, and this information can in turn be used in the discussion concerning the actual multi-field problem.

In Table 4-2, selected slope data from the adaptation comparison plots have been extracted. The slope between two convergence steps can be calculated by using (4.4).

$$\text{slope} = \frac{\log\left(\frac{R_{i,\text{current step}}}{R_{i,\text{previous step}}}\right)}{\log\left(\frac{\text{NDOF}_{\text{current step}}}{\text{NDOF}_{\text{previous step}}}\right)} \tag{4.4}$$

For all combinations of fields and adaptation techniques, three values are presented. These are worst, the best and the average step convergence slope in the respective adaptation process. It was deemed unnecessary to present the full table with all step convergence slopes included, as this would overpopulate the table.

The originality of the piezopyroelectric physics mode in this thesis, makes it impossible to directly find comparison data regarding *hp*-FEM in the literature. From theory, it should be expected to notice the slope of *h*-adaptation revolve around the value of -1, and the slope of *p*-adaptation peak at less than (numerically) -1, e.g. -1.46. Concerning the performance of the three presented *hp*-adaptive algorithms, these have been identified to heavily depend on their program design and they should undergo further refinement in the future.

For the *x*-displacement field, *p*-adaptation has provided the highest step convergence slope at -1.21, followed by the *hp*-keypoint at -1.09 and *h*-adaptation at -0.92. On the average step converge however, when taking all steps into account, the *hp*-keypoint has provided the best result with an average slope of -0.74. The best performing algorithm for the remaining fields can be investigated from Table 4-2 in a similar manner.

Before closing Chapter 4, summarizing discussion is presented in the last paragraphs of the section. The purpose is to communicate a few messages to the respective readers, especially to new researchers who wish to further investigate and experiment with *hp*-FEM adaptive algorithms in the global matrix fully coupled approach. Further summarizing discussion concerned with the example problem cases, is presented at the end of Chapter 5.

It was verified during the example case testing phase, that the selected solver package played a crucial role in the range of output of results that could be obtained. The integration of the latest UMF solver package was essential in order to obtain a sensible solution to the SAW problem, due to physics mode complexity, and also solve for higher numbers of degrees of freedom.

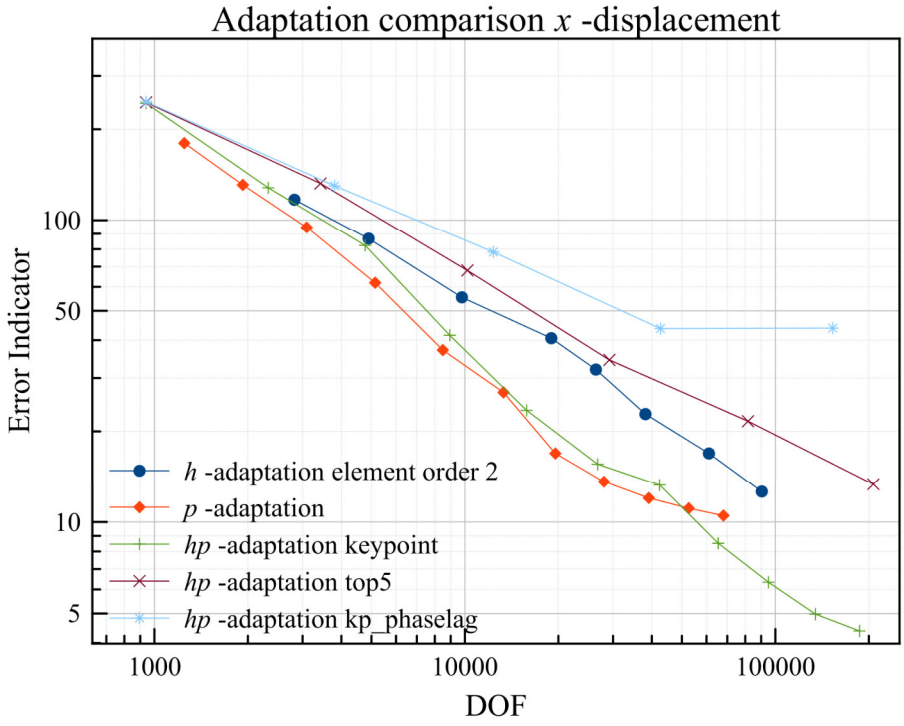

Figure 4-17 Adaptation comparison for the *x*-displacement field with all of the five adaptation techniques

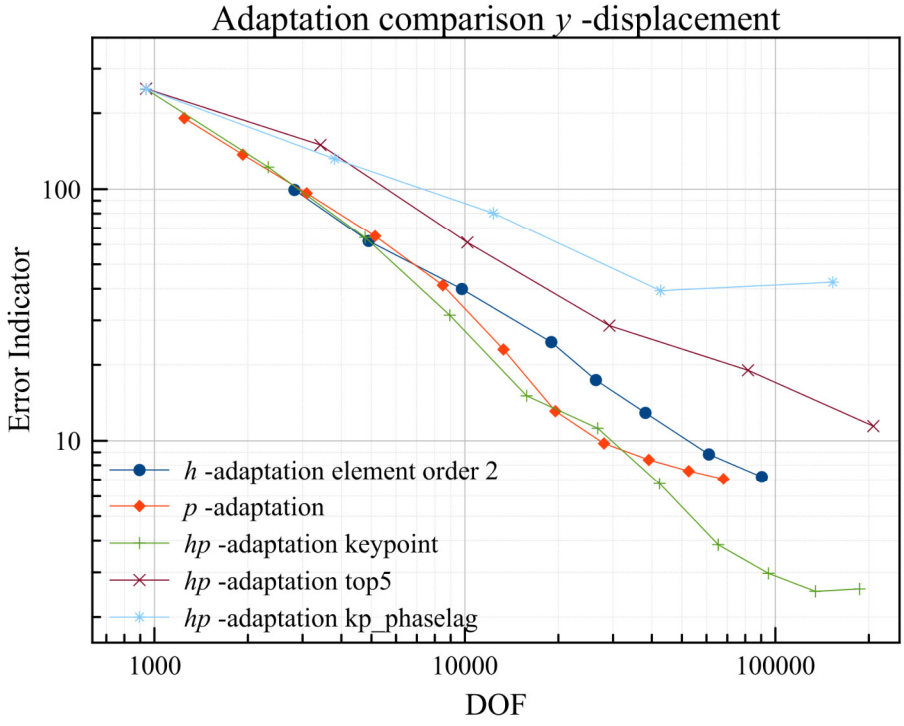

Figure 4-18 Adaptation comparison for the *y*-displacement field with all of the five adaptation techniques

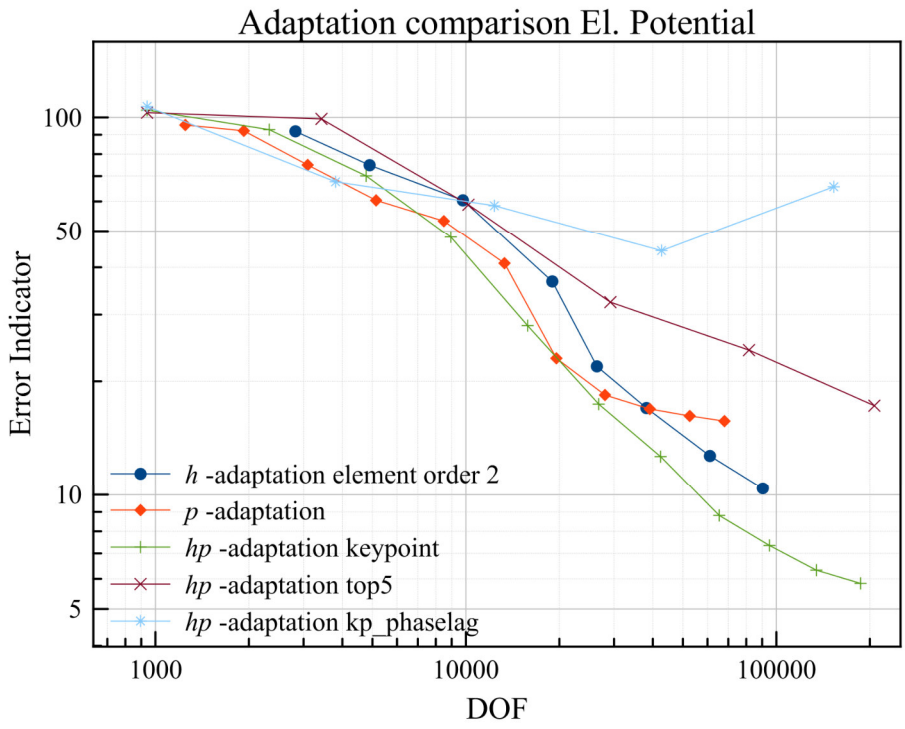

Figure 4-19 Adaptation comparison for the Electric Potential field with all of the five adaptation techniques

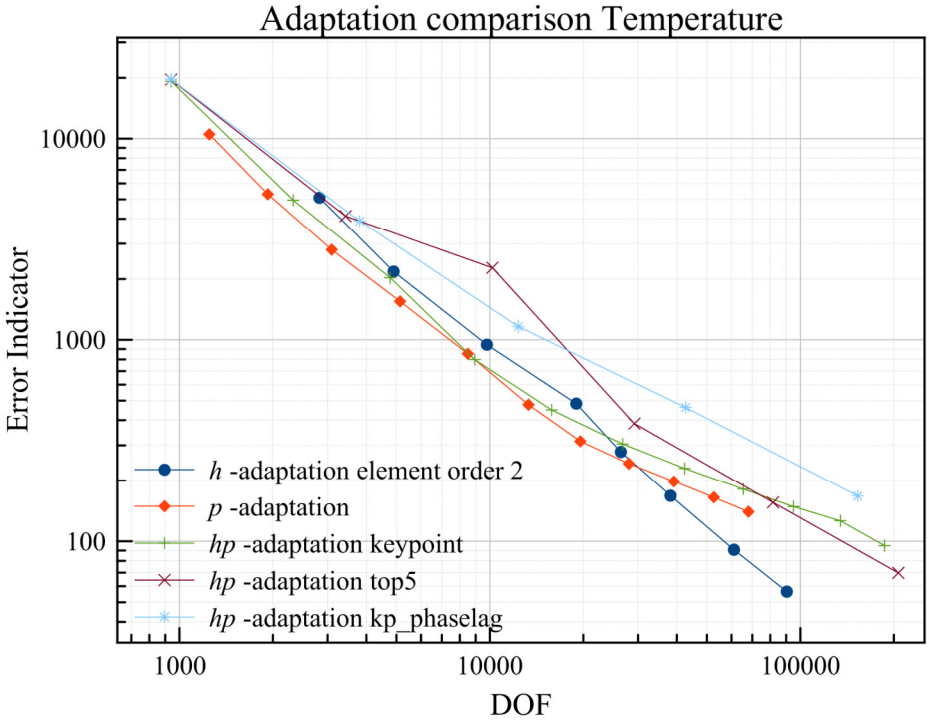

Figure 4-20 Adaptation comparison for the Temperature field with all of the five adaptation techniques

With respect to the SAW problem, the performance of the algorithms was overall quite pleasing. The perfectly matched layer heavily hindered the performance of only the *hp*-kp_phaselag algorithm. The direct alteration of the PML material parameters in the program, in order to achieve the acoustic wave damping, triggered the *hp*-kp_phaselag algorithm to unnecessarily and heavily refine the PML region. As a reminder, the PML was essential in obtaining a realistic wave propagation field-solution for the SAW device.

This thesis has offered an initial investigation in order to prove whether the general scalar-field PDE adaptation approach can be pursued further. The answer is yes. However, before continuing in the path that this thesis has established, it would be vital to simultaneously care for side tasks. These are explicitly the pre-solution conditioning of the global matrix, its adjustment according to the respective matrix solver package, and also further attention on the implementation of crucial FEM program functionality, such as exemplarily perfectly matched layers and appropriate boundary conditions.

Table 4-2 Collective convergence results for the surface acoustic wave device model

h-	*p*-	*hp*-keypoint	*hp*-top5	*hp*-kp_phaselag
		x-displacement		
Worst step convergence				
-0.47	-0.22	-0.35	-0.45	0.00
Best step convergence				
-0.92	-1.21	-1.09	-0.65	-0.47
Average step convergence				
-0.67	-0.67	-0.74	-0.54	-0.34
		y-displacement		
Worst step convergence				
-0.53	-0.29	0.07	-0.40	0.06
Best step convergence				
-1.05	-1.46	-1.29	-0.82	-0.58
Average step convergence				
-0.77	-0.79	-0.82	-0.58	-0.35
		Electric potential		
Worst step convergence				
-0.31	-0.08	-0.13	-0.03	0.31
Best step convergence				
-1.56	-1.50	-0.95	-0.57	-0.33
Average step convergence				
-0.69	-0.44	-0.57	-0.34	-0.09
		Temperature		
Worst step convergence				
-1.01	-0.62	-0.47	-0.55	-0.74
Best step convergence				
-1.67	-1.58	-1.50	-1.69	-1.16
Average step convergence				
-1.33	-1.02	-0.90	-1.04	-0.93

5. Non-linear Application Examples

Sections 5.1 and 5.2 test the adaptive algorithms firstly on a 3-field fluidic problem, and secondly on a 4-field fluidic-electric problem. The purpose of these numerical examples, is to prove feasibility and expected behavior of the application of adaptive multi-field algorithms on non-linear problems.

5.1. Micro-fluidic channel (Incompressible fluid-flow example)

The first example case to be investigated, is a fluidic Navier-Stokes problem, corresponding to the physics mode of Section 2.3.5. The three fields, namely the *x*-velocity, the *y*-velocity and the pressure field are simultaneously solved for. All three variants of the *hp*-adaptive algorithms are investigated.

The peculiarity in the current test case, as well as in the test case of the following section, lies in the fact that for this type of fluidic problems, the element order for the pressure field should always be set to one less than that of the velocity fields. A short literature review on this issue, revealed that the Ladyzhenskaya-Babuška-Brezzi (LBB) condition has to be satisfied [7, 118]. Consequently, to facilitate the accommodation of this type of problem in the PolyDE software, corresponding adjustments have been made in the adaptation algorithm subroutines.

The problem setup is given in Figure 5-1. The higher pressure at the indicated inlet compared to the indicated outlet causes a fluid flow in the shown direction. There is no flow through any other boundary in the structure. The boundary conditions for the sidewalls have been set to the no-slip condition, meaning that both *x*-velocity and *y*-velocity components are set to 0 at these boundaries.

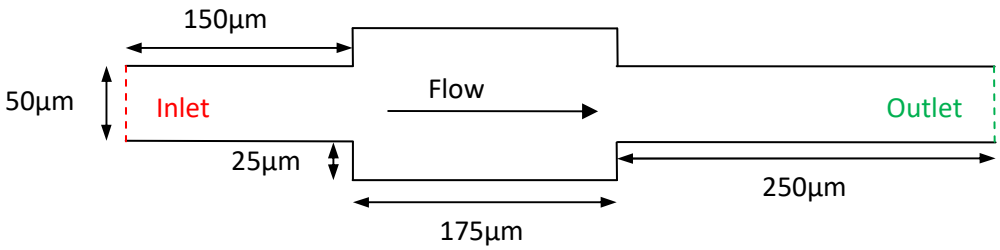

Figure 5-1 Micro-fluidic problem setup showing dimensions and flow direction

The pressure field is given predefined values at the inlet and the outlet - Dirichlet boundary conditions - whereas for the rest of the boundaries it is set to a Neumann boundary condition.

Table 5-1 Material data of micro-fluidic channel model

Material	Property	Value	Units
Water	Material density ρ	1000	$[\mathrm{kg/m^3}]$
	Dynamic viscosity μ	1.002×10^{-3}	$\left[\frac{\mathrm{kg}}{\mathrm{m \cdot s}}\right]$

The dimensions and shape of the structure are those that are presented in [128]. The material data is provided in Table 5-1. In order to obtain the steady-state solution, the iterative solver which was presented in Section 2.2.2 is employed. A value of $\delta = 1 \cdot 10^{-3}$ is selected for the non-linear iteration parameter. For all the fields the expected plots are obtained after only a few iteration steps. This is in accordance with the observed laminar flow solution and therefore a weak problem non-linearity. Table 5-2 and Table 5-3, provide analytical demonstrations of the nonlinear problem error convergence for every *h*- or *p*-adaptation step.

Table 5-2 Convergence of the non-linear fixed point iteration *h*-adaptation

h-adaptation	Uniform element order 3			
	Non-linear iteration step 1		Non-linear iteration step 2	
DOF	$\|\mathbf{x}\|_E$	$\|\Delta\mathbf{x}\|_E$	$\|\mathbf{x}\|_E$	$\|\Delta\mathbf{x}\|_E$
6068	1.40000000232646E-03	1.40000000232646E-03	1.40000000232646E-03	8.35197452521610E-24
7348	1.40000000237299E-03	1.70783702208612E-03	1.40000000232408E-03	9.98900565907439E-16
8915	1.40000000232075E-03	2.43422944114279E-03	1.40000000232283E-03	7.80888504539183E-17
10790	1.40000000232956E-03	2.54975704702661E-03	1.40000000232219E-03	1.83339471675323E-16
13121	1.40000000231926E-03	2.59258987046980E-03	1.40000000232193E-03	6.45156171390672E-17
16149	1.40000000232141E-03	3.12469131310953E-03	1.40000000232182E-03	8.04590585419802E-18
19991	1.40000000232579E-03	2.87552466886746E-03	1.40000000232177E-03	6.78136784529195E-17
24839	1.40000000231022E-03	3.08279168287703E-03	1.40000000232174E-03	1.53481651991843E-16
30853	1.40000000232251E-03	3.15167087915244E-03	1.40000000232173E-03	3.04747648331447E-16
38549	1.40000000232978E-03	2.72059008619302E-03	1.40000000232173E-03	1.88315298990123E-16
48122	1.40000000232102E-03	3.18766085312572E-03	1.40000000232173E-03	1.08541284715808E-16

The *x*-velocity and *y*-velocity plots are given in Figure 5-2 and Figure 5-3 respectively. To avoid confusion, it is explicitly stated that these are contour plots, representing scalar quantities. This is done in consistency with the multiple scalar field approach which is followed in PolyDE. The *x*-velocity value at the narrower parts of the channel stands at $7\ \mu\mathrm{m/s}$. At the wider part of the channel, it stands at $4\ \mu\mathrm{m/s}$. *y*-velocity components are only visible at the areas where the width of channel changes.

Table 5-3 Convergence of the non-linear fixed point iteration *p*-adaptation

p-adaptation	Starting element order 2 for velocities, 1 for pressure			
	Non-linear iteration step 1		Non-linear iteration step 2	
DOF	$\|\mathbf{x}\|_E$	$\|\Delta\mathbf{x}\|_E$	$\|\mathbf{x}\|_E$	$\|\Delta\mathbf{x}\|_E$
2561	1.40000000233344E-03	1.40000000233344E-03	1.40000000233344E-03	8.54403964788691E-24
3529	1.40000000232755E-03	2.08552133839602E-03	1.40000000232646E-03	6.39602376132729E-16
4858	1.40000000232906E-03	1.85652523102818E-03	1.40000000232433E-03	4.10522046289298E-16
6722	1.40000000231642E-03	2.11909697588377E-03	1.40000000232337E-03	3.24583913185885E-16
9268	1.40000000231067E-03	1.99396092510072E-03	1.40000000232285E-03	1.35543165631997E-16
12513	1.40000000230863E-03	2.45679236236043E-03	1.40000000232254E-03	3.18048816978415E-16
16536	1.40000000231902E-03	2.54727462752348E-03	1.40000000232234E-03	2.49337342540192E-16
21376	1.40000000233241E-03	2.26159014005604E-03	1.40000000232221E-03	7.54540190903794E-17
27126	1.40000000232476E-03	2.90049962763904E-03	1.40000000232211E-03	4.08869278690090E-18

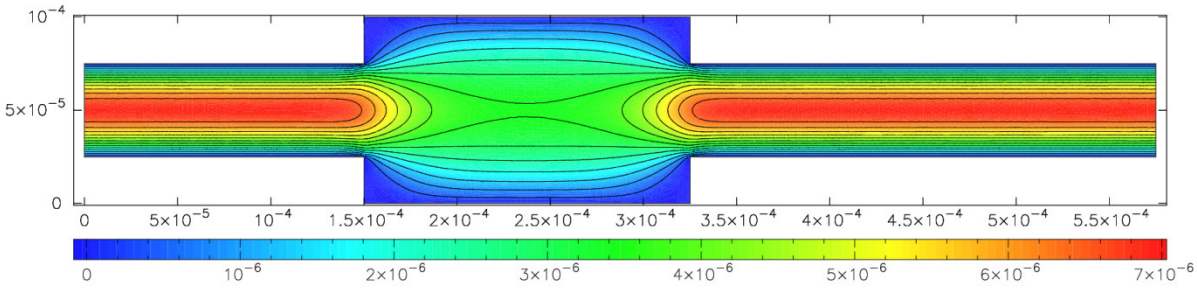

Figure 5-2 *x*-velocity field plot of the fluidic micro-channel

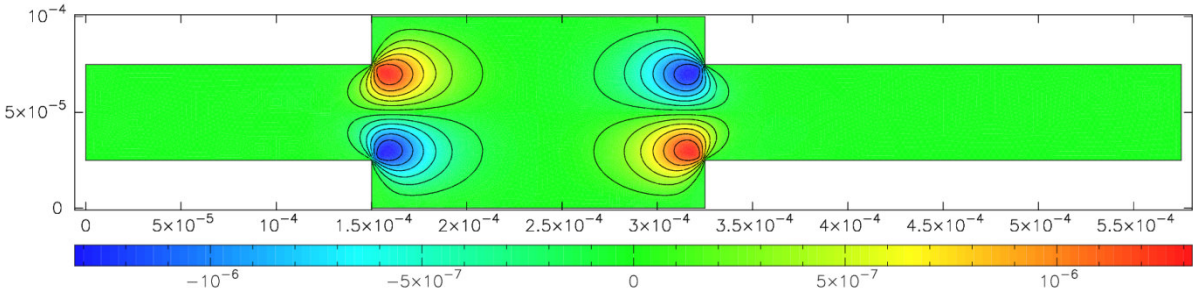

Figure 5-3 *y*-velocity field plot of the fluidic micro-channel

Figure 5-4 presents the more typical vector velocity plot which combines the *x*- and *y*-scalar velocity fields. Figure 5-5 shows the obtained pressure field plot.

Regarding Figure 5-2 and Figure 5-3:

The plot-units of the contour plots are meters per second

Regarding Figure 5-5:

The plot-units of the contour plot are Pascal

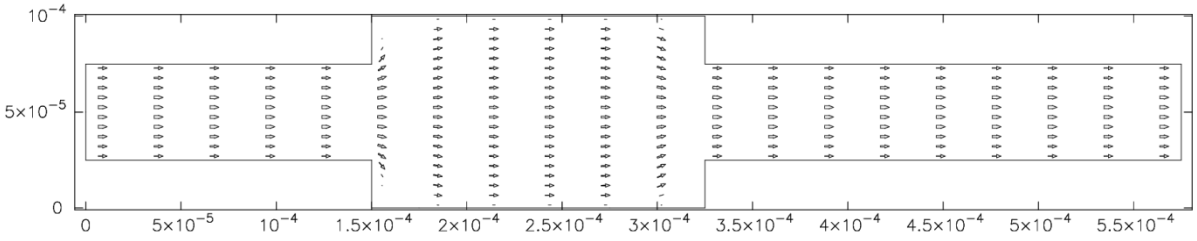

Figure 5-4 Sum-velocity arrow plot of the fluidic micro-channel

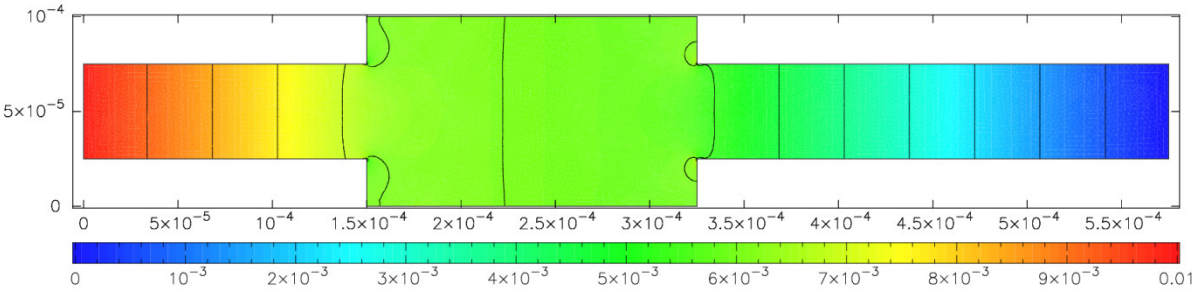

Figure 5-5 Pressure field plot of the fluidic micro-channel

The testing of the adaptive algorithms on the micro-fluidic channel model, was performed in a sequence, similar to that in Chapter 4. Multi-field *h*-adaptation was tested first, with uniform element orders of either 2, 3 or 4 for the velocity fields and respectively one less for the pressure field due to the LBB condition satisfaction. Multi-field *p*-adaptation was tested next by employing the refinement indicator in (3.7). Multi-field *hp*-adaptation was tested last. Results were obtained from all three *hp*-adaptive algorithms. Once results for all algorithms were obtained, a sequence of additional plots was created once again, in order to provide a direct comparison between them on a field-by-field basis. Finally, valuable information was extracted from the error convergence plots.

In order to formulate expectations in the current micro-channel problem, the presence of singularities is already obvious. This leads to the prediction that it will not greatly benefit from the higher order elements. This problem therefore provides an alternative testing platform for the adaptive algorithms compared to the SAW device.

In the following, all adaptation curves are presented in sequence. Regarding the convergence curves for *h*-adaptation, they are presented in Figure 5-6 and Figure 5-7, each time for the respective field, mentioned in the plot. The ones concerned with *p*-adaptation in Figure 5-8 and Figure 5-9. These are followed by the *hp*-adaptation curves in Figure 5-10 and Figure 5-11. Lastly, the adaptive algorithm comparison curves, are given in Figure 5-12 and Figure 5-13. Supplementary plots that were omitted from the main body of the report appear in Appendix A2. These are concerned with mesh size and element order adaptations. Details are given in the respective captions too.

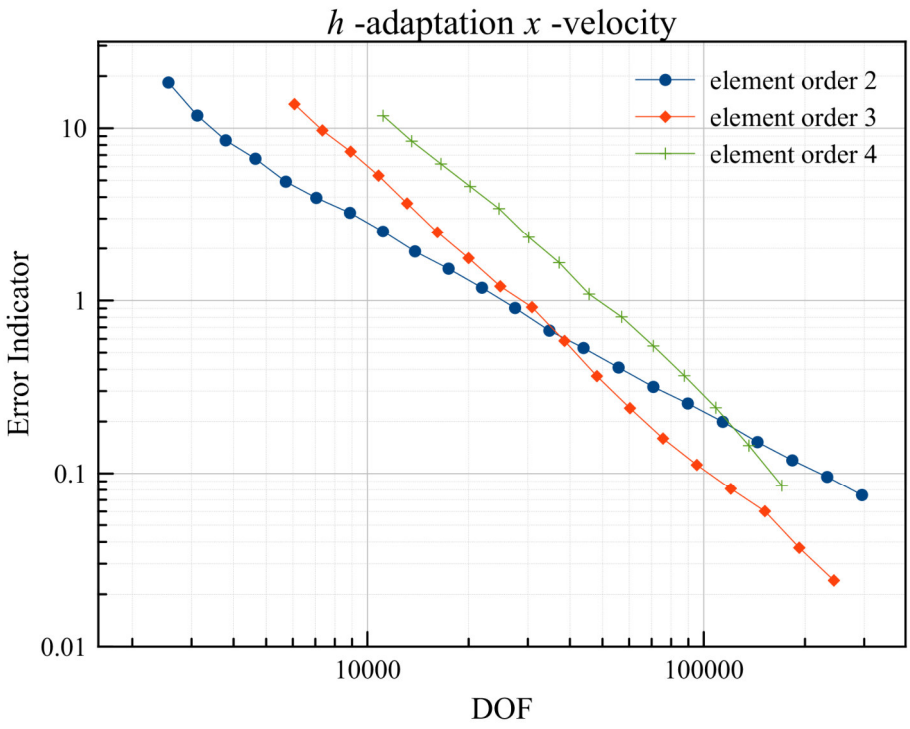

Figure 5-6 *x*-velocity error indicator, plotted against number of degrees of freedom, with *h*-adaptation and for uniform element orders of 2, 3 and 4

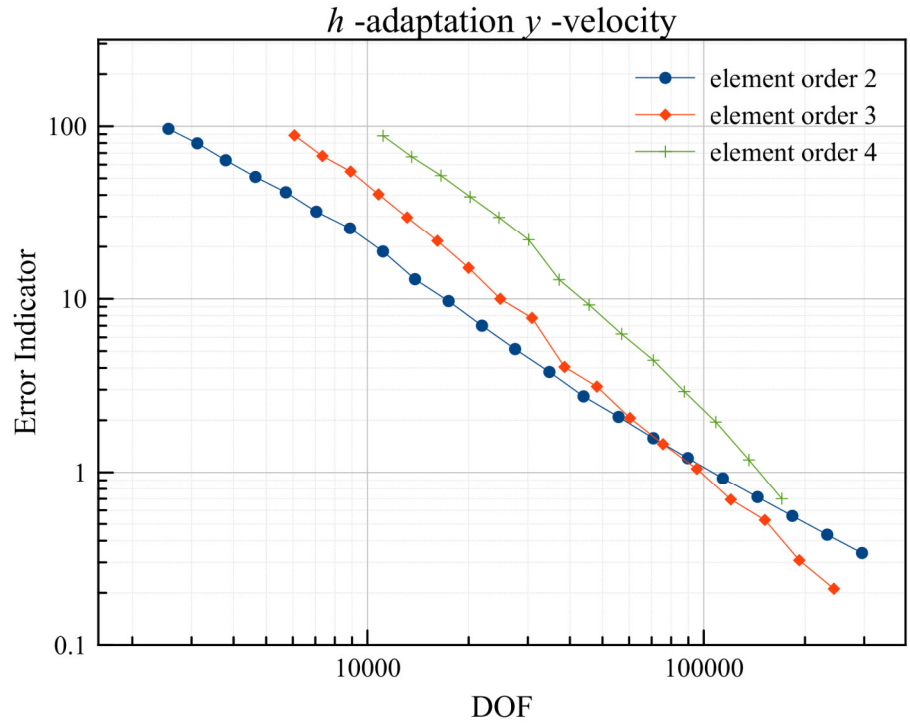

Figure 5-7 *y*-velocity error indicator, plotted against number of degrees of freedom, with *h*-adaptation and for uniform element orders of 2, 3 and 4

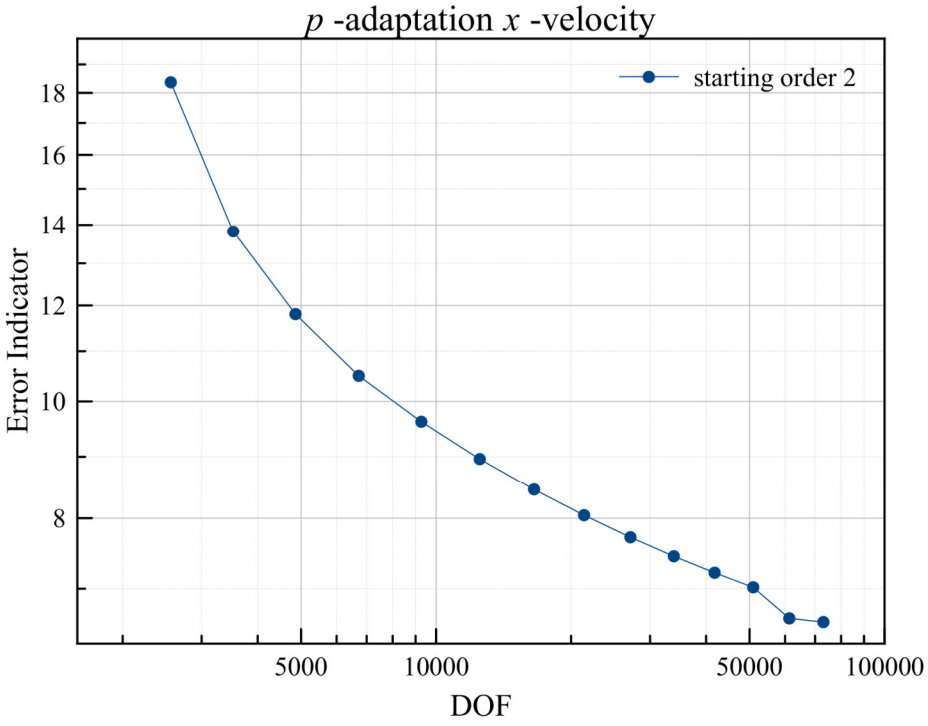

Figure 5-8 *x*-velocity error indicator, plotted against number of degrees of freedom, with *p*-adaptation

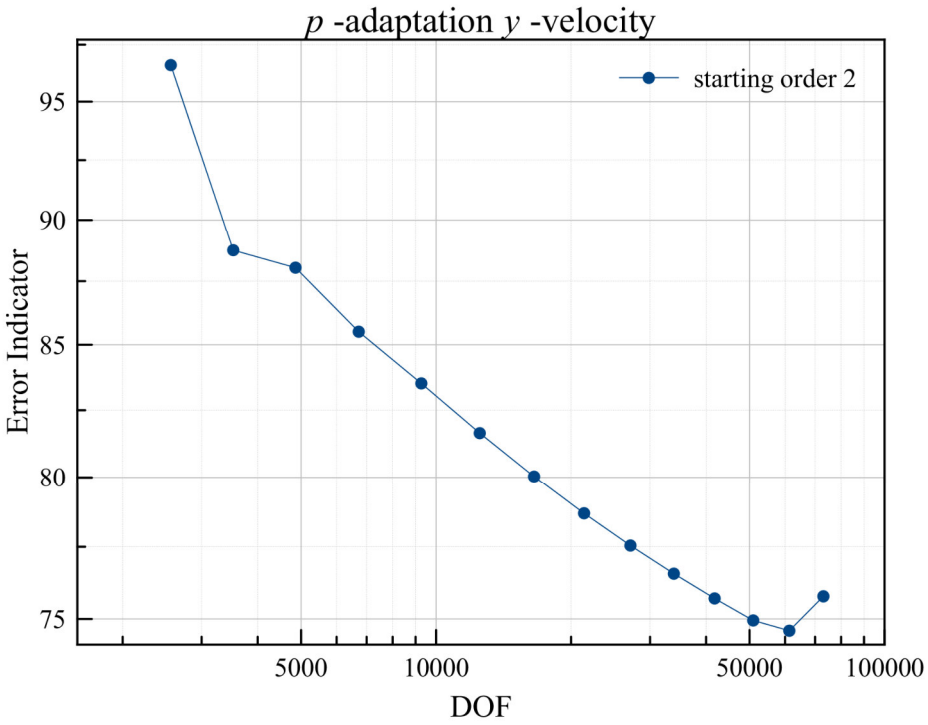

Figure 5-9 *y*-velocity error indicator, plotted against number of degrees of freedom, with *p*-adaptation

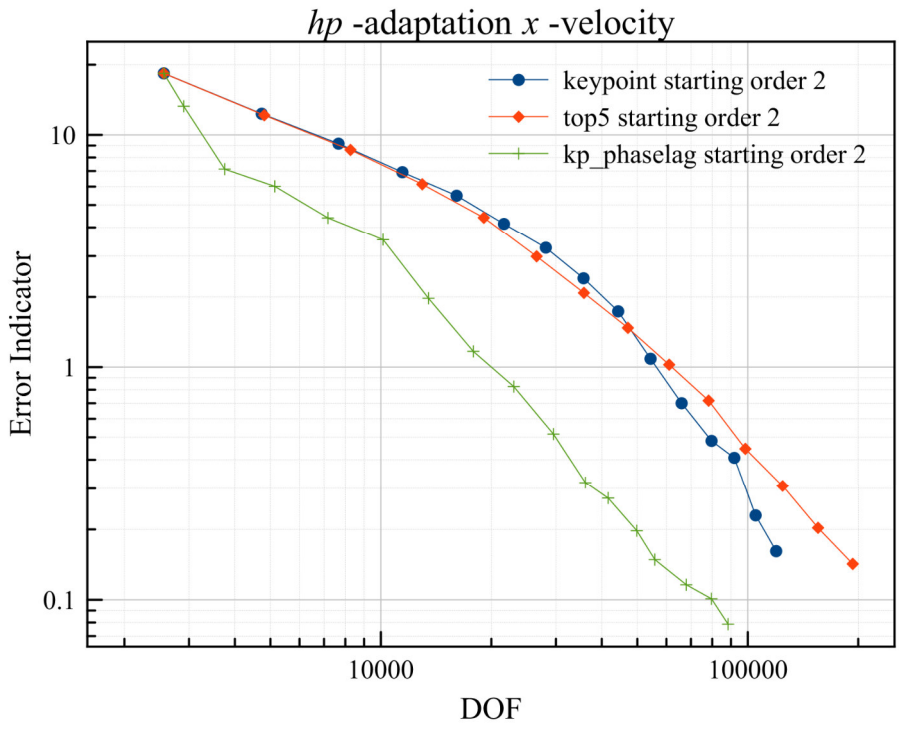

Figure 5-10 *x*-velocity error indicator plotted against number of degrees of freedom, with *hp*-adaptation and for all *hp*-adaptive algorithms

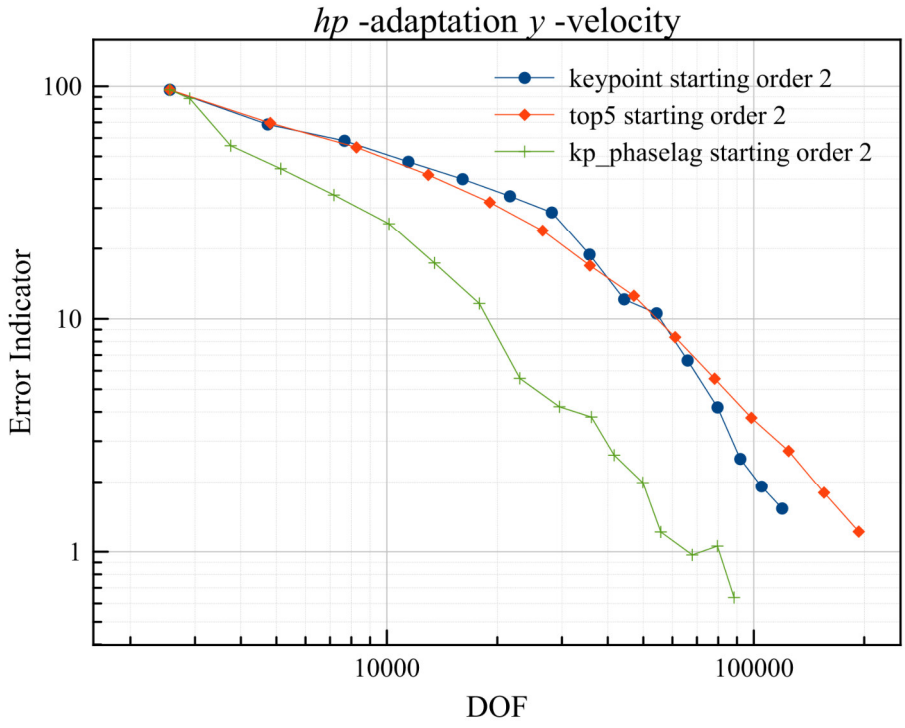

Figure 5-11 *y*-velocity error indicator plotted against number of degrees of freedom, with *hp*-adaptation and for all *hp*-adaptive algorithms

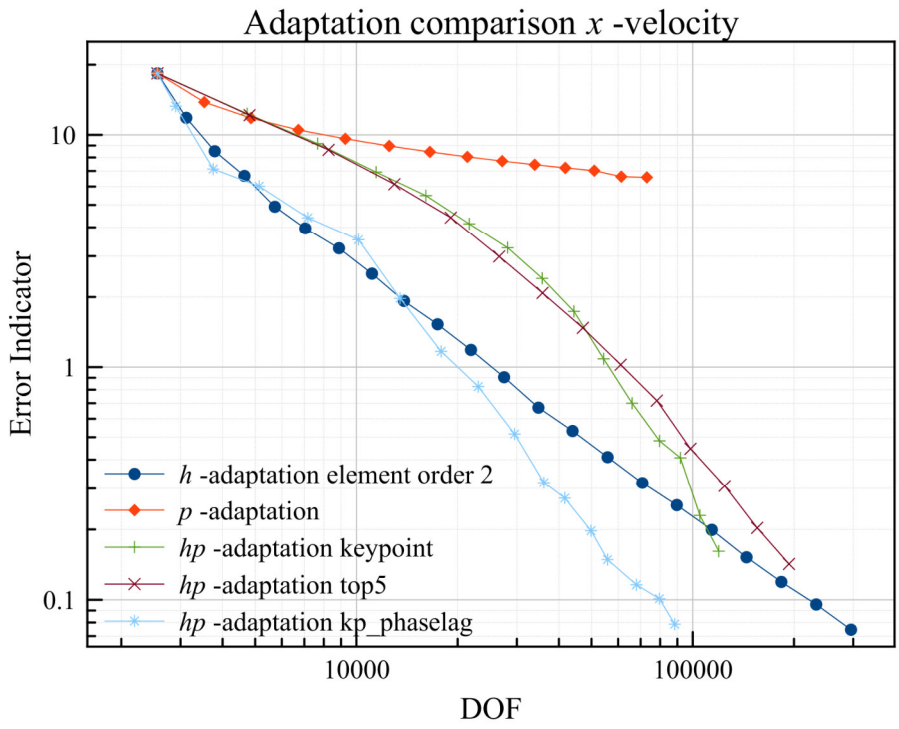

Figure 5-12 Adaptation comparison for the *x*-velocity field with all of the five adaptation techniques

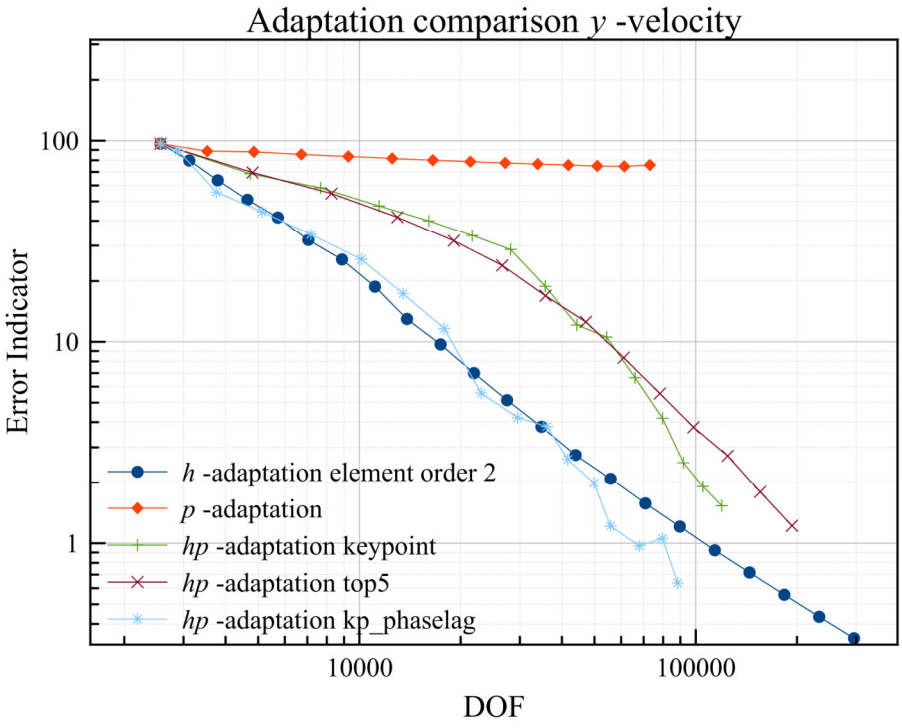

Figure 5-13 Adaptation comparison for the *y*-velocity field with all of the five adaptation techniques

Given the nature of the pressure field equation and the PolyDE capabilities, the calculation of pressure error convergence curves was not possible, therefore none are presented. In all adaptation cases, the "solver" executable continued with its execution up to the point that the finite memory of the machine allowed it to run. During the test-runs, it was observed that higher order elements overpopulate the global matrix with entries, therefore the "solver" could reach a lower number of degrees of freedom. This reaffirms the necessity for pre-solution matrix conditioning investigations when possible. The numerical fluctuation observed in Figure 5-9, is cautiously attributed to the matrix overpopulation and conditioning. The computation time with high order elements was significantly longer compared to the refined mesh technique of *h*-adaptation.

Table 5-4 Collective convergence results for the micro-fluidic channel

h-	*p*-	*hp*-keypoint	*hp*-top5	*hp*-kp_phaselag
		x-velocity		
Worst step convergence				
-0.87	-0.04	-0.61	-0.63	-0.54
Best step convergence				
-2.22	-0.89	-4.30	-2.07	-2.60
Average step convergence				
-1.17	-0.28	-1.57	-1.27	-1.66
		y-velocity		
Worst step convergence				
-0.97	0.09	-0.34	-0.44	0.55
Best step convergence				
-1.69	-0.26	-3.56	-1.87	-4.87
Average step convergence				
-1.19	-0.06	-1.41	-1.18	-1.63

Table 5-4 collectively presents the convergence results for the micro-fluidic channel. The style of presentation is the same as the one described in Chapter 4 and the calculations were once again made by using (4.4). As expected, the *p*-adaptation algorithm was the worst performing with average step convergences of -0.28 and -0.06 for the *x*-velocity and *y*-velocity fields respectively. The *hp*-kp_phaselag was the best performing with average step convergences of -1.66 and -1.63. Concerning *h*-adaptation the values of -1.17 and -1.19 seem to be in agreement with theory where for uniform second order elements and the 2D nature of the problem, a convergence value of -1 would be expected.

5.2. Micro-flow electric regulator (Fluidic-electric example)

The second test case in the current chapter, is a non-linear problem corresponding to the physics mode of Section 2.3.7. Compared to the problem case in the previous section, the number of fields solved for is increased to four, by additionally introducing the electric potential field. A micro-fluidic three-way junction, where inlets and outlets can be interchanged by the influence of an electric field, is investigated.

The dimensions of the geometry can be investigated from Figure 5-14 where meters are the displayed geometry units. Table 5-5 presents the material properties of the model. An electric potential of 0V is applied to the port at the right part of the geometry, whereas an electric potential of 1mV is applied to the two ports at the left part of the geometry. The resulting electric field is shown in Figure 5-18. Due to the presence of the electric field and assuming a liquid with electro-kinetic properties, a flow is generated in the channel. Flow is achieved in the direction towards lower electric potential. The *x*-velocity field plot is given in Figure 5-14, the *y*-velocity field plot in Figure 5-15 and the vector velocity plot in Figure 5-16. Therefore the left ports are now functioning as inlets and the right port as an outlet.

Table 5-5 Material data of micro-flow electric regulator

Material	Property	Value	Units
Water-like liquid	Material density ρ	1000	$[\text{kg}/\text{m}^3]$
	Dynamic viscosity μ	1.002×10^{-3}	$\left[\frac{\text{kg}}{\text{m} \cdot \text{s}}\right]$
	Relative permittivity ε_r	$\begin{bmatrix} 80 & 0 & 0 \\ 0 & 80 & 0 \\ 0 & 0 & 80 \end{bmatrix}$	

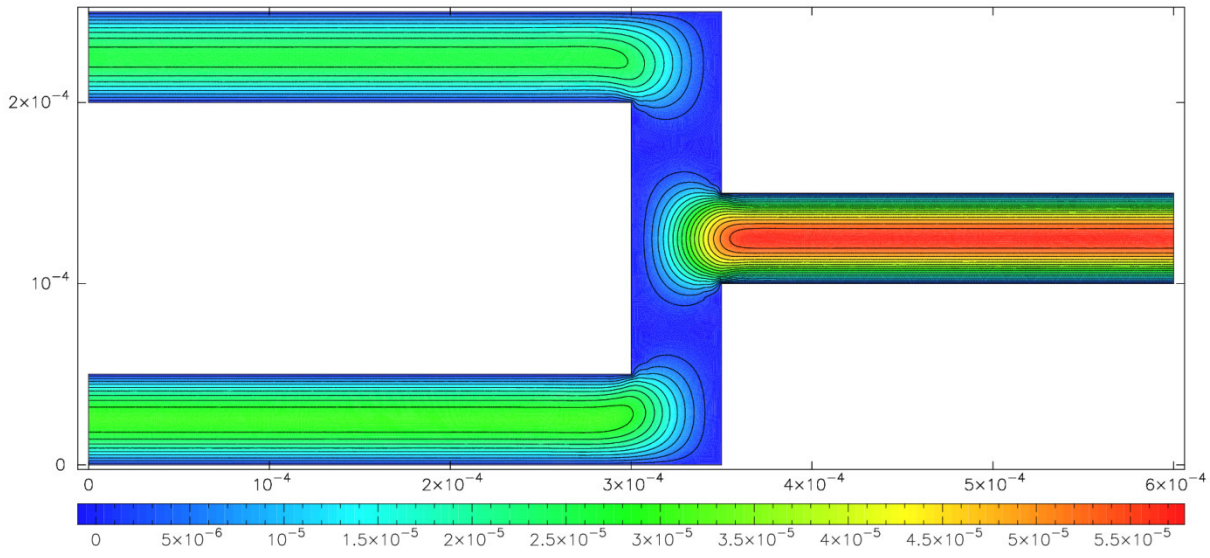

Figure 5-14 *x*-velocity field plot of the micro-flow electric regulator

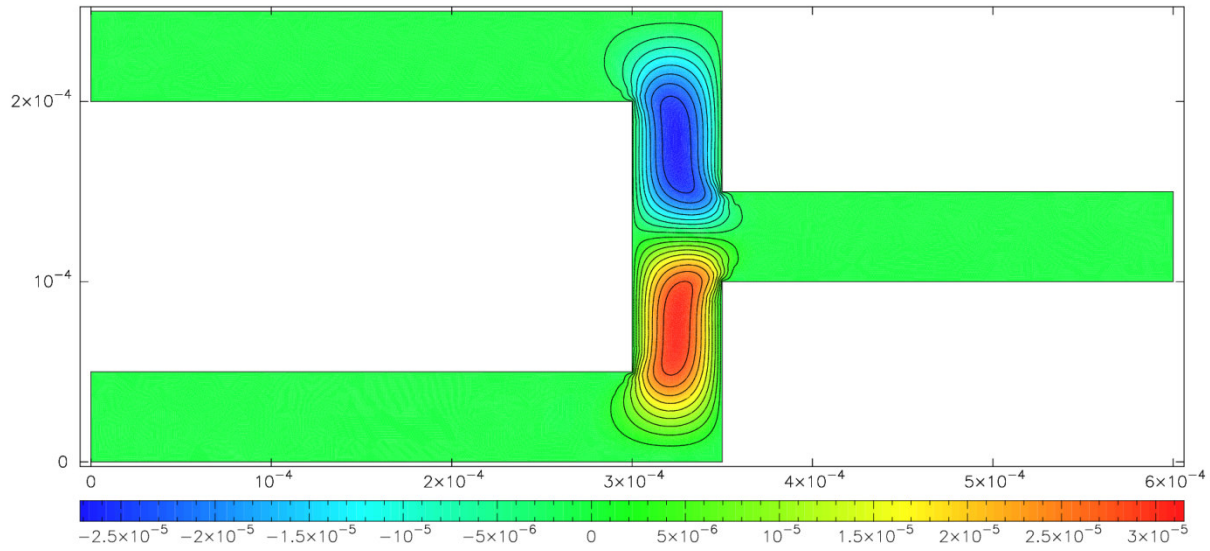

Figure 5-15 *y*-velocity field plot of the micro-flow electric regulator

Figure 5-17 shows the plot of the resulting pressure field. In order to change the functionality of the ports, a modified electric field is applied to the geometry as it is illustrated in Figure 5-22. The obtained modified velocity plots are given in Figure 5-19 for the *x*-velocity component, Figure 5-20 for the *y*-velocity component and Figure 5-21 for the vector velocity sum. At the left part of the geometry, the upper port is now functioning as an inlet, while the lower port has been converted to an outlet. The right port remains an outlet. The number of inlets and outlets has been interchanged.

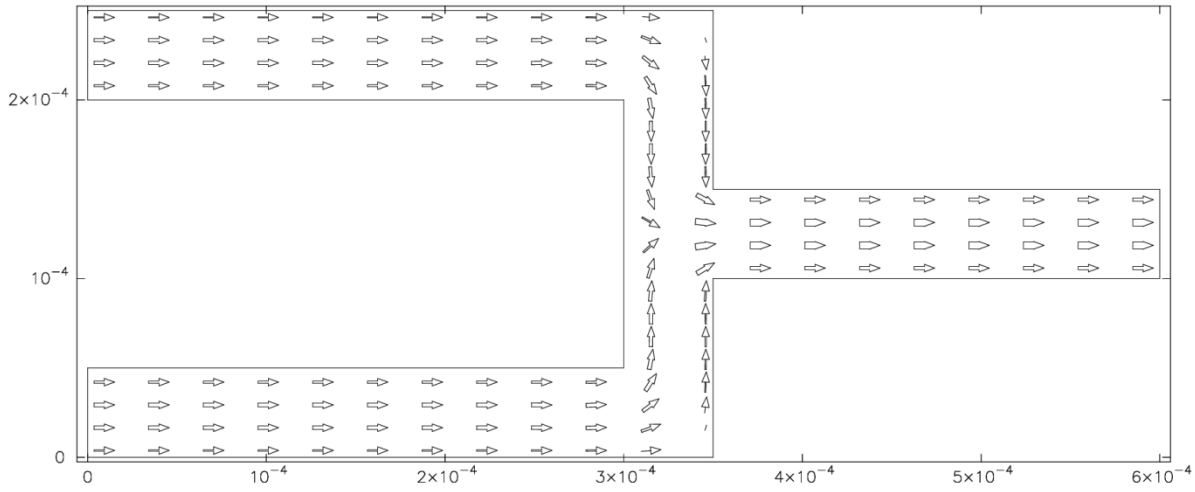

Figure 5-16 Sum-velocity arrow plot of the micro-flow electric regulator

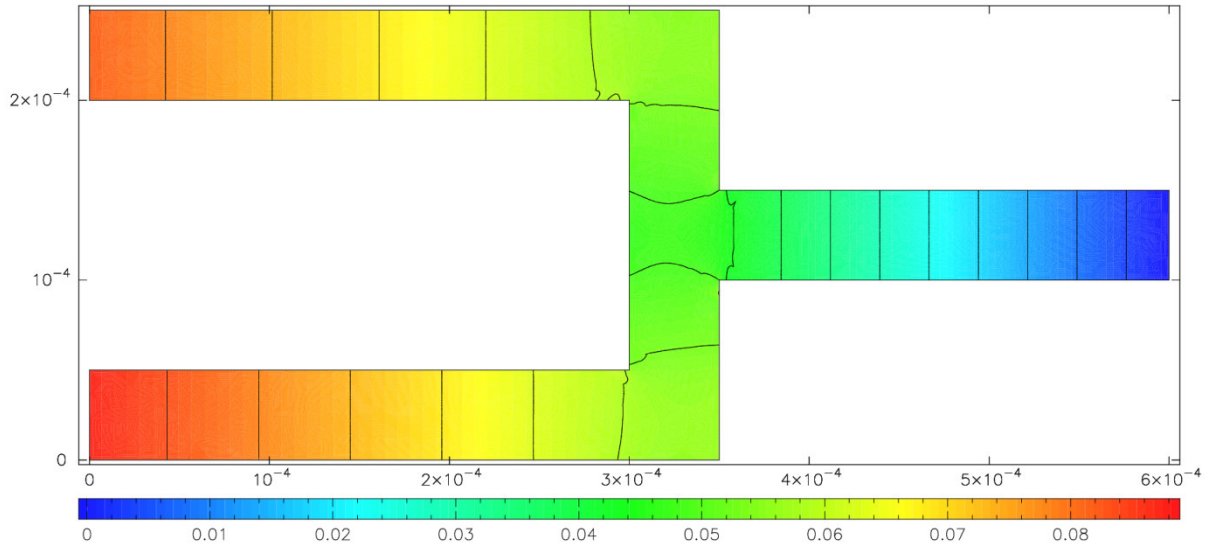

Figure 5-17 Pressure field plot of the micro-flow electric regulator

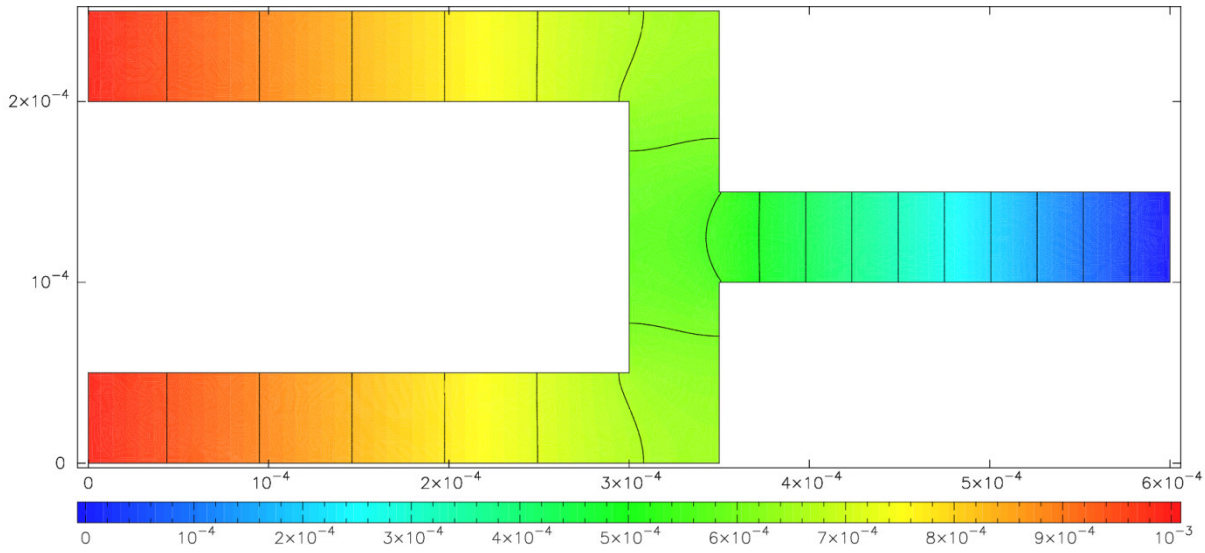

Figure 5-18 Electric Potential field plot of the micro-flow electric regulator

Hint: A space charge density ρ_f of 1 C/m^3 was assumed in the problem setup

Regarding Figure 5-14 and Figure 5-15:
The plot-units of the contour plots are meters per second
Regarding Figure 5-17:
The plot-units of the contour plot are Pascal
Regarding Figure 5-18:
The plot-units of the contour plot are Volts

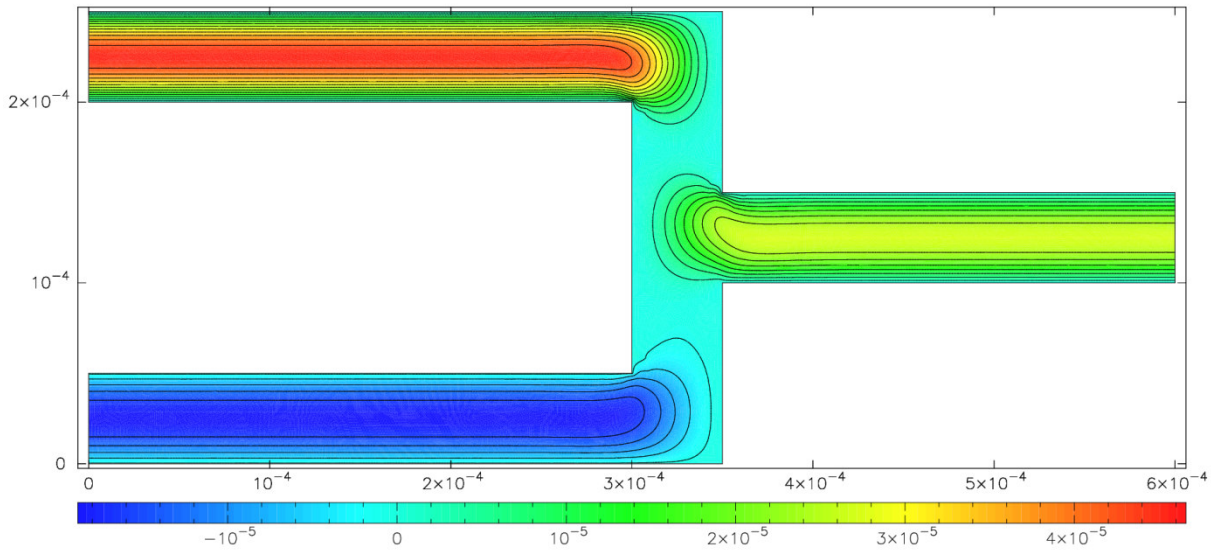

Figure 5-19 *x*-velocity field plot of the micro-flow electric regulator under electrically modified flow condition

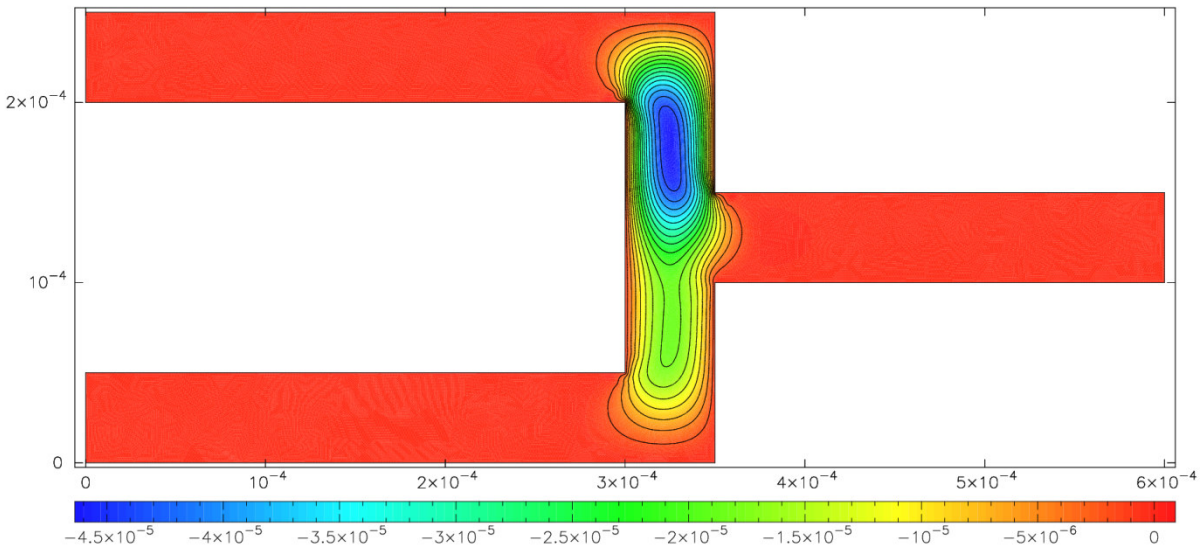

Figure 5-20 *y*-velocity field plot of the micro-flow electric regulator under electrically modified flow condition

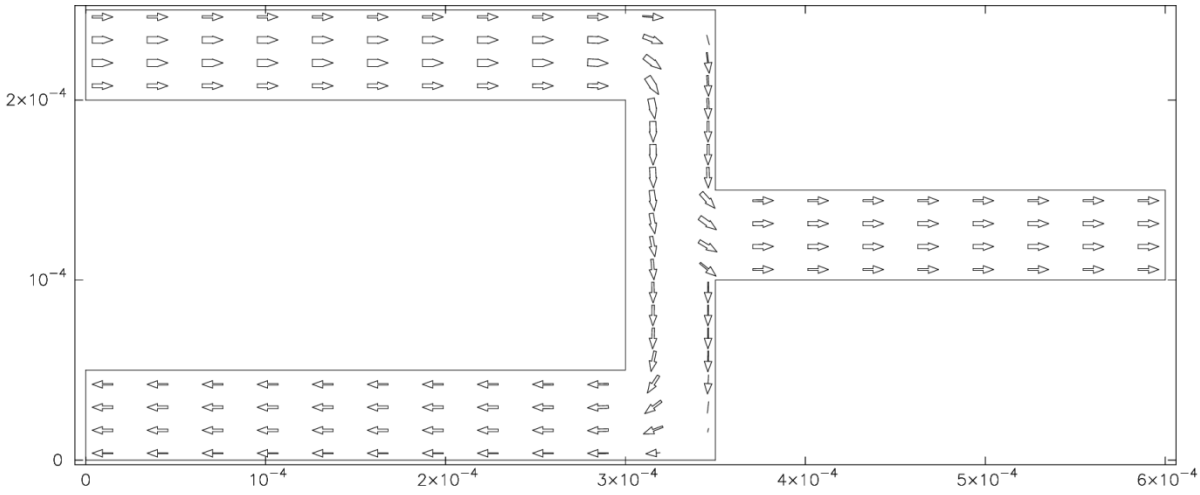

Figure 5-21 Sum-velocity arrow plot of the micro-flow electric regulator under electrically modified flow condition

After having demonstrated microsystem device functionality with two different flow regimes, the first flow regime was further investigated by applying the full set of adaptive algorithms in the same manner with the previous two problems, and concluding with a comparison between the full set of techniques.

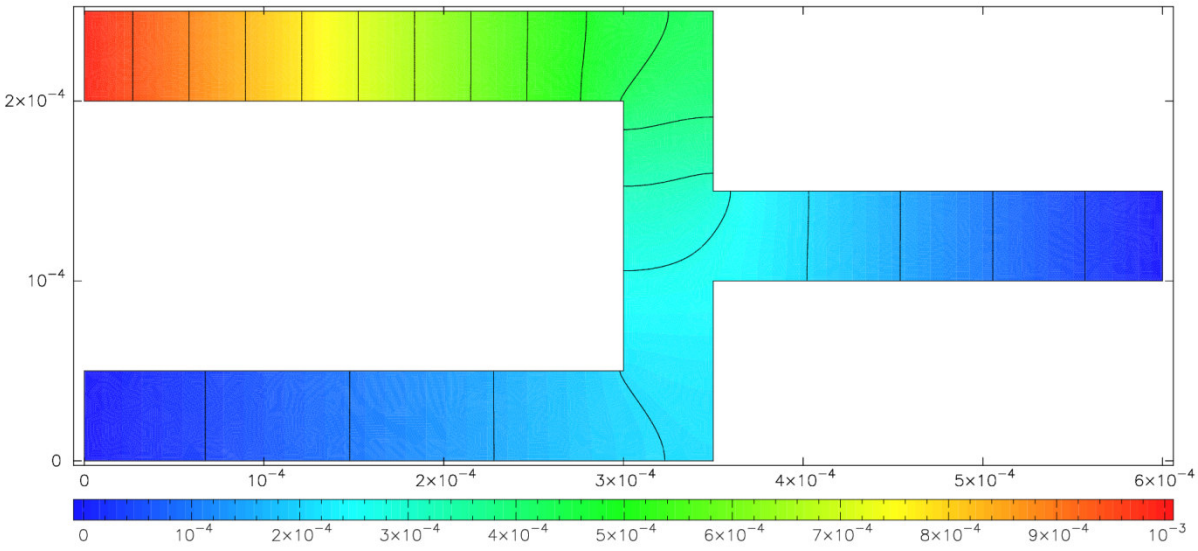

Figure 5-22 Electric Potential field plot of the micro-flow electric regulator under electrically modified flow condition

Regarding the convergence curves for *h*-adaptation, they are presented in the sequence from Figure 5-23 to Figure 5-25, each time for the respective field, mentioned in the plot. The ones concerned with *p*-adaptation in the sequence from Figure 5-26 to Figure 5-28. These are followed by the *hp*-adaptation curves from Figure 5-29 to Figure 5-31. Lastly, the adaptive algorithm comparison curves, from Figure 5-32 to Figure 5-34. Supplementary plots that were omitted from the main body of the report, once again appear in Appendix A2. Details are given in the respective captions too.

In the formulation of error convergence expectations for the micro-flow electric regulator, and before inspecting the obtained results, it could be predicted that this problem would not benefit from *p*-adaptation due to the smooth solution gradients and also the lack of any wave terms. Concerning *h*-adaptation, a slope of around -1 was to be expected once more. The *hp*-algorithms were known to depend on program design, and the question for them was whether they could make preferable decisions on favoring *h*-refinement over *p*-enrichment in this particular problem.

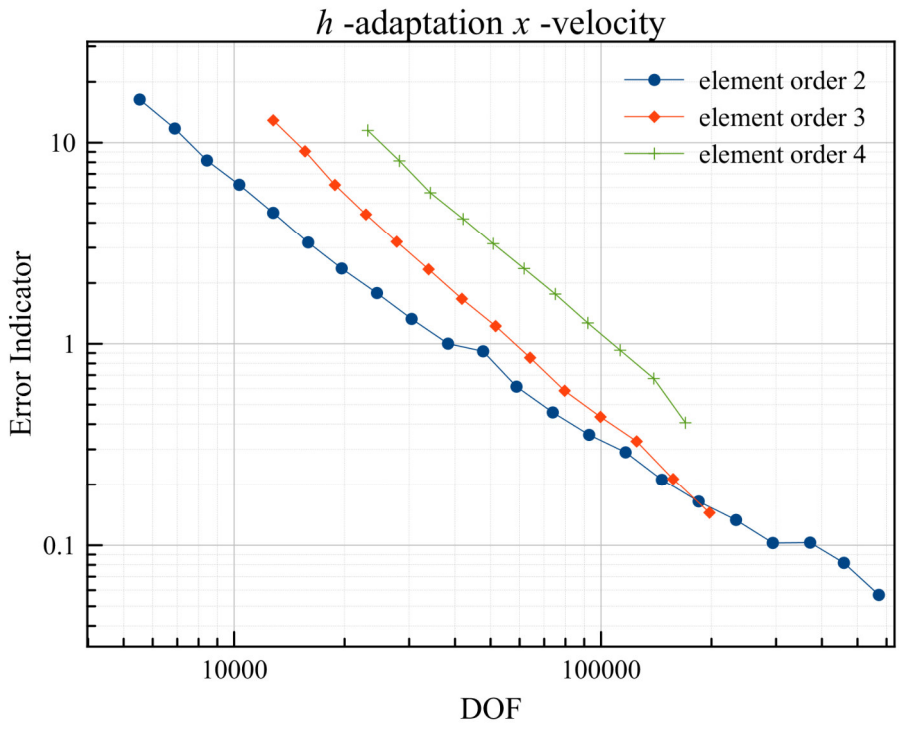

Figure 5-23 *x*-velocity error indicator, plotted against number of degrees of freedom, with *h*-adaptation and for uniform element orders of 2, 3 and 4

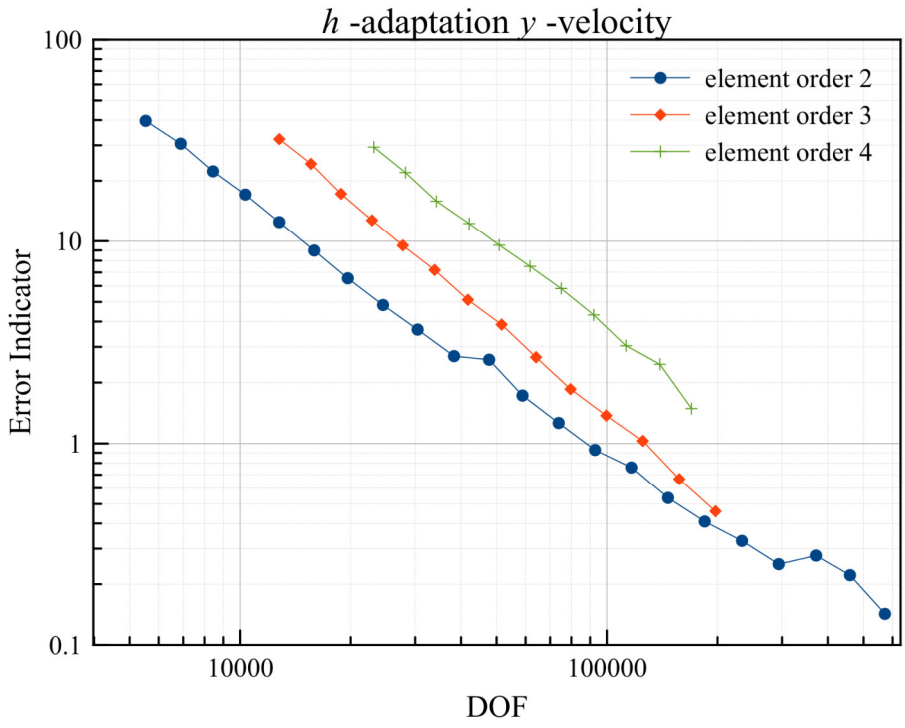

Figure 5-24 *y*-velocity error indicator, plotted against number of degrees of freedom, with *h*-adaptation and for uniform element orders of 2, 3 and 4

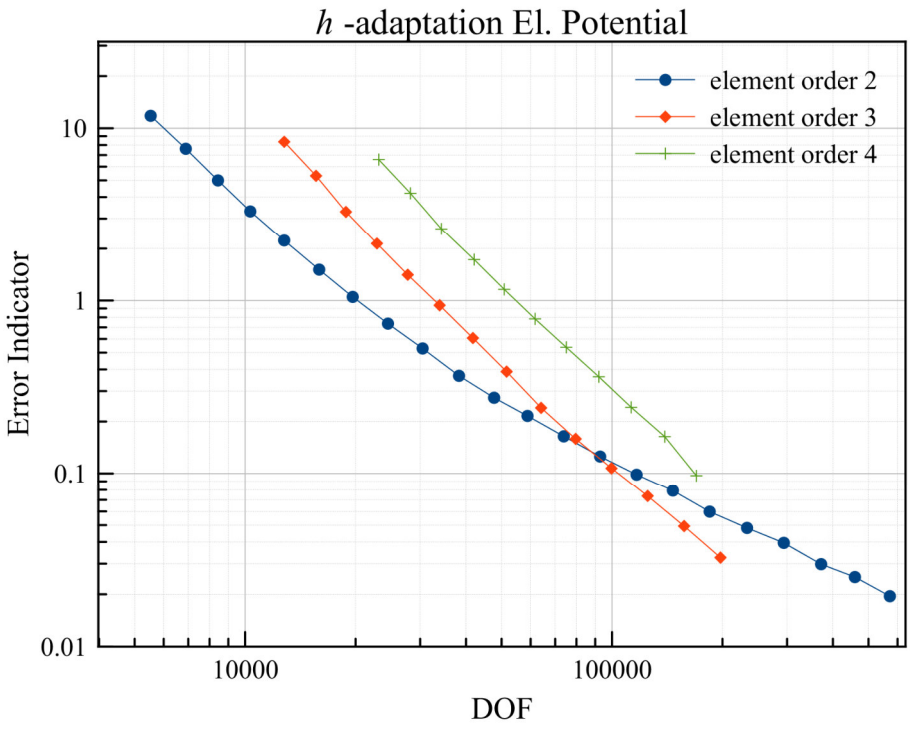

Figure 5-25 Electric Potential error indicator, plotted against number of degrees of freedom, with *h*-adaptation and for uniform element orders of 2, 3 and 4

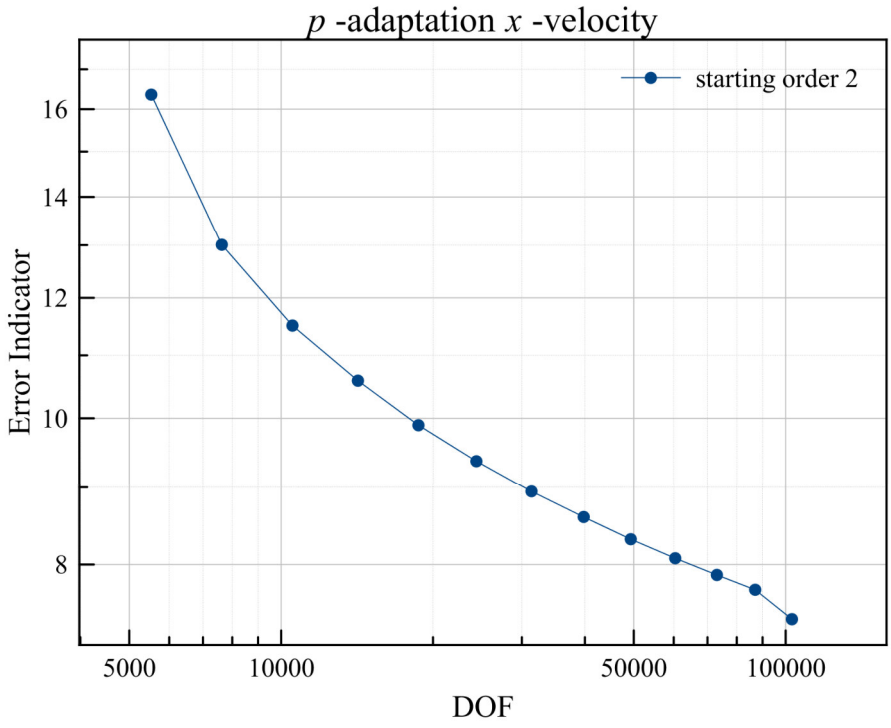

Figure 5-26 *x*-velocity error indicator, plotted against number of degrees of freedom, with *p*-adaptation

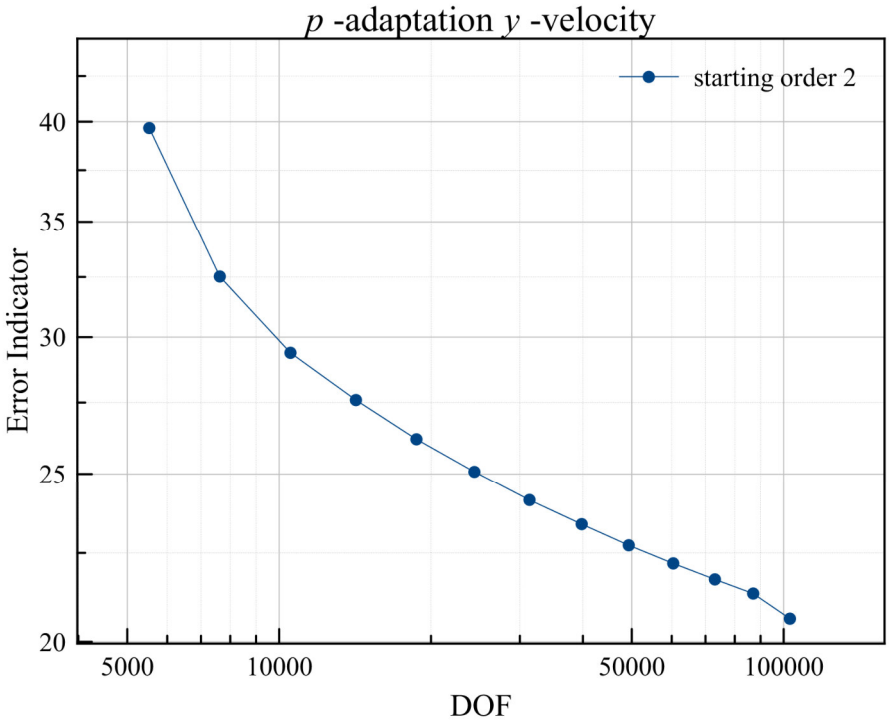

Figure 5-27 *y*-velocity error indicator, plotted against number of degrees of freedom, with *p*-adaptation

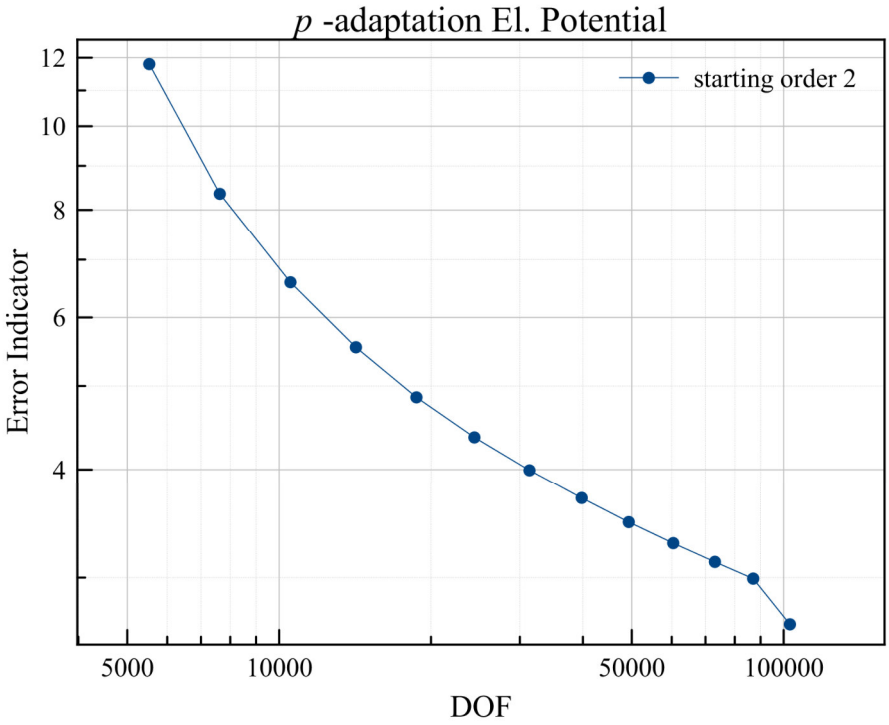

Figure 5-28 Electric Potential error indicator, plotted against number of degrees of freedom, with *p*-adaptation

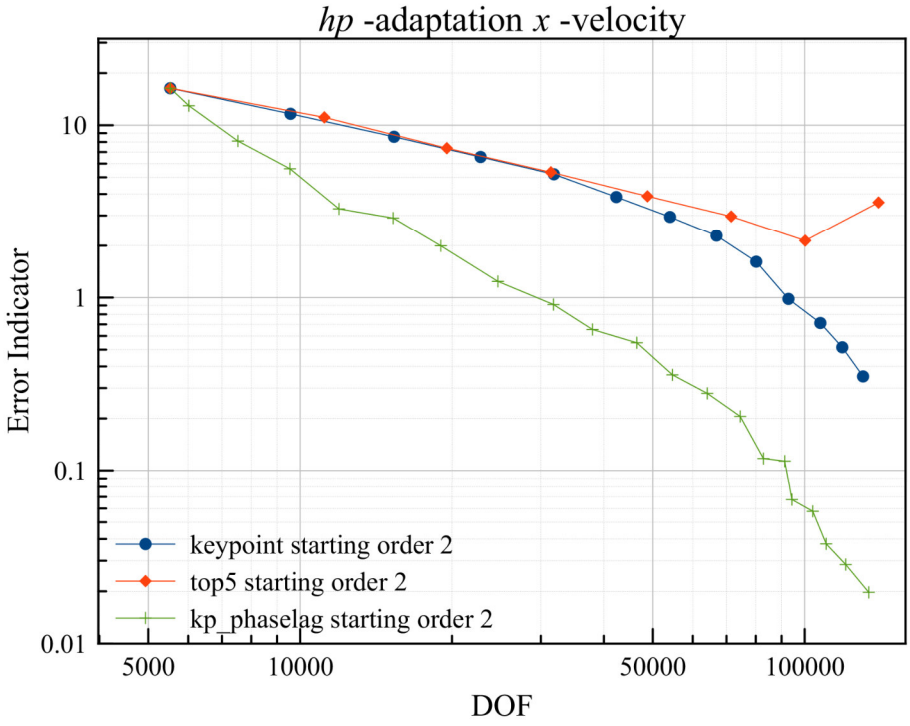

Figure 5-29 *x*-velocity error indicator plotted against number of degrees of freedom, with *hp*-adaptation and for all *hp*-adaptive algorithms

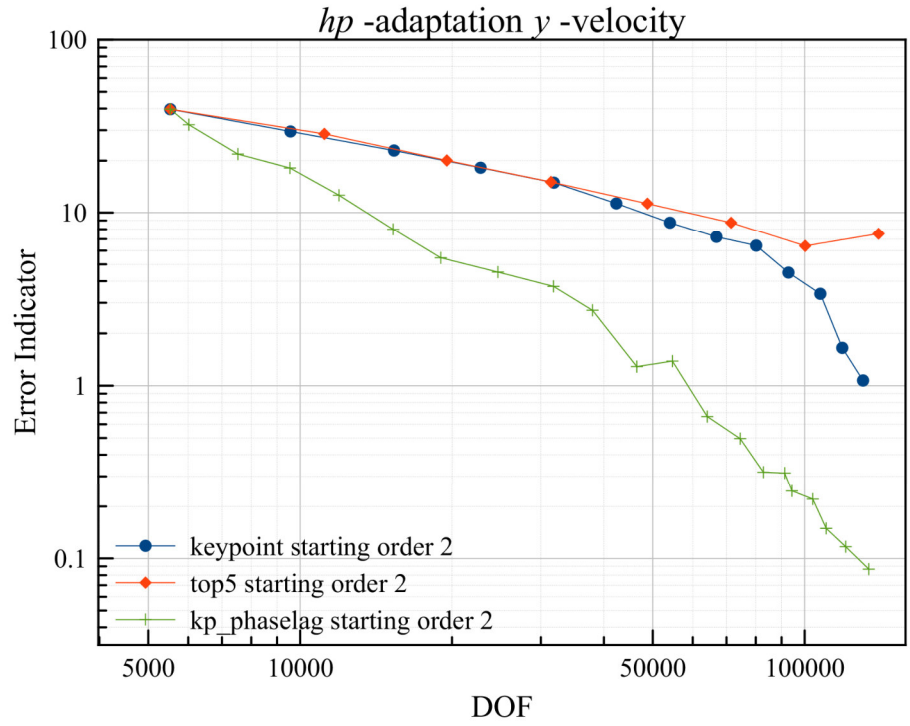

Figure 5-30 *y*-velocity error indicator plotted against number of degrees of freedom, with *hp*-adaptation and for all *hp*-adaptive algorithms

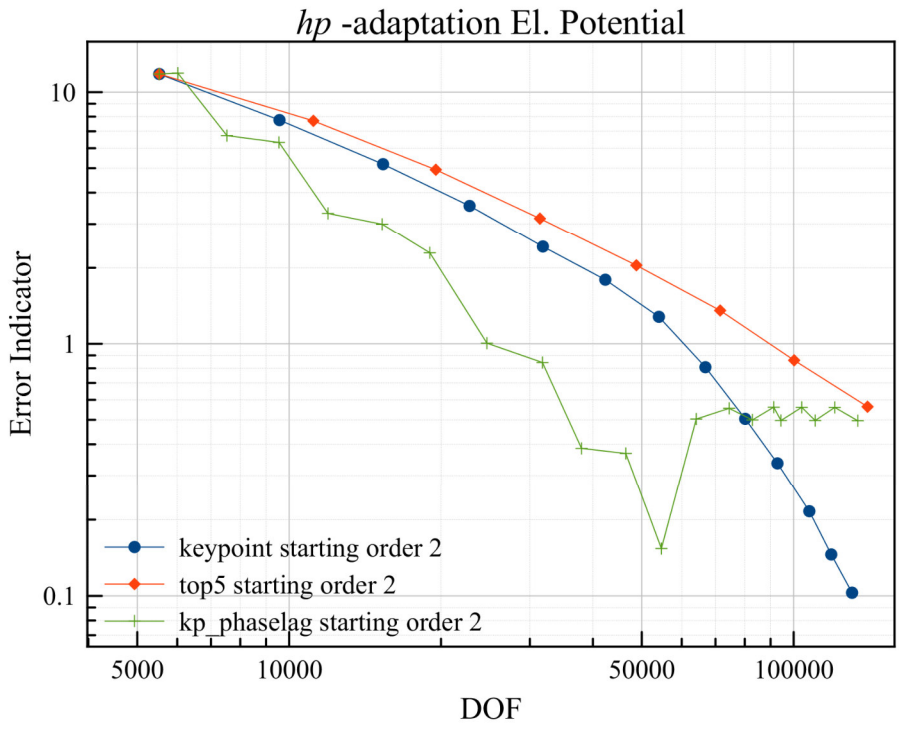

Figure 5-31 Electric Potential error indicator plotted against number of degrees of freedom, with *hp*-adaptation and for all *hp*-adaptive algorithms

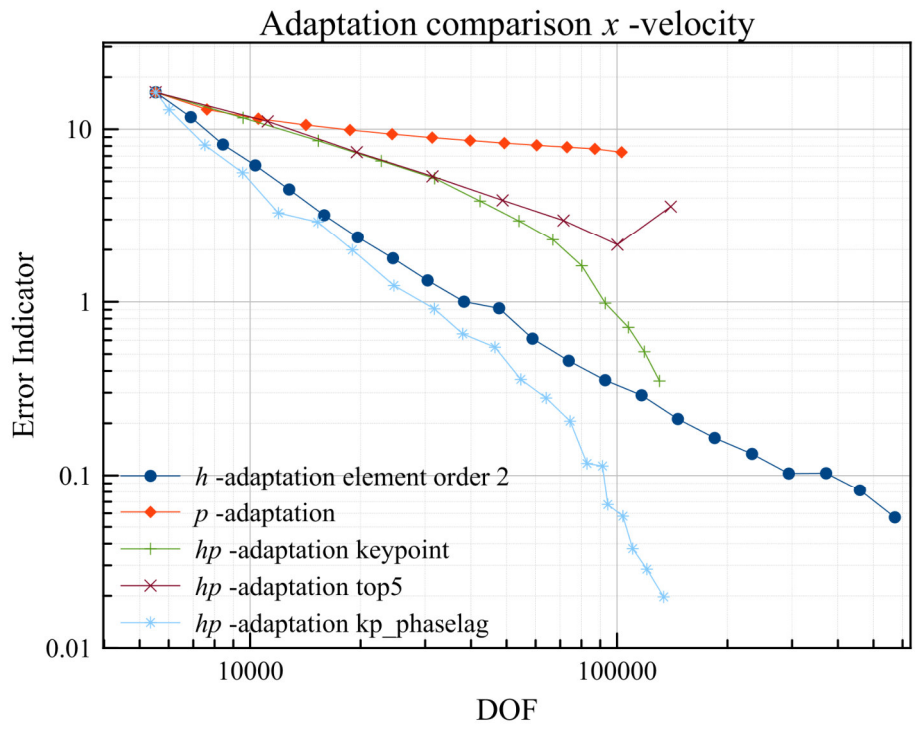

Figure 5-32 Adaptation comparison for the *x*-velocity field with all of the five adaptation techniques

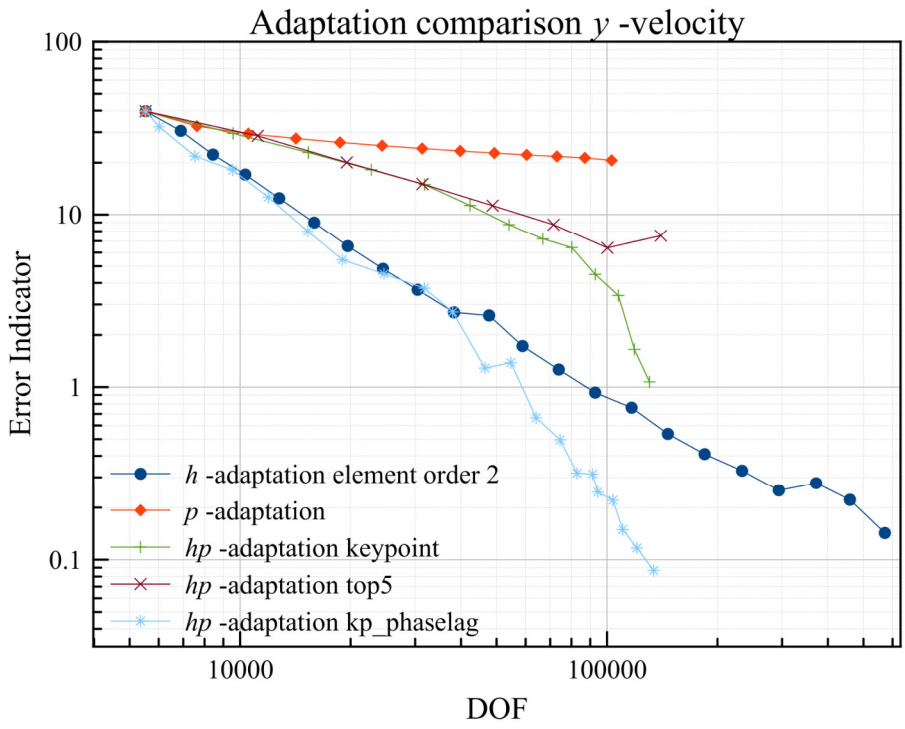

Figure 5-33 Adaptation comparison for the *y*-velocity field with all of the five adaptation techniques

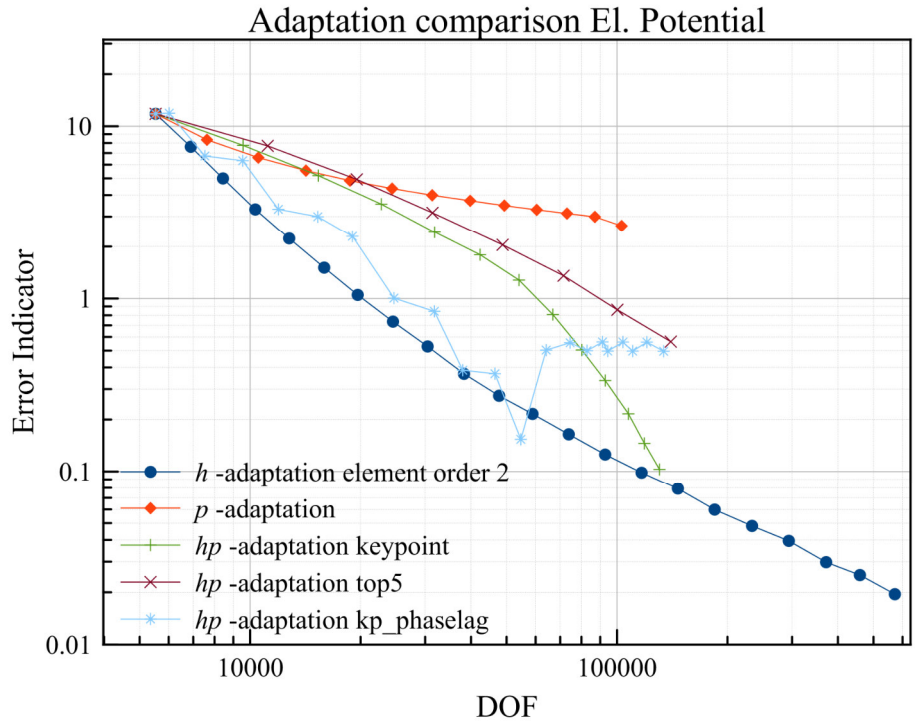

Figure 5-34 Adaptation comparison for the Electric Potential field with all of the five adaptation techniques

Table 5-6 Collective convergence results for the micro-flow electric regulator

h-	*p*-	*hp*-keypoint	*hp*-top5	*hp*-kp_phaselag
		x-velocity		
Worst step convergence				
0.02	-0.13	-0.62	1.53	-0.36
Best step convergence				
-1.92	-0.71	-4.08	-0.97	-15.76
Average step convergence				
-1.23	-0.25	-1.73	-0.40	-2.98
		y-velocity		
Worst step convergence				
0.42	-0.11	-0.54	0.49	0.45
Best step convergence				
-2.01	-0.62	-7.16	-0.93	-7.38
Average step convergence				
-1.22	-0.20	-1.83	-0.50	-2.40
		Electric potential		
Worst step convergence				
-0.80	-0.25	-0.77	-0.61	7.46
Best step convergence				
-2.09	-1.07	-3.93	-1.34	-5.37
Average step convergence				
-1.39	-0.48	-2.03	-1.00	-0.85

Table 5-6 collectively presents the results for the micro-flow electric regulator convergence slopes. The *h*-adaptation method has averaged convergence slopes of -1.23, -1.22 and -1.39 for the respective fields. As expected, the *p*-adaptation method, has averaged worse convergence slopes compared to the *h*-method at -0.25, -0.20 and -0.48. The low performance of *p*-enrichment, is further justified from the observation of the *h*-adaptation plots (Figure 5-23 to Figure 5-25), in which the uniform element order increase beyond 3 does not further improve the *h*-adaptation slopes.

The *hp*-keypoint algorithm has provided strong convergence slopes, however the program solver was not able to proceed to the same number of degrees of freedom as it has done with *h*-adaptation. The *hp*-top5 has performed weakly in this problem. Finally, the *hp*-kp_phaselag has shown the strongest performance with average slopes of -2.98 and -2.40 for the velocities but for the electric potential field, the algorithm eventually reached a region of oscillation.

Concerning adaptive techniques, the overall message is that useful results have been obtained that form the basis for supplementary development. The multi-field *h*- and *p*-versions show the expected behavior, however *hp*-versions heavily depend on program design and correct decision making, and it seems that in successive development attempts, the *hp*-versions should be refined one algorithm and one physics mode at the time.

The dissertation [43] appears to attempt to concentrate on the solution of coupled problems in fluid dynamics, with the employment of the *hp*-finite element method. It is therefore possible to hastily draw a few comparisons with the actual thesis.

An exploration of the document reveals that there is an extensive theoretical analysis behind both triangular and quadrilateral elements. Its demonstrative numerical examples however, mainly employ quadrilateral elements. There did not seem to be an explicit indication as to what from the author's point of view, the advantage of quadrilateral elements is. In contrast to the quadrilateral elements, the actual thesis, has made a statement in Section 2.1.3, according to which, triangular elements offer a high geometrical figure adaptation and are therefore generally preferred.

[43] uses the word monolithic in order to describe multiphysics problems which are solved as one large problem. In that view, the actual thesis is using a monolithic approach. [43] also argues that solving a multi-mesh system in a monolithic manner is generally not feasible. It further argues that refining a common mesh on multiple areas of the geometry due to the refining needs of each solution-field is a waste of degrees of freedom. This is the issue that the actual thesis has tried to tackle, by introducing the normalized element refinement indicator in Chapter 3 and thus making the refining of the common mesh, a more intelligent decision.

A few more comparison statements concerning [43] are given in the following. The document has not put a discussion emphasis on the generality and reusability of their approach, but rather it has heavily focused on the mathematics and their advances in *hp*-FEM implementations. The mostly fluidic-nature examples are presented as proof of the presented algorithms. The actual thesis has derived various physics modes in Chapter 2 for the purpose of proving reusability. Also concerning the actual thesis, it did not design an *hp*-FEM general algorithm from scratch, but due to program code development continuity, used a collection of *hp*-algorithms originally indented for wave problems as a starting point. And it has shown that the further refinement of the *hp*-algorithms on a monolithic framework is possible thanks to the field-energy normalization technique.

6. Suggestions for Further Progress and Conclusions

After the setup and testing of the example problems in the preceding chapters, with the aim of a thesis approach justification, this concluding chapter provides further overall impressions, and mentions a few possible directions for the continuation of the actual coupled problems work. First, in Section 6.1, it brings into perspective the accomplishment of the general partial differential equation framework, with regards to further possible program expansions. Then, in Section 6.2, concluding remarks are derived for the adaptive techniques methodology, together with hints concerning the approximate formation of further research objectives in the FEM adaptation area. Overall impressions and final thoughts are presented in Section 6.3.

6.1. Concluding remarks on the general PDE framework

The general PDE framework has successfully been implemented in a multi-field format, that can accommodate an unrestricted number of fields. A large amount of effort has been invested in experimenting with, and mapping several coupled physics modes to this framework. The essential reusability of the program code and the generality in the approach have been supported by means of example test cases. The potential future developer can from now on benefit from the established fully coupled-field program implementation, and apply this in the design of further complicated physics modes at will.

A primitive nonlinear solver has been implemented in PolyDE during the work in this thesis. It has proven effective with laminar flow micro-fluidic problems. More complicated nonlinear problems shall require more sophisticated nonlinear techniques. The so far developed code structure allows for the swift implementation of the Newton-Raphson or Arc-length and further methods [125], should a future researcher wish to do so. The potential experimentation with further nonlinear coupled physics modes, could add additional credibility to the general framework approach.

A primitive transient solver was programmed in PolyDE during the course of this thesis. It can perform time-stepping based on the Newmark method [69]. Initial results were obtained with a transient heat transfer physics mode. A general framework for transient physics modes is possible, however it would require a significant amount of planning and coding.

Most of the implemented physics modes lead to the construction of non-symmetric global matrices. The direct solver UMFPACK requires a lot of memory especially when the global matrix is overpopulated with entries. Extensive research on the conditioning of the global matrix in order to help the direct solver reach a higher number of degrees of freedom, is suggested as a future task. That should eventually return a more thorough evaluation of the multi-field adaptive techniques.

6.2. Concluding remarks on multi-field adaptive techniques

Multi-field pure *h*-adaptation has provided typical *h*-adaptation slopes in all tested physics modes and fields. The technique has come out very positive, especially due to the single-mesh approach which greatly reduces computation time compared to multi-mesh correspondence. Minimal fluctuations have been observed in the slopes. A common multi-field mesh is simultaneously effective in the error convergence as well as in the solution process time-consumption.

Multi-field pure *p*-adaptation has produced typical *p*-adaptation slopes, however the technique has been heavy on the system and fluctuations have been observed. The technique has been effective on a wave problem but quite ineffective in laminar flow problems as expected. The implementation of element-wise condensation of inner degrees of freedom can be suggested. Additionally, the multi-field 2-order element conformity condition can be further investigated, in order to perhaps provide more independent order adaptation in each field.

Concerning *hp*-adaptation, three previously designed algorithms, which were meant for wave propagation problems, were utilized as a basis for conducting initial research on multi-field problems. To do so, the programming of modifications on them was essential, in order to make them functional in the general coupled problem framework. The "keypoint" *hp*-adaptive algorithm has performed reasonably well in most physics modes and fields. In some cases it has required a large number of degrees of freedom in order to catch up with pure *h*-adaptation.

The "top5" has been the weakest performing *hp*-adaptive algorithm in the given test cases. It is conservative in that it reduces the polynomial order only by 1 when necessary, and this hinders performance.

The "kp_phaselag" has proven to be the most intelligent of the three *hp*-adaptive algorithms. In some field solutions, it has surpassed pure *h*-adaptation by a large margin. The reason for not performing well in the SAW device problem in particular, was due to the specific problem setup with the PML layers. As a suggestion, the future potential investigator could setup a mechanical wave problem that does not make use of any PML layers and after making observations, take the development of the algorithm further from there. In the actual thesis, it was necessary to prove the physics mode by demonstrating device functionality, therefore the PML was not omitted.

None of the so far developed *hp*-adaptive algorithms has shown maximum performance for all problems and fields simultaneously. It would be very optimistic to expect them to do so. However, since the *h*- and *p*-versions alone behave as expected, it is only a matter of designing an *hp*-algorithm with more sophisticated decision making. The obtained thesis observations together with the general PDE framework establishment, provide a good foundation for further *hp*-algorithm development.

6.3. Final thoughts

This thesis has taken on the challenge of implementing a full range of adaptive techniques on a fully coupled general partial differential equation framework. One question to answer is if it was worth the effort. The answer is yes. Compared to the nonlinear fluidic library development described in [64], the new framework is much more reusable, not just single-directionally coupled, and can be utilized in problem areas beyond fluidic problems. In addition to that, it can interoperate with adaptive techniques, whereas in [64], that was not possible. In comparison to [102], the adaptive algorithms can be used in physics modes beyond electromagnetic wave propagation.

Omitting a sequential field solution process in favor of a direct one, gives an impression of straight-forwardness and is a considerable boost to the idea of modern multi-physics simulation of coupling effects. On the other hand, complexities have developed, since solving for a system of multiple fields simultaneously can ambiguously confuse some of the adaptive algorithms. The results of this work provide a foundation, which can be utilized in the future design of more sophisticated methods, with particular emphasis on *hp*-adaptive techniques.

Before closing the report, it should be mentioned to a potential forthcoming investigator of coupled problems and adaptation, that the approach which was followed in the actual thesis, even though it was worth it and also essential, it raised some difficulties. The suggestion for successive work from this point onward would be to perform programming refinement on adaptive techniques, one physics mode and one algorithm at a time. The followed approach of the simultaneous multitude in physics modes and adaptive algorithms has at many points brought confusion, for example during the collection of numerical results.

Appendix A1

This appendix corresponds to Chapter 4 and serves in presenting additional material which was omitted from the main body of the report. The displayed material is essentially a sequence of figures obtained during the solution process of the surface acoustic wave problem. A short description for each of the figures is provided.

Figure A1-1 and Figure A1-2, are meant to demonstrate the effect of the perfectly matched layer implementation in the problem geometry. They were obtained from [19] and the differences between them and the corresponding solution plots in Chapter 4 are clearly visible.

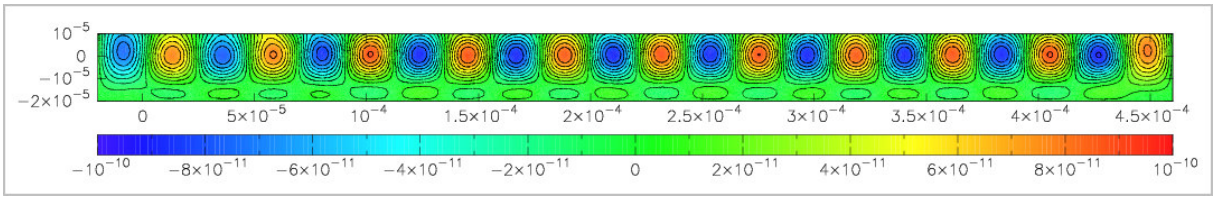

Figure A1-1 Piezoelectric *x*-displacement from [19] where the PML regions were omitted

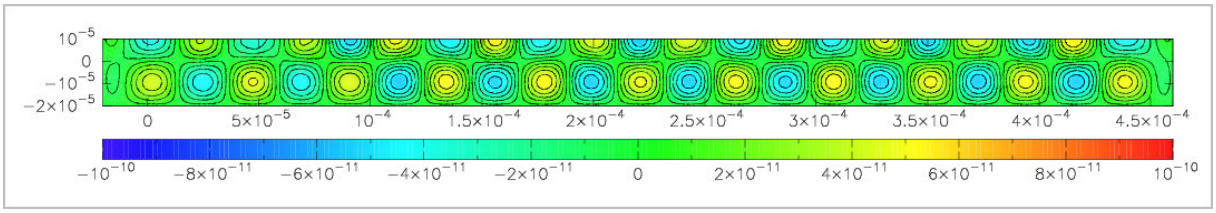

Figure A1-2 Piezoelectric *y*-displacement from [19] where the PML regions were omitted

Figure A1-3 presents the starting coarse mesh of the problem, before the *h*-adaptation process is initiated. Figure A1-4 presents the resulting refined mesh after a sequence of 6 *h*-adaptation steps.

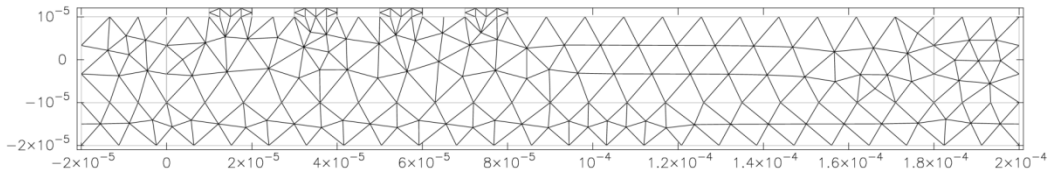

Figure A1-3 Starting coarse mesh for the *h*-adaptation process

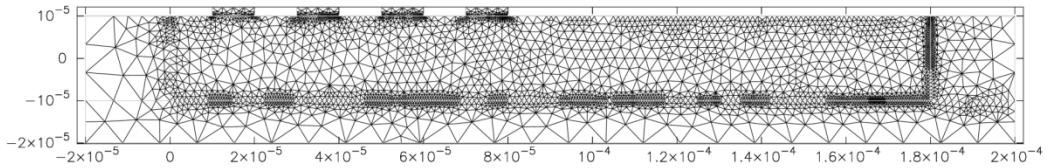

Figure A1-4 Resulting mesh after 6 *h*-adaptation steps

The element order plots starting from Figure A1-5 up to and including Figure A1-8, display the resulting individual element orders after a sequence of 10 *p*-adaptation steps.

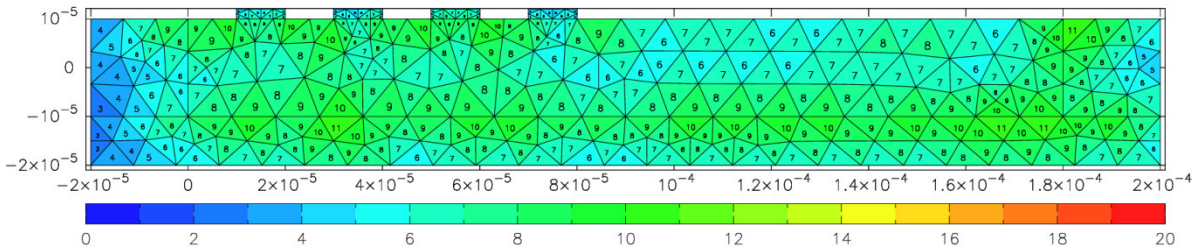

Figure A1-5 Resulting element order for the *x*-displacement field after 10 *p*-adaptation steps using the refinement indicator of (3.7)

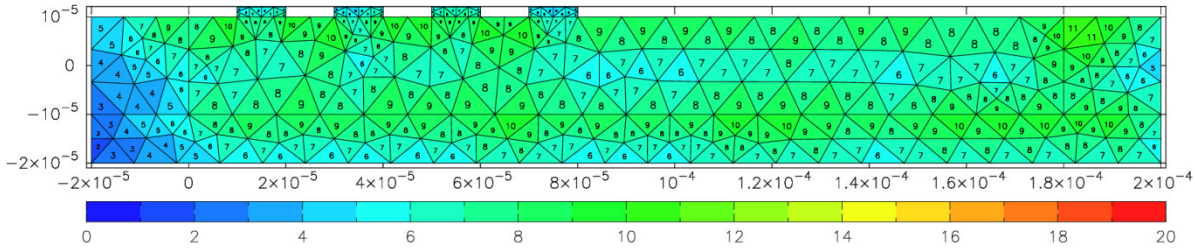

Figure A1-6 Resulting element order for the *y*-displacement field after 10 *p*-adaptation steps using the refinement indicator of (3.7)

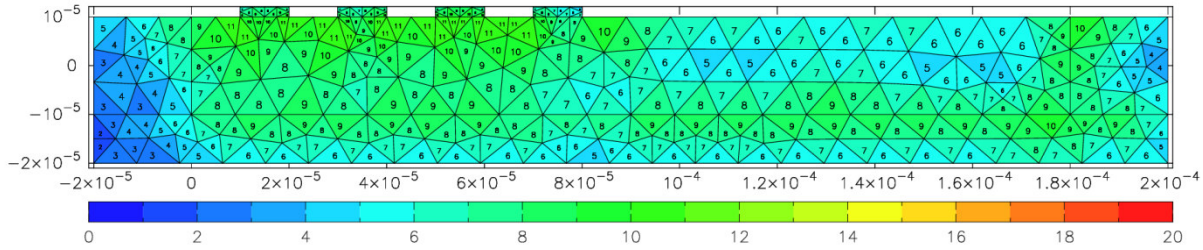

Figure A1-7 Resulting element order for the Electric Potential after 10 *p*-adaptation steps using the refinement indicator of (3.7)

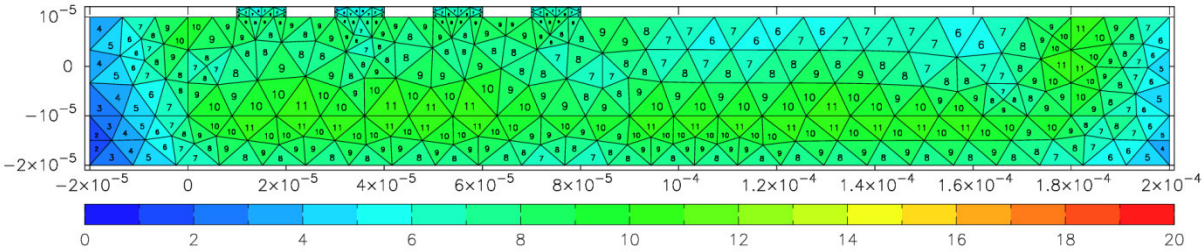

Figure A1-8 Resulting element order for the Temperature after 10 *p*-adaptation steps using the refinement indicator of (3.7)

The remaining plots of the current appendix are concerned with the application of the *hp*-adaptation algorithms. The resulting mesh and element order plots regarding the *x*-displacement field is presented for all *hp*-algorithms in the sequence from Figure A1-9 up to Figure A1-11. To avoid repetition, for the remaining solution fields, only the keypoint algorithm was considered for the plots.

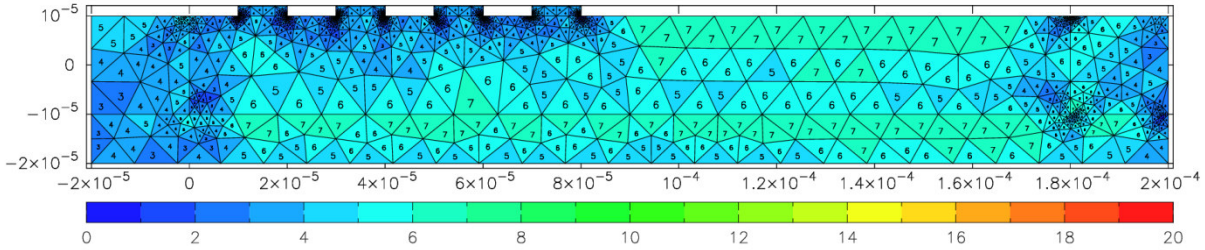

Figure A1-9 Resulting mesh and element order for the *x*-displacement field after 6 *hp*-adaptation steps using the keypoint algorithm

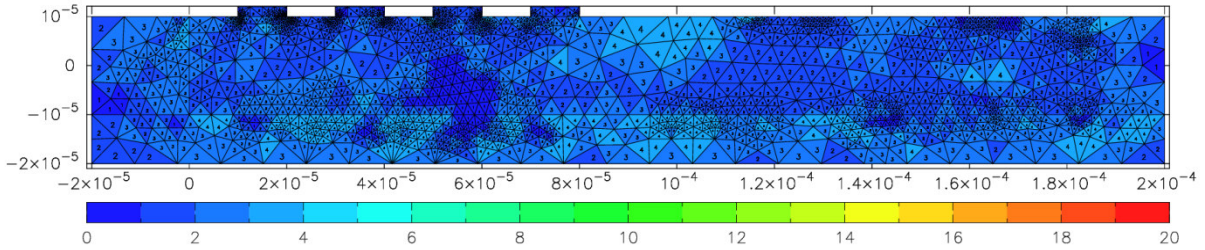

Figure A1-10 Resulting mesh and element order for the *x*-displacement field after 3 *hp*-adaptation steps using the top5 algorithm

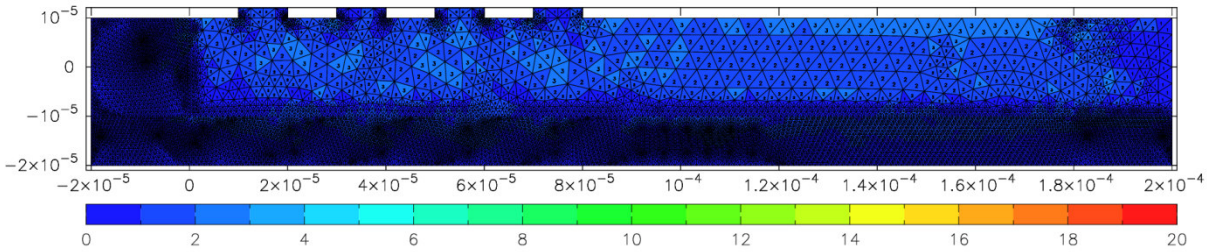

Figure A1-11 Resulting mesh and element order for the *x*-displacement field after 3 *hp*-adaptation steps using the kp_phaselag algorithm

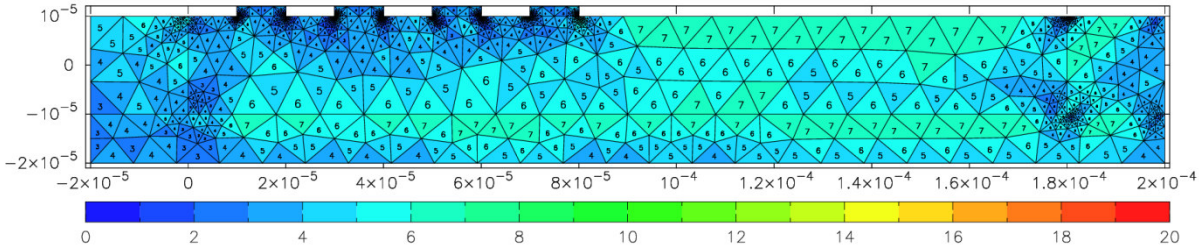

Figure A1-12 Resulting mesh and element order for the *y*-displacement field after 6 *hp*-adaptation steps using the keypoint algorithm

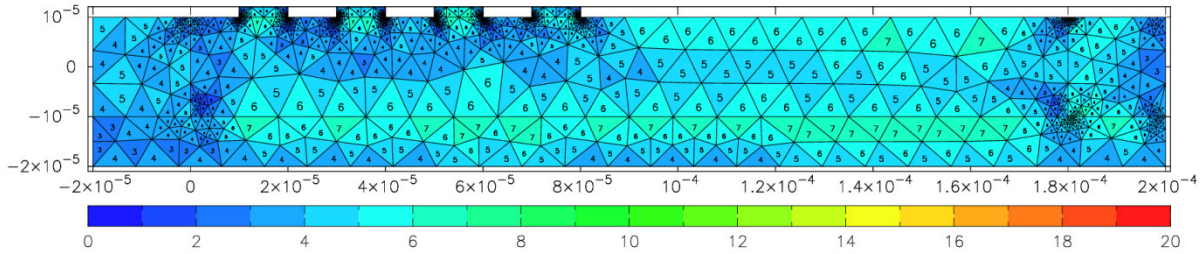

Figure A1-13 Resulting mesh and element order for the Electric Potential field after 6 *hp*-adaptation steps using the keypoint algorithm

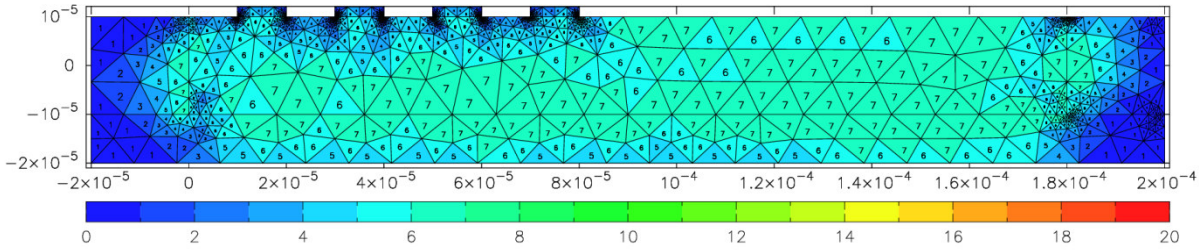

Figure A1-14 Resulting mesh and element order for the Temperature field after 6 *hp*-adaptation steps using the keypoint algorithm

Appendix A2

This appendix displays the plots which were omitted from the main body of the report in Chapter 5. Further discussion is not provided here. It starts with Figure A2-1 where the starting coarse mesh, used in the *h*-adaptation process, for the micro-fluidic channel is presented. The resulting refined mesh after 10 *h*-adaptation steps is presented in Figure A2-2.

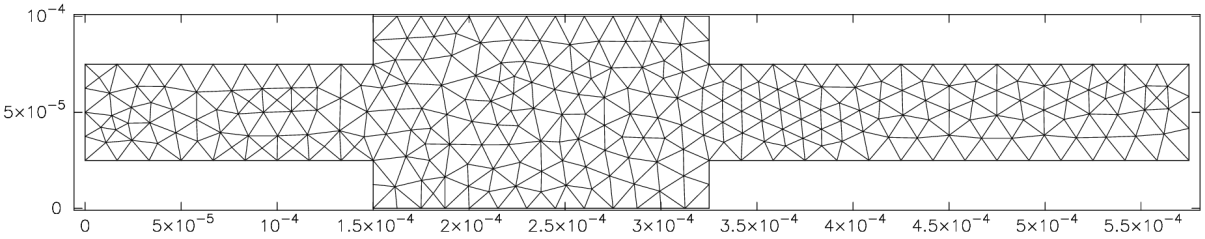

Figure A2-1 Starting coarse mesh for the *h*-adaptation process

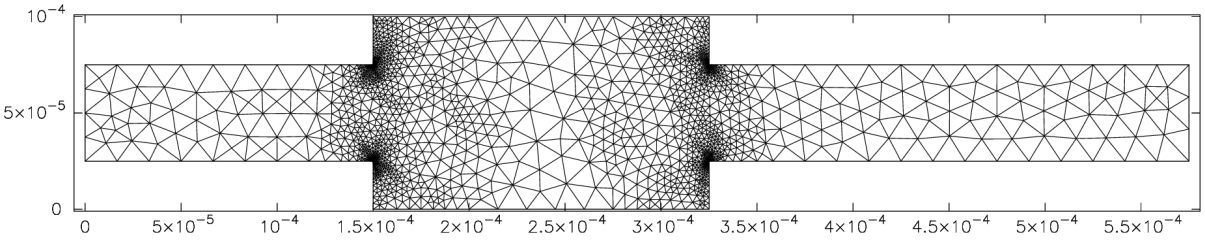

Figure A2-2 Resulting mesh after 10 *h*-adaptation steps

In the plots starting from Figure A2-3 and up to Figure A2-5, the resulting element orders after 8 *p*-adaptation steps, are presented. The corresponding field types are given in the figure descriptions.

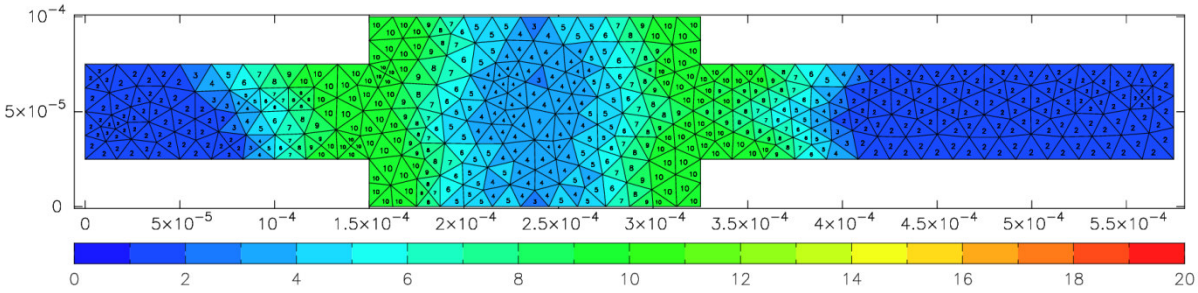

Figure A2-3 Resulting element orders for the *x*-velocity field after 8 *p*-adaptation steps

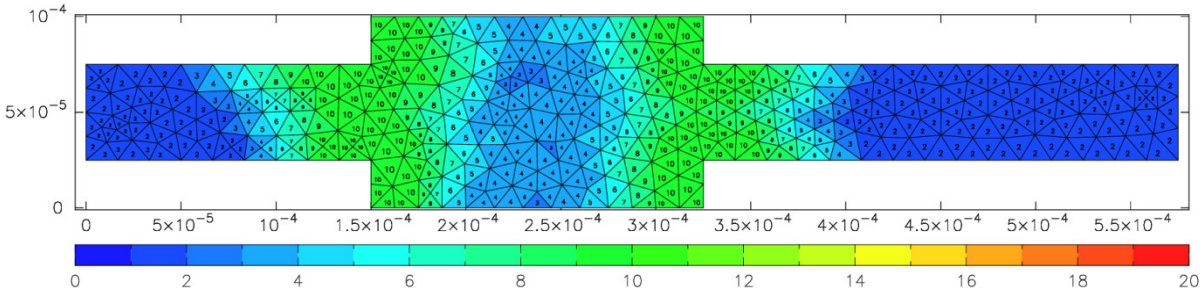

Figure A2-4 Resulting element orders for the *y*-velocity field after 8 *p*-adaptation steps

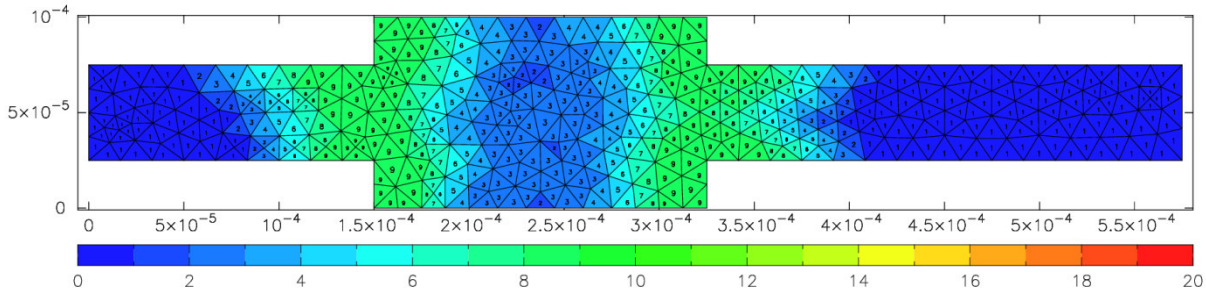

Figure A2-5 Resulting element orders for the pressure field after 8 *p*-adaptation steps

The plots starting from Figure A2-6, up to and including Figure A2-14, are concerned with the *hp*-adaptation process. The corresponding field types and *hp*-algorithms are given in the captions.

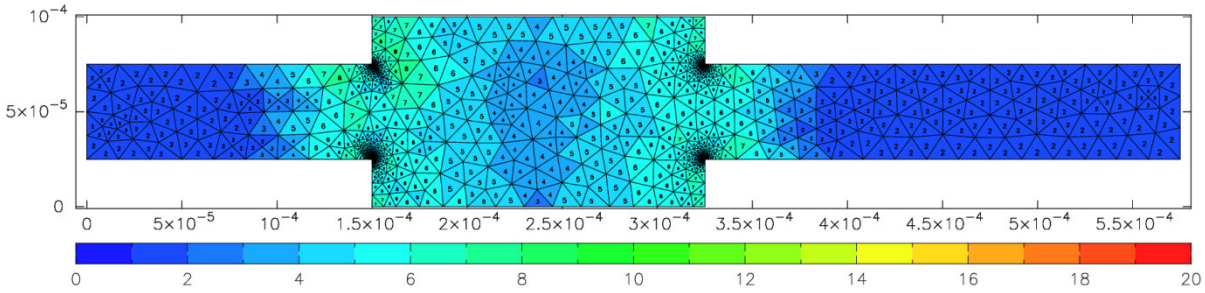

Figure A2-6 Resulting element orders and mesh for the *x*-velocity field after 6 *hp*-adaptation steps with the keypoint algorithm

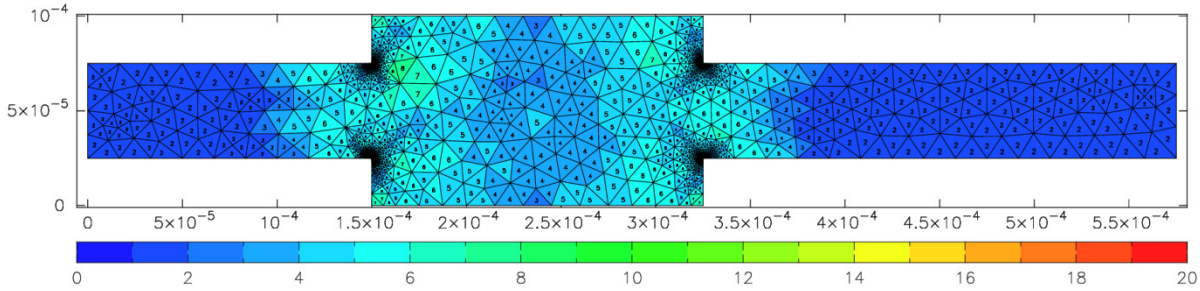

Figure A2-7 Resulting element orders and mesh for the *x*-velocity field after 6 *hp*-adaptation steps with the top5 algorithm

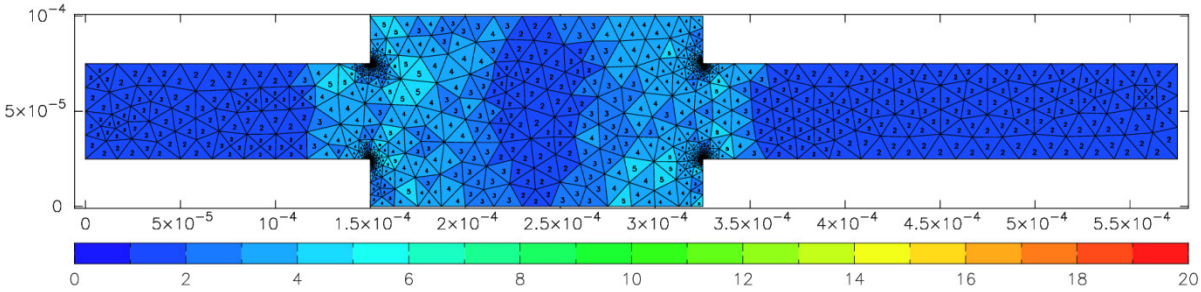

Figure A2-8 Resulting element orders and mesh for the *x*-velocity field after 8 *hp*-adaptation steps with the kp_phaselag algorithm

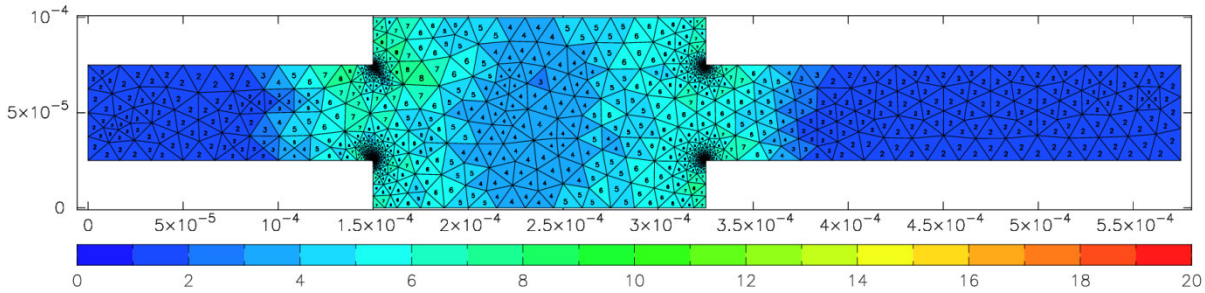

Figure A2-9 Resulting element orders and mesh for the *y*-velocity field after 6 *hp*-adaptation steps with the keypoint algorithm

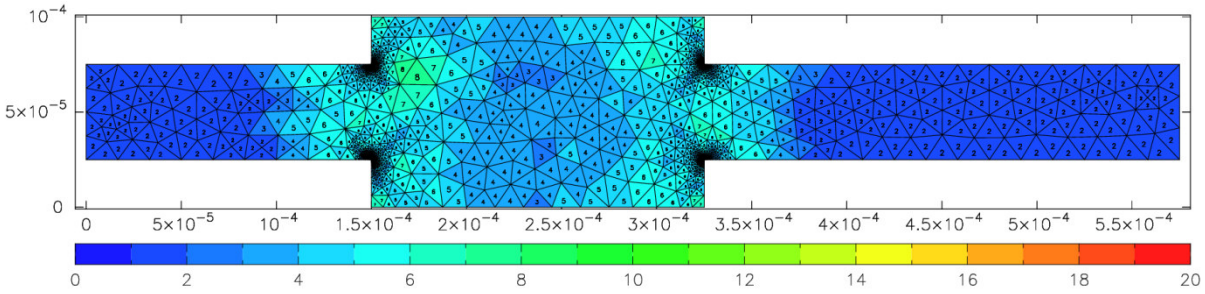

Figure A2-10 Resulting element orders and mesh for the *y*-velocity field after 6 *hp*-adaptation steps with the top5 algorithm

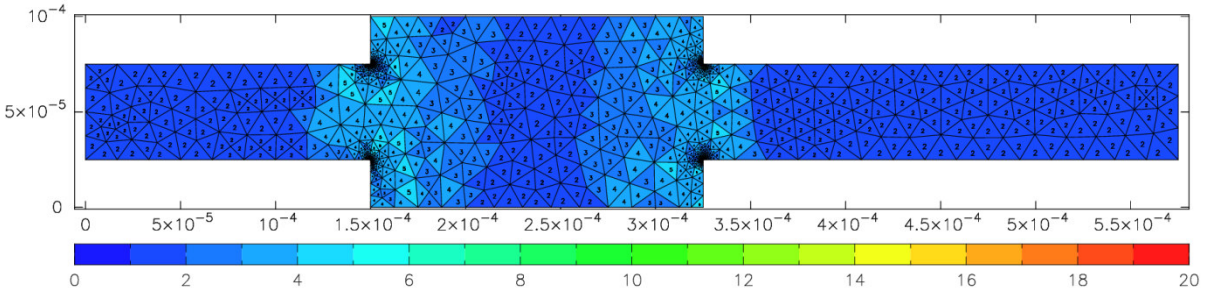

Figure A2-11 Resulting element orders and mesh for the *y*-velocity field after 8 *hp*-adaptation steps with the kp_phaselag algorithm

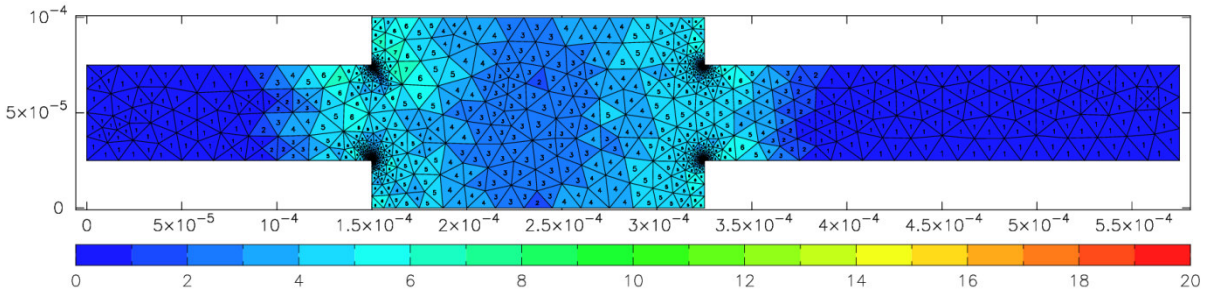

Figure A2-12 Resulting element orders and mesh for the pressure field after 6 *hp*-adaptation steps with the keypoint algorithm

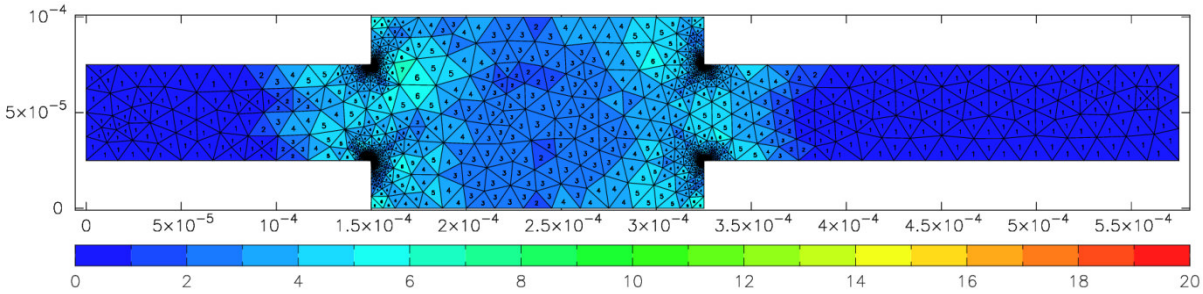

Figure A2-13 Resulting element orders and mesh for the pressure field after 6 *hp*-adaptation steps with the top5 algorithm

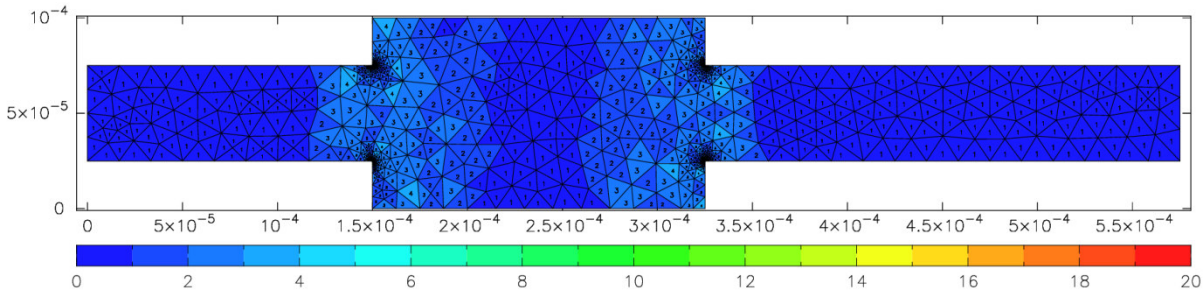

Figure A2-14 Resulting element orders and mesh for the pressure field after 8 *hp*-adaptation steps with the kp_phaselag algorithm

A similar display routine is followed for the micro-flow electric regulator problem. The starting and resulting meshes after a certain number of *h*-adaptation steps, are displayed in Figure A2-15 and Figure A2-16 respectively.

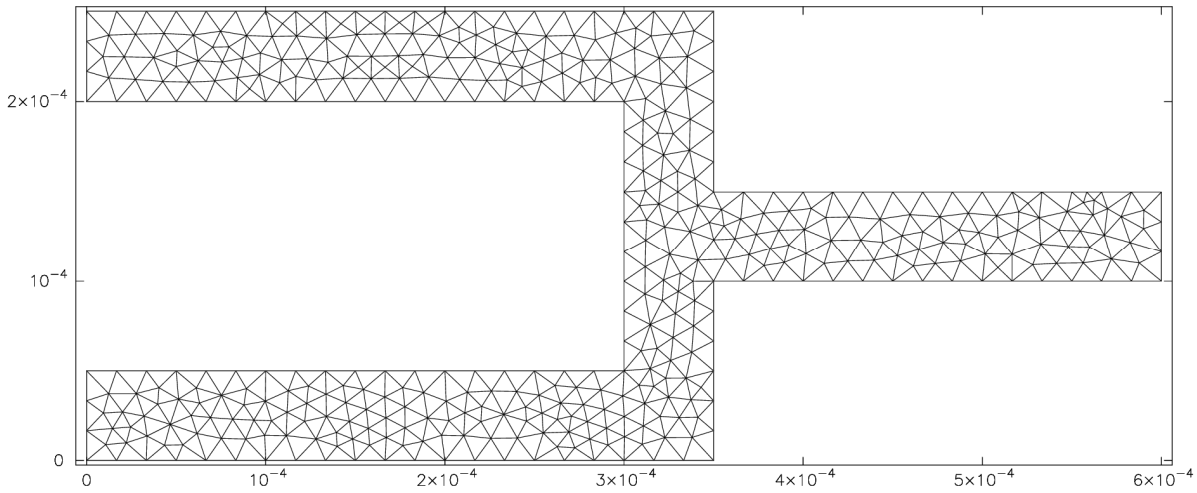

Figure A2-15 Starting coarse mesh for the *h*-adaptation process

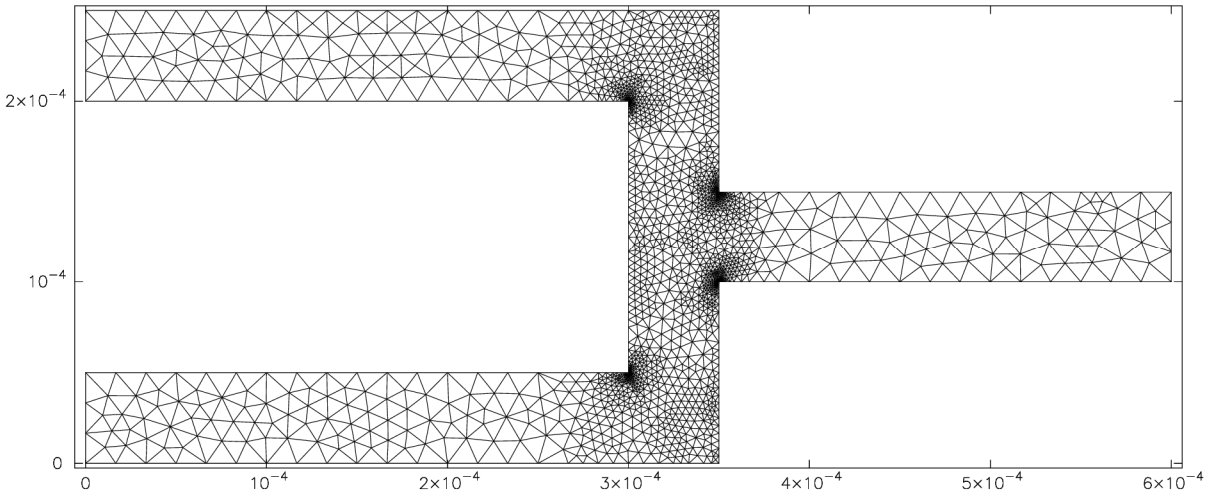

Figure A2-16 Resulting mesh after 8 *h*-adaptation steps

From Figure A2-17 up to Figure A2-19, the *p*-adaptation related plots are presented.

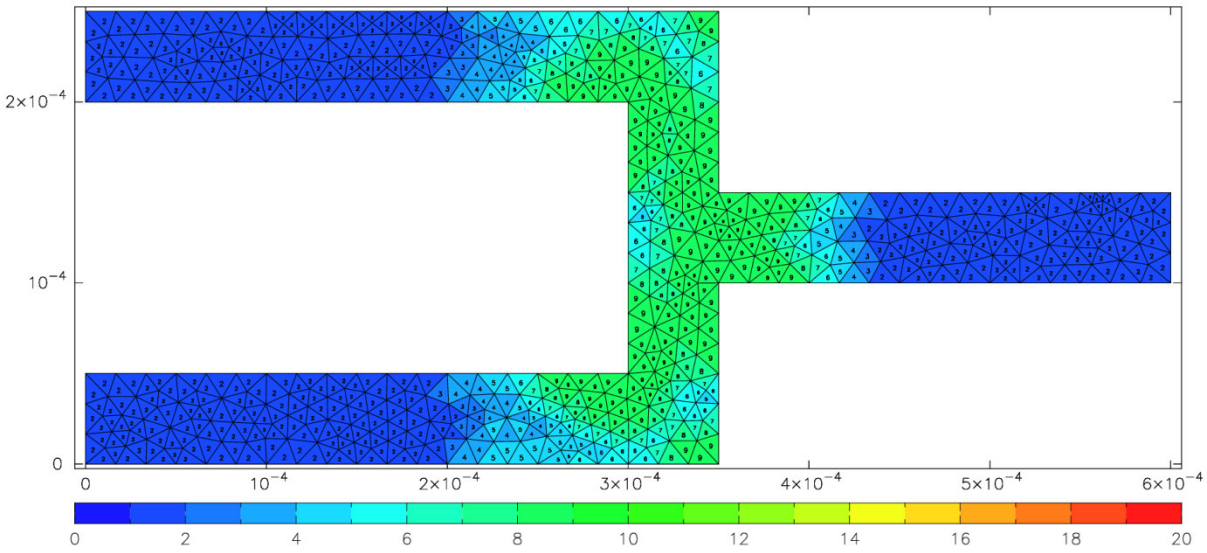

Figure A2-17 Resulting element orders for the *x*-velocity field after 7 *p*-adaptation steps

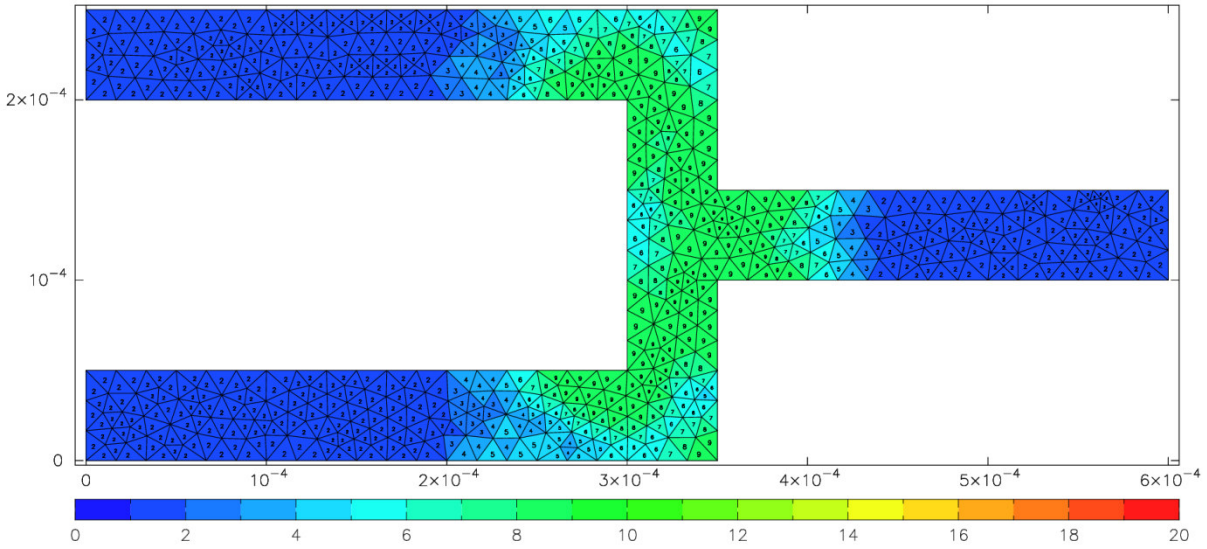

Figure A2-18 Resulting element orders for the *y*-velocity field after 7 *p*-adaptation steps

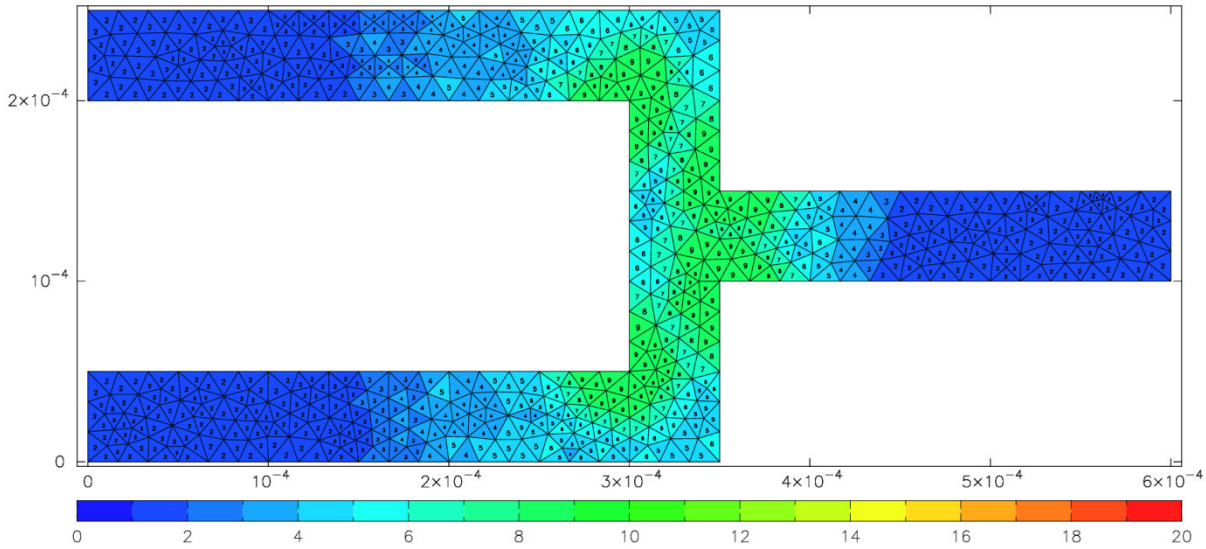

Figure A2-19 Resulting element orders for the Electric Potential field after 7 *p*-adaptation steps

Finally, the *hp*-adaptation related plots are presented in the following figures. Details are provided in the captions.

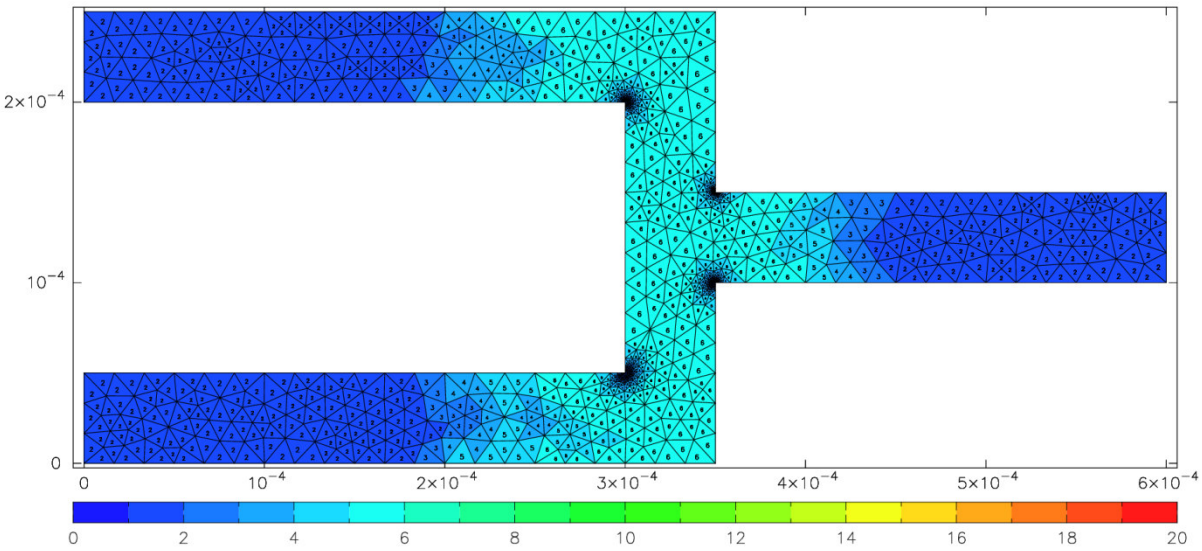

Figure A2-20 Resulting element orders and mesh for the *x*-velocity field after 4 *hp*-adaptation steps with the keypoint algorithm

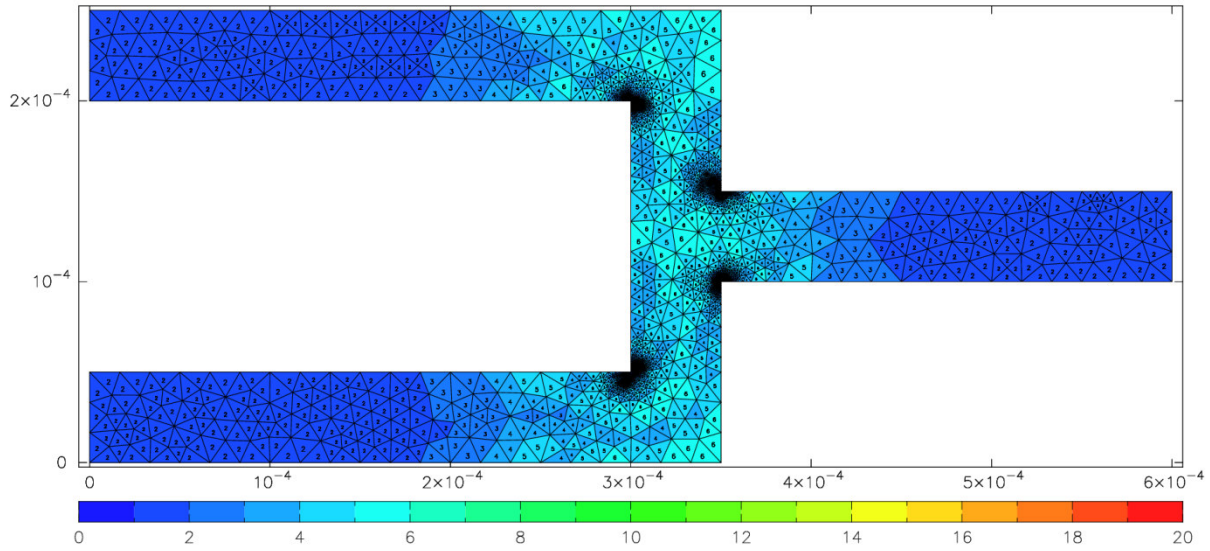

Figure A2-21 Resulting element orders and mesh for the *x*-velocity field after 4 *hp*-adaptation steps with the top5 algorithm

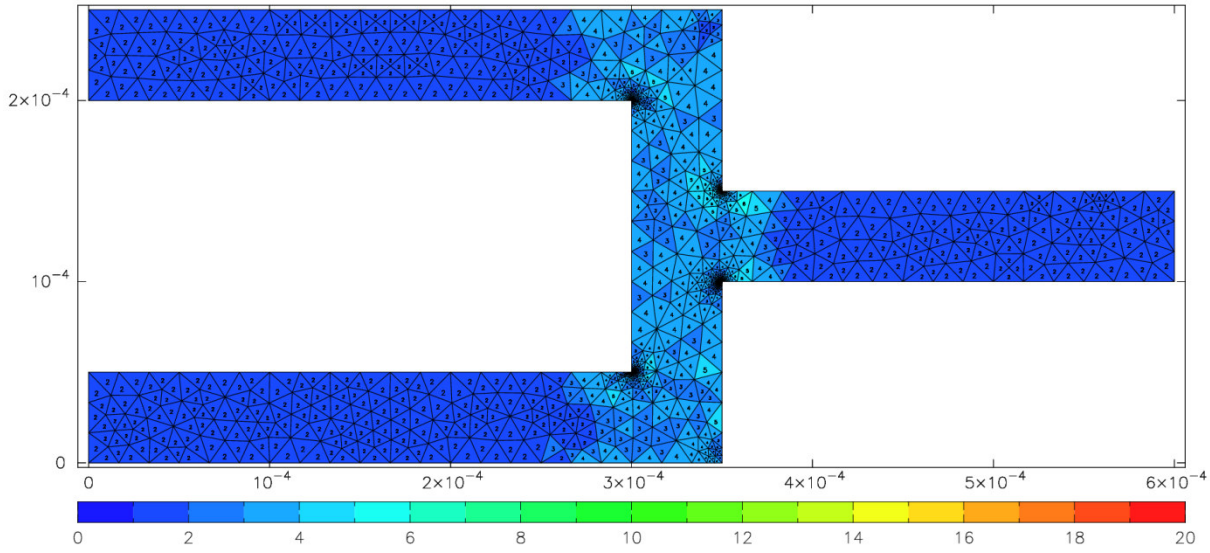

Figure A2-22 Resulting element orders and mesh for the *x*-velocity field after 8 *hp*-adaptation steps with the kp_phaselag algorithm

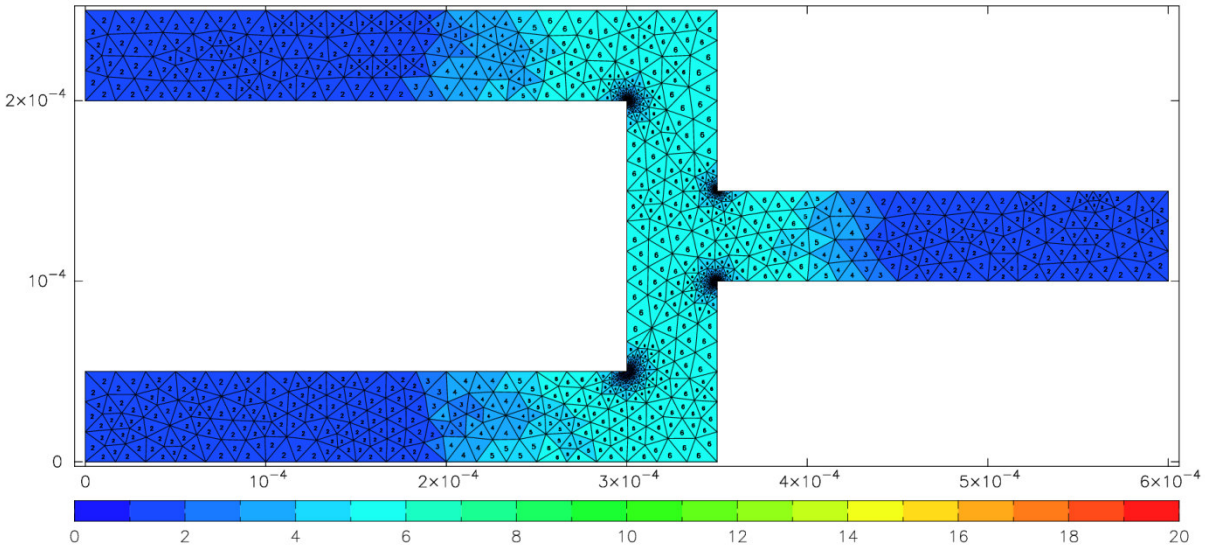

Figure A2-23 Resulting element orders and mesh for the *y*-velocity field after 4 *hp*-adaptation steps with the keypoint algorithm

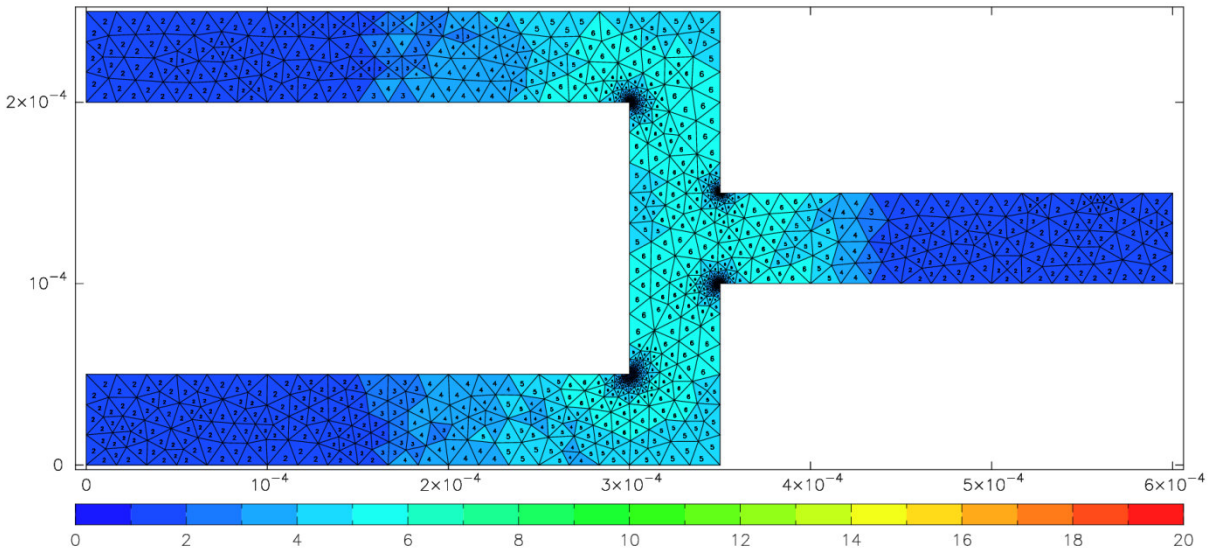

Figure A2-24 Resulting element orders and mesh for the Electric Potential field after 4 *hp*-adaptation steps with the keypoint algorithm

Bibliography

[1] ADINA R & D, Inc.. *Multiphysics - ADINA*. available at: http://www.adina.com/multiphysics.shtml. (accessed 1 December 2015).

[2] M. Ainsworth and J.T. Oden. *A posteriori error estimation in finite element analysis*. John Wiley & Sons, New York, 2000.

[3] P. Alonso and J.A. Garrido García. BEM applied to 2D thermoelastic contact problems including conduction and forced convection in interstitial zones. *Engineering Analysis with Boundary Elements*, Vol. 15, Issue 3, pp. 249–259, 1995.

[4] ANSYS, Inc.. *ANSYS - Simulation Driven Product Development*. available at: http://www.ansys.com/. (accessed 30 November 2015).

[5] ANSYS, Inc.. *ANSYS Multiphysics Solutions*. available at: http://www.ansys.com/Products/Simulation+Technology/Multiphysics. (accessed 1 December 2015).

[6] J.H. Argyris and S. Kelsey. *Energy Theorems and Structural Analysis*. Butterworths, London, 1960.

[7] D.N. Arnold, F. Brezzi, and M. Fortin. A Stable Finite Element for the Stokes Equations. *Estratto da Calcolo*, Vol. XXI, fasc. IV, pp. 337-344, 1984.

[8] Autodesk. *AutoCAD Products*. available at: http://usa.autodesk.com/adsk/servlet/pc/index?id=15409188&siteID=123112. (accessed 25 November 2011).

[9] I. Babuška and B.Q. Guo. The h, p and h-p version of the finite element method: basis theory and applications. *Advances in Engineering Software*, Vol. 15, Issue 3–4, pp. 159–174, 1992.

[10] I. Babuška and T. Strouboulis. *The Finite Element Method and its Reliability*. Oxford University Press, New York, 2001.

[11] R.T. Balmer. *Modern Engineering Thermodynamics*. Academic Press, Burlington, MA, 2011.

[12] R.E. Bank and A. Weiser. Some a posteriori error estimators for elliptic partial differential equations. *Math. Computation*, Vol. 44, pp. 283–301, 1985.

[13] G.K. Batchelor. *An Introduction to Fluid Dynamics*. Cambridge University Press, Cambridge, 1967.

[14] K.J. Bathe and H. Zhang. A mesh adaptivity procedure for CFD and fluid-structure interactions. *Computers and Structures*, Vol. 87, pp. 604–617, 2009.

[15] A. Benjeddou. Advances in Piezoelectric Finite Element Modeling of Adaptive Structural Elements: a Survey. *Computers and Structures*, Vol. 76, pp. 347–363, 2000.

[16] C. Bernardi and R. Verfürth. Adaptive finite element methods for elliptic equations with non-smooth coefficients. *Numerische Mathematik*, Vol. 85, pp. 579–608, 2000.

[17] M.A. Biot. Thermoelasticity and Irreversible Thermodynamics. *Journal of Applied Physics*, Vol. 27, Number 3, March 1956.

[18] S. Brenner and R. Scott. *The Mathematical Theory of Finite Element Methods*. Springer, New York, 2008.

[19] G. Brondani Torri. *Assembly and Residual Parallel Implementation for Adaptive High Order FEM with OpenMP*. Thesis (Master) Hamburg University of Technology. 2010.

[20] J. Burkardt. *Source Codes in Fortran90*. available at: http://people.sc.fsu.edu/~jburkardt/f_src/f_src.html. (accessed 23 November 2011).

[21] R.C. Chen and J.L. Liu. An iterative method for adaptive finite element solutions of an energy transport model of semiconductor devices. *Journal of Computational Physics*, Vol. 189 , No. 2 , pp. 579–606, 2003.

[22] A. Chorin and J.E. Marsden. *A Mathematical Introduction to Fluid Mechanics*. Springer-Verlag, April 2000.

[23] R.W. Clough. Areas of Application of the Finite Element Method. *Computers and Structures*, Vol. 4, pp. 17–40, 1974.

[24] COMSOL Inc.. *COMSOL Multiphysics Reference Manual*. available at: https://doc.comsol.com/5.4/doc/com.comsol.help.comsol/COMSOL_ReferenceManual.pdf. (accessed 24 September 2019).

[25] COMSOL Inc.. *Multiphysics Simulation Software - Platform for Physics-Based Modeling*. available at: https://www.comsol.eu/comsol-multiphysics. (accessed 30 November 2015).

[26] COMSOL Inc.. *What Is Multiphysics? - COMSOL*. available at: http://www.comsol.com/multiphysics. (accessed 1 December 2015).

[27] R. Courant. Variational methods for the solution of problems of equilibrium and vibration. *Bull. Am. Math Soc.*, 49:1–61, 1943.

[28] M. Cross, T.N. Croft, A.K. Slone, A.J. Williams, N. Christakis, M.K. Patel, C. Bailey, and K. Pericleous. Computational Modelling of Multi-Physics and Multi-Scale Processes in Parallel. *International Journal for Computational Methods in Engineering Science and Mechanics,* Vol. 8, No. 2, pp. 63–74, 2007.

[29] CSC - IT CENTER FOR SCIENCE LTD. *Elmer*. available at: https://www.csc.fi/web/elmer. (accessed 30 November 2015).

[30] J. Curie and P. Curie. Développement par compression de l'électricité polaire dans les cristaux hémièdres à faces inclinées. *Bulletin de la Société minérologique de France*, Vol. 3, pp. 90–93, 1880.

[31] Cygnus Solutions, Red Hat. *Cygwin*. available at: http://www.cygwin.com/. (accessed 25 November 2011).

[32] G. Dahlquist and Å. Björck. *Numerical Methods in Scientific Computing, Volume I*. Society for Industrial and Applied Mathematics, 2008.

[33] Dassault Systèmes. *Abaqus Multiphysics*. available at: http://www.3ds.com/products-services/simulia/products/abaqus/multiphysics/. (accessed 1 December 2015).

[34] T. Davis and I. Duff. *UMFPACK Version 2.2*. available at: http://www.netlib.no/netlib/linalg/. (accessed 24 November 2011).

[35] T. Davis. *UMFPACK 5.5*. available at: http://www.cise.ufl.edu/research/sparse/umfpack/. (accessed 15 November 2011).

[36] T. Davis. *suitesparse : a suite of sparse matrix software*. available at: http://faculty.cse.tamu.edu/davis/suitesparse.html. (accessed 11 December 2015).

[37] I. Demirdžić and S. Muzaferija. Numerical method for coupled fluid flow, heat transfer and stress analysis using unstructured moving meshes with cells of arbitrary topology. *Computer Methods in Applied Mechanics and Engineering*, Vol. 125, Issues 1–4, pp. 235–255, 1995.

[38] L. Demkowicz, W. Rachowicz, and Ph. Devloo. A Fully Automatic *hp*-Adaptivity. *Journal of Scientific Computing*, Vol. 17, Nos. 1–4, pp. 117–142, 2002.

[39] J. Donea, S. Giuliani, and J.P. Halleux. An Arbitrary Lagrangian-Eulerian Finite Element Method for Transient Dynamic Fluid-Structure Interactions. *Computer Methods in Applied Mechanics and Engineering*, Vol. 33, pp. 689-723, 1982.

[40] J.J. Dongarra, J. Ducroz, S. Hammarling, and R.J. Hanson. An Extended Set of Fortran Basic Linear Algebra Subprograms. *ACM Transactions on Mathematical Software*, Vol. 14, Issue 1, pp. 1–17, 1988.

[41] J. Driesen, R. Belmans, and K. Hameyer. Computation algorithms for efficient coupled electromagnetic-thermal device simulation. *IEE Proceedings-Science, Measurement and Technology*, Vol. 149, pp. 67–72, 2002.

[42] R. Drouot, F. Sidoroff, and G.A. Maugin. *Continuum Thermomechanics The Art and Science of Modeling Material Behaviour*. Kluwer Academic Publishers, New York, 2002.

[43] L. Dubcova. *hp-FEM for Coupled Problems in Fluid Dynamics*. Thesis (PhD) Charles University in Prague. Prague, 2010.

[44] Encyclopædia Britannica, Inc.. *field | physics*. available at: http://www.britannica.com/science/field-physics. (accessed 1 December 2015).

[45] ETH Zürich. *Numerical C++ Library Concepts*. . available at: http://wiki.math.ethz.ch/Concepts/. (accessed 24 September 2019).

[46] R. Freund and N. Nachtigal. *QMRPACK*. available at: http://www.cs.ucdavis.edu/~bai/ET/lanczos_methods/overview_QMRPACK.html. (accessed 24 November 2011).

[47] T.P. Fries and T. Belytschko. The Extended/Generalized Finite Element Method: An Overview of the Method and its Applications. *International Journal for Numerical Methods in Engineering*, Vol. 84, No. 3, pp. 253-304, 2010.

[48] B.G. Galerkin. Series solution of some problems in elastic equilibrium of rods and plates. *Vestn. Inzh. Tech.*, 19:897–908, 1915.

[49] N.I.M. Gould, Y. Hu, and J.A. Scott. *A numerical evaluation of sparse direct solvers, for the solution of large sparse, symmetric linear systems of equations*. Council for the Central Laboratory of the Research Councils. available at: ftp://ftp.numerical.rl.ac.uk/pub/reports/ghsRAL200505.pdf. (accessed 29 November 2011).

[50] C. Goupil. *Continuum Theory and Modeling of Thermoelectric Elements*. Wiley-VCH, Weinheim, 2016.

[51] D.J. Griffiths. *Introduction to Electrodynamics*. Prentice Hall, New Jersey, 1999.

[52] B. Gustafsson. *High Order Difference Methods for Time Dependent PDE*. Springer-Verlag, Berlin Heidelberg, 2008.

[53] M.A. Hamdi, Y. Ousset, and G. Verchery. A Displacement Method for the Analysis of Vibrations of Coupled Fluid-Structure Systems. *Int. Journal for Numerical Methods in Engineering*, Vol. 13, pp. 139-150, 1978.

[54] K. Hameyer, J. Driesen, H. De Gersem, and R. Belmans. The Classification of Coupled Field Problems. *IEEE Transactions on Magnetics*, Vol. 35, No. 3, pp. 1618–1621, May 1999.

[55] Hermes - hp-FEM Group. *Hermes hp-FEM & hp-DG Library*. available at: http://www.hpfem.org/hermes/. (accessed 24 September 2019).

[56] A. Hrennikoff. Solution of problems in elasticity by the framework method. *J. Appl. Mech., ASME*, A8:169–175, 1941.

[57] D.V. Hutton. *Fundamentals of Finite Element Analysis*. McGraw-Hill, New York, 2004.

[58] F. Ihlenburg. *Finite Element Analysis of Acoustic Scattering*. Springer-Verlag, New York, 1998.

[59] F. Ihlenburg and I. Babuška. *Dispersion Analysis and Error Estimation of Galerkin Finite Element Methods for the Numerical Computation of Waves*. Institute for Physical Science and Technology, U.M., Maryland, 1994.

[60] Institut für Mikrosystemtechnik. *MST > Startseite*. available at: https://www.tuhh.de/mst/startseite.html. (accessed 11 December 2015).

[61] Intel® Software Network. *Getting Started with the Intel(R) Visual Fortran Compiler Professional Edition 11.1 for Windows* OS*. available at: http://software.intel.com/sites/products/documentation/hpc/compilerpro/en-us/fortran/win/start/getting_started_f.pdf. (accessed 23 November 2011).

[62] B. Joe. *GEOMPACK and Mesh Generation Research*. available at: http://members.shaw.ca/bjoe/. (accessed 24 November 2011).

[63] G. Karniadakis and A. Beskok. *Microflows Fundamentals and Simulation*. Springer, New York, 2002.

[64] B. Kasemset. *FEM Simulation of Coupled Problems in Microsystems Technology*. Thesis (Dr.-Ing.) Hamburg University of Technology. Verlag Dr. Hut, München, 2009.

[65] M. Kasper. *Mikrosystementwurf*. Springer-Verlag, Berlin, 2000.

[66] M. Kasper, M.R.A. Rahman, and C. Vokas. *Finite Element Package PolyDE*. available at: http://sourceforge.net/projects/polyde-fem/. (accessed 15 November 2011).

[67] S.W. Key. A Variational Principle for Incompressible and Nearly-Incompressible Anisotropic Elasticity. *Int. J. Solids Structures*, Vol. 5, pp. 951-964, 1969.

[68] Kitware. *CMake*. available at: https://cmake.org/. (accessed 11 December 2015).

[69] X.D. Li, L.F. Zeng, and N.E. Wiberg. A Simple Local Error Estimator and an Adaptive Time-stepping Procedure for Direct Integration Method in Dynamic Analysis. *Communications in Numerical Methods in Engineering*, Vol. 9, pp. 273–292, 2003.

[70] J.H. Lienhard IV and J.H. Lienhard V. *A Heat Transfer Textbook*. J.H. Lienhard V, Cambridge, Massachusetts, 2000.

[71] Linear Technology. *Linear Technology - Design Simulation and Device Models*. available at: http://www.linear.com/designtools/software/. (accessed 30 November 2015).

[72] T. Liszka, W. Tworzydlo, J. Bass, S. Sharma, T. Westermann, and B. Yavari. ProPHLEX—An hp-adaptive finite element kernel for solving coupled systems of partial differential equations in computational mechanics. *Computer Methods in Applied Mechanics and Engineering*, Vol. 150, No. 4, pp. 251–271, 1997.

[73] J. Mackerle. Error estimates and adaptive finite element methods: A bibliography (1990-2000). *Engineering Computations: Int J for Computer-Aided Engineering*, Vol. 18, Nos. 5–6, pp. 802–914, 2001.

[74] E. Markert, M. Schlegel, M. Dienel, G. Herrmann, and D. Müller. Modeling of a new acceleration sensor as part of a 2D sensor array in VHDL-AMS. *Technical Proceedings of the 2005 NSTI Nanotechnology Conference and Trade Show*, Vol. 3, pp. 399–402, 2005.

[75] J. H. Masliyah and S. Bhattacharjee. *Electrokinetic and Colloid Transport Phenomena*. John Wiley & Sons, New Jersey, 2006.

[76] J. C. Maxwell. *A Treatise on Electricity and Magnetism*. At the Clarendon Press, Oxford, 1873.

[77] M. Mayer, S. Zaglmayr, K. Wagner, and J. Schöberl. Perfectly Matched Layer Finite Element Simulation of Parasitic Acoustic Wave Radiation in Microacoustic Devices. *IEEE Ultrasonics Symposium*, New York, 2007.

[78] S. Mcgee and P. Seshaiyer. Finite difference methods for coupled flow interaction transport models. *Electronic Journal of Differential Equations (EJDE)*, pp. 171–184, 2009.

[79] J.M. Melenk and B.I. Wohlmuth. On residual-based a posteriori error estimation in hp-FEM. *Advances in Computational Mathematics*, Vol. 15, pp. 311–331, 2001.

[80] C. Michler, L. Demkowicz, J. Kurtz, and D. Pardo. Improving the performance of Perfectly Matched Layers by means of *hp*-adaptivity. *Numerical Methods for Partial Differential Equations*, Vol. 23, No. 4, pp. 832–858, 2007.

[81] J.G. Michopoulos, C. Farhat, and J. Fish. Survey on Modeling and Simulation of Multiphysics Systems. *Journal of Computing and Information Science in Engineering*, Vol. 5, No. 3, Sept. 2005.

[82] Microsoft Corporation. *Visual Studio 2008 Editions | Microsoft Visual Studio*. available at: http://www.microsoft.com/visualstudio/en-us/products/2008-editions. (accessed 23 November 2011).

[83] R.Z. Moreno and O.V. Trevisan. Finite Differences Solution For Coupled Phenomena in Porous Media. *Computational Methods in Engineering'99*, pp. 171.1–171.20, 1999.

[84] MSC Software Corporation. *MSC Nastran - Multidisciplinary Structural Analysis*. available at: http://www.mscsoftware.com/product/msc-nastran. (accessed 30 November 2015).

[85] N. Neimarlija, I. Demirdžić, and S. Muzaferija. Finite volume method for calculation of electrostatic fields in electrostatic precipitators. *Journal of Electrostatics*, Vol. 67, Issue 1, pp. 37–47, 2009.

[86] T.V. Nguyen and R.E. White. A finite difference procedure for solving coupled, nonlinear elliptic partial differential equations. *Computers & Chemical Engineering*, Vol. 11, Issue 5, pp. 543–546, 1987.

[87] J.T. Oden. A General Theory of Finite Elements II. Applications. *International Journal of Numerical Methods in Engineering*, Vol. 1, pp. 247-259, 1969.

[88] J.T. Oden and B.E. Kelley. Finite Element Formulation of General Electrothermoelasticity Problems. *International Journal for Numerical Methods in Engineering*, Vol. 3, pp. 161-179, 1971.

[89] J.T. Oden, S. Prudhomme, and L. Demkowicz. A Posteriori Error Estimation for Acoustic Wave Propagation Problems. *Archives of Computational Methods in Engineering*, Vol. 12, No. 4, pp. 343–389, 2005.

[90] J.T. Oden and L.C. Wellford. Analysis of Flow of Viscous Fluids by the Finite-Element Method. *AIAA Journal*, Vol. 10, No. 12, pp. 1590-1599, 1972.

[91] L. Onsager. Reciprocal Relations in Irreversible Processes. I. *Physical Review*, Vol. 37, pp. 405-426, 1931.

[92] OpenMP Architecture Review Board. *The OpenMP® API specification for parallel programming*. available at: http://openmp.org/wp/. (accessed 14 December 2015).

[93] E. Pan. A BEM analysis of fracture mechanics in 2D anisotropic piezoelectric solids. *Engineering Analysis with Boundary Elements*, Vol. 23, pp. 67–76, 1999.

[94] M. Paszynski and L. Demkowicz. Parallel, Fully Automatic *hp*-adaptive 3D Finite Element Package. *Engineering with Computers*, Vol. 22, Issue 3-4, pp. 255–276, 2006.

[95] T. Pearson. *PGPLOT Graphics Subroutine Library*. available at: http://www.astro.caltech.edu/~tjp/pgplot/. (accessed 24 November 2011).

[96] J.C.A. Peltier. Nouvelles expériences sur la caloricité des courants électrique. *Annales de Chimie et de Physique*, 56 : 371–386, 1834.

[97] M. Petzoldt. A posteriori error estimators for elliptic equations with discontinuous coefficients. *Advances in Computational Mathematics*, Vol. 16, pp. 47–75, 2002.

[98] M.R.A. Rahman. *High Order Finite Elements for Microsystems Simulation*. Thesis (Dr.-Ing.) Hamburg University of Technology. Cuvillier Verlag, Göttingen, 2008.

[99] N.N. Rogacheva. *The Theory of Piezoelectric Shells and Plates*. CRC Press, Florida, 1994.

[100] Y. Saad. *SPARSKIT A basic tool-kit for sparse matrix computations*. available at: http://www-users.cs.umn.edu/~saad/software/SPARSKIT/index.html. (accessed 23 November 2011).

[101] E.J. Sapountzakis and G.C. Tsiatas. Flexural-torsional Vibrations of Beams by BEM. *Computational Mechanics*, Vol. 39, Issue 4, pp. 409–417, 2007.

[102] M. Schober. *Fehleradaptive Finite-Elemente-Simulation abstimmbarer, integriert optischer Komponenten*. Thesis (Dr.-Ing.) Hamburg University of Technology. Verlag Dr. Hut, München, 2010.

[103] M. Schober and M. Kasper. Comparison of hp-adaptive methods in finite element electromagnetic wave propagation. *COMPEL - The international journal for computation and mathematics in electrical and electronic engineering*, Vol. 26 Issue 2, pp. 431–446, 2007.

[104] T.J. Seebeck. Magnetische Polarisation der Metalle und Erze durch Temperatur-Differenz. *Abhandlungen der Königlichen Akademie der Wissenschaften zu Berlin*, pp. 265–373, 1825.

[105] A.F. Seybert, T.W. Wu, and W.L. Li. A Coupled FEM/BEM for Fluid-Structure Interaction Using Ritz Vectors and Eigenvectors. *Journal of Vibration and Acoustics*, Vol. 115, Issue 2, pp. 152–158, 1993.

[106] A.J. Smits. *A Physical Introduction to Fluid Mechanics*. John Wiley & Sons, New York, 2000.

[107] P. Solin, D. Andrs, J. Cerveny, and M. Simko. PDE-independent adaptive hp-FEM based on hierarchic extension of finite element spaces. *Journal of Computational and Applied Mathematics*, Vol. 233, No. 12, pp. 3086–3094, 2010.

[108] M.T. Solodyak. Mathematical Model of Magnetothermoelasticity of Ferromagnetic Bodies. *Materials Science*, Vol. 36, No. 1, 2000.

[109] C. Taylor and P. Hood. A Numerical Solution of the Navier-Stokes Equations Using the Finite Element Technique. *Computers and Fluids*, Vol. 1, pp. 73-100, 1973.

[110] R.L. Taylor, K.S. Pister, and L.R. Herrmann. On a Variational Theorem for Incompressible and Nearly-Incompressible Orthotropic Elasticity. *Int. J. Solids Structures*, Vol. 4, pp. 875-883, 1968.

[111] J. Trevelyan. *Boundary Elements for Engineers: Theory and Application*. Computational Mechanics Publications, 1994.

[112] C. Truesdell (Editor), S.S. Antman, D.E. Carlson, G. Fichera, M.E. Gurtin, and P.M. Naghdi. *Mechanics of Solids: Volume 2: Linear Theories of Elasticity and Thermoelasticity, Linear and Nonlinear Theories of Rods, Plates, and Shells*. Springer, Berlin, 1984.

[113] M.J. Turner, R.W. Clough, H.C. Martin, and L.J. Topp. Stiffness and Deflection Analysis of Complex Structures. *Journal of the Aeronautical Sciences*, Vol. 23, No. 9, pp. 805-823, 1956.

[114] H.P. Uranus and H.J.W.M. Hoekstra. Modeling of Microstructured Waveguides Using a Finite-element-based Vectorial Mode Solver with Transparent Boundary Conditions. *Optics Express*, Vol. 12, No. 12, pp. 2795-2809, 2004.

[115] T. Vejchodsky, P. Solin, and M. Zitka. Modular *hp*-FEM system HERMES and its application to Maxwell's equations. *Mathematics and Computers in Simulation*, Vol. 76, Issues 1–3, pp. 223–228, 2007.

[116] R. Verfürth. Robust a posteriori error estimators for a singularly perturbed reaction-diffusion equation. *Numerische Mathematik*, Vol. 78, pp. 479–493, 1998.

[117] R. Verfürth. Robust a posteriori error estimates for stationary convection-diffusion equations. *SIAM Journal on Numerical Analysis*, Vol. 43, pp. 1766–1782, 2005.

[118] U. Villa. *Scalable Efficient Methods for Incompressible Fluid-dynamics in Engineering Problems*. Thesis (Ph.D.) Emory University. Atlanta, 2012.

[119] C. Vokas. *Implementation of Coupled Problems using the Finite Element Method*. Thesis (Master) Hamburg University of Technology. 2008.

[120] C. Vokas and M. Kasper. Adaptation in coupled problems. *COMPEL - The International Journal for Computation and Mathematics in Electrical and Electronic Engineering*, Vol. 29, Issue 6, pp. 1626–1641, 2010.

[121] C. Vokas and M. Kasper. Adaptation in Multi-nature Problems. *The 8th International Symposium on Electric and Magnetic Fields*, Mondovi, Italy, May 26-29, 2009.

[122] C. Vokas and M. Kasper. FEM implementation and *p*-adaptation of coupled problems. *Proceedings of the 13th IGTE Symposium*, Graz, Austria, 2008.

[123] A.R. Wieting, P. Dechaumphai, K.S. Bey, E.A. Thornton, and K. Morgan. Application of Integrated Fluid-thermal-structural Analysis Methods. *Thin-Walled Structures*, Vol. 11, Issues 1–2, pp. 1–23, 1991.

[124] K.K. Wong. *Properties of Lithium Niobate*. The Institution of Electrical Engineers, London, 2002.

[125] P. Wriggers. *Nonlinear Finite Element Methods*. Springer-Verlag, Berlin Heidelberg, 2008.

[126] S.C. Xue, N. Phan-Thien, and R.I. Tanner. Numerical study of secondary flows of viscoelastic fluid in straight pipes by an implicit finite volume method. *Journal of Non-Newtonian Fluid Mechanics*, Vol. 59, Issues 2–3, pp. 191–213, 1995.

[127] G.F. Yao. A Computational Model for Simulation of Electroosmotic Flow in Microsystems. *Technical Proceedings of the 2003 Nanotechnology Conference and Trade Show, Volume 1*, San Francisco, USA, 2003.

[128] H.T. Yau, C.C. Wang, C.C. Cho, and M.J. Jang. Numerical Simulation of an Electrokinetic Micromixer Using Harmonic and Chaotic Electric fields. *Proceedings of the 2009 4th IEEE International Conference on Nano/Micro Engineered and Molecular Systems*, Shenzhen, China, 2009.

[129] G. Yu, W.J. Mansur, J.A.M. Carrer, and S.T. Lie. A more stable scheme for BEM/FEM coupling applied to two-dimensional elastodynamics. *Computers & Structures*, Vol. 79, Issue 8, pp. 811–823, 2001.

[130] Y. Zhang, L. Song, M. Deffenbaugh, and M.N. Toksöz. A finite difference method for a coupled model of wave propagation in poroelastic materials. *The Journal of the Acoustical Society of America*, pp. 2847–2855, 2010.

[131] O.C. Zienkiewicz. Origins, Milestones and Directions of the Finite Element Method - A Personal View. *Archives of Computational Methods in Engineering*, Vol. 2, No. 1, pp. 1-48, 1995.

[132] O.C. Zienkiewicz, R.L. Taylor, and J.Z. Zhu. *The Finite Element Method: Its Basis and Fundamentals*. Elsevier Butterworth-Heinemann, Oxford, 2005.

[133] O.C. Zienkiewicz and Y.K. Cheung. The finite element method for analysis of elastic isotropic and orthotropic slabs. *Proc. Inst. Civ. Eng.*, 28:471–488, 1964.